2019

NCREE Research

Programs and Accomplishments

National Center for Research on Earthquake Engineering
National Applied Research Laboratories

Contents

1 **Observed Pulse-Liked Ground Motion and Rupture Directivity Effect in Taiwan Ground Motion Dataset**
Shu-Hsien Chao , Chun-Hsiang Kuo, Hsin-Hua Huang, Chiao-Chu Hsu and Jyh-Cherng Jan

5 **Comparison of Vertical Fourier Amplitude Spectra for S-wave And P-wave Windows in Taiwan**
Jyun-Yan Huang, Yu-Wen Chang, Che-Min Lin and Chun-Hsiang Kuo

9 **Study on Structural Collapse Behavior of Mid- to High-Rise RC Building under Near-Fault Earthquakes**
F.P. Hsiao, P.W. Weng, W.C. Shen, Y.A. Li, Tirza Paramitha, R.J. Tsai, Y.C. Hsu and S.J. Hwang

13 **Fragility Curves of the Simple Single-Degree-of-Freedom Model of the Design Example of the Civil 404-100 Code**
Yeong-Kae Yeh and Te-Kuang Chow

17 **Experimental Study of Embedded Steel Plate Composite High-Strength Reinforced Concrete Coupling Beams of Shear Walls**
Min-Lang Lin, Chao-Hsun Huang and Bo-Yen Chen

21 **Seismic Analysis of Vertically Irregular Buildings**
Jui-Liang Lin, Chih-Chia Tsaur and Keh-Chyuan Tsai

25 **Technology of Seismic Detailed Evaluation and Seismic Retrofit – Development of TEASPA 4.0**
Tsung-Chih Chiou, Yu-Chih Lai and Lap-Loi Chung

28 **Applying Field Inspection Technologies for the Investigation of Pre-stressed Concrete Box Girder Bridges**
Chun-Chung Chen, Chi-Lon Jang, Bo-Han Lee and Sheng-Yuan Shiao

32 **Advanced Web Application Development for Bridge Management and Simulation (I): Technical Survey**
Kuang-Wu Chou and Chia-Chuan Hsu

36 **Development and Application of Bridge Monitoring Management System**
Kuang-Wu Chou , Chia-Chuan Hsu, Ming-Chun Lai, Ming-De, Lu and Yu-Chi Sung

40 **Health Monitoring on a Repaired Earthquake Damaged Bridge by Optic Fiber Differential Settlement Sensors**
Zheng-Kuan Lee and Chia-Chuan Hsu

44 **Truss-type Segmental Composite Structure for Temporary Rescue Bridges**
Fang-Yao Yeh, Yao-Yu Yang, Bo-Han Lee, Chia-Ming Chang and Kuo-Chun Chang

48 **Impact Effect of Moving Vehicles on Bridges**
Bo-Han Lee, Sheng-Yuan Shiao, Chun-Chung Chen, Fang-Yao Yeh and Kuo-Chun Chang

52 **Experimental Beyond Design and Residual Performances of Viscoelastic Dampers**
Chung-Han Yu, Shiang-Jung Wang, Wang-Chuen Lin, Cho-Yen Yang and Kuo-Chun Chang

57 **A Study on Important Structures and Equipment-Suspended Fire Sprinkler Piping Systems Shaking Table Tests**
George C. Yao, Min-Chi Ko and Chen-Pei Hsu

60 **Optimized Seismic Strengthening Strategies for a Typical Sprinkler-Piping System in a Hospital**
F.-R. Lin, J.-F. Chai, Y.-A. Tsai, S.-C. Tseng, P.-R. Wu, C.-Y. Su, Zhen-Yu Lin, Zhi-Yu Lai, Tzu-Chieh Chien and Wen-I Liao

65 **Study of 3D Periodic Foundation for Seismic Mitigation**

Witarto , Cho-Yen Yang , Shiang-Jung Wang , Wang-Chuen Lin , Chung-Han Yu, Yi-Lung Mo and Kuo-Chun Chang

69 **Entropy-Based Structural Health Monitoring System for Damage Detection in Multi-Bay Three-Dimensional Structures**
Tzu Kang Lin and Ana Gabriela Lainez

73 **Metaheuristic Optimization of Controller Design for Active Mass Dampers**
Pei-Ching Chen, Bryan Jevon Sugiarto and Kai-Yi Chien

77 **Study on the Static Loading History of Steel Beam-to-Column Connections with Near-Fault Effects**
Sheng-Jhih Jhuang, Ker-Chun Lin, Huang-Cheng Chen and Chui-Hsin Chen

81 **Bond Slip Behavior of Beam Main Bars within the Reinforced Concrete of Interior Beam–Column Joints**
Kai-Ning Chi, Ker-Chun Lin and Zhi-Kuo Liu

85 **Investigation of Isolation Systems with Geometrically Nonlinear Damping for Seismic Protection of Sensitive Equipment**
Chia-Ming Chang, Ting-Wei Hsu, Shieh-Kung Huang and Kung-Chun Lu

89 **Preliminary Study of the Damage Mechanisms of Hualien Harbor in the February 6, 2018 Hualien Earthquake**
Yuan-Chang Deng, Chih-Chieh Lu and Jin-Hung Hwang

93 **Preliminary Study of the Liquefaction Potential of Gravelly Soils using Shaking Table Tests**
Kuan-Yu Chen, Chia-Han Chen, Hsuan-Chih Yang and Jin-Hung Hwang

97 **Vertical Loading Analysis of Large-Diameter Monopiles using 3D Numerical Model**
Teng-Ruie Yu and Jin-Hung Hwang

101 **Shallow Crustal Velocity Structures along the**

Deformation front of the Taiwan Orogen Revealed by Ambient Seismic Noise
Yu-Chih Huang, Che-Min Lin, Hung-Hao Hsieh, Kuo-Liang Wen and Chau-Huei Chen

106 **Radon Monitoring for Earthquake Precursory and Mud Volcano Studies in Taiwan**
Vivek Walia, Shih-Jung Lin, Arvind Kumar and Ching-Chou Fu

110 **Parametric Study on the Seismic Responses of Simply-supported Bridges Crossing Fault-rupture Zones**
Hsiao-Hui Hung and Chang-Wei Huang

114 **Study of Near-Fault Effect on Sloshing Mode of Storage Liquid in Tanks**
Juin-Fu Chai, Fan-Ru Lin, Liang Shen, Wei-Hung Hsu, Zhi-Yu Lai and Tzu-Chieh Chien

119 **Analytical Study on Effects of Near-Fault Ground Motions on Seismically Isolated Structures**
Wang-Chuen Lin, Cho-Yen Yang, Chung-Han Yu, Jenn-Shin Hwang and Shiang-Jung Wang

123 **Seismic Failure Modes and Assessment of Underground Pipelines**
Hsuan-Chih Yang and Wei-Kuang Chang

128 **A Review of the Earthquake Experiences of Water Supply Systems in Taiwan and Lessons Learnt for Hazard Mitigation**
Gee-Yu Liu

132 **Online Model Updating for Advanced Hybrid Simulations**
Ming-Chieh Chuang, Kung-Juin Wang, Keh-Chyuan Tsai, Ching-Yi Tsai and You-Jin Zhon

136 **Simulation of a Cyclic Loading Test of Reinforced Concrete Column with Plastic Damage**
Wei-Tze Chang

140 **Feasibility Study on the Real-Time Hybrid Simulation of a Building Mass Damper System using a Shaking Table**
Pei-Ching Chen, Meng-Wei Dong and Po-Chang Chen

144 **Structural Control-Deep Learning Applied to Acceleration Control of a Shaking Table**
Jeffery Hsieh, James Chang, June-Shan Chen and Pei-Chin Chen

148 **Development of Seismic Impact Assessment for a Taiwan Road Network**
Cheng-Tao Yang, Chi-Hao Lin, Wei-Hsueh Huang and Yi-Jie Chuang

152 **Simulation Analysis on the Post-Earthquake Congestion of an Emergency Department**
You-Xuan Lin and Chi-Hao Lin

156 **An Application of Shaking Table and Laminar Shear Box: 1/25 Offshore Wind Turbine Model Test**
Shen-Haw Ju, Bai-Yi Huang, Chia-Han Chen, Sheng-Huoo Ni, Kuang-Yen Liu, Yung-Yen Ko, Shang-Yi Hsu, Yu-Wen Chang, Lyan-Ywan Lu and Ging-Long Lin

160 **Introduction of the Multi-Axial Seismic Test System**
Bai-Yi Huang, Chin-Ta Lai, Juin-Fu Cai and Fan-Ru Lin

164 **Hybrid Earthquake Early Warning Services**
Meng-Huang Gu and Pei-Yang Lin

168 **Capacity-Based Inelastic Displacement Spectra for Reinforced Concrete Bridge Columns**
Ping-Hsiung Wang, Kuo-Chun Chang, and Yu-Chen Ou

172 **Piezoelectric Tuned Mass Damper Designed for Footbridges**
Lap-Loi Chung, Yan-Fu Teng, Yong-An Lai and Wei-Ling Zhou

176 **Shear Strength Test of Slabs Applied to Seismic Retrofit of External RC Frames**
Chun-Hung Chen, Xian-Feng Yeh, Tao Lai, Yu-Chih Lai and Lap-Loi Chung

180 **Displacement Restraint Mechanism of Seismic Isolation Buildings**
Yu-Jen Lai, Peng-Yu Lin, Cho-Yen Yang and Lap-Loi Chung

184 **Real-Time Hybrid Testing of Friction-Type Tuned Mass Damper System**
S.Y. Chu, C.J. Kang, C.Y. Hsu, S.W. Yeh and L.Y. Lu

188 **Replacement Prioritization of Water Distribution Pipes of the Taipei Water Department**
Chin-Hsun Yeh and Gee-Yu Liu

192 **Seismic Performance of RC Frames with BRBs connected to Corbels**
An-Chien Wu and Keh-Chyuan Tsai

196 **Semi-active Control for Building Mass Damper Systems**
Yu-Fang Liu, Tzu-Kang Lin and Kuo-Chun Chang

200 **Recent Variations of the Seismic and Geochemical Observations of the Tatun Volcano Group**
Ya-chuan Lai, Hsiao-fen Lee, Li-Chin Chang, Chin-Hsing Liu and Chia-Jui Teng

204 **Seismic Testing, Analysis, and Optimization of Low-Yielding-Strength Steel Panel Dampers in Moment-Resisting Frames**
Ming-Chieh Chuang, Kung-Juin Wang, Keh-Chyuan Tsai, Ching-Yi Tsai, and You-Jin Zhon

208 **Joint Modeling of Receiver Function and Horizontal to Vertical Spectral Ratio for Shallow Shear Velocity Structures**
Che-Min Lin, Chun-Hsiang Kuo, Jyun-Yan Huang and Kuo-Liang Wen

Observed Pulse-Like Ground Motion and Rupture Directivity Effect in Taiwan Ground Motion Dataset

Shu-Hsien Chao[1], Chun-Hsiang Kuo[2], Hsin-Hua Huang[3], Chiao-Chu Hsu[4], Jyh-Cherng Jan[5]

趙書賢 [1]、郭俊翔 [2]、黃信樺 [3]、許喬筑 [4]、詹智丞 [5]

Abstract

In this study, we analyze around 40,000 available three-axis ground motion records in the Taiwan ground motion database by using a pulse indicator. Up to 200 records are identified as pulse-like ground motion with horizontal or vertical velocity pulses. We also analyze the record-specific residual of each record from approximately 300 events in the Taiwan ground motion database. Significant rupture directivity effect can be observed in several earthquakes, e.g., the 2010 JiaXian Earthquake, the 2013 NanTou Earthquake, and the 2016 Mei-Nong Earthquake. Unlike observations from the residual analysis of the NGA-West 2 Project database, we find that the rupture directivity affects the ground motion intensity not only for long-period but also for short-period spectral acceleration. We show that involving the rupture directivity model in the current ground motion model can improve ground motion prediction accuracy significantly, especially for earthquakes with strong rupture directivity effects. We also reveal that around 70% of the pulse-like ground motion records occur within ±55 degrees of the rupture directivity in the azimuthal direction. This helps in the prediction of pulse-like ground motion for future earthquakes. Methodology about how to consider the impact of the rupture directivity effect and near-fault pulse-like ground motion on ground motion intensity are proposed based on the observations in this study.

Keywords: ground motion prediction equation, rupture directivity, pulse-liked ground motion, probabilistic seismic hazard analysis

Introduction

The objective of this study is to evaluate the observed pulse-like ground motion and rupture directivity effect in Taiwan and to propose a model to quantify their impact on ground motion intensity. First, we analyzed approximately 40,000 available three-axis ground motion records in the Taiwan ground motion database by using a pulse indicator (Shahi and Baker, 2014), and up to 200 records were identified as pulse-like ground motion with horizontal or vertical velocity pulses. We also analyzed the record-specific residual of each record from approximately 300 events in the Taiwan ground motion database by using a Taiwan ground motion model (Chao et. al., 2020). A significant rupture directivity effect was observed in several earthquakes, e.g., the 2010 Jia-Xian Earthquake, the 2013 Nan-Tou Earthquake, and the 2016 Mei-Nong Earthquake. Unlike the observations from the residual analysis of the NGA-West 2 Project database, we found that the rupture directivity affects the ground motion intensity not only for long-period but also for short-period spectral acceleration. We showed that involving a rupture directivity model in the current ground motion model can improve ground motion prediction accuracy significantly, especially for earthquakes with strong rupture directivity effects. We also found that around 70% of the pulse-like ground motion records occurred within ±55 degrees of the rupture directivity in the azimuthal direction. This improves the prediction accuracy of the pulse-like ground motion for future earthquakes. Methodology

[1] Associate Researcher Fellow, National Center for Research on Earthquake Engineering, Taipei, Taiwan
[2] Researcher Fellow, National Center for Research on Earthquake Engineering, Taipei, Taiwan
[3] Assistant Researcher Fellow, Institute of Earth Sciences, Academia of Sinica, Taipei, Taiwan
[4] Research Assistant, National Center for Research on Earthquake Engineering, Taipei, Taiwan
[5] Assistant Researcher Fellow, Central Weather Bureau, Taipei, Taiwan

about how to consider the impact of the rupture directivity effect and near-fault pulse-like ground motion on ground motion intensity will be proposed on the basis of the observations in this study.

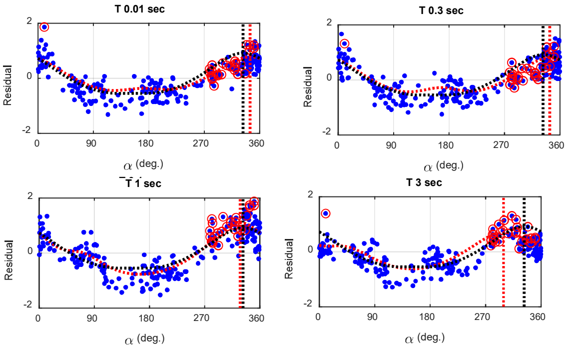

Fig. 1. Record-specific residual of the 2016 MeiNong Earthquake w.r.t. azimuth plots for PGA and Sa of three periods. The red dotted lines show the individually fitted directivity model and the black dotted lines show the fitted directivity model of PGV.

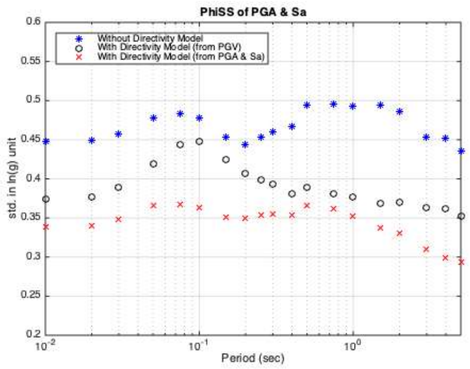

Fig. 2. Comparison of PhiSS of each period with and without considering the directivity model effect from PGV and Sa individually.

Proposed Model for Rupture Directivity Effect

In this study, the following equations are used to fit the record-specific residuals of each event to quantify the rupture directivity:

$$f_D = \ln(0.5\sqrt{\frac{(1+e)^2}{(1-r_v\cos(\alpha-\alpha_D))^2}+\frac{(1-e)^2}{(1+r_v\cos(\alpha-\alpha_D-\phi))^2}}) - \frac{f_D^0}{360} \quad (1)$$

where

$$f_D^0 = \int_0^{360}\ln(0.5\sqrt{\frac{(1+e)^2}{(1-r_v\cos(\alpha-\alpha_D))^2}+\frac{(1-e)^2}{(1+r_v\cos(\alpha-\alpha_D-\phi))^2}})d\alpha \quad (2)$$

Here, α is site-to-hypocenter azimuth; α_D is the site-to-hypocenter azimuth of the rupture directivity direction; r_v is the velocity ratio between the rupture velocity and the shear wave velocity; e is the coefficient of percent unilateral rupture; ϕ is the deviation angle between primary and secondary rupture directions. This function form is revised from the equation proposed by Boatwright (2007), which has been applied in several studies (Convertito et. al., 2017; Jan et. al., 2018). The term f_D^0 is added to represent the zero-mean of the record-specific residuals of each event. Figure 5 illustrates the proposed directivity functions f_D for different model parameters r_v, e, and ϕ. A stronger rupture directivity effect on ground motion will be observed for the event with a larger velocity ratio r_v and greater unilateral rupture while e is close to 1.

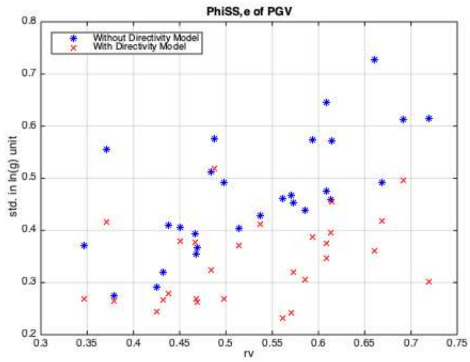

Fig. 3. Comparison of PhiSS,e of PGV with and without considering the directivity model

We inferred the directivity model parameters of each event by fitting the record-specific residuals of each event by two approaches:

[1] Fit the record-specific residuals of PGV as the directivity model parameters for PGA, PGD, and all periods of Sa.

[2] Fit the record-specific residuals of PGA, PGV, PGD and all periods of Sa individually.

Figure 1 illustrates an example of the fitting results. The red dotted lines show the individually fitted directivity model, and the black dotted lines show the fitted directivity model of PGV. The overall trend of the directivity effect for different periods of Sa are similar, but the inferred directivity model parameters are different for each period. Figure 2 shows the comparison of the standard deviation of all record-specific residuals (PhiSS) for each period without considering the directivity model and by considering the directivity effect model from PGV and from individual fitting. Irrespective of the kind of approach used to derive the model parameters of the directivity effect, the standard deviation can be reduced significantly. Figure 3 shows a comparison of the standard deviation of the record-specific residuals per event (PhiSS,e) of PGV versus inferred r_v plot without and by considering the directivity model. The PhiSS,e of events with stronger directivity effect (higher r_v) decreases more significantly. We also surveyed the inferred model parameters of the proposed directivity model. It can be seen that the directivity parameter r_v ranges from 0.4 to 0.7. The model parameters e and ϕ are uniformly distributed from 0 to 1 and from -90 to 90 degree, respectively. This can help us to determine the model parameters while predicting the ground motion intensity for future earthquakes.

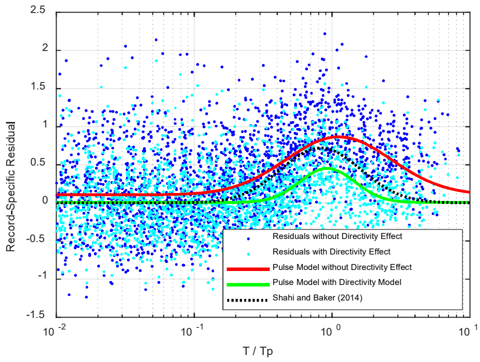

Fig. 4. Record-specific residuals versus T/Tp plots and fitted pulse model before considering the rupture directivity effect and after considering the rupture directivity effect with individual fitting model parameters.

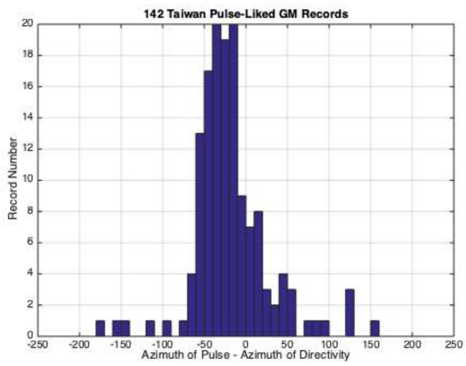

Fig. 5. Histogram of the azimuth difference between pulse-like motion and the directivity direction.

Proposed Model of Pulse-Like Ground Motion

In this study, the following equation is used to fit the record-specific residuals of the selected pulse-like ground motion:

$$f_P = a_0 + a_1 \exp(a_2(\ln(\frac{T}{T_P}) - a_3)^2)\qquad (3)$$

Here a_0–a_3 are model coefficients; Tp is the pulse period of each pulse-like record. This function form is the same as the equation proposed by Shahi and Baker in the Directivity Working Group of NGA-West 2 Project (Spudich et. al., 2014). We fit this pulse model to the record-specific residuals before considering the rupture directivity effect and after considering the rupture directivity effect with individual fitting model parameters. The analysis results are shown in Table 1 and Figure 4. It is found that before considering the rupture directivity effect, the stronger pulse model will be derived because the pulse-like ground motion mostly occurs in the forward directivity direction. Figure 5 shows the histogram of the azimuth difference between pulse-like motion and the directivity direction. Most of the pulse-like ground motion records occur at an azimuthal difference of approximately ±55 degrees of the pulse direction. Based on these analysis results, we suggest that the pulse model should be considered while the azimuth difference is within ±55 degrees, and use the proposed directivity model along with the proposed pulse model fitted by using the record-specific residuals after considering the rupture directivity effect to predict the ground motion intensity of future earthquakes.

Table 1. Model coefficients of pulse model

	Without considering directivity model	**Considering directivity model**
a_0	0.1059	0.0054
a_1	0.7612	0.4478
a_2	-0.6443	-2.3584
a_3	0.1099	-0.0816

Application of the Proposed Models for the 2016 Mei-Nong Earthquake

Based on the result of the previous analysis, we suggest predicting ground motion intensity by using a Taiwan ground motion model (Chao et. al., 2020) with additional two terms to consider the rupture directivity effect and pulse-like ground motion as:

$$\begin{aligned} ln\,S_a = lnS_a^{ref} + S_{source} + S_{path} + S_{site,lin} \\ + S_{site,non} \\ + f_D + f_P I_P + \delta_e + \delta_s + \delta_{r,DP} \qquad (4) \end{aligned}$$

Here $\delta_{r,DP}$ is the record-specific residual after considering the rupture directivity model f_D and pulse model f_P; I_P is 1 for the pulse-like ground motion and 0 for others. Figure 6 shows the observed and predicted ground motion intensity maps of the 2016 Mei-Nong Earthquake by using the proposed model for PGA with and without considering the rupture directivity model and the pulse model. The directivity model parameters from individual fitting are used, and stations within a difference of ±55 azimuthal degrees and with Rrup < 70 km are all assumed as pulse-like ground motion for the prediction in this case study. Tp is calculated based on the previously mentioned Taiwan Mw-Tp relationship for all stations with pulse-like ground motion. The intensity levels are defined based on the intensity level

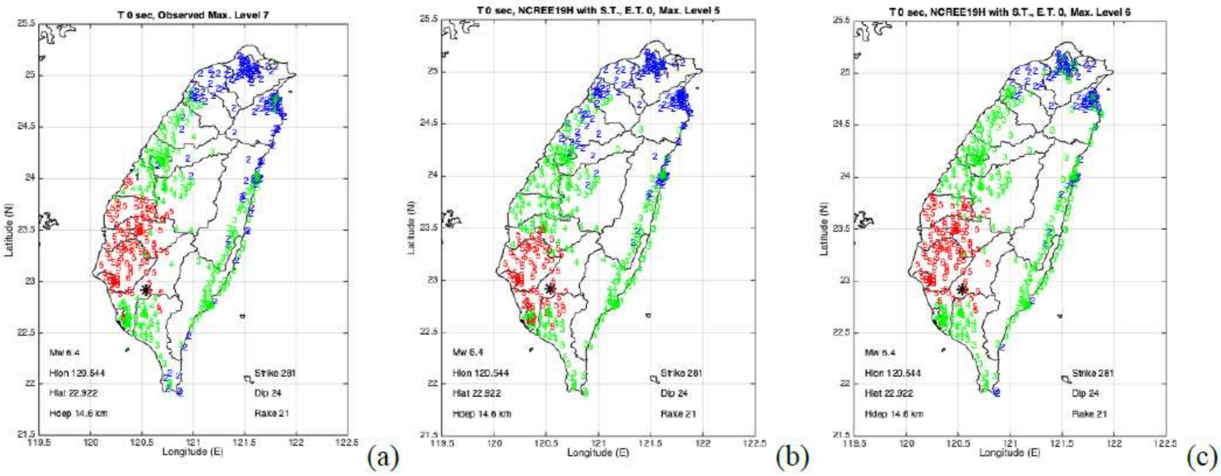

Fig. 6. Intensity map of the 2016 Mei-Nong Earthquake (a) observed intensity of PGA; (b) predicted intensity of PGA without the proposed models; (c) predicted intensity of PGA with the proposed models.

of the ground motion defined by the Center Weather Bureau for PGA. It is found that the ground motion intensity for stations in the rupture directivity direction is significantly underestimated while the rupture directivity model and the pulse model are not considered.

Conclusions

In this study, we analyzed approximately 40,000 available three-axis ground motion records in the Taiwan ground motion database by using pulse indicators, and up to 200 records were identified as pulse-like ground motion with horizontal or vertical velocity pulses. We also analyzed the record-specific residual from around 300 events in the Taiwan ground motion database. Significant rupture directivity effect was observed in several earthquakes, e.g., the 2010 Jia-Xian Earthquake, the 2013 Nan-Tou Earthquake, and the 2016 Mei-Nong Earthquake. Methodology to consider the impact of the rupture directivity effect and the near-fault pulse-like ground motion on ground motion intensity was also proposed based on the observations in this study. Key findings of this study include:

[1] Unlike the observations from the residual analysis of NGA-West 2 Project, we found that the rupture directivity influences the ground motion intensity not only for long-period but also for short-period spectral acceleration.

[2] Most of the pulse-like ground motion records occur at an azimuthal difference of around ±55 degrees of the pulse direction.

[3] The ground motion intensity for stations in the rupture directivity direction will be significantly underestimated while the rupture directivity model and the pulse model are not considered.

The proposed models as well as the inferred model parameters in this study can provide a good basis to predict ground motion intensity for future earthquakes.

References

Boatwright, J. (2007). The persistence of directivity in small earthquakes. Bulletin of the Seismological Society of America, 97, 1850–1861. Seismological Research Letters, 80(5), 682–693. https://doi.org/10.1785/gssrl.80.5.682.

Chao, S. H., Chiou, B., Hsu, C. C. and Lin, P. S. (2020) A horizontal ground-motion model for crustal earthquakes and subduction earthquakes in Taiwan, Earthquake Spectra, published online first. https://doi.org/10.1177/8755293019891711.

Convertito, V., Caccavale, M., De Matteis, R., Emolo, A., Wald, D., and Zollo, A. (2012). Fault extent estimation for near-real-time ground-shaking map computation purposes. Bulletin of the Seismological Society of America, 102(2), 661–679. https://doi.org/10.1785/0120100306

Jan, J. C., Huang, H. H., Wu, Y. M., Chen, C. C., and Lin, C. H. (2018). Near-real-time estimates on earthquake rupture directivity using near-field ground motion data from a dense low-cost seismic network. Geophysical Research Letters, 45, 7496–7503. https://doi.org/10.1029/2018GL078262.

Shahi, S.K. and Baker, J.W. (2014). An efficient algorithm to identify strong velocity pulses in multi-component ground motions. Bulletin of the Seismological Society of America, 104(5), 2456–2466.

Spudich, P., Rowshandel, B., Shahi, S.K., Baker, J.W. and Chiou, B. (2014). Comparison of NGA-West2 Directivity Models. Earthquake Spectra: August 2014, 30(3), 1199-1221.

Comparison of Vertical Fourier Amplitude Spectra for S-wave and P-wave Windows in Taiwan

Jyun-Yan Huang[1], Yu-Wen Chang[2], Che-Min Lin[3] and Chun-Hsiang Kuo[3]

黃雋彥[1]、張毓文[2]、林哲民[3]、郭俊翔[3]

Abstract

Site effects are one of the most important aspects of engineering seismology studies. Traditionally, considerable efforts have focused on horizontal, rather than vertical, motions because the contribution of shear waves to seismic energy is higher and easily correlated with seismic disasters and loss estimation. Researchers are mostly familiar with horizontal site responses for seismic hazard evaluation of a specific site (*e.g.*, power plants) and commonly generate a 1/2th to 2/3rds reduction for vertical motions in the general region and near-fault region, respectively. However, the empirical relationships for horizontal motion still lack sufficient observation and theoretical support. Meanwhile, vertical site responses have received more attention in recent years in site-specific studies through the use of vertical-to-horizontal strong-motion models. In Taiwan, a horizontal seismic hazard of a shear wave velocity of 760 m/s for generic rock conditions has been established and other applications of vertical motions have commenced. Basic concepts of seismic wave propagation suggest that vertical motion should primarily be associated with P waves, which would imply that most seismic events are adequately characterized by P-wave-related parameters (including bulk modulus, P-wave velocity, and vertical kappa) and that S-wave-related parameters (such as Young's modulus, S-wave velocity, and kappa) are not required. In order to verify this, the frequency content of vertical motion should be investigated. This study analyses the Fourier amplitude spectra (FAS) energy associated with vertical motions of Taiwanese earthquakes. The FAS study indicates that most of the energy was generated from shear waves and not from compressional waves even in vertical motion, and this needs to be considered in hazard evaluation in Taiwan. Finally, rock sites in Taiwan with V_{s30} of 600–900 m/s were evaluated to compare vertical site responses.

Keywords: vertical site response, Taiwan, FAS

Introduction

Evaluation of seismic wave attenuation based on Fourier amplitude spectra (FAS) has gained importance in engineering seismology in recent years compared to more commonly used response spectra because increasingly more physical meaning can be extracted and related to the real world. In order to reduce the gap between traditional engineering practices and understanding physically based models, a number of analytical procedures have been widely applied recently. These include FAS-based non-ergodic ground-motion prediction, random vibration theory, kappa-driven adjustable models, and regional difference studies (Bora *et al*., 2014; Bora *et al*., 2015; Campbell, 2014; Hassani and Atkinson, 2018; Landwehr *et al*., 2016). Most of these studies focused on horizontal motions but not vertical ones. In addition, studies pertaining to the vertical-to-horizontal (V/H) ratio between parameters such as peak acceleration (Bommer *et al*., 2011; Bozorgnia and Campbell, 2016) were primarily applied to account for vertical seismic response rather than a traditionally used scale factor derived from horizontal ground motion.

It is seismologically intuitive that P waves should dominate the vertical seismic energy if a pure vertical

[1] Assistant Research Fellow, National Center for Research on Earthquake Engineering
[2] Associate Research Fellow, National Center for Research on Earthquake Engineering
[3] Research Fellow, National Center for Research on Earthquake Engineering

incident wave propagating to a surface site through a homogeneous-layered Earth is assumed. However, many observations suggest that a greater amount of shear-wave energy is involved even in vertical ground motions, and the apportionment of this energy forms the basis of this study. Vertical ground motions were considered to be characterized by the average shear-wave velocity from the surface to a depth of 30 meters (V_{s30}). Sites with V_{s30} = 600–900 m/s were selected from records of the Taiwan Strong Motion Instrumentation Program (TSMIP) and their data were then used to compare the FAS energy of P- and S-wave windows. The results of the study provide a better understanding of the vertical site response for individual sites and will assist in the estimation of future seismic hazards.

Data Analysis

Strong motion records were selected from NCREE (2018; hereafter referred to as the NCREE database), which contains data from TSMIP, and their flat-files were rearranged to suit the purposes of seismic hazard evaluation of important public facilities in Taiwan. Procedures for constructing windowed P- and S-waves and their FAS followed those of the Next Generation Attenuation – East project (NGA-East, Kottke *et al*., 2018) to ensure consistency when applying random vibration theory from FAS to response spectra studies. Smooth and down-sampling (S-DS) FASs were generated for records in both horizontal and vertical ground motions in the NCREE database. Four example windows that were applied are shown in Fig. 1. They are the pre-event 5 s window (preP, purple color, lower diagram in each example), the P-wave window using the P arrival to S arrival time (PW, green color), and the S-wave window from the S arrival to a time corresponding to 90% of the cumulative energy from the S arrival time (SW, red color). Records with no clear P-wave or S-wave arrivals and those lacking pre-event records (preP window length <5 s) were eliminated from this analysis. A total of 32,685 records during the period 1992–2018 were checked initially and, of these, 4889 rock motions were extracted for further discussions of vertical motions.

Results and Discussions

Comparing the frequency contents of the P- and S-wave windows in the example waveforms and FASs in Fig. 1 reveals several general behaviors including either: 1. S waves dominate in the low-frequency band (*i.e.*, below 15 Hz), 2. S waves have higher energy in all frequency bands, 3. S and P waves exhibit similar energy levels, 4. P waves dominated over the whole frequency range. In addition, in high frequency bands, the P and S energies became small and approached a similar level to the pre-event noise level at around 30–50 Hz, which might be due to faster attenuation in the high-frequency band dependent on traveling distance. Meanwhile, the fourth observation might relate to the far-field (*i.e.*, a rupture distance greater than 100 km) characteristics that might result from the different attenuation rates between the P and S waves (*i.e.*, an S wave would attenuate faster since its velocity is lower).

The average FAS ratios of SW/PW were checked to identify which situation controlled the main FAS difference between P and S waves (Fig. 2). The grey region shows the range of SW/PW ratios between 10^{-2} and 10^{2} where, in general, the dominant energy of the P and S waves of vertical motion changed interdependently. However, in the average response from the NCREE database, the S waves clearly dominate in the low-frequency band (*i.e.*, below 15 Hz). S and P energies have similar levels in the mid-frequency range (*i.e.*, 15–30 Hz) and this implies similar influence of the kappa with high frequency because site-related attenuation would be the same for P and S waves in vertical motion. In contrast, high-frequency behaviors from 30 to approximately 60 Hz might be mainly influenced by a distance scaling relation that causes the attenuation rates of seismic waves to differ when they propagate over different distances. Finally, the behaviors in the frequency range above 60 Hz were inconclusive, as the P and S energies might decay to pre-event noise levels and the FAS ratio might include more random effects, although the S wave is still dominant in this frequency range. However, vertical site effects in this range were checked for a subset of data for V_{s30} = 600–900 m/s, indicated by the red lines in Fig. 3. The results show that the vertical site response did not significantly influence the average trends for S and P energies and that there are practically no changes in the FAS ratios in comparison to all data for average site classification.

Surface waves might need to be paid more attention for investigation of vertical motion, but they are not easy to identify and separate from the NCREE database. Examples of FAS from surface wave windows, shown in Fig. 4, indicate that surface waves might have half the energy level or less in the low-frequency range compared to P or S waves in vertical motion. This might need to be taken into account in the near future.

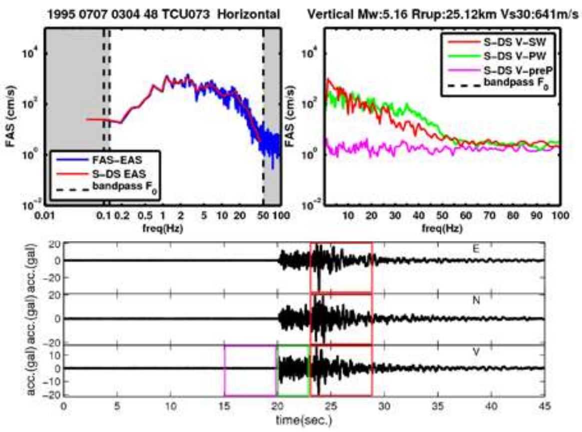

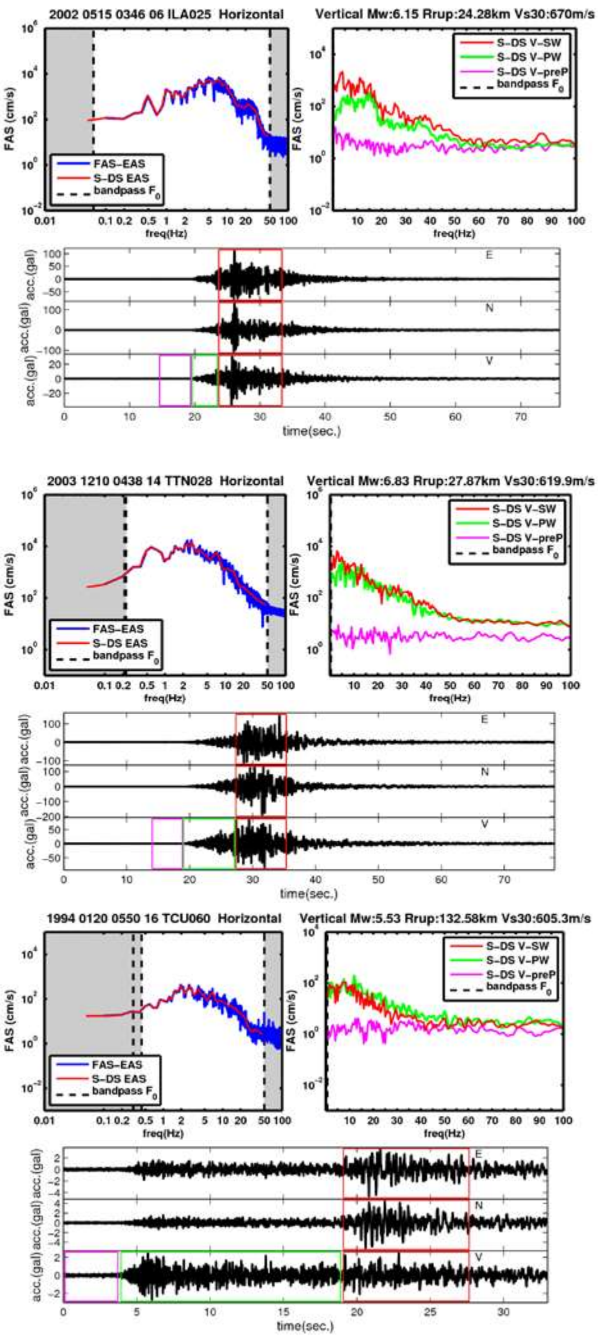

Fig. 1. Examples of horizontal and vertical FAS values from the NCREE database. Smoothed and down-sampled (S-DS) effective amplitude spectra (EAS) were used for horizontal motion and S-DS preP, PW, and SW were calculated for vertical motion.

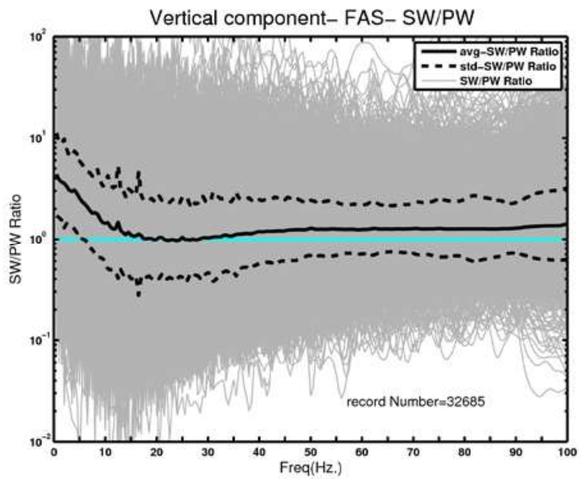

Fig. 2. FAS ratios SW/PW for vertical motions. Grey lines are individual records, the solid black line is the average, and dashed black lines are the standard deviation. The light blue line indicates a ratio equal to 1.

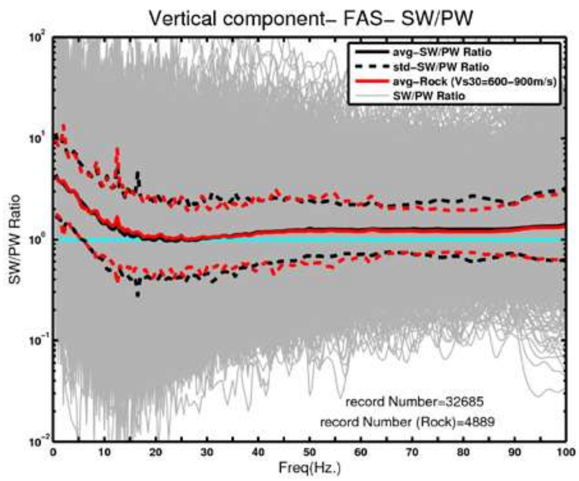

Fig. 3. Subset of FAS ratios for ground motions with V_{s30} = 600–900 m/s.

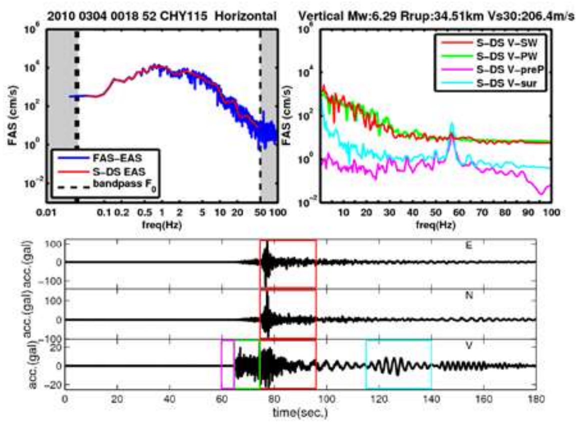

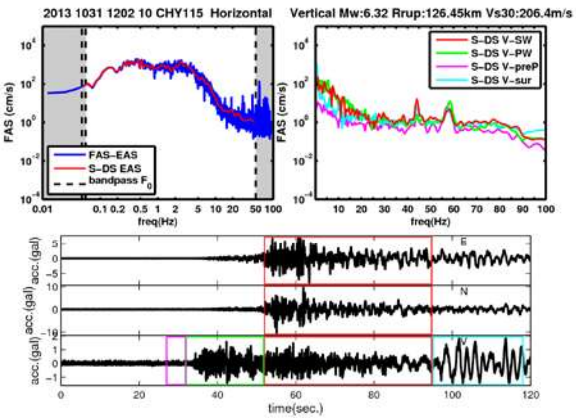

Fig. 4. Examples of apparent waveforms and FAS for surface waves.

Conclusions

In this study, the frequency contents of different sampling windows, including P waves, S waves, and pre-events, of the vertical component of Fourier amplitude spectra were established. In general, the energies in the P- and S-wave windows were changed interdependently in different frequency bands. Examination of the average SW/PW ratio for vertical motion indicated that S waves dominated at low frequency, have similar energy levels to P waves in the mid-frequency range, and became slightly larger in the higher-frequency band. In addition, when ground motion was subtracted, the vertical site response from the SW/PW ratios did not show a difference in comparison to all site classifications. However, the energy of surface waves might influence the spectral shape, which will need to be considered in future applications.

References

Bommer, J. J., Akkar, S. and Kale, Ö. (2011), "A Model for Vertical-to-Horizontal Response Spectral Ratios for Europe and the Middle East", *Bull. Seism. Soc. Am.* 101(4), 1783-1806.

Bora, S. S., Scherbaum, F., Kuehn, N. and Stafford, P. (2014), "Fourier Spectral and Duration Models for the Generation of Response Spectra Adjustable to Different Source, Propagation, and Site Conditions", *Bull. Earthquake Eng.* 12, 467-493.

Bora, S. S., Scherbaum, F., Kuehn, N., Stafford, P. and Edwards, B. (2015), "Development of a Response Spectral Ground-Motion Prediction Equation (GMPE) for Seismic-Hazard Analysis from Empirical Fourier Spectral and Duration Models", *Bull. Seism. Soc. Am.* 105(4), 2192-2218.

Bozorgnia, Y. and Campbell, K. W. (2016), "Ground Motion Model for the Vertical-to- Horizontal (V/H) Ratios of PGA, PGV, and Response Spectra", *Earthquake Spectra* 32(2), 951-978.

Campbell, K. (2014), "An Evaluation of Eastern North American Ground-Motion Models Developed Using the Hybrid Empirical Method", *Bull. Seism. Soc. Am.* 104(1), 347-359.

Hassani, B. and Atkinson, G.M. (2018), "Adjustable Generic Ground-Motion Prediction Equation Based on Equivalent Point-Source Simulations: Accounting for Kappa Effects", *Bull. Seism. Soc. Am.* 108(2), 913-928.

Kottke, A., Abrahamson, N. A., Boore, D. M., Bozorgnia, Y., Goulet, C., Hollenback, J., Kishida, T., Kiureghian, A. D., Ktenidou, O. J., Kuehn, N., Rathje, E. M., Silva, W. J., Thompson, E. and Wang, X. (2018), "Selection of Random Vibration Procedures for the NGA-East Project", PEER 2018/05, Pacific Earthquake Engineering Research Center, University of California, Berkeley, California, pp46.

Landwehr, N., Kuehn, N. M., Scheffer, T. and Abrahamson, N., (2016). "A Nonergodic Ground-Motion Model for California with Spatially Varying Coefficients", *Bull. Seism. Soc. Am.* 106(6), 2574-2583.

National Center for Research on Earthquake Engineering (NCREE) (2018), Web Page for Reevaluation of Probabilistic Seismic Hazard of Nuclear Facilities in Taiwan Using SSHAC Level 3 Methodology Project, available at http://sshac.ncree.org.tw.

Study on Structural Collapse Behavior of Mid- to High-Rise RC Building under Near-Fault Earthquakes

F.P. Hsiao[1], P.W. Weng[2], W.C. Shen[2], Y.A. Li[3], Tirza Paramitha[2], R.J. Tsai[2] , Y.C. Hsu[2] and S.J. Hwang[2]

Abstract

The near-fault effect on buildings and infrastructures is a significant issue for the safety of human life and property in Taiwan, because there are numerous active faults in the island. It is well known that near-fault earthquakes possess special characteristics of large displacement and high velocity. However, it is difficult to reproduce such near-fault earthquake records using the existing test facilities of the National Centre for Research on Earthquake Engineering (NCREE), thus limiting experimental studies on the near-fault effect. Furthermore, many buildings were severely damaged in the Meinong earthquake in 2016. Among them, some mid-to-high-rise buildings were severely damaged or collapsed and resulted in numerous casualties. In recent years, an increasing number of residential or commercial buildings have been constructed. Thus, the casualty risk caused by the collapse of mid-to-high-rise buildings should not be underestimated, and developing methods of seismic assessment for mid-to-high-rise buildings to identify those with high collapse risk is a critical issue. The NCREE established at the Tainan Laboratory a high-performance six-degree-of-freedom seismic simulation testing system that can simulate near-fault motions. Since the completion of this facility, the NCREE has been providing improved seismic experimental services to government agencies, academia, and industries, which is beneficial to improving public safety during earthquake disasters.

This study focuses on the experimental results of collapse tests conducted on the new shaking table at the Tainan Laboratory. The test results are compared with the results of the proposed seismic assessment method. This study can offer abundant information on reinforced concrete (RC) frame collapse behavior and help researchers upgrade existing analytical models to improve the prediction of seismic behavior of RC buildings, as well as enhance economic improvement.

Keywords: Near-fault effect; Reinforced concrete structure; Shaking table test; Mid- and high-rise building.

Introduction

The effect of near-fault earthquakes on buildings and infrastructures is a significant issue for the safety of human life and property in Taiwan, which has numerous active faults. It is well known that near a fault, earthquake ground motions exhibit large displacements and high velocity. However, it was difficult to reproduce such near-fault earthquake ground-motion records using the existing test facilities of the National Center for Research on Earthquake Engineering (NCREE), thus limiting experimental studies on the near-fault effect. In 2016, many buildings were severely damaged during the Meinong earthquake. Among them, some mid-to-high-rise buildings were severely damaged or collapsed and resulted in numerous casualties. Recently, more residential or commercial buildings have been constructed. Thus, the casualty risk caused by the collapse of mid-to-high-rise buildings should not be underestimated, and the method of seismic assessment for mid-to-high-rise buildings to identify those with high collapse risk is a critical issue. The NCREE established a laboratory in Tainan equipped with a high-performance $8 \text{ m} \times 8 \text{ m}$ six-degree-of-freedom seismic simulation testing system, which can simulate near-fault ground motions. Since the completion of the Tainan Laboratory facility, the NCREE has been

[1] National Center for Research on Earthquake Engineering, Taipei, Taiwan; Department of Civil Engineering, National Cheng Kung University, Tainan, Taiwan
[2] National Center for Research on Earthquake Engineering, Taipei, Taiwan
[3] Department of Civil Engineering, National Chung Hsing University, Taichung, Taiwan

providing better seismic experimental services to government agencies, academia, and industries, which is beneficial to improving public safety during earthquake disasters.

This study focuses on the experimental results of the collapse tests conducted on the new shaking table at the Tainan Laboratory. The test results are then compared with the results of the proposed seismic assessment method. Finally, it is confirmed that the proposed experimental method can provide abundant information regarding the collapse behavior of reinforced concrete (RC) frames and help researchers to upgrade existing analytical models, thereby achieving better predictions for RC buildings' seismic behavior, as well as enhancing economic improvement.

Since the occurrence of the Chi-Chi earthquake on September 21st, 1999, the Taiwan government has been working on seismic evaluation and retrofitting of public buildings that have been identified as old buildings with insufficient seismic capacity. Among many cases, seismic retrofitting for public schools is a program promoted by the Ministry of Education and executed by the NCREE. It is considered a success as 90% of the public school buildings have been retrofitted. However, recent earthquakes such as the 0206 Meinong earthquake and Hualien earthquake have shifted our retrofitting attention from public buildings to private buildings as many of them do not have sufficient seismic performance. Commercial and residential mixed buildings are easily damaged during earthquakes because of their soft and weak story behavior. A similar tendency is found in Japan as well.

Experimental Specimen Design

We used the new facility to perform a series of start-up tests during the grand opening and conduct an international blind competition.

Figures 1–3 show the setup of the start-up tests on 3-, 7-, and 9-story RC structures (at half scale). A demonstration test with the 3-story specimen was conducted during the grand opening of the NCREE Tainan Laboratory on August 9 in 2017. The 7-story specimen was tested for an international blind competition held the following year.

A development platform for collapse prevention technology for mid--to-high-rise buildings was established after the project was completed. Numerical analysis was compared with experimental results to understand the structural behavior of RC buildings under near-fault earthquakes. This study focuses on the experimental results of the collapse tests and discusses the failure types of specimens. The shaking table test results are compared with the results of existing analytical models. The comparison reveals the insufficiency of the existing analytical models.

The design of the 7-story RC building specimen with soft and weak story behavior has the following characteristics:

1. A half-scale RC structure with non-ductile detailing.

2. Modulus design assembled with a 9-story, 7-story, 5-story, or 3-story structure.

3. Asymmetric structure design.

4. High ceiling for the 1st floor and soft story behavior.

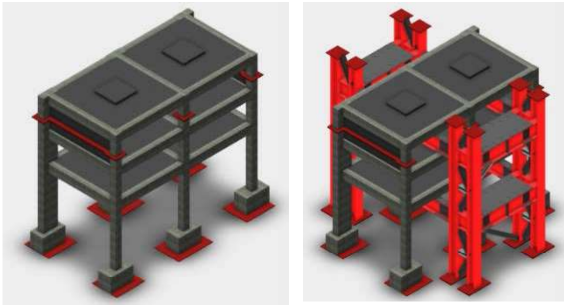

(a) Half-scale specimen (b) Specimen with a collapse prevention frame

Figure 1. Setup of the start-up test of the 3-story RC structure.

(a) Half-scale specimen (b) Specimen with a collapse prevention frame

Figure 2. Setup of the start-up test of the 7-story RC structure.

(a) Half-scale specimen

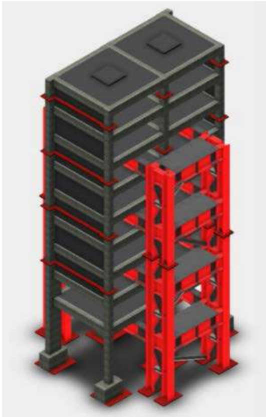

(b) Specimen with a collapse prevention frame

Figure 3. Setup of the start-up test of the 9-story RC structure.

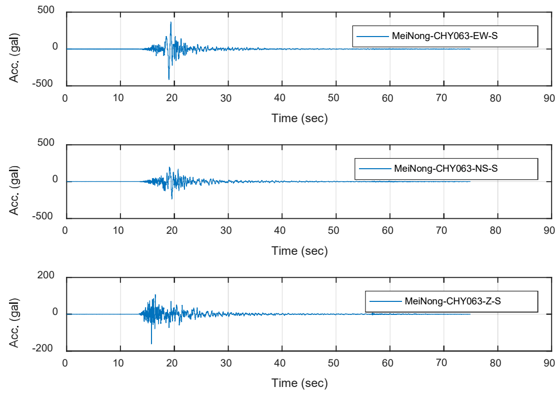

Figure 5. Tri-axial acceleration time histories for near-field earthquake data from CHY063.

Test Program and Results

Tri-axial ground-motion acceleration data recorded at seismic stations CHY015 and CHY063 were used in this study. The record from CHY015 (Fig. 4) during the 921 Chi-Chi earthquake is treated as far-field earthquake data, whereas the record from CHY065 (Fig. 5) during the 0206 Meinong earthquake is treated as near-fault earthquake data. Figure 6 shows the 7-story RC building specimen on the shaking table at the NCREE Tainan Laboratory. The ground-motion records from CHY063 with 70% intensity and those from CHY063 with 50% and 100% intensities were used as input ground motion for the test conducted on November 14. Next, the ground-motion records from CHY063 with 150% and 200% intensities were used as input ground motion for the test conducted on November 15. According to the test results, the specimen shifted from linear to nonlinear behavior, until total collapse occurred. The structural damage and collapse behavior of the 7-story RC frame building are shown in Figure 7.

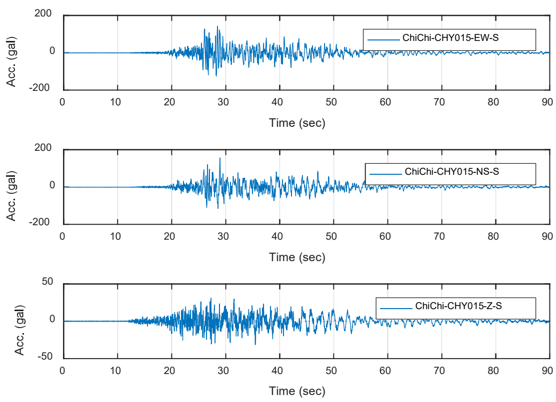

Figure 4. Tri-axial acceleration time histories for far-field earthquake data from CHY015.

(a) Small-column side-view of specimen

(b) Large-column side-view of specimen

Figure 6. 7-Story RC frame building specimen with soft and weak stories for shaking table tests.

		
(a) Overview of specimen	(b) Damage status of small column	(c) Damage status of large column

Figure 7. Structural damage and collapse behavior of the 7-story RC frame building.

Conclusions

In past years, the NCREE has conducted experimental studies on the collapse mechanisms of columns. However, it has not yet expanded to either vertical members or structural systems. Unfortunately, there are many active faults in Taiwan. A near-fault effective area is defined as that within 10 km on both sides of a first-type active fault and it affects one-third of Taiwan's population, which is over 8.6 million. Due to the characteristic high-velocity pulses and large displacements of near-fault earthquakes, the damage to buildings affected by near-fault effects is much more serious than that caused by general earthquakes. Therefore, further research on the collapse behaviors of buildings affected by near-fault effects is needed.

In 2017, the NCREE completed construction of the advanced tri-axial seismic simulator in the Tainan Laboratory located at National Cheng Kung University, Kuei-Jen Campus. This shaking table testing system has the capability of reproducing near-fault earthquake acceleration ground motion. To study the effect of near-fault seismic waves on the collapse behavior of structures, this current project conducted mega-structure experiments using this shaking table system. A shaking table test of a 3-story RC building structure was conducted during the grand opening of the facility. In this test, the acceleration ground-motion data from seismic stations TCU075 and CHY047 were inputted to compare the effects of far-field and near-fault earthquakes. In November 2018, NCREE conducted collapse experiments on a specimen of a 7-story RC frame building with soft and weak story behavior. To take near-fault earthquake effects into account, the acceleration ground-motion data from CHY015 and CHY063 were inputted. At the same time, an international blind analysis contest was held to attract attention from earthquake engineering researchers and scholars around the world and to increase the international visibility of the newly built Tainan Laboratory of the NCREE.

References

Andreas Stavridis, I. Koutromanos & P. B. Shing (2011). “Shake-table tests of a three-story reinforced concrete frame with masonry infill walls”, Earthquake Engineering Structural Dynamic, 41(6), 1089-1108.

Babak Moaveni, Xianfei He, Joel P. Conte, José I. Restrepo & Marios Panagiotou (2011). “System Identification Study of a 7-Story Full-Scale Building Slice Tested on the UCSD-NEES Shake Table,” Journal Struct. Engineering, 137(6).

G. Q. Wang, X. Y. Zhou, P. Z. Yang & H. Igel (2002). “Characteristics of Amplitude and Duration for Near Fault Strong Ground Motion from the 1999 Chi-Chi, Taiwan Earthquake”, Soil Dynamics and Earthquake Engineering, 22(1), 73-96.

Marios Panagiotou, José I. Restrepo & Joel P. Conte (2011). “Shake-Table Test of a Full-Scale 7-Story Building Slice. Phase I: Rectangular Wall,” Journal Struct. Engineering, 137(6).

Sofia Gavridou, John W. Wallace, Takuya Nagae, Taizo Matsumori, Kenich Tahara & Kunio Fukuyama (2017). “Shake-Table Test of a Full-Scale 4-Story Precast Concrete Building. I: Overview and Experimental Results,” Journal Struct. Engineering, 143(6).

Sofia Gavridou, John W. Wallace, Takuya Nagae, Taizo Matsumori, Kenich Tahara & Kunio Fukuyama (2017). “Shake-Table Test of a Full-Scale 4-Story Precast Concrete Building. II: Analytical Studies,” Journal Struct. Engineering, 143(6).

Fragility Curves of the Simple Single-Degree-of-Freedom Model of the Design Example of the Civil 404-100 Code

Yeong-Kae Yeh [1] and Te-Kuang Chow [2]

葉勇凱 [1]、周德光 [2]

Abstract

At present, the nonlinear pushover analysis based on the capacity spectrum method is used as a detailed seismic evaluation method for existing buildings in Taiwan. However, for mid-rise buildings, owing to the contribution of high modes, this analysis may yield incorrect conclusions. Nonlinear incremental dynamic analysis (IDA) may be used to correctly simulate a structure's response to earthquakes, so it is more suitable for evaluating the seismic performances of mid-rise buildings. A structure's fragility curve can be constructed using the results of IDA and may be used to examine whether the performance target will be achieved under a design-level earthquake. If the life safety standard is used as a performance demand under a design earthquake with a 475-year return period, then the probability of collapse of the structure must be less than 10%. However, due to the large amount of computation time required for the nonlinear dynamic analysis, this method is not generally accepted by engineers. In this paper, the original multi-degree-of-freedom (MDOF) model is replaced by the equivalent single-degree-of-freedom (SDOF) model to process the IDA and fragility analysis. Although the SDOF model will be less precise, it can effectively reduce the required computation time and may therefore be easily utilized to perform detailed seismic evaluations for mid-rise buildings. In this paper, a sample building based on the Civil 404-100 concrete engineering design code is used to determine how to establish the backbone curve of an equivalent SDOF model. This curve is determined from the capacity curve of the pushover analysis, IDA and fragility analysis of this SDOF are utilized for comparison with the results obtained using the original MDOF. The results show that the difference between the fragility analysis results of the equivalent SDOF system and those of the original MDOF system is highly dependent on the lateral-force distribution model that is used. Using the equivalent SDOF to process the IDA and fragility analysis can effectively reduce the computation time required for the nonlinear dynamic analysis. They can be used as a tool for detailed seismic evaluation of mid-rise buildings. However, this model will underestimate the probability of the GI state, and the performance requirement can be set to a GI state probability of less than 5%.

Keywords: detailed seismic evaluation, nonlinear pushover analysis, capacity spectrum method, incremental dynamic analysis

Introduction

Currently, seismic evaluation methods are used to examine the seismic capacities of existing buildings. The performance demands for existing buildings under a 475-year design earthquake event are not required to meet the conservative demands of new designs, but they must also meet certain performance demands to ensure adherence to life safety standards. It is difficult to obtain objective standards that consider the probabilities of buildings adhering to various performance levels. In the American PEER CENTER design guidelines for high-rise buildings

[1] Research Fellow, National Center for Research on Earthquake Engineering, ykyeh@ncree.narl.org.tw

[2] Assistant Technician, National Center for Research on Earthquake Engineering, tkchow@ncree.narl.org.tw

(PEER, 2010), it is recommended for new-build buildings under the maximum considered earthquake (MCE) that the collapse of the structure or a structural instability should have a small probability of occurrence, which may be set below 10%. This value is based on performance demands that ensure life safety standards. Therefore, a collapse probability of less than 10% can be utilized as the performance demand of an existing building under the 475-year design earthquake event.

To determine the collapse probability of a building at a specific level of earthquake, fragility analysis should be utilized, and the results of incremental dynamic analysis (IDA) (Vamvatsikos and Cornell, 2002) can be used establish the structure's fragility curve. Because nonlinear dynamic analysis requires a large amount of computation time, this method is hard to promote to the engineering community, and it is necessary to find ways to reduce the required computation time. In recent years, many scholars (Nassar and Krawinkler, 1991) have discussed using the capacity curve obtained by nonlinear pushover analysis as the backbone curve of an equivalent single-degree-of-freedom (SDOF) system. This SDOF system replaces the original multi-degree-of-freedom (MDOF) system utilized for nonlinear dynamic analysis to reduce computation time. The capacity curve obtained by pushover analysis depends on the corresponding lateral force distribution model. The SDOF system based on an appropriate lateral force distribution model can yield more accurate results for nonlinear dynamic analysis.

The authors have previously targeted the newly designed ten-story reinforced concrete building constructed utilizing the civil engineering design code Civil 404-100 and used IDA to study the seismic fragility of this newly designed building. This paper uses different lateral force distribution models to establish their capacity curves. Based on these capacity curves, the equivalent SDOF systems of this sample structure are established. The IDA is also used to study the seismic fragility of the SDOF system, and then compared with the original structure's seismic fragility in order to determine the most appropriate lateral force distribution model and the corresponding analysis errors.

Establishment of an Equivalent SDOF System

The capacity curve obtained from the nonlinear pushover analysis is used as the backbone curve of the equivalent SDOF system, and the SDOF system is used instead of the original MDOF system to perform nonlinear dynamic analysis to reduce the required computing time.

When performing a nonlinear static pushover analysis, the distribution of lateral force on each floor of a building must first be determined. In section 3.3.3.2 of FEMA 273, there are two models of lateral force distribution:

(1) If the modal mass participation factor of the dominate mode of the structure is higher than 75%, then the dominate mode is the equivalent mode and the lateral force distribution is as follows:

$$f_j = V\frac{m_j\phi_{j1}}{\sum_{i=1}^{N} m_i\phi_{i1}} \tag{1}$$

where V is the base shear; f_j is the lateral force assigned to the j-th floor; m_j is the mass of the j-th floor; ϕ_{j1} is the component of the dominate mode on the j-th floor and N is the total number of floors.

(2) By combining several modes that possess a total mass participation factor of greater than 90%, the value is increased to 95% in this paper. The lateral force distribution model according to the principle of response spectrum analysis is as follows:

1. For the n-th mode, calculate the distribution lateral force f_{in} of the i-th floor according to the following formula:

$$f_{in} = PF_n m_i \phi_{in} A_n \tag{2}$$

where A_n is the spectral acceleration of the input earthquake at the modal period, ϕ_{in} is the component of the mode at the i-th floor, and PF_n is the modal participation factor:

$$PF_n = \frac{\sum_{i=1}^{N} m_i\phi_{in}}{\sum_{i=1}^{N} m_i\phi_{in}^2} \tag{3}$$

2. Calculate the shear force V_{jn} at the j-th floor according to the following formula for the n-th mode:

$$V_{jn} = \sum_{i=j}^{N} f_{in} \tag{4}$$

3. Calculate the shear force V_j at the j-th floor from all participating M modes according to the square root of the sum of the squares (SRSS) procedures:

$$V_j = \sqrt{\sum_{i=1}^{M} (V_{ji})^2} \tag{5}$$

4. Then according to the shear force at each floor as determined by equation (4), the lateral force of each floor is derived.

5. For each floor, divide the lateral force by the floor mass to obtain the component of the equivalent mode.

Utilizing the lateral force of each floor derived in the previous section, a non-linear pushover analysis is performed to obtain the capacity curve, that is, the relationship between the base shear V and the roof displacement U_{roof}. This relationship can be converted into the relationship between the spectral acceleration and the spectral displacement of a SDOF system as follows:

$$S_a = \frac{V}{\alpha \sum_{i=1}^{N} m_i} \tag{6}$$

and

$$S_d = \frac{U_{roof}}{PF \phi_{roof}} \tag{7}$$

where ϕ_{roof} is the roof layer component of the equivalent mode, α is the mass participation factor of the equivalent mode, and PF is the modal participation factor of the equivalent mode, that is:

$$\alpha = \frac{\left(\sum_{i=1}^{N} m_i \phi_i\right)^2}{\sum_{i=1}^{N} m_i \sum_{i=1}^{N} m_i \phi_i^2} \tag{8}$$

and

$$PF = \frac{\sum_{i=1}^{N} m_i \phi_i}{\sum_{i=1}^{N} m_i \phi_i^2} \tag{9}$$

Considering the relationship curve of S_a and S_d, an equivalent SDOF system can be established. Using a massless single-curvature column, the system period T can be expressed as follows:

$$T = 2\pi \sqrt{\frac{S_d}{S_a}} = 2\pi \sqrt{\frac{M_{eff}}{K_{eff}}} \tag{10}$$

where M_{eff} is the equivalent mass adding at the top of the single-curvature column and K_{eff} is the equivalent stiffness that is equivalent to the stiffness of the single-curvature column:

$$M_{eff} = \alpha \sum_{i=1}^{N} m_i \tag{11}$$

and

$$K_{eff} = \frac{V}{S_d} = \frac{3EI}{L^3} \tag{12}$$

Here, E is the elastic modulus of the column, I is the moment of inertia of the section of the column, and L is the length of the column.

The relationship between S_d and the maximum story drift $\theta_{\max}$ can be established via a pushover analysis of the previous MDOF system. Nonlinear dynamic analysis can be performed on this single-curvature column to obtain S_d, the displacement of the top of the column, and the corresponding $\theta_{\max}$ of the original MDOF system.

Nonlinear Dynamic Analysis of a Simplified SDOF Model of a Design Example of the Civil 404-100

The demonstration example is a ten-story reinforced concrete building. The x-direction frame is a binary system with a ductile moment-resisting frame and shear wall, and the x-direction modes are the third, eighth, and thirteenth modes. The third mode is the dominate mode with period 0.733 s and a mass participation factor of 68.97%, which is lower than the requirement of FEMA 273 considering the single-mode pushover analysis. The cumulative mass participation factor of the first three modes is 95.71%, which is higher than the preset 95%. The analysis results of the second model SDOF system are closer to those of the original MDOF system. A comparison of the fragility curves of the performance levels is shown in Figure 1. The performance target $S_a(T_1)$ is 1.5513g, as obtained from the detailed seismic evaluation with a pushover analysis in the x direction and the structural performance indicates moderate damage. The probability of each damage state can be calculated from the structure's fragility curves and compared with the original MDOF system, as shown in Table 1. The probability of an unstable state of the structure, GI, is 1.04%, while it is 0.72% for the original MDOF system. Both are less than 10% and are therefore acceptable.

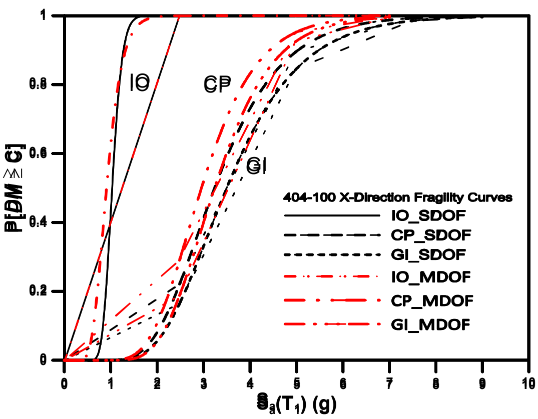

Fig. 1 Comparison of the fragility curves of the performance-levels for the x-direction frame

Table 1 Probability of each damage state of the x-direction frame under the action of the performance target earthquake

	P[DM≧IO]	P[DM≧CP]	P[DM≧GI]
SDOF	99.32%	1.66%	1.04%
MDOF	96.73%	2.08%	0.72%

The y-direction frame is a ductile moment-resisting frame, and the y-direction modes are the second, fifth, and eighth modes. The second mode is the dominate mode with a period of 1.24 s and the mass participation factor is 83.38%, which is higher than the requirement of FEMA 273 concerning the single-mode pushover analysis. The cumulative mass participation factor of the first three modes is 97.23%, which is higher than the preset of 95%. The analysis results of the first model SDOF system are closer to those of the original MDOF system. A comparison of the fragility curves of the performance levels is shown in Figure 2. The performance target $S_a(T_1)$ is 0.5909 g obtained from the detailed seismic evaluation with a pushover analysis in the y direction and the structural performance demonstrates moderate damage. The probability of each damage state can be calculated from the structure's fragility curves and compared with the original MDOF system, as shown in Table 2. The probability of an unstable state of the structure, GI, is 13.29%, while it is 25.87% for the original MDOF system. Both are greater than 10% and are therefore not acceptable. The evaluation results of the IDA are inconsistent with the results of the nonlinear static pushover analysis, but the evaluation results of the SDOF and MDOF systems are consistent. The probability of an unstable state of the structure, GI, estimated by the SDOF system is approximately 50% of that of the MDOF system.

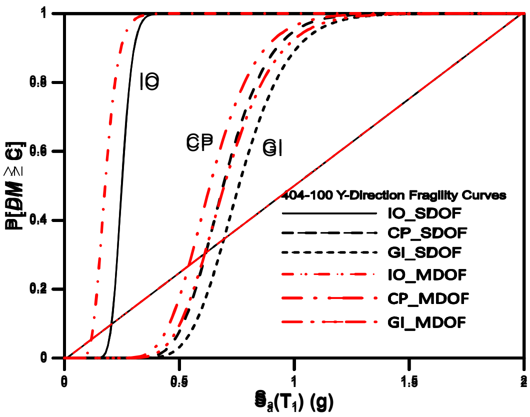

Fig. 2 Comparison of the fragility curves of the performance-levels for the y-direction frame

Table 2 Probability of each damage state of the y-direction frame under the action of the performance target earthquake

	P[DM≧ IO]	P[DM≧ CP]	P[DM≧ GI]
SDOF	100.00%	24.52%	13.29%
MDOF	100.00%	39.24%	25.87%

Conclusions

This paper tested an equivalent SDOF system for use in place of a complex MDOF system for IDA and fragility analysis. The capacity curve obtained from the pushover analysis was used as the capacity curve of the equivalent SDOF system and to define the mechanical properties of this SDOF system. Two types of lateral-force distribution models were used for the pushover analysis, and the results differed greatly. The difference between the fragility analysis results of the equivalent SDOF system and those of the original MDOF system was highly dependent on the lateral-force distribution model used. If the mass participation factor of the dominate mode is greater than 75%, then the dominate mode could be used as the equivalent mode to build the equivalent SDOF system. If the mass participation factor of the dominate mode was less than 75%, then the equivalent SDOF system could be established utilizing the lateral force distribution combined with the first few modes according to SRSS procedures and the cumulative mass participation factor of these modes must be higher than 95%.

The above principles are based on the results obtained in this study and also comply with the recommendations of FEMA 273 for lateral-force distribution. Using the equivalent SDOF model to process the IDA and fragility analysis can effectively reduce the computer time for nonlinear dynamic analysis and can be used as a tool for the detailed seismic evaluation of mid-rise buildings. However, this system will underestimate the occurrence probability of the GI state, and the performance requirement can be set to a GI structural instability state probability of less than 5%.

References

Nassar AA, and Krawinkler H. (1991), "Seismic demands for SDOF and MDOF systems", Report No. 95, The John A. Blume Earthquake Engineering Center, Stanford University, Stanford, CA.

PEER (2010), "Guidelines for performance-based seismic design of tall buildings", Report No. 2010/05, Pacific Earthquake Engineering Research Center, College of Engineering University of California, Berkeley, Page 7.

Vamvatsikos, D., and Cornell, C. A. (2002), "Incremental dynamic analysis", Earthquake Engineering and Structural Dynamics, 31, pp. 491-514.

Experimental Study of Embedded Steel Plate Composite High-Strength Reinforced Concrete Coupling Beams of Shear Walls

Min-Lang Lin[1], Chao-Hsun Huang[2] and Bo-Yen Chen[3]

林敏郎 [1]、黃昭勳 [2]、陳柏言 [3]

Abstract

In this study, cyclic loading tests of embedded steel plate composite high-strength reinforced concrete coupling beams of shear walls are conducted to improve the performance of conventional reinforced concrete coupling beams. The proposed steel plate and beam composite, and steel plate end anchor design theory are verified. The test results show that the high-strength reinforced concrete coupling beam specimens composited with embedded steel plates with a span-to-depth ratio of 2 have no composite failure and end anchor failure. It is confirmed that the proposed design theory is reasonable and conservative. The specimens all showed a ductile failure mode and reached about 4% of the lateral drift capacity. This shows that the specimens have excellent ductility performance.

Keywords: coupling beams, shear steel plate, shear capacity, shear studs, PBL

Introduction

The coupling beam is a key member of the ductile reinforced concrete shear wall system. In Taiwan's Civil 401 and ACI 318 design codes, coupling beams with a span-to-depth ratio of less than 2 and shear requirements must be configured with diagonal reinforcement. However, it is very difficult to apply this diagonal reinforcement to the actual construction site.

Previous studies have shown that traditional straight reinforcing coupling beam specimens have a similar bending moment capacity to diagonal reinforcing specimens. However, the ductility performance is not as good as that of diagonally reinforcing specimens.

If the steel plate embedded in the beam can increase the shear strength of the beam and delay the degradation of shear strength, the ductility performance of traditional reinforced connection beams may be improved. Therefore, the traditional straight reinforcing coupling beams composited with steel plates have good seismic performance and can solve the problem of difficult construction of diagonal steel bars.

In this study, the cyclic loading tests of embedded steel plate composite high-strength reinforced concrete coupling beams of shear walls are constructed to evaluate the behavioral response of the coupling beams. The proposed steel plate and beam composite, and steel plate end anchor design theory are also verified.

The embedded steel plate increases the beam's shear capacity. It also increases the bending moment capacity, which in turn increases the beam's shear requirements. To reduce the increase of the moment capacity of the beam caused by the embedded steel plate, the embedded steel plate can be partially cut off in the plastic hinge zone of the beam.

Specimen Design

The experiment was conducted at the National Earthquake Engineering Research Center. To simulate the deformation of the reinforced concrete

[1] Associate Researcher, National Center for Research on Earthquake Engineering
[2] Associate Professor, National Taipei University of Technology
[3] Graduate Assistant, National Taipei University of Technology

coupling beam under actual earthquakes, a test frame was designed to allow the test beam to produce a double curvature deformation. In this study, a beam section of 30 cm × 50 cm was selected. The length of the beams was 100 cm, and the corresponding span-to-depth ratio was 2.

In this study, a total of six coupling beam specimens were analyzed. Of these, four specimens were tested in this study (CB20P1, CB20P2, CB20P3, CB20P4), and two (CB20SP1, CB20SP2) were tested in the previous year. All specimens were made of high-strength steel and concrete. The longitudinal main reinforcement is #8 SD685, the stirrup is #4 SD785, and the concrete strength is 70 MPa. Further, the embedded steel plate is A36.

CB20SP1 is a benchmark specimen. The details of the reinforcement configuration of CB20SP1 are shown in Figure 1. CB20SP2 is a specimen with insufficient anchorage of the embedded steel plate. CB20P1 uses holes in the embedded steel plate and passes through lateral tie bars (perfobond shear connector, PBL) as a composite mechanism between the embedded steel plate and the reinforced concrete. The CB20P2 specimen uses shear studs as a composite mechanism (see Figure 2). In addition, the anchor length at the ends of the two specimens is 75 cm. We used a longer anchor length to avoid damage due to insufficient anchoring. The two specimens with the different composite mechanisms between the embedded steel plate and the reinforced concrete were compared. CB20P3 is a specimen that is partially cut off from the steel plate at the end of the beam. Its purpose is to reduce the increased bending moment of the embedded steel plate. The details are shown in Figure 3. CB20P4 is a specimen with a minimum requirement of 45 cm for the end anchor design and it is used to verify the end anchor design theory.

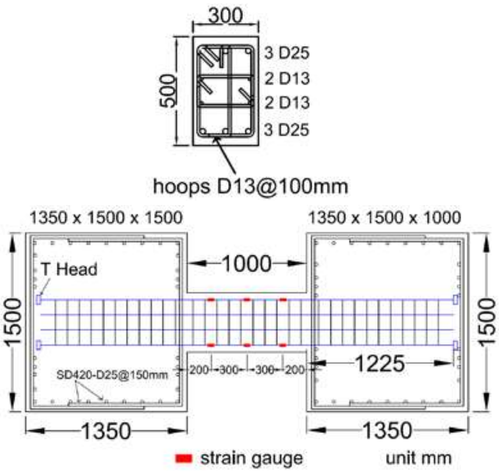

Fig. 1 Details of Specimen

(a) PBL (b) shear stud

Fig. 2 Details of the composite mechanism

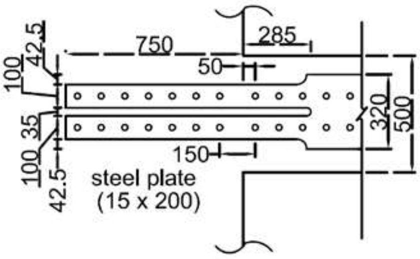

unit: mm

Fig. 3 Details of steel plate for CB20P3

Test Setup and Cyclic Loading Tests

In this test, the deformation of the double curvature when the specimen was subjected to seismic force was simulated. An L-shaped steel frame and two vertical MTS actuators were used to ensure that the upper foundation does not rotate during the test. Two horizontal MTS actuators were used to apply a progressively increasing displacement to the test specimen. The setup for the test is shown in Figure 4.

Fig. 4 Test setup

To simulate the repetitive characteristics of earthquakes, this test refers to the loading protocol of ACI 374.1-05. A total of three loops were performed for each displacement load. The displacement increments were 0.25%, 0.375%, 0.5%, 0.75%, 1%, 1.5%, 2%, 3%, 4%, 5%, 6%, 8%, and 10%, respectively. The increment of lateral displacement is shown in Figure 2.

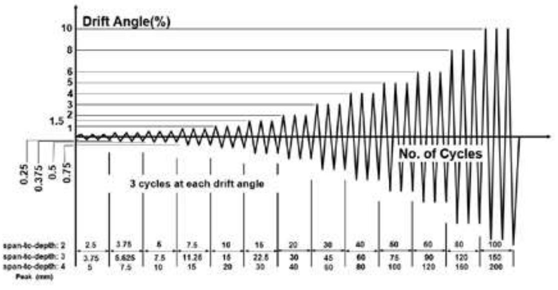

Fig. 5 Test protocol

Test Results

The load and displacement hysteresis loop curves of all specimens are shown in Figure 6, and the response envelope curves of the specimens are shown in Figure 7. A comparison of the initial stiffness of the specimen is shown in Table 1. The damage to the specimens after testing is shown in Figure 8.

The CB20SP1 is a benchmark specimen without embedded steel plates. The CB20SP2 and CB20P1 were embedded with a 1.5-cm-thick steel plate. The maximum lateral force strength of the insufficiently anchored specimen CB20SP2 increased from 1034.7 kN to 1241.2 kN (approximately 20% increase), and the maximum lateral force strength of the sufficiently anchored specimen CB20P1 increased from 1034.7 kN to 1354 kN (approximately 30% increase). In addition to improving the shear strength, the steel plate also significantly increased the lateral strength of the test body. Because the foundation of CB20SP1 was damaged during the test, the steel plate lost its anchoring ability early, resulting in unsustainable strength development. An adequately anchored specimen CB20P1 can further enhance the lateral force strength. The ultimate displacement drift ratios (UDR) of the specimens CB20SP1, CB20SP2, and CB20P1 were 3.32%, 3.45%, and 3.95%, respectively. The displacement capacity of the CB20SP2 specimen was only increased by 0.1% due to insufficient anchoring, but the UDR of the CB20P1 was improved by 0.6%. This shows that the specimen CB20O1 has a good ductility performance of 3.95%.

The specimens CB20P1 and CB20P2 were embedded with a 1.5 cm-thick steel plate, but the shear studs and PBLs were used for beam composite and end anchoring, respectively. The maximum lateral strength of the specimens CB20P1 and CB20P2 both occurred at about 3% drift. The maximum lateral strength was 1354 kN and 1413 kN, respectively. The maximum strength of CB20P2 was slightly higher than that of CB20P1. The main steel bars and steel plates of the two specimens yielded before reaching the maximum strength, and there was no separation between the embedded steel plates and the RC beams. The UDRs of CB20P1 and CB20P2 were 3.95% and 4.05%, respectively. Both specimens had good ductility performance. This proves that the use of shear studs or PBLs can effectively protect composite embedded steel plates and RC beams. Consequently, the shear strength of the embedded steel plates can be developed and the shear strength of the coupling beams can be improved. In addition to avoiding shear failure of the RC beam specimen, the displacement ductility of the specimens was also improved.

CB20P3 is based on CB20P1 as the prototype, but the embedded steel plate will be partially cut. The maximum strength of both CB20P1 and CB20P3 occurred when the lateral drift ratio was close to 3%. The maximum lateral strength of the two specimens was 1354 kN and 1188 kN, respectively. The maximum lateral strength of CB20P3 was reduced by about 14% compared with CB20P1. The UDRs of the specimens CB20P1 and CB20P3 were 3.95% and 3.92%, respectively, and the UDR of the two specimens differed only by 0.03%, indicating that the two specimens had similar ductility capabilities.

The anchorage length of the steel plate of specimen CB20P4 was 45 cm, and the composite mechanism of the steel plate and RC beam was PBLs. The maximum lateral strength of the specimen CB20P4 was 1309 kN. During the test, none of the specimen CB20P4 was found to be damaged at the anchoring end. The UDRs of the specimens CB20P1 and CB20P4 were 3.92% and 3.83%, respectively, and the difference between the UDR capacities was only 0.09%. The mechanical responses of the two specimens were quite close, indicating that the anchoring was still sufficient. This implies that the design method should be reasonable and conservative.

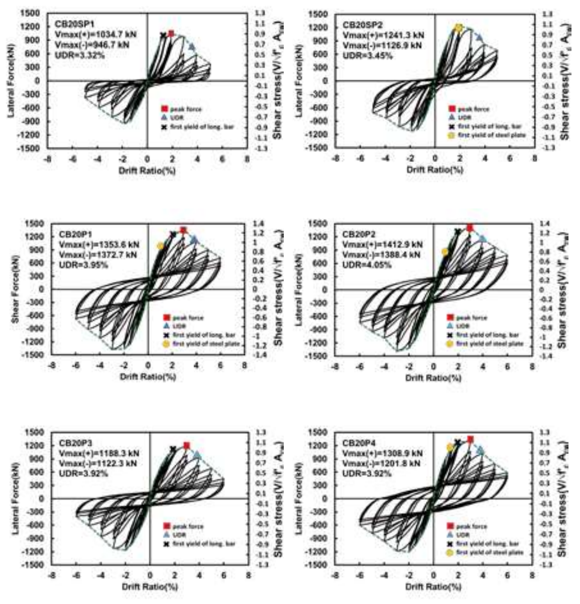

Fig. 6 Hysteretic loops of specimens

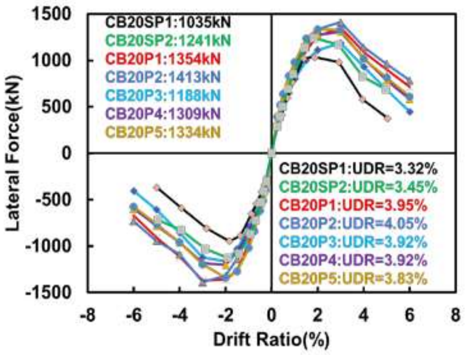

Fig. 7 Envelop curves of specimens

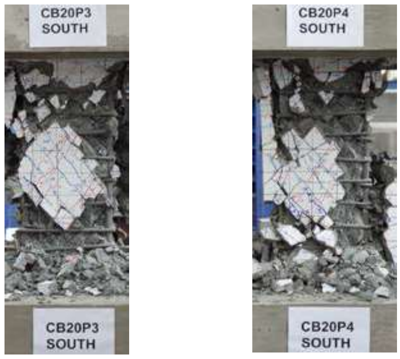

CB20P3 CB20P4

Fig. 8 Failure mode of specimens

Table 1 Initial stiffness of specimens

Specimen	Initial stiffness (kN/mm)			
	+	-	Average	Increase
CB20SP1	756.9	711.8	734.4	-
CB20SP2	820.6	826.6	823.6	12.1%
CB20P1	878.1	969.6	923.9	25.8%
CB20P2	916.2	901.7	908.9	23.8%
CB20P3	794.1	766.8	780.5	6.3%
CB20P4	934.2	852.0	893.1	21.6%

The all specimens with embedded steel plates showed an increase in initial stiffness but the increase was different for different specimens. The initial stiffness of the fully anchored specimens CB20P1, CB20P2, and CB20P4 all increased by more than 20% compared to the benchmark CB20SP1. The increase of CB20SP2 is only 12.1%, which shows that insufficient end anchoring affects strength development and initial stiffness. The initial stiffness of the CB20P3 specimen embedded in the steel plate for partial cutting only increased by 6.3%, showing that the steel plate cutting treatment can reduce the increase in bending moment strength and the amount of increase in the stiffness of the coupling beam caused by the embedded steel plate.

CB20SP1 CB20P1 CB20P2

Conclusions

This study explores the seismic behavior of high-strength reinforced concrete connecting beams embedded with steel plates. The test results confirmed that the ductility performance of the traditional coupling beam specimens with a span-to-depth ratio of 2 was not good enough, and the embedded steel plate can increase the shear capacity of the coupling beam. This improved the ductility performance of the specimen. None of the steel-embedded specimens underwent any compound failure or end anchor failure, which confirmed that the proposed design theory is accurate and conservative. The maximum strength of CB20P3 decreased by 12% compared with the uncut specimen, showing that this can effectively reduce the amount of bending moment increase caused by the embedded steel plate.

References

1. ACI Committee 318, Building Code Requirements for Structural Concrete (ACI 318-14) and Commentary (ACI 318R-14), American Concrete Institute, Farmington Hills, 2014.
2. ACI Committee 374, Acceptance Criteria for Moment Frames Based on Structural Testing and Commentary, American Concrete Institute, Farmington Hills, 2005.
3. Lin, M.L., Huang, C. S., and Yao, P., H., "Seismic Behavior for Steel Plate Reinforced Concrete Coupling Beams of Shear Walls", National Center for Research on Earthquake Engineering, Report No. NCREE-18-013 (2018).

Seismic Analysis of Vertically Irregular Buildings

Jui-Liang Lin [1], Chih-Chia Tsaur [2] and Keh-Chyuan Tsai [3]

林瑞良 [1]、曹智嘉 [2]、蔡克銓 [3]

Abstract

Vertically irregular buildings with strong or stiff-and-strong lower stories such as setback buildings are common in engineering practice. However, besides a sophisticated nonlinear response history analysis, there seems to be no simplified seismic analysis method suitable for this type of building. Thus, this study explores a two-degree-of-freedom (2DOF) modal system for representing each vibration mode of such buildings. The upper and lower degrees of the 2DOF modal system respectively simulate the modal responses of the two distinct parts (*i.e.*, the upper stories and the lower stories) of a building with strong or stiff-and-strong lower stories. Instead of a conventional single degree-of-freedom modal system, the 2DOF modal system is employed in the modal response history analysis of buildings with the specific vertical irregularities. The effectiveness of the proposed seismic analysis method is verified by investigating four nine-story and four twenty-story buildings, which have lower stories that are stronger or stiffer-and-stronger than the upper stories. Each of the eight example buildings is subjected to three ensembles of ground motion records.

Keywords: vertically irregular buildings, setback buildings, modal system, modal response history analysis, pushover analysis

Introduction

Vertically irregular buildings, which may possess mass, stiffness, or strength irregularities over their heights, are very common in engineering practice. For example, setbacks in upper stories, heavy mechanical mid-stories, and elevated bottom stories usually result in vertical irregularities. Therefore, vertically irregular buildings have been the subject of a significant amount of research (Soni and Mistry, 2006). Chintanapakdee and Chopra (2004) found that a combined stiffness-strength irregularity has a more significant effect on the seismic demand of their investigated frames than a pure strength irregularity. In addition, a stiffness irregularity has less effect on seismic demand as compared with a strength irregularity. The sophisticated nonlinear response history analysis (NRHA) was the only suggested method for evaluating the seismic demands of irregular frames with a strong or stiff-and-strong first story/lower half (Chintanapakdee and Chopra, 2004). In other words, vertically irregular buildings with strong or stiff-and-strong lower stories are the most challenging cases for simplified seismic analysis methods.

Some building codes, *e.g.*, IBC (2000), do not permit the application of the equivalent lateral force method in the design of vertically irregular buildings. Therefore, rather than performing a complicated and time-consuming NRHA, developing simplified methods to analyze the seismic responses of vertically irregular buildings may benefit engineering practice. Therefore, this study aims to develop a simplified seismic analysis method suitable for vertically irregular buildings, specifically those with stronger lower stories or stiffer-and-stronger lower stories than the upper stories. This study develops two-degree-of-freedom (2DOF) modal systems instead of SDOF modal systems to characterize

[1] Research Fellow, National Center for Research on Earthquake Engineering, jllin@ncree.narl.org.tw.

[2] Graduate Student, Department of Civil Engineering, National Taiwan University, r00521203@ntu.edu.tw

[3] Professor, Department of Civil Engineering, National Taiwan University, kctsai@ntu.edu.tw.

the distinctly different modal responses of the upper-structure and base-structure. The proposed simplified seismic analysis method involves performing the uncoupled modal response history analysis (UMRHA) (Chopra and Goel, 2002), in which the SDOF modal systems are replaced by the proposed 2DOF modal systems.

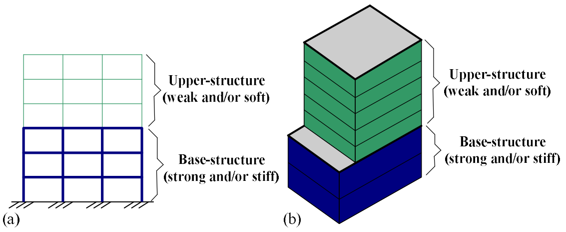

Fig 1. (a) A schematic drawing of a building frame with a strong or stiff lower half. (b) A schematic drawing of a setback building.

Theoretical Background

Based on the approach of constructing the 2DOF modal system to represent each vibration mode of a one-way asymmetric-plan building (Lin and Tsai, 2007), this study further develops the 2DOF modal system for the vertically irregular buildings with strong or stiff-and-strong lower stories as follows.

Elastic properties of 2DOF modal systems

Considering an N-story building, whose base-structure contains the first to j-th stories and the upper-structure contains the $(j + 1)$-th to N-th stories, the equation of motion of this building is

$$\mathbf{M}\ddot{\mathbf{u}} + \mathbf{C}\dot{\mathbf{u}} + \mathbf{K}\mathbf{u} = -\mathbf{M}\boldsymbol{\iota}\ddot{u}_g \tag{1a}$$

where

$$\mathbf{u} = \begin{bmatrix} \mathbf{u}_p \\ \mathbf{u}_b \end{bmatrix}_{N\times 1}, \quad \mathbf{M} = \begin{bmatrix} \mathbf{m}_p & \mathbf{0} \\ \mathbf{0} & \mathbf{m}_b \end{bmatrix}_{N\times N}$$
$$\mathbf{C} = \begin{bmatrix} \mathbf{c}_{pp} & \mathbf{c}_{pb} \\ \mathbf{c}_{bp} & \mathbf{c}_{bb} \end{bmatrix}_{N\times N}, \quad \mathbf{K} = \begin{bmatrix} \mathbf{k}_{pp} & \mathbf{k}_{pb} \\ \mathbf{k}_{bp} & \mathbf{k}_{bb} \end{bmatrix}_{N\times N} \tag{1b}$$

and $\boldsymbol{\iota}$ and $\ddot{u}_g$ are the influence vector and the ground acceleration record, respectively. In Eq. 1b, the subscripts p and b denote the corresponding quantities belonging to the upper-structure and base-structure, respectively. Each floor of the considered building is assumed to be a rigid floor diaphragm with only one translational degree of freedom. Therefore, $\mathbf{u}_p$ and $\mathbf{u}_b$ are $(N - j) \times 1$ and $j \times 1$ column vectors, respectively, and the sizes of the sub-matrices shown in Eq. 1b are determined accordingly. The earthquake load, *i.e.*, the right-hand side of Eq. 1a, can be expressed as

$$-\mathbf{M}\boldsymbol{\iota}\ddot{u}_g = -\sum_{n=1}^{N} \mathbf{s}_n \ddot{u}_g = -\sum_{n=1}^{N} \Gamma_n \mathbf{M}\boldsymbol{\varphi}_n \ddot{u}_g \tag{2}$$

where Γ_n and $\boldsymbol{\varphi}_n$ are the n-th modal participation factor and the mode shape, respectively, and $\mathbf{s}_n$ is the n-th modal inertia force vector, which is equal to $\Gamma_n \mathbf{M}\boldsymbol{\varphi}_n$. When the building is subjected to $\mathbf{s}_n \ddot{u}_g$, only the n-th modal displacement vector, denoted as $\mathbf{u}_n$, is excited. Therefore, Eq. 1a can be expressed as

$$\mathbf{M}\ddot{\mathbf{u}}_n + \mathbf{C}\dot{\mathbf{u}}_n + \mathbf{K}\mathbf{u}_n = -\mathbf{s}_n \ddot{u}_g \tag{3a}$$

where

$$\mathbf{u}_n = \Gamma_n \boldsymbol{\varphi}_n D_n = \Gamma_n \begin{bmatrix} \boldsymbol{\varphi}_{pn} \\ \boldsymbol{\varphi}_{bn} \end{bmatrix} D_n \tag{3b}$$

and D_n is the n-th generalized modal coordinate. In the UMRHA (Chopra and Goel, 2002), $D_n(t)$ (Eq. 3b) is obtained by solving the n-th SDOF modal equation of motion. The relationship between the restoring force and the generalized modal coordinate of the n-th SDOF modal system is represented as a bilinear curve, which is idealized from the n-th modal pushover curve of the target building presented in the acceleration–displacement–response spectra (ADRS) format. The n-th modal pushover curve is the force versus displacement relationship of the target building pushed using $\mathbf{s}_n$. The total displacement history of the target building $\mathbf{u}(t)$ is equal to the arithmetic summation of $\mathbf{u}_n(t)$, where $n = 1 \sim N$. While computing $\mathbf{u}_n(t)$, the elastic mode shape $\boldsymbol{\varphi}_n$ and the elastic modal participation factor Γ_n are used in Eq. 3b, irrespective of elastic or inelastic modal responses. The single generalized modal coordinate D_n appears insufficient when the upper-structure yields, whereas the base-structure remains elastic. To reflect the likely different dynamic characteristics between the upper structure and the base structure, two generalized modal coordinates, denoted as D_{pn} and D_{bn}, are separately assigned to the upper structure and the base structure by carrying out matrix partition. The basic assumptions or approximations adopted in the UMRHA remain in the proposed approach, except for the single generalized modal coordinate being replaced by the two generalized modal coordinates. This study thus rearranges Eq. 3b as

$$\mathbf{u}_n = \Gamma_n \begin{bmatrix} \boldsymbol{\varphi}_{pn} & \mathbf{0}_{pb} \\ \mathbf{0}_{bp} & \boldsymbol{\varphi}_{bn} \end{bmatrix}_{N\times 2} \begin{bmatrix} D_{pn} \\ D_{bn} \end{bmatrix}_{2\times 1} = \Gamma_n \boldsymbol{\Phi}_n \mathbf{D}_n \tag{4a}$$

where

$$\boldsymbol{\Phi}_n = \begin{bmatrix} \boldsymbol{\varphi}_{pn} & \mathbf{0}_{pb} \\ \mathbf{0}_{bp} & \boldsymbol{\varphi}_{bn} \end{bmatrix}_{N\times 2}, \quad \mathbf{D}_n = \begin{bmatrix} D_{pn} \\ D_{bn} \end{bmatrix}_{2\times 1} \tag{4b}$$

and $\mathbf{0}_{pb}$ and $\mathbf{0}_{bp}$ are the $(N - j) \times 1$ and $j \times 1$ zero vectors, respectively. Substituting Eq. 4a into Eq. 3a and pre-multiplying both sides of Eq. 3a by $\mathbf{\Phi}_n^T$ result in

$$\mathbf{M}_n \ddot{\mathbf{D}}_n + \mathbf{C}_n \dot{\mathbf{D}}_n + \mathbf{K}_n \mathbf{D}_n = -\mathbf{M}_n \mathbf{1} \ddot{u}_g \tag{5a}$$

where

$$\mathbf{M}_n = \begin{bmatrix} \boldsymbol{\varphi}_{pn}^T \mathbf{m}_p \boldsymbol{\varphi}_{pn} & 0 \\ 0 & \boldsymbol{\varphi}_{bn}^T \mathbf{m}_b \boldsymbol{\varphi}_{bn} \end{bmatrix}_{2\times2}$$

$$\mathbf{C}_n = \begin{bmatrix} \boldsymbol{\varphi}_{pn}^T \mathbf{c}_{pp} \boldsymbol{\varphi}_{pn} & \boldsymbol{\varphi}_{pn}^T \mathbf{c}_{pb} \boldsymbol{\varphi}_{bn} \\ \boldsymbol{\varphi}_{bn}^T \mathbf{c}_{bp} \boldsymbol{\varphi}_{pn} & \boldsymbol{\varphi}_{bn}^T \mathbf{c}_{bb} \boldsymbol{\varphi}_{bn} \end{bmatrix}_{2\times2}$$

$$\mathbf{K}_n = \begin{bmatrix} \boldsymbol{\varphi}_{pn}^T \mathbf{k}_{pp} \boldsymbol{\varphi}_{pn} & \boldsymbol{\varphi}_{pn}^T \mathbf{k}_{pb} \boldsymbol{\varphi}_{bn} \\ \boldsymbol{\varphi}_{bn}^T \mathbf{k}_{bp} \boldsymbol{\varphi}_{pn} & \boldsymbol{\varphi}_{bn}^T \mathbf{k}_{bb} \boldsymbol{\varphi}_{bn} \end{bmatrix}_{2\times2} \tag{5b}$$

and $\mathbf{1} = [1\ 1]^T$. Eq. 5 is the n-th 2DOF modal equation of motion for the considered building.

A mechanical analogy model corresponding to Eq. 5 is needed for the nonlinear modal response history analysis. Figure 2a shows the proposed physical model of the n-th 2DOF modal system, whose vibration is represented as the n-th 2DOF modal equation of motion (Eq. 5). The n-th 2DOF modal system consists of two rigid bars with lengths equal to l_{pn} and l_{bn}, respectively (Fig. 2a). Two lumped masses, denoted as m_{pn} and m_{bn}, are located at the tops of the upper and lower rigid bars, respectively. The upper rigid bar is pin-connected to the lower rigid bar by a rotational spring with a rotational stiffness of k_{pn}. Similarly, the lower rigid bar is pin-connected to the ground by a rotational spring with a rotational stiffness of k_{bn} (Fig. 2a). For the simple structural model shown in Fig. 2a, its corresponding mass matrix $\tilde{\mathbf{M}}_n$, stiffness matrix $\tilde{\mathbf{K}}_n$, and displacement vector $\tilde{\mathbf{D}}_n$, which is defined as the two translations at the two lumped masses, are formulated as

$$\tilde{\mathbf{D}}_n = \begin{bmatrix} \tilde{D}_{pn} \\ \tilde{D}_{bn} \end{bmatrix}_{2\times1}, \quad \tilde{\mathbf{M}}_n = \begin{bmatrix} m_{pn} & 0 \\ 0 & m_{bn} \end{bmatrix}_{2\times2}$$

$$\tilde{\mathbf{K}}_n = \begin{bmatrix} \dfrac{k_{pn}}{l_{pn}^2} & \dfrac{-k_{pn}}{l_{pn}^2}\left(1+\dfrac{l_{pn}}{l_{bn}}\right) \\ \dfrac{-k_{pn}}{l_{pn}^2}\left(1+\dfrac{l_{pn}}{l_{bn}}\right) & \dfrac{k_{pn}}{l_{pn}^2}\left(1+\dfrac{l_{pn}}{l_{bn}}\right)^2 + \dfrac{k_{bn}}{l_{bn}^2} \end{bmatrix}_{2\times2} \tag{6}$$

By setting $\tilde{\mathbf{D}}_n = \mathbf{D}_n$, $\tilde{\mathbf{M}}_n = \mathbf{M}_n$, $\tilde{\mathbf{K}}_n = \mathbf{K}_n$, and $l_{pn} = 1$, the elastic properties of the n-th 2DOF modal system are obtained as

$$m_{pn} = \boldsymbol{\varphi}_{pn}^T \mathbf{m}_p \boldsymbol{\varphi}_{pn}, \quad m_{bn} = \boldsymbol{\varphi}_{bn}^T \mathbf{m}_b \boldsymbol{\varphi}_{bn},$$

$$l_{bn} = -\left(\frac{\boldsymbol{\varphi}_{pn}^T \mathbf{k}_{pb} \boldsymbol{\varphi}_{bn}}{\boldsymbol{\varphi}_{pn}^T \mathbf{k}_{pp} \boldsymbol{\varphi}_{pn}} + 1\right)^{-1}, \quad k_{pn} = \boldsymbol{\varphi}_{pn}^T \mathbf{k}_{pp} \boldsymbol{\varphi}_{pn}$$

$$k_{bn} = l_{bn}^2 \left(\boldsymbol{\varphi}_{bn}^T \mathbf{k}_{bb} \boldsymbol{\varphi}_{bn} - \frac{\left(\boldsymbol{\varphi}_{pn}^T \mathbf{k}_{pb} \boldsymbol{\varphi}_{bn}\right)^2}{\boldsymbol{\varphi}_{pn}^T \mathbf{k}_{pp} \boldsymbol{\varphi}_{pn}}\right) \tag{7}$$

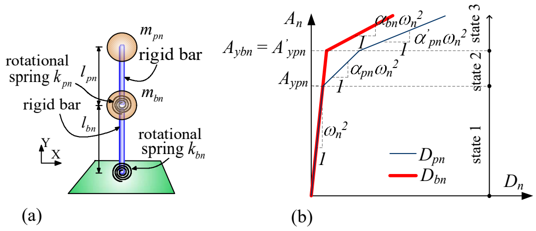

Fig. 2. (a) The n-th 2DOF modal system. (b) The pushover curves A_n versus D_{pn} and A_n versus D_{bn} relationships.

Inelastic properties of 2DOF modal systems

When a building with the specific vertical irregularities is pushed by the n-th modal inertia force $\mathbf{s}_n$, a pushover curve can be obtained, which represents the relationship between the base shear V_{bn} and the displacement at the top of upper-structure, denoted as $u_{n,tp}$. A second pushover curve can be simultaneously obtained, which represents the relationship between the base shear V_{bn} and the displacement at the top of the base-structure, denoted as $u_{n,tb}$. The two pushover curves are transformed into the ADRS format as

$$D_{pn} = \frac{u_{n,tp}}{\Gamma_n \phi_{n,tp}}, \quad D_{bn} = \frac{u_{n,tb}}{\Gamma_n \phi_{n,tb}}, \quad A_n = \frac{V_{bn}}{\Gamma_n^2 M_n} \tag{8}$$

, in which $\phi_{n,tp}$ and $\phi_{n,tb}$ are the components of the n-th mode shape at the tops of the upper structure and the base structure, respectively. Additionally, M_n is the modal mass, which is equal to $\boldsymbol{\varphi}_n^T \mathbf{M} \boldsymbol{\varphi}_n$. The two pushover curves are approximately represented as two polygonal lines (Fig. 2b). When the building remains completely elastic (*i.e.*, State 1 shown in Fig. 2b), the two pushover curves overlap with a slope equal to ω_n^2, in which ω_n is the circular frequency of the n-th vibration mode of the building. When the upper structure yields and the base structure remains elastic (*i.e.*, State 2 shown in Fig. 2b), the slopes of the two pushover curves A_n—D_{pn} and A_n—D_{bn} are $\alpha_{pn}\omega_n^2$ and ω_n^2, respectively. The ordinate of the inflection point of the pushover curve A_n—D_{pn} is denoted as A_{ypn} (Fig. 2b), which represents the yielding acceleration of the upper structure. Furthermore, when both the upper structure and the base structure become inelastic (*i.e.*, State 3 shown in Fig. 2b), the slopes of the two pushover curves A_n—D_{pn} and A_n—D_{bn} are $\alpha'_{pn}\omega_n^2$

and $\alpha_{bn}\omega_n^2$. The ordinate of the inflection point of the pushover curve A_n—D_{bn} is denoted as A_{ybn} (Fig. 2b), which represents the yielding acceleration of the base structure. A_{ybn} also represents the ordinate of the second inflection point of the pushover curve A_n—D_{pn}, which is denoted as A'_{ypn} (*i.e.*, $A'_{ypn} = A_{ybn}$).

Likewise, two pushover curves are available when the n-th 2DOF modal system (Fig. 2a) is pushed by its active modal inertia force. One of the two pushover curves represents the relationship between the base shear and the displacement at the top of the upper rigid bar. The other pushover curve represents the relationship between the base shear and the displacement at the top of the lower rigid bar. The two pushover curves obtained from the n-th 2DOF modal system presented in the ADRS format are expected to be equal to those obtained from the building model pushed by its n-th modal inertia force $\mathbf{s}_n$. In addition, when the n-th 2DOF modal system (Fig. 2a) is pushed by its active modal inertia force, three states are considered. In State 1, both the rotational springs of the 2DOF modal system remain elastic. In State 2, the lower rotational spring remains elastic, whereas the upper rotational spring yields, which has a stiffness of k'_{pn} . In State 3, the lower rotational spring yields, which has a stiffness of k'_{bn}, and the stiffness of the upper rotational spring becomes k''_{pn} . Therefore, the lower spring is simulated as a bilinear rotational spring, whose yielding moment is denoted as M_{ybn}. In addition, the upper spring is simulated as a trilinear rotational spring, whose moments corresponding to the first and second inflection points are denoted as M_{ypn} and M'_{ypn} , respectively. The values of the six parameters k'_{pn} , k''_{pn} , k'_{bn} , M_{ypn}, M'_{ypn} , and M_{ybn} can be determined in terms of the six parameters α_{pn} , α'_{pn} , α_{bn} , A_{ypn}, A'_{ypn} , and A_{ybn}, whose values are available from the building's pushover curves (Fig. 2b). The six parameters k'_{pn} , k''_{pn} , k'_{bn} , M_{ypn}, M'_{ypn} , and M_{ybn} of the two rotational springs used in the n-th 2DOF modal system are expressed as

$$k'_{pn} = \frac{m_{pn}}{\dfrac{\dfrac{m_{pn}}{k_{pn}} + \dfrac{(l_{bn}+1)(l_{bn}+m_{pn})}{k_{bn}}}{\alpha_{pn}} - \dfrac{(l_{bn}+1)(l_{bn}+m_{pn})}{k_{bn}}}$$

$$k''_{pn} = \frac{m_{pn}}{\dfrac{\dfrac{m_{pn}}{k_{pn}} + \dfrac{(l_{bn}+1)(l_{bn}+m_{pn})}{k_{bn}}}{\alpha'_{pn}} - \dfrac{(l_{bn}+1)(l_{bn}+m_{pn})}{k'_{bn}}}$$

$$\begin{aligned} &k'_{bn} = \alpha_{bn}k_{bn}, \quad M_{ypn} = A_{ypn}m_{pn}, \quad M'_{ypn} = A_{ybn}m_{pn} \\ &M_{ybn} = A_{ybn}\left[(1+l_{bn})m_{pn} + l_{bn}m_{bn}\right] \end{aligned} \tag{9}$$

Conclusions

This study decomposed the conventional single-degree-of-freedom (SDOF) modal equations of motion for vertically irregular buildings with strong or stiff-and-strong lower stories into two-degree-of-freedom (2DOF) modal equations of motion. In addition to the 2DOF modal equations of motion, the two pushover curves simultaneously obtained from the n-th modal pushover analysis were used together to construct the n-th 2DOF modal system for the target buildings. This study showed that the 2DOF modal system is identical to the SDOF modal system for elastic buildings with these specific vertical irregularities. In addition, it was found that the more inelastic excursions a building with these specific vertical irregularities experiences, the less effective is the SDOF modal system for simulating the distinct modal responses of the upper and base structures. The proposed 2DOF modal system precisely overcame the stated deficiency of the SDOF modal system for buildings with these specific vertical irregularities. The investigation results highlight that the drastic change in the peak inter-story drift ratios, over the two stories where the abrupt change in strength occurs, is poorly reflected when using the SDOF modal systems. In contrast, the 2DOF modal system adequately capture this characteristic.

References

Soni, D. P. and Mistry, B. B. (2006), "Qualitative review of seismic response of vertically irregular building frames", *ISET Journal of Earthquake Technology*, *Technical Note*, 43(4), 121-132.

Chintanapakdee, C. and Chopra, A. K. (2004), "Seismic response of vertically irregular frames: response history and modal pushover analyses", *Journal of Structural Engineering*, ASCE, 130(8), 1177-1185.

UBC (1994), *Uniform building code*. International Conference of Building Officials, Whittier, CA.

Chopra, A. K. and Goel, R. K. (2002), "A modal pushover analysis procedure for estimating seismic demands for buildings", *Earthquake Engineering and Structural Dynamics*, 31, 561-582.

International Code Council (2000), *International Building Code*. International Conference of Building Officials, Whittier, CA.

Lin, J. L. and Tsai, K. C. (2007), "Simplified seismic analysis of asymmetric building systems", *Earthquake Engineering and Structural Dynamics*, 36, 459-479.

Technology of Seismic Detailed Evaluation and Seismic Retrofit – Development of TEASPA 4.0

Tsung-Chih Chiou[1], Yu-Chih Lai[2] and Lap-Loi Chung[3]

邱聰智 [1]、賴昱志 [2]、鍾立來 [3]

Abstract

The Taiwan Earthquake Assessment for Structures by Pushover Analysis (TEASPA), developed by NCREE, has now been updated to V4.0. This new version will still use P-M hinges on columns (which is the same as V3.1). V4.0 improves simulated methods for members and methods of seismic retrofit as researched by NCREE. In addition, V4.0 has added standard and evaluation methods of interim seismic retrofit into a handbook to assist with the prevention of collapse by soft and weak floors in mid-to-high-rise buildings. NCREE cooperated with Sinotech while developing V4.0 (which is different to previous versions) to develop a web-system for TEAPSA users. In this new version, users can upload models to the website to set nonlinear hinges and evaluate seismic capacity. NCREE will collect the uploaded structural information for future research.

Keywords: detailed evaluation, seismic retrofit, soft and weak floor, interim seismic retrofit

Introduction

The seismic evaluation program TEASPA (Taiwan Earthquake Assessment for Structures by Pushover Analysis), which was developed by NCREE, has now been updated to V4.0. While similar to V3.1, the new version adopts P-M nonlinear hinges for columns. V4.0 refers to the newest research and has increased and adjusted lots of contents. The section and backbone curve of opening walls are included and the new version also adjusts the backbone curve of other members. The new version adds lots of retrofit methods such as adding external frames, opening walls, setting elevator supplemental concrete walls and a combination of column-jacketing supplemental beams. To comply with the Construction and Planning Agency, Ministry of the Interior (CPAMI) policy, V4.0 added a chapter of interim seismic retrofit, which introduces evaluation methods to avoid soft and weak floors.

Unlike V1.0–V3.0, NCREE has cooperated with Sinotech in V4.0 to develop a web system for TEAPSA users. Users can choose functions for seismic evaluations online. This online system can also collect structural information that is uploaded by users. NCREE will use the information collected from the TEAPSA system for future research and give back to society.

Analysis Method and Backbone Curve

V3.1 has been recognized by CPAMI and can be used on buildings higher than six floors. V4.0 uses P-M nonlinear hinges on columns and can adjust the bending stiffness (the column is either in elastic form after cracking or in nonlinear form) of columns. The bending stiffness of the column is evaluated according to the initial axial force of each member.

In addition, according to the newest research, V4.0 modifies the stiffness and ultimate strength of three-sided confined brick walls. After modification, the stiffness and ultimate strength evaluated by theory will be closer to test results. V4.0 increases the backbone curve of opening walls, using a wall pier (Fig.1) to simulate the opening wall. Because there are window openings and door openings in buildings in Taiwan, considering opening walls in seismic evaluation will provide closer results to real behavior.

[1] Associate Researcher, National Center for Research on Earthquake Engineering
[2] Assistant Technologist, National Center for Research on Earthquake Engineering
[3] Deputy Director General, National Center for Research on Earthquake Engineering

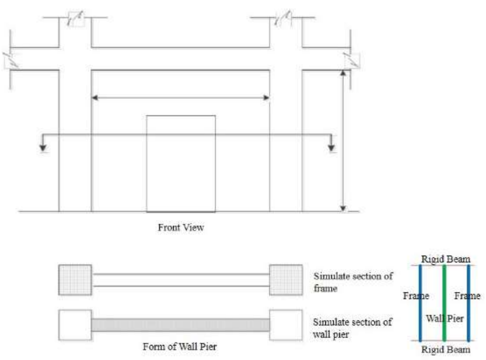

Fig. 1. Using wall pier to simulate an opening wall.

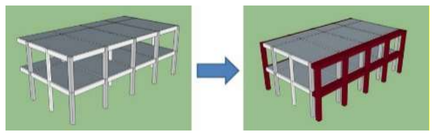

(a) 3D drawing of adding external frames.

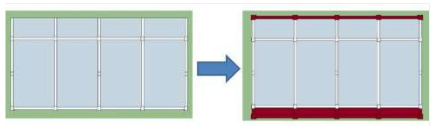

(b) Plan drawing of adding external frames.

Fig. 2. Schematic drawing of adding external frames.

Method of Seismic Retrofit

In V4.0, retrofit methods found in previous versions (such as RC jacketing, wing wall, RC wall, and compound column) are included, but several new retrofit methods have also been introduced. This includes adding external frames, adding opening walls, setting elevator supplemental concrete walls and a combination of column-jacketing supplemental beams. This allows engineers to select a suitable retrofit method.

The retrofit method of adding external frames (Fig. 2) involves adding at least one external frame outside of two weak sides. This method can reduce the influence of existing buildings, which can be used on functional buildings that cannot be affected during retrofit. The method of adding RC walls with openings is similar to adding RC walls, but this method better suits buildings because it considers doors or windows. Therefore, the effect of ventilation and lighting usages can be reduced. For old apartments without an elevator, the method "of setting elevator supplemental concrete walls" is suggested in the handbook. This method will not only add an elevator to the apartment building, but it will also raise the seismic capacity of the building due to the addition of RC walls and opening walls outside of the elevator. This method can be used on buildings with lower floors and higher floors. The method of "combination of column-jacketing supplemental beams" is a method that adds extra beams in two nearby columns that are retrofitted by RC jacketing. Supplemental beams will contribute extra moment resistant, increasing the extra lateral force resistance of the whole structure.

The new version of TEASPA suggests new retrofit methods to better allow engineers to select suitable retrofit methods. Engineers also can combine two or more methods on retrofit designs. Several new retrofit methods are introduced in V4.0 to make seismic retrofit design more convenient.

Interim Retrofit to Prevent Soft and Weak Floor Damages

For buildings that cannot be retrofit to satisfy seismic demand due to the reasons other than construction, the "Code and Commentary for Seismic Design of Buildings" (which is revising chapter 8.5) suggests that buildings can implement retrofitting to prevent soft and weak floor damages. This can reduce the risk of collapse from soft and weak floors.

The TEASPA 4.0 handbook has added a chapter about interim retrofitting—preventing buildings from soft and weak floor damages. The handbook suggests various evaluation methods for engineers. This handbook separates interim retrofit methods into two categories; Method A and Method B. Method A is used to prevent soft and weak floor damages and it is connected with the strength and stiffness of soft and weak floors. Although Method A does not require a detailed evaluation (pushover analysis) for buildings and the seismic capacity is less than the seismic demand, the method can prevent buildings from soft and weak floor damages. Alternatively, Method B should include a detailed evaluation of the structure, and the CDR (ratio of seismic capacity and seismic demand) of the structure after retrofit should be more than 0.8. Method B should also confirm that soft and weak floor damages will be prevented. Although the CDR of Method B is less than 1.0, the CDR is over 0.8 so soft and weak floor damages will be prevented within the building.

The handbook also suggests two evaluation methods. One of the methods involves evaluating the building structure model and allows users to use the model to evaluate the strength and stiffness of each floor. The other method is a simplified one, which approximates the vertical member area of each object type and uses simplified parameters to evaluate the strength and stiffness of each floor.

Development of TEASPA Web System

NCREE cooperated with Sinotech to develop a web system (Fig.3) for TEASPA 4.0. The system separates the analysis process into four modules (Fig. 4). The four modules are SecGEN, Framelnfo, HingeProp, and PAG. These modules can assist users to set frame sections and evaluate material stiffness, sort out members that should be assigned nonlinear hinges by the model and EXCEL files uploaded by users, assist to assign nonlinear hinges, and evaluate seismic capacity.

Users can download the Website-System-Manual and EXCEL template from the website. Each page in the EXCEL template includes building information (such as site, weight of each floor, and mode shape), material properties, section properties of each object (such as column, beam, RC wall, opening RC wall, brick wall, and RC jacketing), the members needed to assign nonlinear hinges, etc. Users should input the information into the EXCEL file and provide the text format of the analysis model. For the HingeProp module, users only have to provide the location of the assigned nonlinear hinges. The system will then not only assign hinges for the user, but will modify the stiffness of members. Otherwise, the system will output incorrect errors for users to modify if the information users provide cannot operate successfully.

On page “1.1 Bldg.Info” in the EXCEL template, users can input building information such as site, area of each floor, weight of each floor, and mode shape. The system will not only use the provided information to assist users with a seismic evaluation, but will also collect the provided information. NCREE will use the collected building information of real buildings for future research. The system will then benefit both users and NCREE.

Fig. 3. Web system of TEASPA 4.0.

Fig. 4. Analysis module of TEASPA 4.0.

Conclusions and Prospect

This report adopted the latest research from NCREE to improve seismic evaluation and seismic retrofit methods. NCREE has cooperated with Sinotech to develop the V4.0 web system. The system will not only assist engineers to conduct seismic evaluation and retrofit design but will also collect structural information from the users’ upload. NCREE will then use the collected information from the TEAPSA system for future research. TEASPA methods will update with the newest research (such as simulate methods or retrofit methods) and will provide feedback to society for the improvement of the process of seismic evaluation and retrofit design.

References

Fi-Pei Hsiao, Lap-Loi Chung, Yeong-Kae Yeh, Wen-Yu Chien, Wen-Cheng Shen, Tsung-Chih Chiou, Te-Kuang Chow, Yi-Feng Chao, Pu-Wen Weng, Yao-Sheng Yang, Yu-Lung Chu, Yaw-Shen Tu, Juin-Fu Chai, and Shyh-Jiann Hwang, (2013). ″Technology Handbook for Seismic Evaluation and Retrofit of School Buildings Third Edition,″ NCREE, Report Number NCREE-13-023.

Tsung-Chih Chiou, Fu-Pei Hsiao, Lap-Loi Chung, Jian-Huang Weng, Chi-Hang Li, Chien-Chun Liu, Qiang Xue, Yu-Shan Ho, Shing-Jiun Chen, Chih-Ping Yang, Pu-Wen Weng, Wen-Cheng Shen, Yaw-Shen Tu, Yao-Sheng Yang, Yi-An Li, Yeong-Kae Yeh, and Shyh-Jiann Hwang, (2018). ″Taiwan Earthquake Assessment for Structures by Pushover Analysis (TEASPA V3.1),″ NCREE, Report Number NCREE-18-015.

Applying Field Inspection Technologies for the Investigation of Pre-stressed Concrete Box Girder Bridges

Chun-Chung Chen[1], Chi-Lon Jang[2], Bo-Han Lee[3] and Sheng-Yuan Shiao[4]

陳俊仲[1]、江奇融[2]、李柏翰[3]、蕭勝元[4]

Abstract

The pre-stressed concrete box girder is a commonly used bridge superstructure in highway, urban, and railway road systems. Due to the importance of bridge structures, management authorities have recently placed increasing attention on the maintenance and monitoring of the structural safety of these structures. However, many unavoidable factors might cause the reduction of the pre-stress in the box girder and thus threaten the safety of bridge structures. Furthermore, long-term exposure to the natural environment will also cause the structural components of the bridge to degrade. To ensure the bridge functions as intended, the proper maintenance of structural components is required, with necessary detection and investigation methods taken for bridge elements that have been observed to have significant deterioration or damage. In this study, a bridge is taken as an example to illustrate the application of technologies for the field investigation of pre-stressed concrete box girder bridges. The primary purpose of the investigation is to provide feedback on the current bearing capacity of the bridge and to formulate the analysis parameters of the corresponding reinforcement improvement plan.

Keywords: concrete box girder, vehicle ground-penetrating radar, impact-echo method, vibration-based identification method

Introduction

Pre-stressed concrete box girder bridges characteristically have systematic segments, which can meet short construction periods and economic requirements. Therefore, new bridges constructed during boom periods of national socioeconomic development often are of the pre-stressed concrete box girder type. However, many environmental or non-environmental factors might deteriorate the structures during their service life. For pre-stressed concrete box girder bridges, loosening of tendons and the deterioration of the concrete are two factors that require careful attention. Furthermore, long-term exposure to the impacts of natural disasters also causes structural component and systemic degradation of bridges. Thus, the bridge management authorities must know the structural service and safety conditions at all times. Concrete box girder bridges must be adequately and comprehensively maintained and managed to ensure safe bridge use. As for bridge maintenance and management operations, there are current regulations in Taiwan that specify specific practices to be followed. Since an informative investigation record could significantly help in evaluating the current condition of the bridge structure, practical and feasible inspection methods should be appropriately applied and studied. For example, deck maintenance work, such as pavement construction, may cause the static loadings of the superstructure to vary slightly from the original design loading, which might affect the safety of the bridge and require an investigation to accurately determine the real thickness of the pavement. In this study, a prestressed concrete box girder bridge is taken as an example. The purpose of the field investigation is to assess the current situation of the bridge and provide relevant analytical parameters. The distinctive inspection and survey items include vehicle ground penetrating radar (GPR) for detecting the thickness of the pavement and the bridge deck, and quantitatively evaluating the static load distribution of the current bridge pavement. Additionally, the impact-echo method is used to verify the inspected deck thickness. To understand the current prestress of the prestressed

[1] Associate Researcher, National Center for Research on Earthquake Engineering
[2] Associate Technologist, National Center for Research on Earthquake Engineering
[3] Assistant Researcher, National Center for Research on Earthquake Engineering
[4] Research Assistant, National Center for Research on Earthquake Engineering

tendon, the vibration-based measurement method is used. The results of the investigation may provide a valuable reference for advanced applications of related technology research and development.

Applied Field Inspection Technologies

The investigation items of in the present study include the detection of the thickness of the bridge deck asphalt concrete (AC) pavement and concrete top web, observation of the crack depth in the box girder, the concrete material elastic modulus, estimating the stiffness of the box girder, and the existing pre-stressed tendon tension force. A visual inspection was performed on the outward appearance of tendons. Moreover, instrumental measuring methods were applied, including the vehicle GPR detection method, the impact-echo inspection method, and the vibration-based measurement method, as shown in Table 1.

Table 1. Investigation items and inspection methods.

Investigation items	Inspection methods
Deck AC Thickness	Vehicle GPR
Girder Top Web Reinforced Concrete (RC) Thickness	Vehicle GPR / Impact-echo
Crack Depth	Impact-echo
RC Young’s Module	Impact-echo
Girder Stiffness	Vibration-based Measurement
Pre-stressed Forces	Vibration-based Measurement

1. Vehicle ground-penetrating radar

When conducting field inspections or experiments on in-service bridges, the impact on traffic is usually one of the primary considerations. Thus, the vehicle GPR detection method provides a feasible and low traffic impact means of inspection, as it uses a moving vehicle equipped with a GPR detection device. As shown in Figure 1, the vehicle performs GPR detection on the bridge at a constant velocity (30-60 km/hr). The GPR device uses a transmitting antenna to emit high-frequency electromagnetic waves at frequencies ranging from 1 MHz to 2 GHz (commonly known as radar waves) to penetrate an inspected structure or a detected object, and to identify the interface between different electrical media such as the concrete, steel bars, pipelines, and hollow defects in concrete structures. The radar generates the transmitting signals, receives the reflected signals from the receiving antenna, and then analyzes and processes the reflected signals to identify the material interface distribution of the inspected structure or the dimensions and the locations of steel bars or internal hollow defects. The transmission time of the reflected signal is proportional to the transmission distance to the detected interface and inversely proportional to the wave velocity of the electromagnetic wave transmission in the materials. The relationship between the signal strength and the transmission time of the electromagnetic wave is analyzed. I.e., the position of the reflection interface and the corresponding dielectric constant can be estimated. This method can also be used to understand the fluctuation distribution of the thickness of materials or the characteristics of reflection layers. A photo of a vehicle equipped with GPR for bridge deck detection is shown in Figure 2, which has been proven to reduce significantly the impacts on traffic and to be capable of reliable detection.

(a) GPR system

(b) GPS antenna

(c) Data Recorder

(d) Vehicle GPR

Fig. 1. Vehicle GPR system and instrumentation.

Fig. 2. A vehicle performing a GPR inspection.

2. Impact-echo method

The impact-echo method mainly uses the pulse elastic stress wave generated by an impactor, such as steel balls or hammers, to import strain waves into the inspected medium, with the reflected time-domain signal received in return. By converting the time-history signal to the frequency domain spectrum in the post-processing procedure, inspectors can determine the size or shape of the inspected structure. Figure 3 shows the equipment used in the impact-echo method. The source of the impactor for generating elastic stress waves is steel balls with diameters of 3 to 20 mm. As shown in Figure 4, the inspector strikes the concrete surface with the steel ball to generate low-frequency strain waves, with the generated wave frequencies in the concrete structure ranging from 1 to 150 kHz. Once the strain waves detect the boundary between different materials or internal defects, the strain wave will be reflected to the impact surface, and the surface disturbance displacement caused by these reflected waves is recorded with a detector sensor close to the impact source point. A data logger measures the reflected elastic strain wave and generates analog voltage signals that are proportional to the displacement response. These time-varying signals are digitized by a data acquisition system and passed to a data processing computer. The signals are converted into spectrum responses using the Fast Fourier Transform method and the peak frequency corresponding to the peak amplitudes shown in the converted spectrum, which is related to the multiple reflections of strain waves in the inspected structure, providing beneficial information for determining the size, integrity, and location of defects.

3. Vibration-based identification method

The vibration-based measurement method is used in the present study to evaluate the effective stiffness of the box girder and the current pre-stress force of the tendons. Accelerometers were installed on the tendons to record the vibration signal to identify the relationship between the current pre-stress force and the vibration frequency of the tendon. Through transforming the vibration time domain signal to the frequency domain, the representative frequency of the tendon vibration modal can be obtained, and thus the current tendon force can be found from the modal frequency and related tendon parameters. Additionally, vibration measurement sensors were distributed on the bridge box girders. The measurement results were further converted into signal spectrum information to obtain the representative value of the natural vibration frequency of the structural system in the vertical direction. Figure 4 shows the vibration-based measurement method for the box girder.

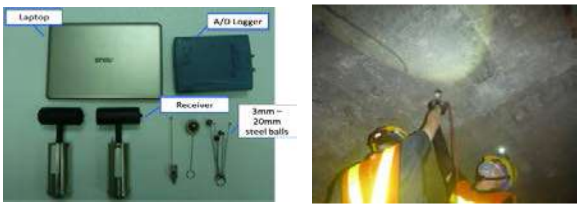

(a) Instrumentation (b) Measurements

Fig. 3. The impact-echo method.

(a) Girder stiffness (b) Pre-stressed force

Fig. 4. Vibration-based measurement on the girder.

Investigation Signal and Result

The vehicle ground-penetrating radar result provides a comprehensive picture of the thickness distribution of the AC pavement on the bridge deck and the concrete top web of the girder, as shown in Figure 5 (a), with a three-dimensional illustration obtained as shown in Figure 5 (b). As the static loadings can be set according to the actual thickness of the pavement in the structural analysis model, the investigated thickness of the pavement provides practical and informative loading data for conducting the analysis work. Moreover, the crack depth inspected by the impact-echo method can be used to evaluate the actual deterioration state, which could be used to tune material properties. The external tendon pre-stress and the representative fundamental frequency of the bridge unit girders obtained by the vibration-based measurement can be adjusted by the feedback analysis model so that the structural analysis can genuinely reflect the current characteristics of the bridge structure and help in developing practical and feasible improvement plans.

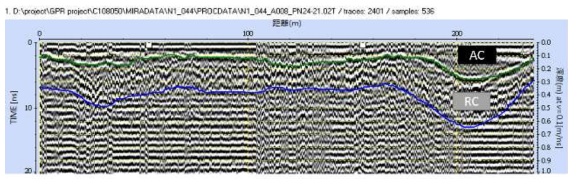

(a) GPR inspection data

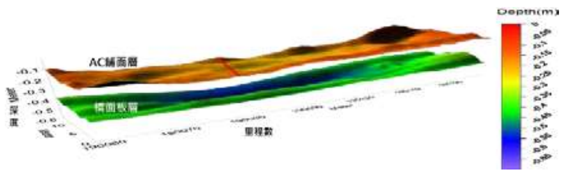

(b) 3D image of the thickness of the AC and deck

Fig. 5. Vehicle ground-penetrating radar results.

Figure 6 (a) shows the frequency spectrum of the measured signal from using the impact-echo method to estimate the concrete deck thickness of the box girder. The corresponding peak frequency was obtained by converting the vibration signal to the frequency spectrum. Furthermore, the wave travel distance, which is considered as the thickness of the inspected deck, was deduced from the peak frequency and the propagation velocity of the elastic pulse wave in the concrete. Additionally, the impact-echo method was applied to the detection of the crack depth in the concrete. Figure 6 (a) and (b) present the detected signal and the obtained spectrum signal, respectively.

(a) AC thickness

(b) Crack depth

Fig. 6. Resulting signals from the impact-echo method.

By measuring the vibration signal, the dynamic characteristics of the structure can be identified. Thus, the result of the vibration-based measurement method presents the stiffness of the box girder as well as further indicating the pre-stressed tendon current stress status with the representative frequency, as shown in Figure 7 (a) and Figure 7 (b), respectively.

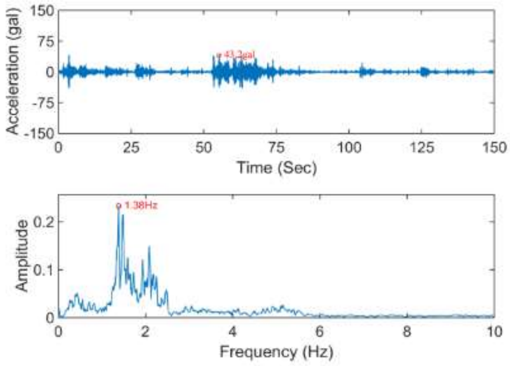

(a) The vibration signal and the spectrum of a girder

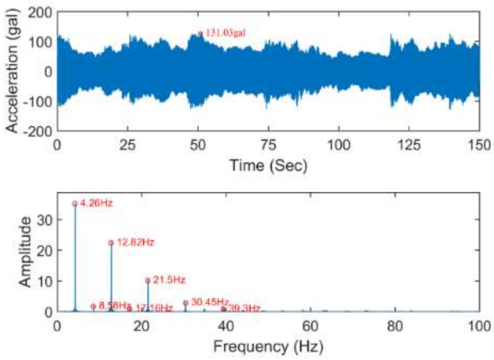

(b) The vibration signal and the spectrum of a tendon

Fig. 7. Result of the vibration-based measurement.

Conclusions

Although the results of regular inspections or the long-term monitoring of bridges can provide valuable reference information for the practical assessment of the current structural service condition, it is occasionally necessary to conduct a specific investigation due to the effects of deterioration or unexpected factors to evaluate the current characteristics of the structure. This study applied and proved the feasibility of several inspection technologies, including the vehicle ground-penetrating radar method, the impact-echo method, and the vibration-based identification method. The primary contribution of this work is to integrate various information and practical feedback on the assessment procedures of bridge conditions. There are many uncertain factors to be considered in the evaluation of real bridge structures. The studied inspection technologies could be useful in assisting bridge management authorities and consultants in formulating practical improvements, and it is expected that the excellent management plan can complete the proper maintenance and ensure the safety of passersby.

Advanced Web Application Development for Bridge Management and Simulation (I): Technical Survey

Kuang-Wu Chou[1] and Chia-Chuan Hsu[2]

周光武[1]、許家銓[2]

Abstract

This study investigates advanced methods of developing applications that can efficiently perform bridge management and simulations. The investigation focuses on distributed computing to integrate various independent computing systems, considering that it is often insufficient to exploit only a single computer, much less expecting the computer installed with all required computing resources. Internet offers a universal way of enabling communication between the components of a distributed system that supports the developed applications. Web browsers are used to provide the user interfaces of these applications. Development of advanced, native-like or desktop-like web applications is targeted.

Keywords: web application, distributed computing, Internet

Introduction

In the past, desktop applications have been preferred to create software because they can provide users with much richer graphical user interfaces than web applications. But recently, the browser user interfaces (BUI) provided by web applications become richer. Supporting BUI development, several web frameworks or libraries emerged and become more mature, such as Google's Angular and Facebook's React. While it is unlikely to decouple desktop applications from their dependencies on operating system, running web applications need no dependencies to be installed in advance. The only requirement to run a web application is to enter into browsers the uniform resource locator (URL) or IP address of the application. Then the application can be displayed and run in browsers of different operating systems and devices.

Because everyone can easily get and use browsers from computers, laptops, or mobile devices, the Web (World Wide Web) and web browsers are great places to distribute and run applications. Any user doesn't need to manually install and update web applications because their updates and installations are performed on web servers. The Web and web browsers are so ubiquitous that we intend to develop web applications instead of desktop ones.

This study is inspired by Electron, an open source framework of application development, which helps users use web technologies to create cross-platform desktop applications, including the famous Visual Studio Code and Facebook Messenger. This study also intends to use web technologies to create applications not only looking like but performing as desktop applications.

This study tries to create web applications that not only can help manage bridge information but also can perform simulations of bridges through Internet. Considering that such simulations could consume significant computational resources, we investigate state-of-the-art web technologies to find out a web application design able to afford asynchronous computations by many users on the Web, a better design able to offer competitive application performance.

What Is a Web Application

A web application is a computer program executed through web browsers. As a client-server program, a web application is hosted on a web server to serve requests from clients. The requests are transmitted through Internet. To the web server, clients

[1] Associate researcher, National Center for Research on Earthquake Engineering
[2] Assistant researcher, National Center for Research on Earthquake Engineering

sends such requests by using web browsers. Web browsers graphically show the user-friendly interfaces of web applications to help clients send their requests to the web servers.

It is simple to run a web application. Users only need to specify in browsers the URL of the web application. The URL may be merely an IP address, which may refer to a web application that a private local network provides.

How a Web Application Works

Fig. 1 shows how a web application works. Its working is enabled by communication between a client (browser) and its web server.

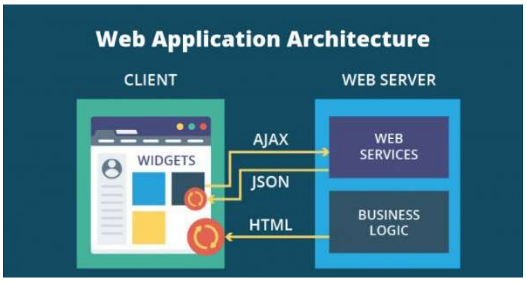

Fig. 1. Client-server interaction architecture of a web application [Banga 2020]

After typing the URL of a web application in the address bar of a web browser, we may request a resource from a web server of the web application. The resource may be a HTML (hypertext markup language) file that browsers use to create a web page. To respond to that request, the server sends files related to that resource to the browser. Then the browser processes those files to show the requested resource.

To represent a web application, a web page often contains widgets, i.e., user interface (UI) components that help users interact with the application. Behind widgets, the Asynchronous JavaScript and XML (AJAX) technology enables browsers to directly send further user requests to the web server. The web server may return JavaScript Object Notation (JSON) files to the browser as the responses of those requests.

Architecture of a Web Application

Fig. 2 shows that in general, a web application comprises its GUI (Graphical User Interface), web server, and database. In the above, we have already talked about how the GUI or browser cooperates with the web server to serve user requests. It seems that the GUI and web server suffice to compose a web application.

Nevertheless, a web server often needs at least a database system to store the information exchanged between the web server and the browser or the result generated by the business logic running inside the web server. In some web applications, an application server is separated from the web server. Such an application server might be responsible for running a specific software application, which either cannot be executed by the operating system running the web server or would consume much CPU time because of performing some analysis or simulation.

Therefore, there is at least one advantage of separating the application server from a web server. The web server could avoid blocking due to running a time-consuming analysis, capable of timely responding to user requests regardless of the progress of the analysis. As shown in Fig. 3, the application server is to implement the business logic, the logic that the application is supposed to serve users. The web server may be responsible for managing databases and representing the web application in browsers. In fact, representing web applications could be further moved to the client end by using the approach of single-page application (SPA), which is detailed below.

Fig. 2. Simplified architecture of a web application [Raj 2016]

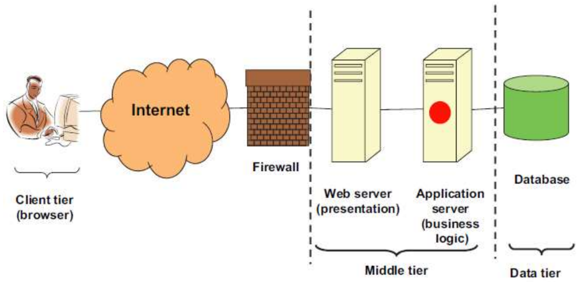

Fig. 3. Web application architecture [IBM 2020]

Single-Page Application versus Multiple-Page Application

There are two main approaches of designing a web application: traditional-page application and single-page application (SPA). A traditional-page application is also called a multiple-page application. Both approaches have three layers in common, data, presentation, and business logic. The presentation layer implements the logic to represent and to operate the GUI, so also called the presentation logic layer. The presentation logic layer may be at either the server side or the client side, depending on which design approach is applied. For the approach of multiple-page application, the presentation layer works at the web server. For the approach of single-page application, the presentation layer works at the client side.

Fig. 4 shows two round-trip patterns of communication between the client and server, one the traditional-page lifecycle, the other the SPA lifecycle.

Fig. 4. Traditional-page (multiple-page) application lifecycle versus single-page application (SPA) lifecycle [SCAND 2019]

In the traditional-page (multiple-page) lifecycle, the web server creates each new view (or page indicated by HTML in Fig. 4) and sends it to the client (browser), for the client to reload the view. Such views include the page the client requests initially from the server and pages that are new or updated in response to the client's sending data to the server. Typically, a view or a web page is represented by a HTML file, CSS (cascade style sheet) files, and JS (JavaScript) files, as shown in Fig. 5. These are all resource files for browsers to represent a web page and enable the web page to graphically interact with users.

Server-side rendering

To show a web page and to interact with users efficiently, a multiple-page application often applies server-side rendering (SSR). In response to the navigation of users, SSR creates a full HTML file on the web server to avoid additional roundtrips the client needs to request and to template data [Miller and Osmani 2019]. Then the web server sends the created full HTML file to the browser, for the browser to display the web page and to activate it with minimum time. Because SSR could enable the web server to send the client the minimum amount of JavaScript code, web pages could become interactive in the browser as soon as possible.

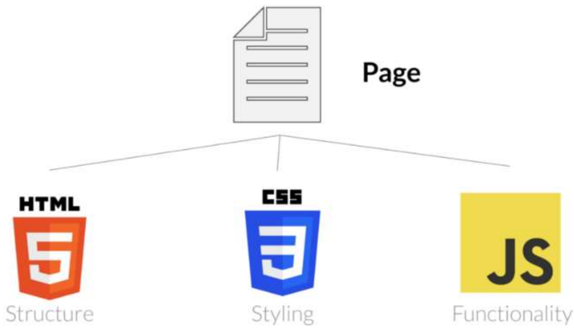

Fig. 5. Resource files that web browsers parse to show a web page and make it interactive [Kononenko 2018]

The SPA lifecycle has a different story. During that lifecycle, the web server sends to the client a view (a web page indicated by HTML in Fig. 4) only once. That means the client never needs to reload any further web page. Following the initial request to the server for the only web page, all client-server round trips are either the client's AJAX requests for data or the server's responses as JSON or XML files carrying the requested data. JSON files are often preferred. This is because JSON is simpler, more concise for describing object structures than XML and parsing JSON is more efficient. Fig. 6 shows a comparison between a JSON file and an XML file, both representing the same data.

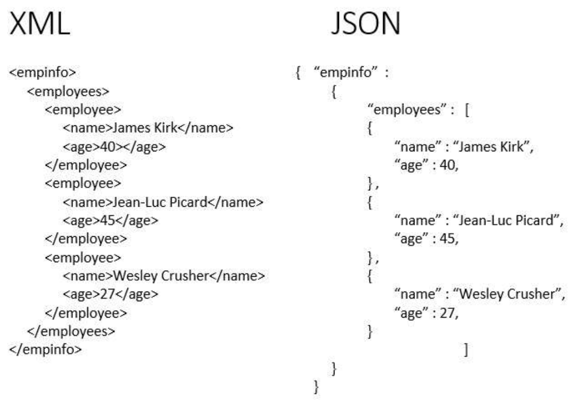

Fig.6. XML versus JSON [Hoi 2017]

Client-side rendering

To run as mentioned above, a SPA applies client-side rendering (CCR). CCR renders a SPA in a browser by entirely using JavaScript. The JavaScript code is linked by the only HTML file the web server sends. Though the HTML file has no concrete content, the linked JavaScript code contains all the concrete HTML content or templates of the SPA as strings. This means after loading the HTML file, the browser shows no content until fetching all the JavaScript code. In other words, the browser renders the concrete content after compiling the HTML file and all the JavaScript code.

Since all the JavaScript code the SPA requires to render in the browser are downloaded only once, the SPA needs only requesting data objects from (as the AJAX call and returned JSON in Fig. 4) or sending them to the web server. As a result, the web server behaves as a pure data provider. Focusing on providing data, the web server of a SPA could work more efficiently than that of a multi-page application.

SPA: the front-end Javascript codes consuming the back-end Web API

Supported by client-side rendering, a web server may be implemented as providing an application programming interface, i.e., a Web API able to get or send data objects in JSON format. Such a Web API is independent of the JavaScript codes rendering the SPA at the client side. But those JavaScript codes might need to consume the Web API to run the SPA.

The above also indicates that a Web API may be developed independently of any JavaScript code. On the other hand, the JavaScript code consuming the Web API may be implemented with the help of front-end JavaScript frameworks, such as Angular or React. The Web API and the JavaScript code may be developed by two teams, one developing the back end (the Web API), the other responsible for the front end development (the JavaScript codes).

Conclusions

This study investigated the general architecture of a web application, which could comprise a web server, an application server, and databases. While the web server and databases are essential for the architecture, the architecture would need the application server that focuses on performing computations that could consume significant computational resources. Through the web server, the application server may use databases to access bridge model data and to store the simulation results. On the other hand, the application server provides the progress of simulations and simulation results in response to requests from Internet. As a data provider, the application server may be implemented to offer a Web API, which any web application may call to perform simulations, showing the simulation progress and results in browsers.

To efficiently show the information of simulations, a web application may be designed according to two approaches: single-page application (client-side rendering) and multiple-page application (server-side rendering). On desktops, single-page applications could perform smoothly and efficiently, capable of behaving as desktop-like applications. But for mobile devices whose CPU power is limited, we might need to apply the multiple-page design to create a web application. Applying a hybrid of both design approaches is also possible for optimizing the performance of the web applications that we develop.

References

Banga, Swapnil (2020). Web Application Architecture: Definition, Models, Types, and More. Available from https://hackr.io/blog/web-application-architecture-definition-models-types-and-more.

Facebook, Inc. (2020). React [Web programming framework]. Available from https://reactjs.org/

GitHub, Inc. (2020). Electron [Web programming framework]. Available from https://www.electronjs.org/

Google LLC (2020). Angular [Web programming framework]. Available from https://angular.io.

Hoi, Sunny (2017). JSON vs XML: Which Format To Use For Your API?. Available from https://www.1337pwn.com/json-vs-xml-format-use-api/

IBM (2020). Web Application Architecture. Available from https://developer.ibm.com/

Kononenko, Kevin (2018). The relationship between HTML, CSS and JavaScript explained by building a city. Available from https://www.freecodecamp.org/news/the-relationship-between-html-css-and-javascript-explained-by-building-a-city-a73a69c6343/

Miller, Jason and Osmani, Addy (2019). Rendering on the Web. Available from https://developers.google.com/web/updates/2019/02/rendering-on-the-web

Raj (2016). What are the advantages of web application over software?. Available from http://icynta.com/blog/advantage-web-application-over-standalone-software/

Saxton, Patrick (2015). How a webpage is loaded and displayed. Available from https://varvy.com/pagespeed/display.html

SCAND (2019). Single Page Application vs Multi Page Application. Available from https://scand.com/company/blog/single-page-application-vs-multi-page-application/

Development and Application of Bridge Monitoring Management System

Kuang-Wu Chou[1], Chia-Chuan Hsu[2], Ming-Chun Lai[3], Ming-De, Lu[4] and Yu-Chi Sung[5]

周光武 [1]、許家銓 [2]、賴明俊 [3]、盧明德 [4]、宋裕祺 [5]

Abstract

This study develops a web application to help monitor a bridge in real time: the bridge monitoring management system, BMMS. BMMS collects the real-time data of sensors installed on the bridge, from on-site computers connected with data loggers. Working in the world wide web, BMMS can help users remotely access the real-time bridge responses through browsers. BMMS offers a browser user interface that uses 2D interactive graphics to show a bridge, enabling users to pick a sensor at the bridge and then showing real-time data of the sensor in a browser.

Keywords: real time, web application, time-series database, web API, InfluxDB, Angular, ASP.NET Core

Introduction

In Taiwan, the bureaus who manage or maintain bridges care about the safety and reliability of those bridges. Every year, they allocate budgets for retrofitting bridges and for the short-term, mid-term, or long-term projects of monitoring new or post-retrofit bridges. They try to figure out whether contiguous natural disasters alter the safety of a bridge. Once the safety could not be ensured, they need to announce safety warning to prevent people and vehicles from any possible disaster. While the fast progress of information technology dramatically reduces the cost of creating systems to monitor a bridge, most important bridges built or retrofitted in recent years are planned to be monitored in a short, medium, or long period of time. In general, besides monitoring devices, a robust bridge monitoring system needs a software system to manage those devices and to record and maintain the data from those devices.

In the past, developers have preferred to create software as desktop applications because such applications can serve users with much richer graphical user interfaces than web applications. But recently, the browser user interfaces (BUI) web applications provide become richer. Supporting BUI development, several web frameworks or libraries development emerged and gets more mature, such as Google's Angular and Facebook's React. While it is unlikely to decouple desktop applications from their dependencies on operating system, running web applications need no dependencies to be installed in advance. The only requirement to run a web application is to enter into the browser the uniform resource locator (URL) or IP address of the web application. Then the application can show and work in browsers of various operating systems and devices.

NCREE develops a bridge monitoring management system (BMMS) as a web application. Through browsers, users can monitor the status of managed bridges and view the real-time responses of those bridges. Users can also configure the system to send warning messages whenever the system gets abnormal or the real-time bridge responses are found unusual. Fig. 1 shows some uses of the system.

[1] Associate researcher, National Center for Research on Earthquake Engineering
[2] Assistant researcher, National Center for Research on Earthquake Engineering
[3] Chief technologist, Bridge-Enlightenment Co., Ltd.
[4] Chief technologist, V3 Co., Ltd.
[5] Dean, College of Engineering, National Taipei University of Technology

Fig. 1. Uses of Bridge Monitoring Management System

Architecture of Bridge Monitoring Management System

Fig. 2 shows how BMMS works. To help monitor a bridge, BMMS works between a user and the on-site computer system measuring the response of the bridge. Through a web browser, an authorized user can contact BMMS, using its web application (BMMS WebAPP) to examine the status and response of the bridge. BMMS routinely captures the monitored response of the bridge from a Dropbox storage, a storage shared with the on-site local server installed in the bridge. The local server keeps collecting the monitored bridge response sent by a data logger also installed in the bridge and keeps saving the bridge response data as files in the Dropbox storage for BMMS to access.

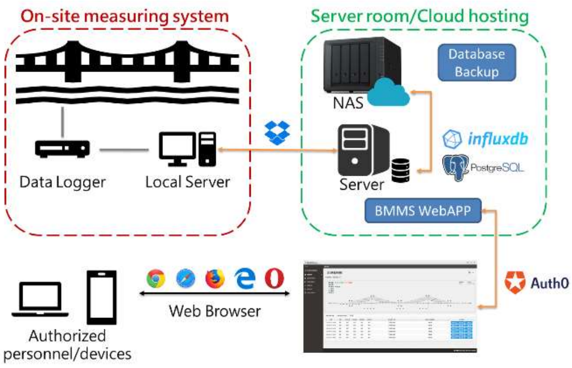

Fig. 2. Working architecture of BMMS

Fig. 3 shows the software architecture of BMMS. BMMS comprises four layers: representation, logic, data, and data storage. Each layer is illustrated below:

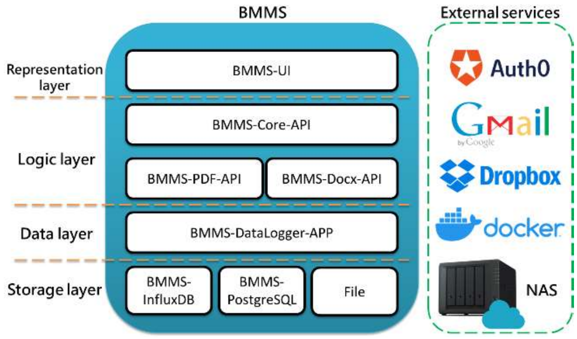

Fig. 3. BMMS software architecture

1. Representation layer: this layer uses the services of the logic layer and offers the user interface of BMMS (BMMS-UI). This layer is implemented with technologies including HTML (hyper-text markup language), CSS (cascading style sheet), and Angular. Angular is a framework to generate JavaScript codes giving web pages dynamic behaviors. This layer is responsible for managing every monitoring project, reviewing the status of monitored bridges, conducting and notifying users of abnormal events, and managing databases.

Fig. 4 shows the user interface design of BMMS. The user interface of BMMS has three modules: user verification, project management, and monitored data presentation. The project management module helps users maintain the project list, add and remove projects, configure the people who BMMS should notify of events or other issues, and manage the personnel working with projects. The monitored data representation module helps manipulate the sensor data and configure bridge parameters, the people who BMMS notifies of messages, and the privileges of the personnel to use BMMS. The sensor data manipulation offers tables of measured data, 2D interactive graphics, and the interface to notify people of messages. 2D interactive graphics is used to show the monitored bridge, enabling users to pick a sensor at the bridge and showing real-time data of the sensor in browsers. Fig. 5 shows a user picks a sensor measuring the angle of rotation at a point of a monitored bridge, the sensor pointed by a red arrow. BMMS shows the real-time measurement and the time history of the rotation angle in past hours.

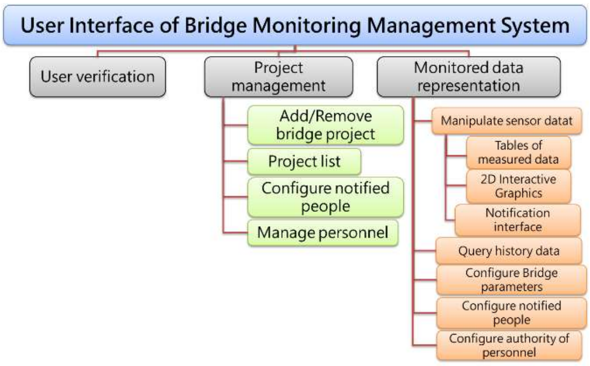

Fig. 4. User interface design of BMMS

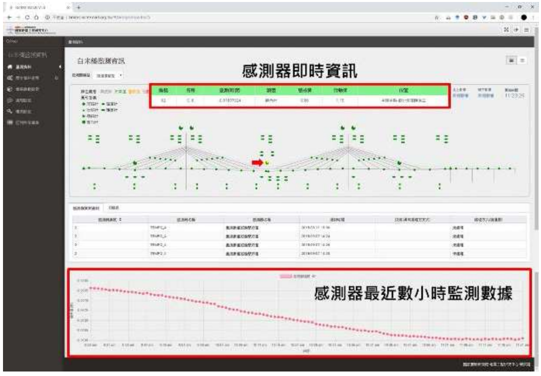

Fig. 5. Real-time measurement and time history of a sensor picked at the 2D graphics of a monitored bridge

2. Logic layer: this layer offers three web application programming interfaces (web API): Core API, Docx API, and Pdf API. The three web APIs are implemented with ASP.NET Core. Besides, OAuth, an open authentication and authorization protocol, is applied to secure any usage connection to these APIs. This layer is responsible for computation, exchanging data between clients and the system, and creating reports. Fig. 6 shows how Core API serves other modules, APIs, applications, and systems by providing them an interface of data bus.

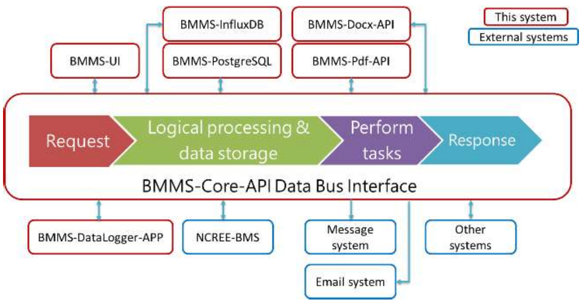

Fig. 6. Services of BMMS Core API

3. Data layer: this layer (BMMS-DataLogger-APP) is a console application (app). This app is used to resolve the physical quantities from the sensor data in a Dropbox folder. The Dropbox folder is shared with an on-site server, which keeps getting data from sensors and writing them into the Dropbox folder.

Fig. 7 shows this app routinely stores the resolved physical quantities into the time-series database, BMMS-InfluxDB. In addition, this app compares those quantities with the predefined action and alert values, deciding whether to call Core API at the logic layer to report errors or warnings by using messages or emails.

Fig. 8 shows how this app reacts to an event. Once an event file is created in the Dropbox folder, this app resolves the event from this file and sends the information to Core API, letting Core API call the email and message system to notify people of this event. This app also conducts the sensor data and physical quantities corresponding to the event, then notifying Core API of the update of those data and quantities. The notification drives Core API to determine the status of the monitored bridge, call Docx API to create a report, and notify people of the status of the bridge for this event.

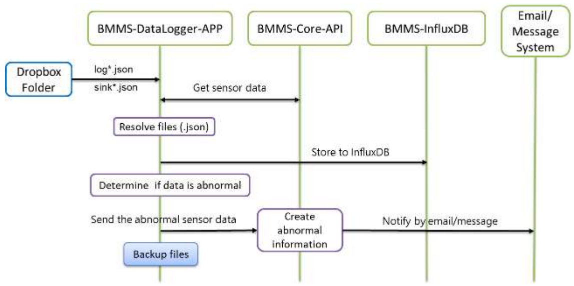

Fig. 7. Routine operations of the DataLogger app

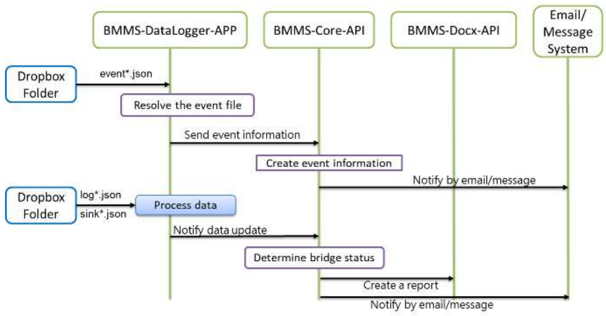

Fig. 8. Event-driven operations of the DataLogger app

4. Storage layer: BMMS uses three types of data storage: file, time-series database, and relational database. Files store reports and the data synchronized with those in the Dropbox of the on-site server, a computer collecting data of sensors from the data logger. Time-series databases collect and support computations on real-time data from the monitoring devices or IoT sensors. BMMS adopts InfluxDB to create time-series databases. Fig. 9 shows the design of the BMMS time-series database. The relational database uses tables to store the configurations of BMMS, monitoring projects, sensors, and users.

BMMS adopts PostgreSQL to manage relational databases. Fig. 10 shows some tables of the PostgreSQL database. These tables store the data of a BMMS project of monitoring a bridge.

The storage layer is planned to cooperate with NAS (network attached storage), which will back up all the data of BMMS to ensure the safety of data storage as well as the recovery of the services of BMMS.

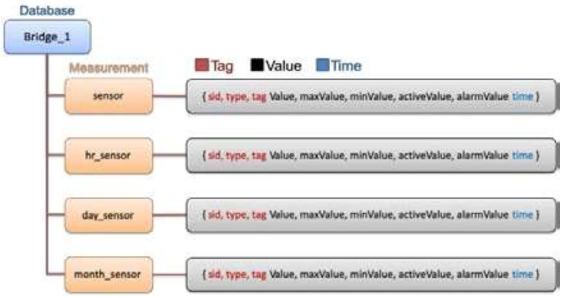

Fig. 9. Design of BMMS InfluxDB time-series database

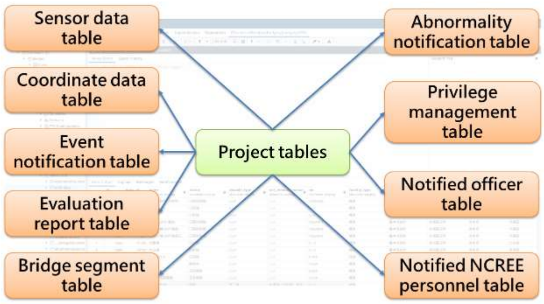

Fig. 10. Tables of BMMS PostgreSQL database

Conclusions

This study develops BMMS by integrating various software, computers, and devices. BMMS keeps recording the real-time responses of monitored bridges, successfully supporting the long-term monitoring of those bridges. BMMS enables efficient computations and massive data queries from users because of using the time-series database InfluxDB to record the long-term data of the monitoring sensors. According to the real-time data of those sensors, BMMS could offer users a safety evaluation of those bridges at any time. Moreover, BMMS could determine whether to notify the bureaus who manage those bridges of crucial events or warnings, helping bridge managers prevent disasters. After crucial events or even disasters, BMMS could quickly examine the health of the monitored bridges. BMMS has been applied to monitor Bai-Mi Landscape Bridge of Su-Hua Provincial Highway No.9, No. 24 bridge of Provincial Highway 86, and three extradosed bridges. The three extradosed bridges are Tai No. 61 Western Coast Expressway's WH10-A bridge, WH50-2 bridge, and Fangli Da'an bridge.

References

Google LLC (2020). Angular [Web programming framework]. Available from https://angular.io.

InfluxData Inc (2020). InfluxDB [Time-series database]. Available from https://influxdata.com.

Microsoft (2020). ASP.NET Core [Web programming framework]. Available from https://docs.microsoft.com/en-us/aspnet.

The PostgreSQL Global Development Group (2020). PostgreSQL [Relational database management system]. Available from https://postgresql.org

Health Monitoring on a Repaired Earthquake Damaged Bridge by Optic Fiber Differential Settlement Sensors

Zheng-Kuan Lee[1] and Chia-Chuan Hsu[2]

李政寬 [1] 許家銓 [2]

Abstract

This paper is about the design and application of optical-fiber differential settlement measurement (DSM) sensor for bridges. By using the law of connected vessels, bouncy principle, forces equilibrium condition, and the photo elasticity of Fiber Bragg Grating (FBG), the DSM sensor is easily manufactured and sensitive to the level change. Besides the design principle, this study illustrates the application of the DSM sensors on underpass bridges. From the field case, it is shown that the proposed DSM sensors are stable and precise to monitor the behavior of multiple-span underpass bridges. In this paper, to share the optical fiber DSM field-experience is the aim of this study. Based on the field experience, enhancement design for the DSM sensor will be discussed for the future application.

Keywords: bridge safety monitoring, settlement sensor, FBG

Introduction

Bridges are large-scale linear structures used to cross obstacles to extend traffic routes (e.g., roads and railways), cross natural barriers (e.g., rivers, straits, and canyons), or cross artificial barriers (e.g., highways and railway lines). Bridges connect urban and rural areas, as well as transport water and energy, making them indispensable structures in modern civilization [1] .

Bridges are profoundly affected by the environment, such as from external forces of nature including earthquakes, typhoons, and floods, as well as by the aging problem of materials, such as the bridge deformation due to creep and shrinkage of concrete [2]. Therefore, regular manual level survey for bridge elevation is important work in bridge inspections.

However, because of the growth of cities, the increasing number of bridge demands more efforts for the inspections. Therefore, adapting technologies from other domain knowledge for the bridge level survey to save human resources and enhance efficiency has continuously been a concern to bridge managers and engineers. With the advent of the Internet of Things(IOT), it is expected that automatic bridge safety monitoring technologies for will flourish.

This study designed and produced a Fiber Bragg Grating–based differential settlement sensor (DSM), which was applied to the in-situ monitoring on elevation changes in bridges. Based on application results, it is shows that the proposed DSM sensor can be used as an instrument for the automatic leveling of bridge elevation.

Brief Review on the Development of Laser, Optical Fiber, and Fiber Bragg Grating

The invention of lasers and optical fibers in the mid-20th century has substantially improved quality of life and facilitated convenient worldwide communication, an influence that was difficult to imagine at the time they were invented. The key periods in optical communication are as follows: (1) Albert Einstein first predicted the possibility of stimulated emission in his 1917 paper [3]. (2) Light-transmitting optical fibers were invented in the 1930s; however, they could only be used as art lighting and endoscopes. (3) In 1960, Maiman produced a laser by stimulating a ruby through high-intensity light,

[1] Associated Research Fellow, National Center for Research on Earthquake Engineering
[2] Assistant Research Fellow, National Center for Research on Earthquake Engineering

thereby providing the first necessary condition for light to transmit information. (4) In 1966, Kao and Hockham discovered that rapid loss of light was mainly due to impurities within optical fibers, and determined that increasing the purity of glass enabled the transmission distance of optical signals to exceed 100 km. (5) In 1970, a low-loss optical fiber was mass-produced by Corning Inc. (6) In 1977, the world's first optical fiber communication system was developed for commercial use in Chicago in the United States. (7) In 1978, Hill and colleagues discovered the photosensitivity of an erbium-doped optical fiber and used an argon-ion laser to induce chemical changes in photosensitive optical fibers. [4] (8) In 1989, Meltz and colleagues employed high-energy ultraviolet lasers by using the transverse holographic method to change the molecular structure of a photosensitive optical fiber, turning it into an optical filter [5]. (9) In 1993, Hill and colleagues developed the phase-mask method to produce fiber Bragg grating (FBG), thereby enabling the production technology of FBG to mature [6]. Today, FBGs are mass-produced and commercialized, enabling them to be purchased and applied in various fields.

Introduction to FBG

This study only describes the application of FBG; a detailed explanation of FBG can be found in [7]. Fig. 1 shows the optical and the mechanical behavior of FBG: the amount of change in the wavelengths of reflected light would depend on the amount of change in strain and temperature.

If both ends of one FBG are clamped using a heat-shrink tube as in Fig. 2, through which the force medium is introduced, the local organization forms sensing elements.

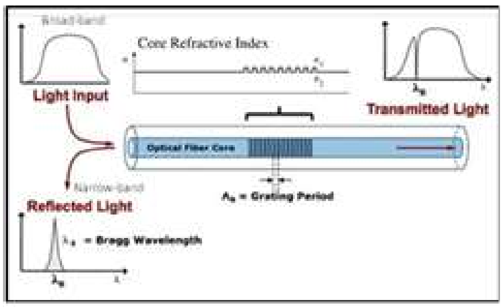

Fig. 1 Structure and spectral response of FBG

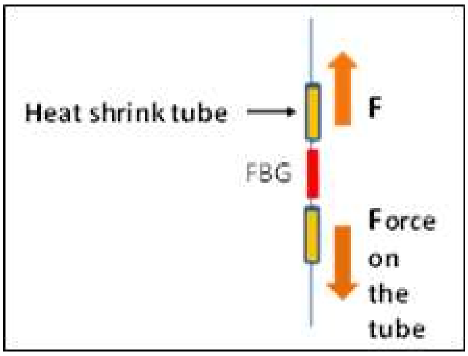

Fig. 2 Heat-shrink tubes placed on both ends of the FBG act as the application medium for external force F.

FBG-based Differential Settlement Sensor

Fig. 3 shows the structure of a set of FBG-based differential settlement sensors, which contain two water-filled containers connected by a communicating tube. The upper and lower ends of the FBG were clamped by two heat-shrink tubes, with one end fixed at the top of the container and the other end fixed with the cylinder buoy to withstand part of the cylinder weight [8]. The elevations of the two sensors in Fig. 3 may change into those elevations in Fig. 4. From the wavelength signals, the elevation difference between Fig. 3 and Fig. 4 could be calculated.

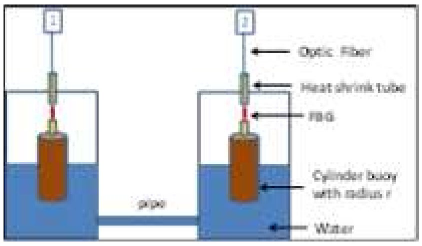

Fig. 3 FBG-based differential settlement sensors

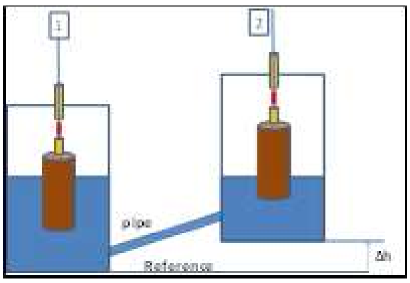

Fig. 4 Elevation change of the sensors

Bridge Monitoring Project

Fig. 5 shows three DSM sensors were deployed within each box girder and connected by pipes to observe the midpoint deflection as well as the elevation difference at both ends of the girder. In addition, optical fiber thermometers were placed on the roof plate and base plate inside some girders of a continuous 14-span underpass bridge at Tainan City, Taiwan. [9]

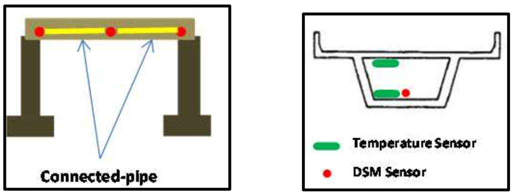

Fig. 5 Three DSM sensors deployed at each span; optical fiber thermometers in some girders

Fig. 6 shows the monitoring data of Span 1 about 24 hours, with the abscissa and ordinate representing time (min) and length (cm), respectively. The blue lines show the deflection variations at the midpoints Span 1; while the red lines indicate the elevation changes at both ends of the girder. Fig. 7 presents the temperature (°C) data collected by the optical fiber thermometer in the box girder. The blue line and the red line show the temperature variation on the roof plate and the base plate inside the girder, respectively. Obviously, the deflection of the girder is affected by the temperature, and there is a time-delay effect.

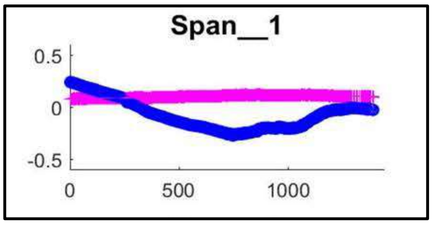

Fig. 6 Observation from 19:00 on June 10, 2018 to 18:30 on June 11, 2018. Blue line represents changes at the midpoint girder deflection and the red line represents the elevation changes at both ends of the girder. Abscissa and ordinate represent minutes and centimeters, respectively.

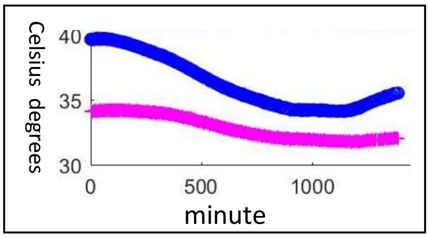

Fig. 7 Temperature observation of the box girder. The blue line and the red line indicate the temperature change of the roof plate and the base plate, respectively.

Discussion on the Bridge Structure Based on the Monitoring Data

The monitoring was conducted for more than 1 year with sampling rate 0.5 Hz. Fig. 8 graphs the maximum deflections (absolute value) by month and by span. The maximum deflections took place at the abutment spans (Span 1 and Span 14) and at those spans on both sides of the expansion joint between Span 7 and Span 8. Fig. 8 shows that the bridge deflection was stable with a fixed "W" pattern. Fig. 9 graphs the maximum elevation difference between two ends of each girder by month and by span, revealing that all spans were stable within a range from 0.03 to 0.37 cm.

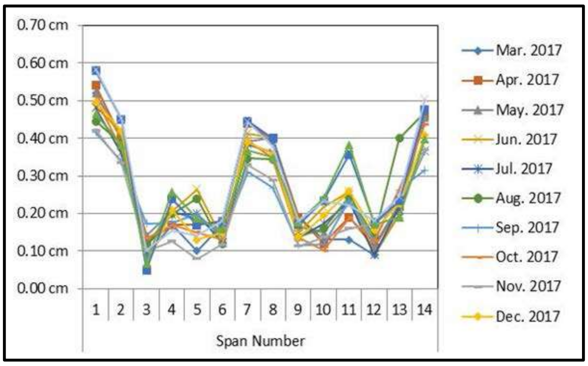

Fig. 8 Maximum girder deflection (absolute value) by month and by span.

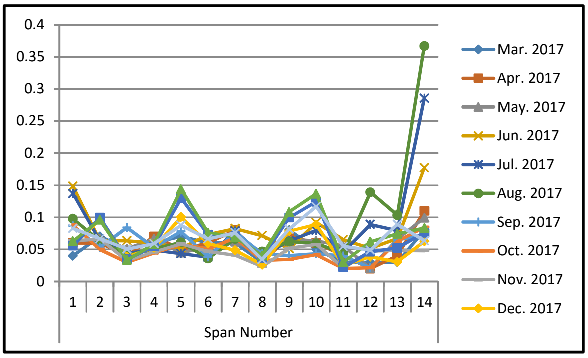

Fig. 9 Maximum elevation difference (absolute value) between two ends of each girder by month and by span.

Discussion on the Sensor Maintenance

Water in the sensors is vaporized anytime. In average, every three months, supplying water into the sensors is the maintenance work. It is a tedious and labor work inside the girder. The water vaporing problem should be considered in the future.

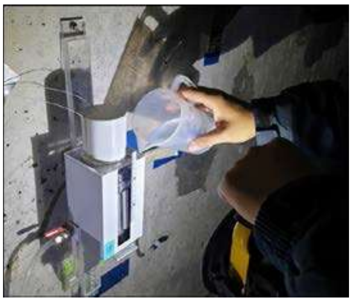

Fig. 9 Supplying water into the sensors

Conclusion

1. This study briefly introduces the development in history of laser, optical fiber, and FBG. It is realized that science and material science facilitate the progress of engineering technologies.

2. This paper proposes a simple design method for DSM sensor, integrated with the law of connected vessels, buoyancy principle, the equilibrium condition for two-force member, and the photo elasticity of FBG.

3. A 14-span underpass bridge was monitored with the proposed DSM sensor. It is proved the sensors are sensitive and reliable enough to clarify some subtle behavior of bridge structure.

4. From the field case in this study, it is shown that optical fiber and FBG sensor demonstrates great advantages especially for the long and multiple-span bridges.

Reference

[1] “Bridge,” Wikipedia, Retrieved July 18, 2018 from https://en.wikipedia.org/wiki/Bridge

[2]“Koror–Babeldaob Bridge,” Wikipedia, Retrieved July 18, 2018 from https://en.wikipedia.org/wiki/Koror%E2%80%93 Babeldaob_Bridge

[3]“Einstein Predicts Stimulated Emission,” APS NEWS, American Physical Society, Retrieved July 18, 2018 from https://www.aps.org/publications/apsnews/200508/history.cfm

[4]K. O. Hill, Y. Fujii, D. C. Johnson, and B. S. Kawasaki, "Photosensitivity in optical fiber waveguides: application to reflection fiber fabrication," Appl. Phys. Lett. 32 (10): 647, 1978.

[5]G. Meltz, W. W. Morey, W. H. Glenn, "Formation of Bragg gratings in optical fibers by a transverse holographic method," Opt. Lett. 14, 823-825, 1989.

[6]K. O. Hill, B. Malo, F. Bilodeau, D. C. Johnson, and J. Albert ,“Bragg gratings fabricated in monomode photosensitive optical fiber by UV exposure through a phase mask” Appl. Phys. Lett. 62, 1035, 1993.

[7]“Fiber Bragg grating,” Wikipedia, Retrieved July 18, 2018 from https://en.wikipedia.org/wiki/Fiber_Bragg_grating

[8]Z.K. Lee, “Bridge safety monitoring integrated system with full optical fiber and the method for sensing thereof,” U.S. Patent No. 9183739, November 10, 2015.

[9]B. S. Huang, C. H. Chiang, Y. H. Chen, “Restoration of Lateral Deviation in Bridge No. 24 at Provincial Highway 86 after the 2016 Southern Taiwan Earthquake,” Journal of the Chinese Institute of Civil & Hydraulic Engineering, Vol. 44, No. 3, pp.20–26, June 2017.

Truss-type Segmental Composite Structure for Temporary Rescue Bridges

Fang-Yao Yeh[1], Yao-Yu Yang[2], Bo-Han Lee[3], Chia-Ming Chang[4] and Kuo-Chun Chang[5]

葉芳耀[1]、楊耀畬[2]、李柏翰[3]、張家銘[4]、張國鎮[5]

Abstract

Typhoons and earthquakes, which occur frequently in Taiwan, often lead to the washout or collapse of river bridges, thereby causing traffic interruption. When a bridge structure loses workability, constructing a temporary rescue bridge is an effective disaster relief operation. In this study, a truss-type segmental composite temporary rescue bridge is proposed to improve the stiffness of longer span (50 m) bridges. A 50-m-span asymmetric self-anchored truss-type segmental cable-stayed bridge is designed, and experimentally validated. The autonomous assembly technology proposed for construction is validated via an on-site experiment and a simulation. The assembly process is found to improve worker safety during bridge construction and shorten the assembly time of the bridge. Two construction processes, namely the cantilever erection method and the incremental launching method, are compared to improve worker safety. The results of this study indicate that (1) the truss-type segmental composite bridge can improve the stiffness of a 50-m-span temporary rescue bridge, thus meeting the required deflection-to-span ratio; (2) autonomous assembly technology for bridge construction significantly improves worker safety and shortens the assembly time of the temporary rescue bridge; (3) the incremental launching method has greater operational efficiency than the cantilever erection method; and (4) the incremental launching method can avoid construction of the bridge over a river, thus providing better safety to the workers.

Keywords: temporary rescue bridge, truss type segment, safety of worker, automated assembly

Introduction

Typhoons and earthquakes, which occur frequently in Taiwan, often lead to the washout or collapse of river bridges, thereby causing traffic interruption. When a bridge structure loses its workability, constructing a temporary rescue bridge is an effective disaster relief operation. Yeh *et al*. applied glass-fiber-reinforced plastic (GFRP) material in a segmental temporary rescue bridge design, making it light-weight and reusable [1]. The live load capacity of the GFRP bridge was 5 t, and the span length was 20 m. However, when taking the actual working environment into consideration, the span length may be too short and assembly of this bridge may be difficult. The reasons are that the weather may not be suitable for construction and ensuring safety of on-site construction workers is difficult.

To address these problems, we use a truss-type segmental structure to improve the stiffness of a longer span (50 m) bridge and analyze the process of constructing the GFRP temporary rescue bridge. The assembly process is critical as it significantly affects the construction progress and worker safety during the bridge construction. Two different processes, namely the cantilever erection method and incremental launching method, are compared in terms of worker safety.

Design and Experiment for a Composite Bridge

[1] Research Fellow, National Center for Research on Earthquake Engineering
[2] Ph. D. Candidates, Department of Civil Engineering, National Taiwan University
[3] Assistant Researcher, National Center for Research on Earthquake Engineering
[4] Associate Professor, Department of Civil Engineering, National Taiwan University
[5] Professor, Department of Civil Engineering, National Taiwan University

Design of a truss-type composite bridge

For the design, a case of communities isolated by Typhoon Morakot in 2009 was considered. A river bridge with a 50 m span length was washed away by the floods, interrupting traffic to and from surrounding areas. A temporary rescue bridge needed to be completed within 8 h so that small trucks weighing 3.5 tons could access and transport relief materials into the isolated area.

This study develops a temporary rescue bridge system by using a self-balancing approach with a cantilever erection method and with an incremental launching method. An asymmetric self-anchored truss-type segmental composite cable-stayed bridge is proposed. Truss-type GFRP segmental bridge systems were studied to assess the structural requirements necessary to meet the following design requirements recommended by USDA: 50 m span, 3 m width, 5 t live load capability, and a deflection-to-span ratio of L/400 [2]. Fig. 1(a) shows the deformation shape and finite element method (FEM) model of the asymmetric self-anchored truss-type segmental composite cable-stayed bridge. The main girders of the bridge system with truss-type structural segments were composed of 203 mm × 60 mm × 9.5 mm C-shaped and 101 mm × 101 mm × 6 mm box-shaped GFRP composite members. The material properties of the GFRP were as follows: Young's modulus = 20.03 GPa, density = 1.72 g/cm^3, and allowable stress = 207 MPa. Fig. 1(b) shows the deflections under various loading positions. The maximum displacement is 10.67 cm, which meets the design requirement for a deflection-to-span ratio of L/400.

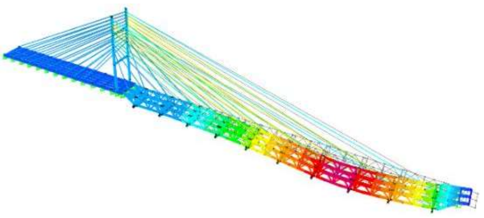

(a)

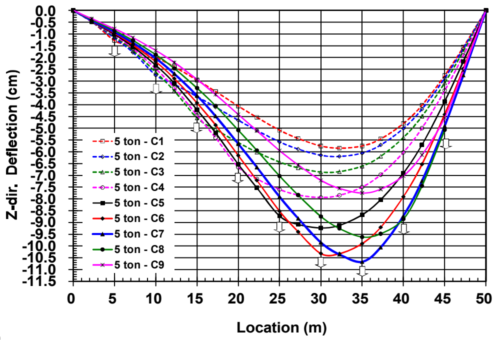

(b)

Fig. 1. Design results for a 50-m-span temporary rescue bridge: (a) the deformation shape and (b) deflections (for various loading positions).

Experiment for a truss-type composite segment

The typical experimental setup for a flexural test is shown in Fig. 2. The test program included a flexural test to measure the deflection and stiffness of the truss-type composite segment in order to calibrate the FEM model.

The specimen was tested using flexural loadings applied at the mid-span of the specimen. The tests were performed by controlling the load with a design target loading of 50 kN. Comparisons of laboratory measurements and analytical results obtained using the FEM model are presented in Fig. 3. It shows the deflection of the G2 girder at an applied load of P = 20–50 kN at the mid-span. The solid and dashed lines denote the analytical results and experimental measurements, respectively. As shown in these figures, the FEM model can predict the GFRP bridge deflection with satisfactory accuracy. Therefore, the FEM model is validated by comparing the analytical and experimental results.

Fig. 2. Experiment setup for the flexural test with the applied loading at the mid-span of the specimen.

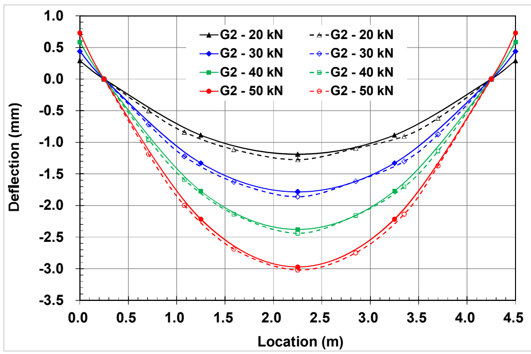

Fig. 3. Comparison of results for the deflection of the specimen at an applied load of P = 20–50 kN.

Autonomous Assembly Technology for Construction

Development of autonomous assembly technology

In the research, we utilized a connector from previous research for autonomous beam assembly [3]. The automated beam-assembly framework identified critical elements for research development and proposed a construction process based on an automated approach utilizing a mobile crane to construct a temporary rescue bridge. The critical elements were categorized into two parts: structure and automated process. The structure part, which is lightweight and includes the segmental structure and structural connector, defines the requirement of the material and structural geometry to be applied in the construction. The automated process part considers the technical requirement for a mobile crane to complete hoisting and assembly tasks without any worker on site.

Experiment and results

The framework and the construction process were validated through the experiment described in this section. The proposed assembly process was validated through an on-site experiment and simulation.

The on-site experiment measured the deviation from the target position of a hoisted structural component for assembly (Fig. 4). A crane with a hydraulic retractable boom with a maximum load capacity of 3.4 tons was used in the experiment. The payload was approximately 80 kg and the beam was 1.45 m long. In the experiment, the crane operation was executed by a graduate student, who learnt crane operation from a professional crane operator and practiced the required operation of sway reduction before the experiment. Fig. 5 shows the on-site experiment environment and results of the automated process. On average, the X deviation was 3.03 cm and the Y deviation was 1.37 cm.

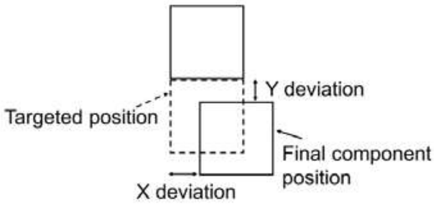

Fig. 4. Framework for automated beam assembly.

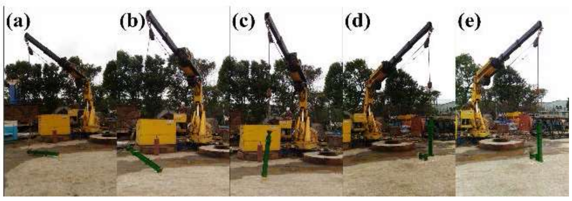

Fig. 5. On-site experiment environment and results of the automated process.

The process of releasing the beam for assembly triggered by gravity was validated through a simulation. We created a model structural component and used a virtual mobile crane to simulate the rotation of the structural connector. The model was created on a commercial physics engine, Unity3D. Fig. 6 shows the results of beam assembly by a mobile crane in the simulation. The simulation successfully demonstrated the process of releasing the beam for assembly triggered by gravity.

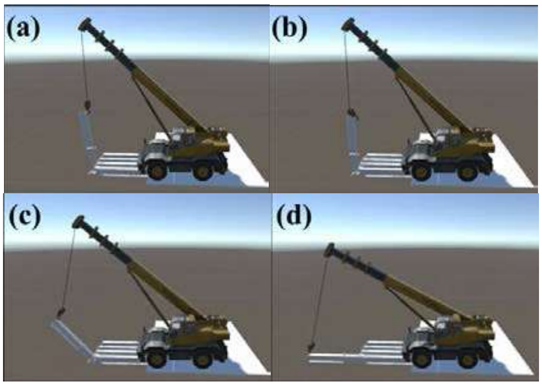

Fig. 6. Results of virtual beam assembly by a mobile crane.

Construction Operational Efficiency Analysis

Description of efficiency analysis

The operational efficiency analysis for the task of disaster relief using temporary rescue bridges compares the operational efficiency indicators of the cantilever erection method (Fig. 7) and of the incremental launching method (Fig. 8). The efficiency indicators include (1) safety of workers, (2) construction time, (3) equipment and labor required for construction, and (4) demand for counterweights, *etc*.

Safety of workers is the first indicator for consideration. For the cantilever erection method, a mini-crawler crane is used instead of workers for the river-crossing process, thus improving safety of workers. In the incremental launching method, the assembly is carried out on the river side and then the bridge is pushed forward to the isolated end to avoid construction over the river, which ensures worker safety.

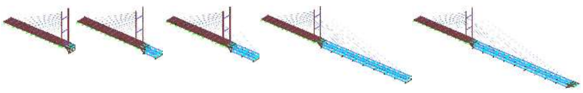

(a) (b) (c) (d) (e)

Fig. 7. Cantilever erection method for rescue bridge construction: (a) assembly of segments of the weight-balance module, (b) assembly of the first GFRP truss segment of the crossing structural module and lifting it across the river, (c, d) repeating stage (b) for the second to ninth GFRP truss segments, and (e) completion of the construction sequence across the river.

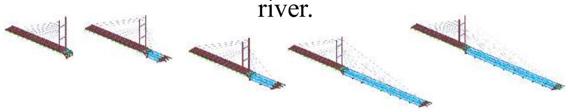

(a) (b) (c) (d) (e)

Fig. 8. Incremental launching method for rescue bridge construction: (a) assembly of segments of the weight-balance module, (b) assembly of the first

GFRP truss segment and installing launching noise, (c) assembly of the second GFRP truss segment and pushing it forward, (d) repeating stage (c) for the third to ninth segments, and (e) completion of the construction sequence across the river.

Construction time analysis

The construction time analysis for a 50-m-span temporary rescue bridge compares the total construction time taken by the original construction method without autonomous assembly technology, that using the cantilever erection method with autonomous assembly technology, and that using the incremental launching method.

Fig. 9 shows the results of construction time analysis for the three different construction processes for a 50-m-span temporary rescue bridge. The gray line represents the original construction method, whose total construction time is approximately 540 minutes; this does not meet the requirement of being within 8 hours. The red line represents the cantilever erection method; owing to the autonomous assembly technology, the total construction time is shortened to 430 minutes, thus meeting the requirement of being within 8 hours. The blue line represents the incremental launching method; because the construction process over the river is avoided, the total construction time is drastically shortened to 370 minutes, thus meeting the requirement of being within 8 hours.

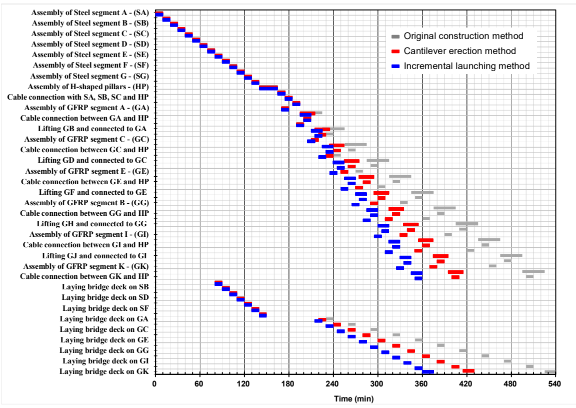

Fig. 9. Results of construction time analysis of the three construction processes for a 50-m-span temporary rescue bridge.

Demand for additional counterweight

The truss-type composite temporary rescue bridge is constructed using a self-balancing approach with the cantilever erection method or the incremental launching method. Before completion of the composite bridge, additional counterweight is needed for balancing the weight of the mini-crawler crane and the self-weight of composite segments during construction.

Fig. 10 shows the results for demand for additional counterweight of both construction processes for a 50-m-span temporary rescue bridge. The red line represents the cantilever erection method; the required additional counterweight is 1.8–25.8 tons during the river-crossing process. The blue line represents the incremental launching method; the required additional counterweight is 3.8–8.9 tons during the river-crossing process.

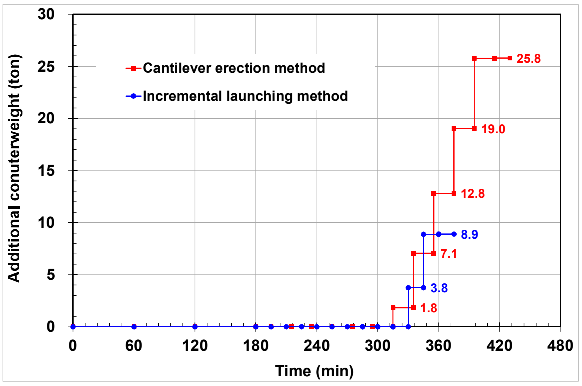

Fig. 10. Results for demand for additional counterweight for the two construction processes for a 50-m-span temporary rescue bridge.

Conclusions

The results of this study showed that (1) a truss-type segmental composite bridge could improve the stiffness of a 50-m-span rescue bridge to meet the required deflection-to-span ratio; (2) autonomous assembly technology for bridge construction can have a significant contribution to improving worker safety and shortening the assembly time of the rescue bridge; (3) the incremental launching method has greater operational efficiency than the cantilever erection method; and (4) the incremental launching method can avoid construction over the river, thus ensuring better worker safety.

References

1. Yeh, F.Y., K.C. Chang, Y.C. Sung, H.H. Hung and C.C. Chou, A novel composite bridge for emergency disaster relief: Concept and verification, Composite Structures, 2015, 127 (Supplement C): p. 199-210.
2. USDA Forest Service, A guide to fiber-reinforced polymer trail bridges, 2nd edition, United States Department of Agriculture, 2011.
3. Yang, Y.Y., C.M. Chang and S.C. Kang, Framework of automated beam assembly and disassembly system for temporary bridge structures, Proceeding of 35th International Symposium on Automation and Robotics in Construction, Berlin, Germany, 2018, p. 230-235.

Impact Effect of Moving Vehicles on Bridges

Bo-Han Lee[1], Sheng-Yuan Shiao[2], Chun-Chung Chen[3], Fang-Yao Yeh[4] and Kuo-Chun Chang[5]

李柏翰 [1]、蕭勝元 [2]、陳俊仲 [3]、葉芳耀 [4]、張國鎮 [5]

Abstract

In recent years, rapid urbanization associated with large urban population growth has placed significant demands on urban transport infrastructure. As a result, more and more elevated highways, usually using long piers, have been erected in urban areas to ease urban traffic pressures. However, the high volume traffic on such highway bridges can cause significant vibrations. To study the effects of vibrations caused by bridge traffic, this study monitored the acceleration of an isolated bridge for twenty-four hours. The fast Fourier transform method and the system implementation method are then used to analyze the acceleration measurements and thus to calibrate the system parameters of the bridge and the building. Additionally, the displacement from the deck to the pier and the deck acceleration were measured to investigate how vehicle transport affects the structural performance of the deck and pier. The results can be used as a future reference for improving vibration problems caused by bridge traffic.

Keywords: Bridge vibration, signal processing

Introduction

Earthquake engineering research focuses on the seismic performance of structures, in particular structural safety and life safety. With the intensification of urbanization, an increasing number of urban roads and bridges have been developed, reshaping the landscape of large cities. However, the vibrations caused by bridge vehicles may to some extent exceed human comfort levels, thus affecting the daily life of nearby citizens. Previous bridge vibration studies have focused on three areas: the impact of wind-induced bridge vibrations on vehicle ride comfort, the characteristics of bridges under wind excitation, and the failure of expansion joints caused by vehicles (Wang, et al., 2014; Ding, et al., 2016). Following the results of previous research, this study aims to investigate the effects of vehicle-induced bridge vibrations on nearby buildings.

Methodology

Root Mean Square (RMS) Acceleration

The obtained three-axis vibration measurements are shown in the direction of bridge traffic (*X*), transverse to bridge traffic (*Y*), and in the vertical direction (*Z*), respectively. The readings of the servo speedometer are analyzed to determine the floor acceleration using the following function according to ISO 2631-1 (1997),

$$a_w = \left[\frac{1}{T} \int_0^T a_w^2(t)dt \right]^{\frac{1}{2}} \tag{1}$$

where $\boldsymbol{a_w(t)}$ is the acceleration measurement (m/s^2), T is the measurement period (s), and $\boldsymbol{a_w}$ is the root mean square (RMS) acceleration (m/s^2).

Time-frequency Analyses

Time-frequency analyses are typically used to investigate structure vibration responses. To perform the time-frequency transform of the floor acceleration signals, this study employed the discrete fast Fourier transform (FFT) algorithm (Equation 2), which was derived from Cooley and Tukey's FFT algorithm (1965),

$$\mathbf{X}(\boldsymbol{f})_{\boldsymbol{k}} = \sum_{k=0}^{n-1} x_k e^{\frac{-2\pi i}{n} jk}, j = 0, 1, \cdots, n-1. \tag{2}$$

Case Study

For the investigated elevated expressway bridge, the local traffic management department reported clear

[1] Assistant Researcher, National Center for Research on Earthquake Engineering

building vibrations in the adjacent area and the subsequent discomfort caused to the local residents due to the bridge traffic. In this case study, a specially designed obstacle was embedded in the ground (twenty meters deep) between the pier and the adjacent building to reduce the impact of the bridge vibration caused by the passing vehicles on the adjacent building. To evaluate the effect of this vibration isolation implementation, the floor vibration of the adjacent residential building was monitored and analyzed. The target reinforced concrete (RC) frame building is five stories high with a basement above the roof and an additional lightweight sheet metal structure (Figure 2). The distance between the building and the bridge is approximately twenty-five meters.

In this study, uniaxial servo velocity meters (VSE-15D, Tokyo Sokushin Co., Ltd.) were employed at six measurement locations (triaxial vibration measurements at each location) in the target building (Fig. 1). A portable ambient vibration monitoring system (SPC-51, Tokyo Sokushin Co., Ltd.) was used for data acquisition for these servo velocity meters before and after the vibration isolation implementation. The floor vibration was measured in accordance with the national standard for measuring the ambient vibration level (NIEA P204.90C, 2005), and the sampling rate was 200 Hz.

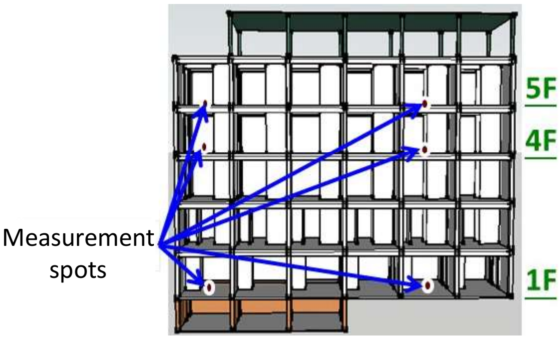

Fig. 1. Distribution of vibration measurement locations in the target building.

Vibration Response Analysis

Target Building

The vibration responses of the target building are depicted in Fig. 2. Prior to the implementation of the vibration isolation, the acceleration readings exhibited considerable vibration responses from 6:00 to 18:00, and the maximum RMS acceleration in the *X*-, *Y*-, and *Z*-directions were 0.014, 0.013, and 0.015 m/s^2, respectively. Subsequently, the vibration isolation substantially diminished the building vibration in all three directions: the maximum RMS acceleration in the *X*-, *Y*-, and *Z*-directions reduced to 0.008, 0.01, and 0.013 m/s^2, respectively. According to the discrete FFT analysis of the acceleration signal of the first floor, the peak vibration frequency in the *X*-direction was 3.09 Hz (Fig. 3), representing the dominant frequency of the building.

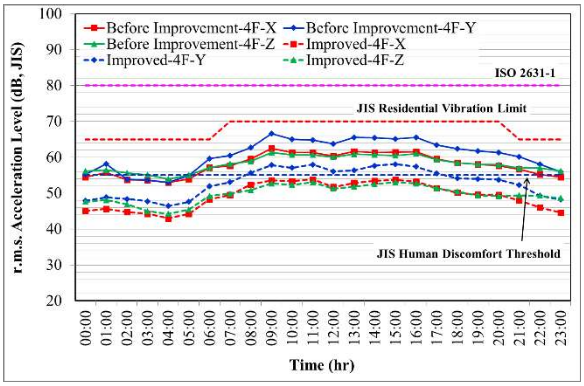

Fig. 2. Floor vibration responses of the target building over a 24-hour period.

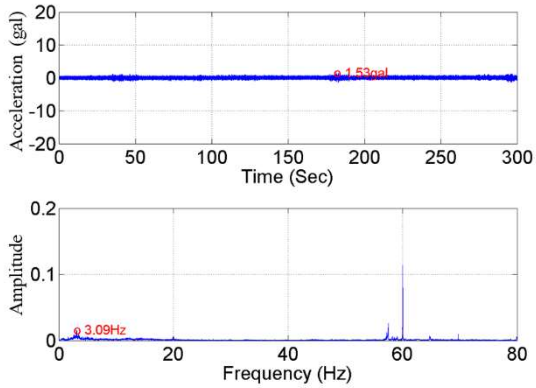

Fig. 3. Discrete FFT analysis of the *X*-direction vibration responses of the first floor.

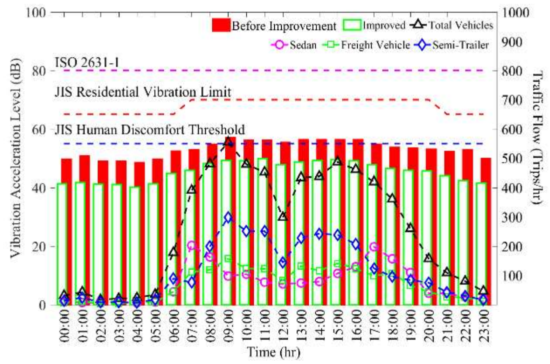

Fig. 4. Building responses in relation to bridge vehicle volume before and after the implementation of the vibration isolation.

Vehicle type (i.e., sedans, freight vehicles, and trailers) can affect the bridge vibrations and thus influence the adjacent buildings; therefore, to assess such effects, this study determined the average vehicle volume and trends over a 24-hour period (Table 1). Table 1 indicates that the daily rush hour periods for bridge traffic are from 8:00 to 11:00 and from 14:00 to 17:00; and during these periods, semi-trailers occupy a large percentage of the total vehicle volume, followed by freight vehicles. In contrast, the sedan volume peaks at 7:00 and 17:00. According to Fig. 4, the building vibration trend is consistent with the total vehicle volume trend. Furthermore, intense floor vibrations are significantly associated with trailers driving over the bridge.

Table 1. Vehicle volume crossing the bridge over a twenty-four hour period.

Time	Vehicle Type			Total Vehicles
	Sedan	Freight Vehicle	Semi-Trailer	
00:00	11	6	00:00	11
01:00	7	12	01:00	7
02:00	6	3	02:00	6
03:00	9	4	03:00	9
04:00	6	10	04:00	6
05:00	9	8	05:00	9
06:00	44	45	06:00	44
07:00	203	112	07:00	203
08:00	163	119	08:00	163
09:00	98	157	09:00	98
10:00	104	124	10:00	104
11:00	77	123	11:00	77
12:00	71	83	12:00	71
13:00	74	132	13:00	74
14:00	79	116	14:00	79
15:00	107	141	15:00	107
16:00	130	124	16:00	130
17:00	198	98	17:00	198
18:00	157	108	18:00	157
19:00	110	66	19:00	110
20:00	39	43	20:00	39
21:00	39	27	21:00	39
22:00	26	24	22:00	26
23:00	19	11	23:00	19

A comparison of the floor vibration responses in all three directions before and after the implementation of the vibration isolation is presented in Fig. 5. The comparison indicates that the vibration acceleration of all three measured floors was lowered by approximately 20 % due to the improvement from the implemented isolation mechanism. Moreover, the first-floor vibration responses in all three directions did not exceed the human vibration comfort threshold prescribed in the JIS standards (JIS Z8735, 1981; JIS C1510, 1995; JIS C1513, 2002). For the fourth floor, despite the vibration in the *Y*-direction, the acceleration in the other two directions was lower than the JIS threshold. The acceleration of the fifth floor also decreased, and the *X*- and *Z*-direction acceleration approached the JIS threshold.

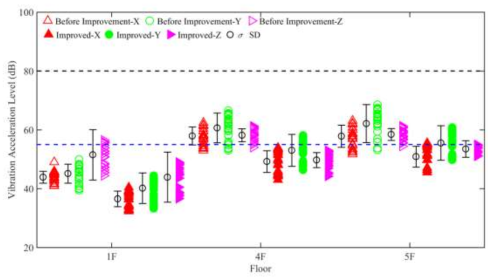

Fig. 5. Comparison of the vibration responses on each floor before and after the implementation of the vibration isolation.

Bridge Vibration

In this study, the measurements of the vibration in five different locations were set up in the vertical direction. During rush hour traffic, the vibration is generated at the center of the bridge and gradually moved towards the pier. The response at the center span is approximately 77 dB. The response at the bottom and top of the pier is approximately 55 and 53 dB, respectively, with the vibrations being similar to each other. The response at the diaphragm is approximately 68 dB and at the building base the response is approximately 47 dB. The attenuation ratio is 12 % at the diaphragm, 31 % at the pier top, 29 % at the pier bottom, and 39% at the building base.

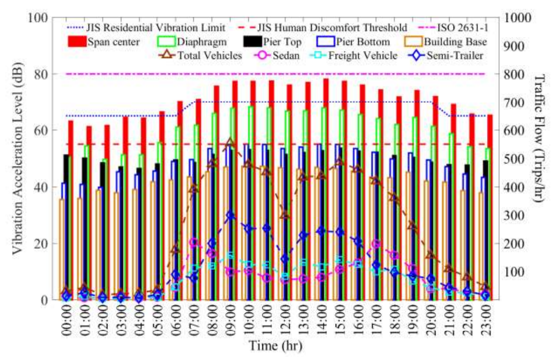

Fig. 6. Bridge responses with respect to vehicle volume on the bridge.

Conclusions

The vibration analyses of the target residential building revealed that during the period from 6:00 to 21:00, the vibration of all three monitored floors (i.e., the first, fourth, and fifth floors) exhibited significant vibration responses. For the first floor vibration, the vibration responses in the *Z*-direction were larger than those in the other two directions, with the maximum RMS acceleration of 0.021 m/s^2 and an ISO RMS acceleration of 86.3 dB. In contrast, for the fourth and fifth floors, the *Y*-direction vibration had more intense responses than the other two directions, with a maximum RMS acceleration of 0.063 and 0.079 m/s^2, respectively, and an ISO RMS acceleration of 96.0 and 97.9 dB, respectively.

The FFT analyses suggested that the vibration frequency of the first floor in the *Z*-direction (3.4 Hz) and the fifth floor in the *Y*-direction (3.02 Hz) approximated the dominant frequency of the building.

References

Tao Wang, Wanshui Han, Fei Yang, and Wen Kong, "Wind-vehicle-bridge coupled vibration analysis based on random traffic flow simulation", Journal of Traffic and Transportation Engineering 1(4), pp 293-308, 2014.

Yong Ding, Wei Zhang, and Francis T.K. Au, "Effect of dynamic impact at modular bridge expansion joints on bridge design", Engineering Structures 127, pp 645-662, 2016.

ISO 2631-1, "Mechanical vibration and shock evaluation of human exposure to whole-body vibration, Part 1: General requirements", International Organization for Standardization, Geneva, 1997.

JIS Z8735, "Methods of Measurement for Vibration Level", Japanese Industrial Standard, Japan, 1981.

JIS C1510, "Vibration level meters", Japanese Industrial Standard, Japan, 1995.

JIS C1513, "Octave-band and third-octave-band analyzers for sounds and vibration", Japanese Industrial Standard, Japan, 2002.

J. W. Cooley and J. W. Tukey, "An Algorithm for the Machine Calculation of Complex Fourier Series", Mathematics of Computation 19(90), pp 297-301, 1965.

NIEA P204.90C, National standard for measuring ambient vibration level, Environmental Analysis Laboratory, Taiwan, 2005.

Experimental Beyond Design and Residual Performances of Viscoelastic Dampers

Chung-Han Yu[1], Shiang-Jung Wang[2], Wang-Chuen Lin[3], Cho-Yen Yang[1] and Kuo-Chug Chang[4]

游忠翰 [1]、汪向榮 [2]、林旺春 [3]、楊卓諺 [1]、張國鎮 [4]

Abstract

Most analytical and experimental research relevant to viscoelastic (VE) dampers installed in structures has been aimed at their design (or pre-damage) performance. In reality, under shaking conditions caused by earthquakes, the shear deformation of VE dampers may exceed or even be much larger than their nominal design range, thus leading to damage to the VE material. Under such circumstances, the structural design may no longer be conservative when the viscoelastically damped structure is a retrofit design or not a supplemental damping design. In this study, the beyond design and residual performances of full-scale VE damper specimens that have suffered damage are experimentally tested. The results indicate that VE dampers can remain relatively undamaged and maintain their design performance characteristics after being subjected to severe shear strains, that they become weaker at higher strains, but that their mechanical properties tend to approach constant values under both extreme and residual conditions. For engineering purposes, a suitable and conservative empirical post-damage model is derived by applying deduced reduction factors to the Kelvin-Voigt model. The new model produces accurate predictions of post damage behavior of dampers.

Keywords: beyond design performance, damage, empirical post-damage model, full scale, residual performance, viscoelastic damper

Introduction

As so-called velocity-type dampers, viscoelastic (VE) dampers generally owe their stiffness and energy dissipation capabilities to the shear deformation of polymer composite (or VE) material layers sandwiched between steel plates. Many performance tests on small- and full- scale VE dampers have been conducted since the 1990s to investigate their force-deformation (or stress-strain) relationships and their mechanical behavior. These studies have resulted in an improved knowledge of the effects of displacement amplitudes, excitation frequencies, ambient temperatures, temperature rises, softening, hardening, and cumulative energy absorption on their behavior.

Most past research relevant to VE dampers has been aimed at their design (or pre-damage) performance. Once the shear deformation of installed VE dampers exceeds their nominal design range this may cause damage to the dampers. If this occurs, the design might not prove to be economical when the viscoelastically damped structure has supplemental damping and may lead to non-conservative designs in retrofitted buildings. Thus, new buildings designed with VE dampers as supplemental damping may, at worst, be uneconomical if the effect of damaged VE dampers is not considered, but the structural safety is still guaranteed. However, for existing buildings retrofitted with VE dampers, damage to the dampers may not result in a conservative design and, most importantly, the structural safety will not be guaranteed. This study addresses the beyond design and residual performances of full-scale VE dampers after suffering damage. It presents experimental results of investigations of two VE specimens and

[1] Assistant Researcher, National Center for Research on Earthquake Engineering
[2] Associated Professor, National Taiwan University of Science and Technology & Research Fellow, National Center for Research on Earthquake Engineering
[3] Associated Researcher, National Center for Research on Earthquake Engineering
[4] Professor, National Taiwan University

discusses the implications of the derived stress-strain relationships. Furthermore, with considering the appropriate reduction factors, the Kelvin-Voigt model is adopted to conservatively approximate the beyond design and residual performances of the dampers.

Test Setup and Protocols

Two full-scale VE dampers, identical in configuration and material, were used as the test specimens in this study. They are denoted as Specimens A and B, which were manufactured by the Nippon Steel & Sumitomo Metal Corporation, and their assembly is illustrated in Fig. 1; the left and top right picture show the prepared specimen and detail arrangement of steel plates and VE material, respectively; the bottom right is the schematic diagram of the specimen. Each damper specimen comprised four VE material layers (Type ISD111) of thickness 5 mm and surface area 2500 cm^2. The nominal shear force capacity of each damper was 500 kN. Their performance under maximum shear strains ($\gamma_{\max}$) not exceeding 300% were tested by Wang *et al.* (2018). Their test results are termed the pre-damage (or design) performance, and will be used as a comparative base for this study.

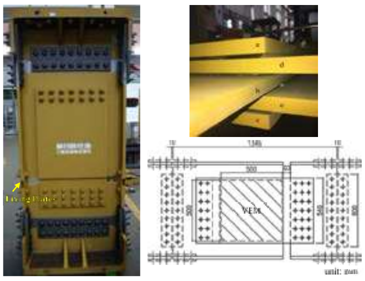

Fig. 1. VE damper specimen

The VE damper specimens were dynamically tested using the high-performance damper testing facility at the National Center for Research on Earthquake Engineering (NCREE) under reversed uniaxial loading. The testing facility and specimen setup are shown in Fig. 2.

Fig. 2. Testing facility and estup of the specimen

Specimens A and B were used for different purposes. To gain a better experimental understanding of the pre-damage results as well as the ultimate and beyond design performances of the specimens, various maximum shear strains greater than 300% were applied to Specimen A. This was done in sequentially increasing steps of 120% of shear strain from 480% to 960%. After being subjected to each of these shear strain increments, the specimen was tested under maximum shear strains of 60% and 200%, which are identical to those used by Wang *et al.* (2018). These tests are referred to here as residual performance tests, and they serve to constrain the performance of the VE damper before and after it suffers potential damage in an unbiased manner.

Experiments on Specimen B were designed to preclude the possible influence of previously experienced deformation and damage that may have been incurred during the sequential experiments on Specimen A. Beyond design and residual performance assessments of this specimen were performed after only one maximum shear strain, *i.e.* 1000%, was directly applied. The other test conditions in all of these experiments were an excitation frequency of 0.3 Hz, an ambient temperature of 20°C, and a cycle number of six. The test program in this study is summarized in Table 1.

Table 1. Test protocols of VE damper specimens

Specimen		A		B	
	Excitation frequency (Hz)	0.3			
Sinusoidal reversal loading	Maximum shear strain (%)	480, 600, 720, 840, 960	60, 200 (after each shear strain level)	1000	60, 200 (after 1000% shear strain)
	Ambient temperature (°C)	20 (±2°C tolerance)			
	Number of cycles	6			

Test Results and Discussion

The experimental force-displacement relations for Specimen A after applying shear strains of 480% to 960% and a photograph of the appearance of the specimen after the tests are shown in Fig. 3. The corresponding diagrams for Specimen B after 1000% shear strain are shown in Fig. 4. Calculated characteristics of specimens are tabulated in Table 2. These are the average shear storage stiffness $K_{d,avg}$, the damping coefficient $C_{d,avg}$, the average maximum shear force response $F_{\max,avg}$ (determined from test data from the intermediate five complete cycles, *i.e.* excluding the first half and last half cycles), and the initial maximum shear force response $F_{\max,beginning}$ (obtained from the first half cycle).

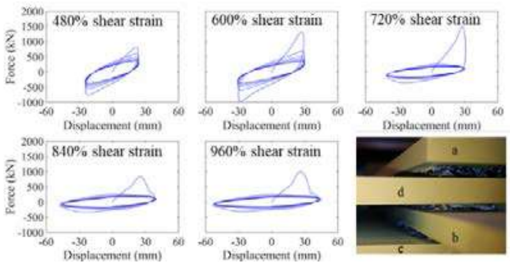

Fig. 3. Experimental performances and

appearance of Specimen A

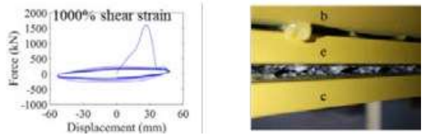

Fig. 4. Experimental performances and appearance of Specimen B

It is evident from Fig. 3 that the maximum shear force for Specimen A in the first half cycle, 1488.33 kN (Table 2), occurs at 613% shear strain. Similarly, Table 2 and Fig. 4 show that the corresponding values for Specimen B are 1610.22 kN and 622% shear strain. In addition, it was visually observed that the VE material layers had apparent damage in a tear failure mode at almost the same shear strain levels during the tests of both specimens. As indicated in Table 2, Specimen A suffers apparent tear damage, the experimental mechanical properties are greatly decreased under 720% shear strain compared with those under 600% shear strain, but there is no further obvious reduction under higher shear strain (*i.e.* 840% and 960%). Similar results are evident when examining the patterns of the residual shear storage stiffness and damping coefficient of the specimens before and after suffering damage (Table 2). These parameters become smaller when the samples are subjected to applied strains above 600%, but the residual performance of Specimen A under shear strain greater than 720% and of Specimen B at 1000% show no further obvious reduction in these parameters at the higher applied strains. The reason for this behavior at high applied strain is that the damaged VE material is in a paste-like state, in which there still exist a certain degree of bonding and frictional forces between separate molecules.

Table 2. Performance of Specimens A and B

		Maximum shear strain (%)	$K_{d,avg}$ (kN/mm)	$C_{d,avg}$ (kN-s/mm)	$F_{max,avg}$ (kN)	$F_{max,beginning}$ (kN)
Specimen A	Post-damage	720	2.79	2.78	201.16	1488.33
		60	11.85	5.91	52.86	52.73
		200	10.60	5.23	162.58	192.05
		840	2.05	2.34	201.25	844.93
		60	12.12	5.78	53.03	55.12
		200	9.68	4.63	145.37	169.62
		960	1.63	2.00	193.16	992.61
		60	11.10	5.17	47.72	47.89
		200	9.80	4.64	144.84	167.48
Specimen B	Post-damage	1000	1.50	1.73	196.63	1610.22
		60	11.47	5.50	50.59	51.87
		200	9.60	4.67	141.29	148.55

Based on the test results, it is reasonable to conclude that the specimens can retain their design performance and remain almost intact without severe damage until the shear strain exceeds approximately 600%. Furthermore, the almost identical behavior of the two specimens during testing implies that the influence of previously, albeit not continuous, experienced deformation on the occurrence and degree of their damage is of little significance.

Comparison between Test Results and Prediction

A convenient and quantitative way of comparing the results is to study the reduction ratios of the experimental mechanical properties after the samples were pre-forced to the beyond design levels. Reduction ratios for shear storage stiffness and damping coefficient from tests under both 60% and 200% shear strain are plotted against the maximum applied deforming shear strain (*i.e.* between 480% and 1000%) in Fig. 5. The results reveal that once the specimens tear (under maximum shear strains greater than 600%), these parameters remain steady and can be estimated by multiplying the original values by a constant reduction factor. A value of 0.5 appears to be an appropriate reduction factor for estimating both the residual shear storage stiffness and damping coefficient of the damaged specimens under 60% and 200% shear strain (Fig. 5).

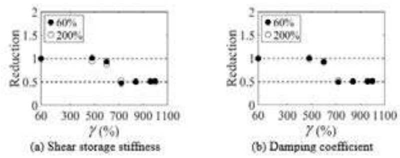

Fig. 5. Reduction ratio of residual performances after tests with pre-test shear strains (γ) larger than 600%

The reduction ratios of experimental mechanical properties to the mechanical properties calculated from the pre-damage analytical results under maximum shear strains larger than 300% (not under the 60% and 200% shear strain test)are presented in Fig. 6. In this case appropriate constant reduction factors are 0.15 and 0.42 respectively.

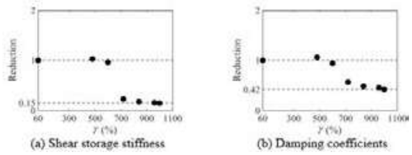

Fig. 6. Reduction ratio of beyond design performances after tests with pre-test shear strains (γ) larger than 600%

A consequence of the reduction values plotted in Figs 5 and 6, is that the residual and beyond design hysteretic behaviors of the damaged specimens can be simply and practically predicted by a Kelvin-Voigt model. The model applicable to the results presented here consists of a spring with the reduced shear storage stiffness $K_{d,reduced}$ and a dashpot with the reduced damping coefficient $C_{d,reduced}$ connected in parallel. The reduced parameter values are given by Equations

(1) and (2).

$$K_{d,\,reduced} = \kappa_1 K_{d,\,avg} \tag{1}$$

$$C_{d,\,reduced} = \kappa_2 C_{d,\,avg} \tag{2}$$

where κ_1 and κ_2 are the reduction factors for estimating the reduced shear storage stiffness and damping coefficient of damaged VE dampers, and $K_{d,avg}$ and $C_{d,avg}$ are the average shear storage stiffness and average damping coefficient calculated from the pre-damage analytical results.

The experimental performance of the damaged specimens (considering only data from the intermediate five test cycles) are compared with predictions made by applying the above empirical models in Figs 7 and 8. Fig. 7 shows the observed and predicted force-displacement relationships (tested at 60% and 200% strain) for the *residual* performance of Specimen A after 960% shear-strain damage (top diagram) and B after 1000% shear strain damage (bottom diagram). Fig. 8 shows the *beyond design* force-displacement relationships for Specimen A (left) and B (right) under the same shear strain damage.

To quantitatively evaluate the prediction accuracy, the coefficient of determination for force histories, R^2_{force}, and an author-defined energy dissipation ratio, EDR, were calculated using Equations (3) and (4) and are provided in the figures.

$$R^2_{force} = 1 - \frac{\sum_{i=1}^{m}\left[\left(F_{test}\right)_i - \left(F_{prediction}\right)_i\right]^2}{\sum_{i=1}^{m}\left[\left(F_{test}\right)_i - \left(F_{test}\right)_{mean}\right]^2} \tag{3}$$

$$EDR = \frac{W_{D,\,prediction}}{W_{D,\,test}} \tag{4}$$

where $F_{prediction}$ and F_{test} are the predicted and experimental shear forces at time step *i*, respectively, the subscript *mean* represents the mean value for all data points during six cycles, *m* represents the total number of data points, and $W_{D,prediction}$ and $W_{D,test}$ are the predicted and experimental enclosed hysteresis loop areas, respectively.

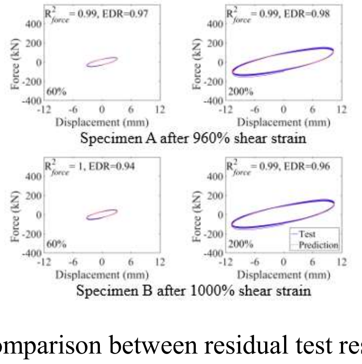

Fig.7. Comparison between residual test results and empirical post-damage predictions for Specimens A and B after suffering damage

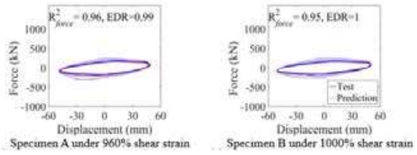

Fig.8. Comparison between beyond design test results and empirical post-damage predictions for Specimens A and B after suffering damage

It is apparent from these error estimates that the predicted values, found by simply using reduction factors in the Kelvin-Voigt model, are sufficiently accurate and conservative. Although this empirical approach makes practical engineering sense, an exact post-damage analytical model for predicting the beyond design performance of damaged VE dampers is still required and will be the focus of future investigations. Such a model will enable accurate predictions if the effect of the shear force amplification in the first half test cycle on the overall structural seismic performance is not negligible.

Conclusions

The beyond design and residual performances of full-scale VE damper specimens that have suffered damages were experimentally investigated in this study. The findings contribute significantly to relevant research in engineering seismology and its practical applications. The test results indicate that VE dampers can retain their design performance characteristics and almost remain intact without severe damage after being subjected to shear strains of up to approximately 600%. When the dampers undergo tear damage above 600% shear strain, their beyond design and residual performances decrease significantly compared with the original undamaged dampers, but mechanical properties approach constant values under higher shear strains. For practical engineering purposes, an empirical post-damage model, which incorporates reasonable and conservative reduction factors in the Kelvin-Voigt model, is proposed to assess the experimental performances of damaged VE dampers. It is demonstrated that predictions based on this empirical model produce sufficiently accurate and conservative results.

References

Chang KC, Soong TT, Lai ML, Nielsen EJ, (1993). ″Viscoelastic dampers as energy dissipation devices for seismic applications,″ *Earthquake Spectra*, 9(3): 371-387.

Wang SJ, Chiu IC, Yu CH, Chang KC, (2018). ″Experimental and analytical study on design performance of full-scale viscoelastic dampers,″ *Earthquake Engineering and Engineering*

Vibration, 17(4): 693-706.

Wang SJ, Chang KC, Hwang JS, Huang YN, Lin WC, Yang CY, (2017). "Recent progress in Taiwan on seismic isolation, energy dissipation, and active vibration control," *Proceedings of New Zealand Society for Earthquake Engineering (NZSEE) Annual Conference and Anti-seismic Systems International Society (ASSISi) 15th World Conference on Seismic Isolation, Energy Dissipation, and Active Vibration Control of Structures*, Wellington, New Zealand.

Nippon Steel & Sumitomo Metal Corporation. http://www.nssmc.com/.

A Study on Important Structures and Equipment-Suspended Fire Sprinkler Piping Systems Shaking Table Tests

George C. Yao[1] Min-Chi Ko[2] Chen-Pei Hsu[3]

姚昭智 [1] 柯敏琪 [2] 許宸珮 [3]

Abstract

There are various piping systems in a hospital, with the most vulnerable being the sprinkler piping systems. During the 1999 Chi-chi earthquake and the 2010 Jia-xian earthquake in Taiwan, many sprinkler piping systems underwent large displacements and suffered collision with other overhead building elements. This led to leaks, medical equipment damage from water, and ceilings that had absorbed water collapsing in large areas. In these situations, hospitals cannot provide immediate first aid services and the post-earthquake resilience was reduced. Based on the damage state of the piping systems, a series of suspended piping system shaking table tests were performed to investigate the dynamic reactions and system ID with different retrofit components.

Keywords: suspended fire sprinkler system, shaking table tests, system identification

Introduction

There are various types of piping systems in a hospital, with the suspended fire sprinkler piping system being one of the most important systems. In the 1999 Chi-chi earthquake and the 2010 Jia-xian earthquake, suspended fire sprinkler piping systems suffered large displacements, colliding with other systems. The resulting leaks, broken medical equipment, and water satiated ceiling collapse prevented the hospital from being capable of immediate first-aid operation. If the sprinkler piping systems could be strengthened to increase their seismic capability and to decrease the probability of their structural failure with an effective method, hospital emergency resilience would be improved.

This study uses a shaking table to study fire sprinkler piping systems designed by code NFPA13 (National Fire Protection Association, 2009) and the retrofit strategy. With full-scale shaking table tests, we can investigate the dynamic characteristics and time-series reactions under seismic sway bracings that were certified by FM(Factory Mutual). Based on the test results, accurate piping system numerical models can be established.

Shaking Table Tests Methodology

A fire sprinkler piping system is composed of the feed main, cross main, and branches. The sprinkler is installed at the end of a branch. The cross main supplies water for branches, and the feed main supplies water for the cross main. This study aims to investigate the natural frequency and dynamic reaction, as well as study the reaction of the steel angle that was installed at the end of the branch. The natural frequency and reaction are compared before and after retrofitting the piping system.

In these tests, two groups of suspended piping systems of the same size were suspended on the ceiling of Frame A, which belongs to the National Center for Research on Earthquake Engineering (NCREE) (Fig 1.). The differences between the two piping systems were the seismic components used (Fig 2.). The specifications and measurements for the piping systems were: (1) the pipeline used CNS6445 with diameters of 4”, 2”, and 1.5”. 3/8” was chosen for the diameter of the suspended screw threaded rods. (2) The piping systems dimensions were 6.65 m x 4.74 m, and the length of suspension was 60 cm. (3) The weight of each piping system was 200 kgf, and the total weight was 400 kgf. (4) The seismic bracing

[1] Distinguished Professor, National Cheng Kung University
[2] Ph. D Student, National Cheng Kung University
[3] Master Student, National Cheng Kung University

components were certified by FM. The diameter for the round tube for bracing was chosen to be 1-1/4" (Fig 3.). The retrofit cables were certified by UL, and the diameter was 3.5 mm (Fig 4.). The installed angle for the bracing and cable were both 45°. (5) The specification for the steel angle was 50 mm x 50 mm, with a 3 mm thickness (Fig 5.).

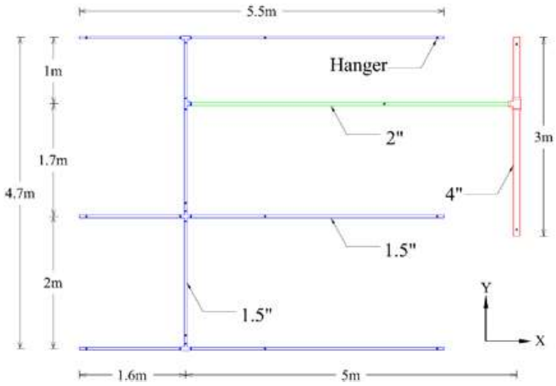

Fig 1. The dimensions for each piping system.

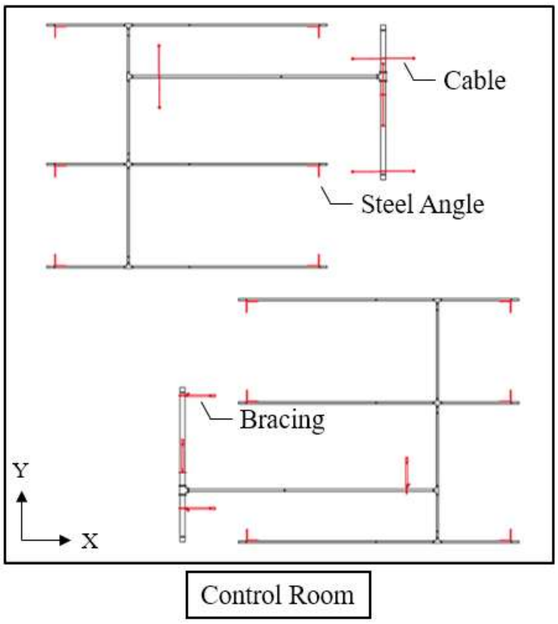

Fig 2. The retrofit method and configuration for the piping systems.

Fig 3. Bracing installation (Case 1).

Fig 4. Cable installation (Case 2).

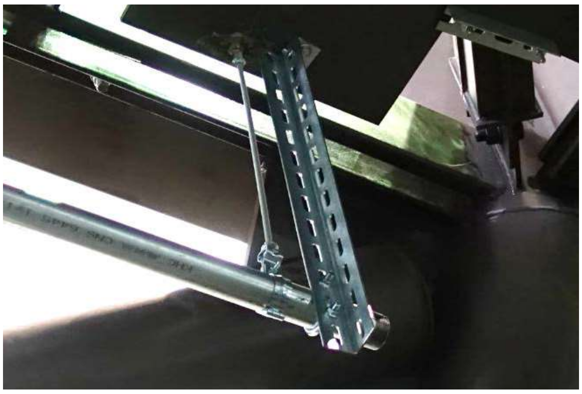

Fig 5. Steel angle at the end of the branch.

We performed white noise tests and excitations with different scales of JMA Kobe for the 10th floor's acceleration time history excitations (GL 27.4 m). Considering the performance of the shaking table and the response of the suspended frame, the time histories were revised. The actual acceleration responses and input excitation direction are shown in Table. 1.

Table 1. JMA Kobe time history input direction and peak floor acceleration (PFA) of the suspended frame.

Time History	PFA (g)	Direction
KOBE10%_10F	*X* 0.24 g *Y* 0.24 g	Biaxial
KOBE25%_10F	*X* 0.75 g *Y* 0.75 g	Biaxial
KOBE50%_10F	*X* 1.46 g *Y* 1.48 g	Uniaxial

Shaking Table Tests Analysis

The considered cases included with and without retrofit. For the retrofitted case, vertical steel angles were used at the of branch, a local practice.

For the white noise tests, the white noise acceleration responses at the cross main and second branch were used to analyze the natural frequency using the transfer function method. The natural frequencies are 20 Hz in the *X*-direction and 9.5 Hz in the *Y*-direction for Case 1, and 6 Hz in the *X*-direction and 4 Hz in the *Y*-direction for Case 2 (Fig 6.). Under Kobe25%_10F time history excitation, the maximum relative displacement is 6.5 cm in the *X*-direction at the 2nd main pipe and 5.4 mm in the *Y*-direction at the end of the 3rd branch for Case 1. The maximum relative displacement is 10 mm in the *X*-direction at the 1st main pipe and 13 mm in the *Y*-direction at the end of the 3rd branch for Case 2 (Fig 7.).

For the case without retrofit, the natural frequencies are 1.9 Hz in the *X*-direction and 2.1 Hz in the *Y*-direction. The maximum relative displacement in the *X*-direction is 309 mm at the 1st branch and 137 mm in the *Y*-direction at the 1st main pipe, under Kobe25%_10F excitation (Fig 8.).

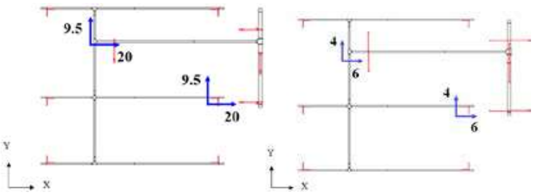

Fig 6. Natural frequencies for Case 1 and Case 2. (Hz, left: bracing, right: cable)

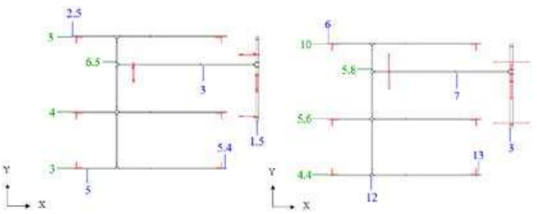

Fig 7. Maximum relative displacement under Kobe25%_10F excitation. (mm, left: bracing, right: cable)

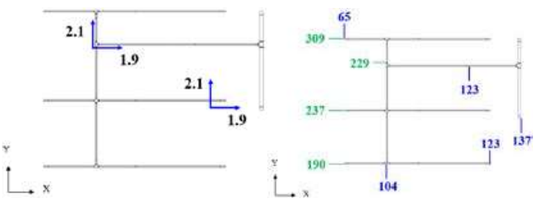

Fig 8. Natural frequency (Hz) and maximum relative displacement (mm) under Kobe25%_10F excitation for the case without a retrofitted piping system.

Conclusions

From the suspended fire sprinkler piping systems shaking table tests, we analyzed the natural frequencies, finding that they are approximately 2.0 Hz in both the *X*- and *Y*-directions for the un-retrofit piping system. Under the time history excitation, the vibration for this system was drastically reduced after retrofitted. Generally, as the piping systems are 90% full of water, the natural frequency will be less than 2.0 Hz, and the possibility of resonance with the building is high. Resonance can magnify the vibration, the piping system may break to leakage, and the post-earthquake resilience could be reduced.

Retrofitted suspended fire sprinkler piping system tests were performed by referencing the existing US code NFPA13. From the results, efficient retrofit strategies can reduce vibration and resonance problems for bracing and cables.

However, there are few retrofitted piping systems at the on-site construction sites. We expect that by using different retrofit strategies under shaking table tests to understand the vibrations, the dynamic reaction from numerical models can be analyzed to investigate the construction feasibility and economics of retrofit methods in the future.

References

National Fire Protection Association (2009). NFPA13: Standard for the Installation of Sprinkler, 2013 Ed., NFPA, Massachusetts, USA.

Huang, T.L. (2018). A Study on Seismic Retrofit of Suspension Piping Systems in Buildings: A Case Study of Fire Protection Sprinkler Piping System, National Cheng Kung University, Taiwan: Tainan.

Optimized Seismic Strengthening Strategies for a Typical Sprinkler-Piping System in a Hospital

F.-R. Lin[1], J.-F. Chai[2], Y.-A. Tsai[3], S.-C. Tseng[4], P.-R. Wu[5], C.-Y. Su[5], Zhen-Yu Lin[3], Zhi-Yu Lai[3], Tzu-Chieh Chien[3], Wen-I Liao[6]

林凡茹[1]、柴駿甫[2]、蔡詠安[3]、曾劭鈞[4]、吳佩儒[4]、蘇承諺[4]、林震宇[3]、賴姿妤[3]、簡子婕[3]、廖文義[6]

Abstract

Based on recent earthquakes in Taiwan, losses do not necessarily result from the damage of building structures but rather from non-structural components and systems. For instance, the leakage of the fire protection sprinkler systems in hospitals during small earthquakes can result in the shortage of medical functions and fire protection, and the malfunction and repairs of medical equipment. The breakage of sprinkler systems caused by strong earthquakes can even harm the safety of buildings. Taking a sample sprinkler piping system in a medium-scale hospital as an example, this research aims to verify seismic strengthening strategies based on NFPA 13 to improve the seismic performance of fire protection sprinkler systems in critical buildings. The design concepts, which include numerical analysis simulating the original piping, the design of input motion, and the test specimen, and a strengthening strategy established based on the consideration of improving the seismic performance in specific damage states, were introduced. Additionally, preliminary results of shaking table tests for four strengthening strategies are discussed to propose a more applicable seismic design guideline for sprinkler piping systems in Taiwan.

Keywords: sprinkler-piping, failure mode, seismic evaluation, strengthening strategies

Introduction

In Taiwan, there is no mandatory requirement for the seismic design of nonstructural components in the Building Act (MOI, 2011). For fire sprinkler systems of general buildings, NFPA 13 (NFPA, 2010) provides a common code of practice for seismic installation. Instead of stress analysis, a rule-based approach is proposed by the NFPA standard. However, the efficiency of the seismic strengthening provided by the NFPA method is questionable due to the effect of stress concentrations on the piping at the bracing point (G&E, 2009). To upgrade efficiently the seismic performance of sprinkler piping systems, a long-term research program on assessment and improvement strategies for the typical configuration of sprinkler piping systems in hospitals was organized by the National Center for Research on Earthquake Engineering (NCREE).

Using the fire protection sprinkler system in a sample hospital as an example, design concepts are first introduced, which include a numerical analysis simulating the original piping, the design of input motion and the test specimen, and a strengthening strategy established to improve seismic performance in specific damage states. Additionally, the preliminary results of shaking table tests for four strengthening strategies are discussed to propose an applicable seismic design guideline for sprinkler piping systems. The results will be applied to propose an applicable seismic design guideline for sprinkler piping systems in Taiwan.

[1] Associate Researcher, National Center for Research on Earthquake Engineering
[2] Research Fellow and Deputy Director General, National Center for Research on Earthquake Engineering
[3] Assistant Researcher, National Center for Research on Earthquake Engineering
[4] Graduated Student, National Cheng-Kung University
[5] Graduated Student, National Taipei University of Technology, Taipei Tech
[6] Professor, National Taipei University of Technology, Taipei Tech

Design of the Test Specimen

Based on NFPA 13, four strengthened cases for piping systems are proposed. First, the earthquake-resistant diagonal bracing is installed on the main pipe as shown in Fig. 1(a). The purpose is to suppress the displacement of the main pipe. The position of the main pipe bracing and the affected area and distribution are calculated according to NFPA 13 or the strengthening guidelines for hospitals (Chai et al., 2015). However, the proposed design created using NFPA 13 did not effectively inhibit the displacement of the sprinkler head. To prevent possible impact and the tearing of ceiling boards caused by the adjacent sprinkler head, this study added three additional designs. According to NFPA 13 recommendation, as shown in Fig. 1(b), the second design includes adding braces to the branch pipes beside the braces for the main pipes. As shown in Fig. 1(c), the third design includes adding four steel wires to each sprinkler head in addition to the above-mentioned seismic strengthening devices. To understand the effect of the steel wire on suppressing the displacement of the sprinkler head, a fourth design is added in this study. As shown in Fig. 1(d), the fourth design includes adding four steel wires to each sprinkler head and earthquake-resistant diagonal bracing on the main pipe. Table 1 lists the strengthening components of each design, the modal frequency, and the mass partition ratio of the numerical model.

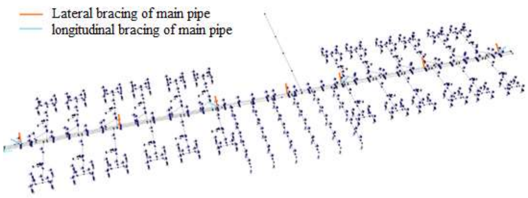

(a)

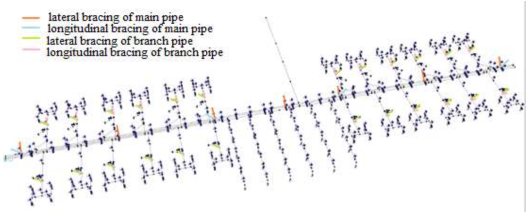

(b)

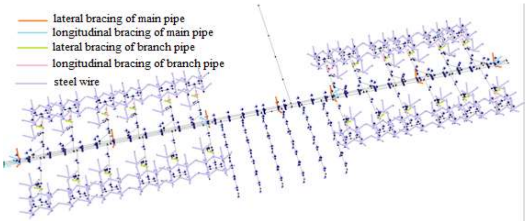

(c)

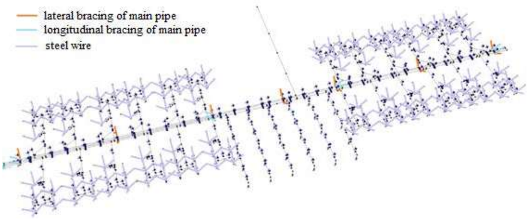

(d)

Fig. 1 Configuration of each strengthened case: (a) Case 1; (b) Case 2; (c) Case 3; and (d) Case 4.

Table 1 Configuration of the sprinkler-piping systems.

Configuration		Original	Case 1 (AXX)	Case 2 (ABR)	Case 3 (SBH)	Case 4 (AHL)	AXF
Main pipe bracing		-	V	V	V	V	V
Branch pipe bracing		-	-	V	V	-	-
Sprinkler head w/ steel wire		-	-	-	V	V	-
1-inch pipe replaced by Flexible Hose		-	-	-	-	-	V
Complete System Analysis	Fund. Freq. of transverse mode (Hz)	1.3	3.07	8.71	8.75	4.23	-
	Mass participation ratio	0.31	0.2	0.3	0.3	0.25	-
Fund. Freq. of transverse mode of Test specimen (Hz)		2.8	5	4.7	5	4.7	4
Performance		Leakage at 10%	Deformed attachment	Leakage at 60%	No Leakage / Deformed attachment	No Leakage	No Leakage / Deformed attachment

V: installed devices

Limited to the scale of the shaking table, only part of the sprinkler piping system was duplicated in the laboratory. This included the branches found in a patients room and a part of the cross main pipe along the corridor. To obtain a reasonable approximation for the boundary conditions of the tested segment of the cross main in the shaking table tests, detailed numerical models of the complete piping system on the sixth floor and a preliminary analysis for the test specimen were both established according to an in-situ investigation on the configuration and restraint conditions in the hospital and that of the actual test specimen (Fig. 2). The boundary of the test specimen was carefully designed to simulate the unduplicated part of the main pipe (Fig. 3). When comparing the system identification results of ambient vibration tests and the numerical analysis, it was found that the restraint conditions of the boundaries might be different under ambient vibration or strong motions. For example, to obtain the fundamental frequency in the transverse direction of the cross main pipe, the restraints of the sprinkler heads adjacent to the ceiling systems are assumed to be hinges. However, it is more reasonable to regard sprinkler heads as free ends of pipes while the mineral fiber ceiling board ceiling boards are torn during strong earthquakes.

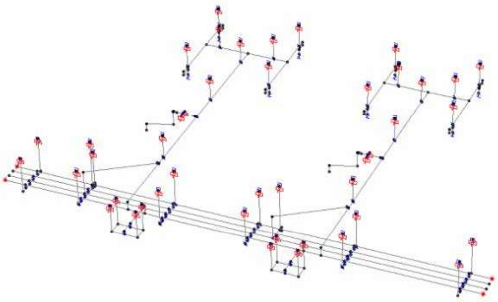

Fig. 2 Test range of the piping system.

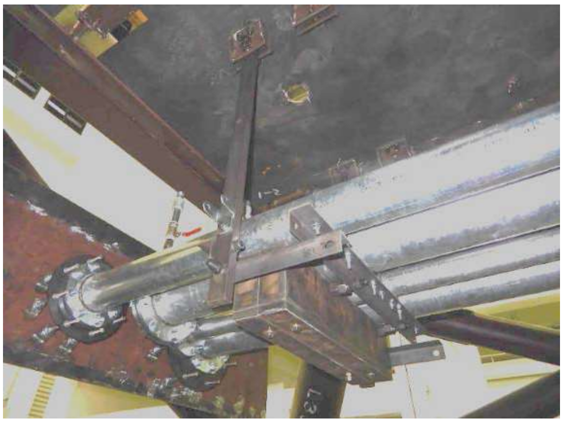

Fig. 3 Boundary of the test specimen.

Input Motion to the Piping System

The sample hospital is a shear-wall reinforced concrete (RC) structure with six floors above ground and one floor under ground. To obtain the floor response to the input motion for the dynamic analysis of the sample sprinkler piping, the hospital structure was simulated in a nonlinear time-history finite element analysis of the RC structure under strong ground motion, performed using MIDAS Gen 2018 v2.1. Fig. 4a depicts the fundamental modal shapes at frequencies of 2.4 Hz and 2.73 Hz in the longitudinal (along "flanges") and transverse (along the "web") directions of the floor plan, respectively. These natural frequencies can be considered as the main frequency contents of the floor responses derived in the following analysis since the mass participation ratios of both modes exceeds 70%. To investigate the possible resonant behavior of the suspended piping system in the top roof level of the mid-rise building, a numerical model of a fourteen-level SC building was adopted to obtain a flexible floor response (Fig. 4b) (Su 2018).

(a)

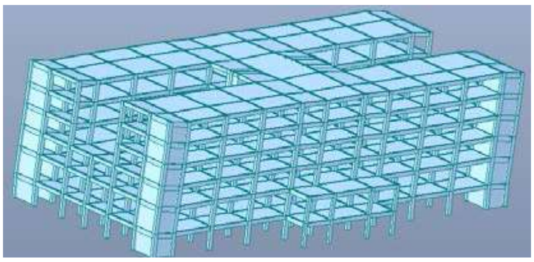

(b)

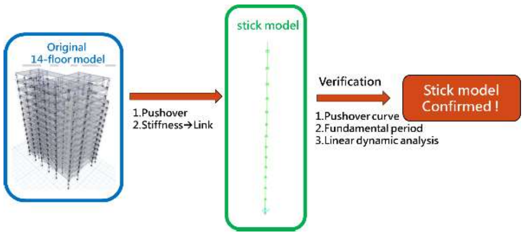

Fig. 4 Numerical models of the simulated buildings: (a) the sample RC hospital, and (b) a 14-floor SC building.

The simulated floor responses were generated from the roof level of the two numerical models under three types of ground motions. Table 2 presents detailed data on the designated ground motions. To simulate the conditions of the Jiashian earthquake in the sample hospital, the first test was equal to the measured ground motion recorded at the nearest seismic station. Referring to FEMA P695 (ATC 2009), the other two ground motions were selected from the PEER West NGA database (PEER) and are all measured at Duzce, with one being a near-fault ground motion (RSN 1605) and the other a far-field ground motion (RSN1158). The three types of ground motions were normalized to 320 gal based on the geometric mean value of the horizontal peak ground acceleration (PGA) and then input into the building models. Finally, the floor response at the roof level was obtained (Fig. 5) and was further checked to ensure it was smaller than the limitation of the shaking table in the NCREE Tainan Laboratory.

Table 2 Input motion for the analysis of the building.

Event RSN No. or Station	Item	PGA(gal)* geomean(H1,H2)	PGA(gal)* max(H1,H2)	PGA(gal)* EW | NS PGA	PGV(cm/s) geomean(H1,H2)	PGV(cm/s) max(H1,H2)	Direction Ground-building-Piping (Trans. of Pipe = Y dir. of Table)	Floor Response
Kocaeli (RSN1158Duzce)	FQ9(320gal)	319.77	345.35	296 | 345	55.27	56.79	EW-Lateral-Y	FDH
Duzce (RSN1605Duzce)	NQ12(320gal)	319.75	416.94	245 | 417	58.65	63.97	EW-Lateral-Y	NDH
Kocaeli (RSN1158Duzce)	FQ9(320gal)	319.77	345.35	296 | 345	55.27	56.79	EW-Lateral-Y	FDL
Duzce (RSN1605Duzce)	NQ12(320gal)	319.75	416.94	245 | 417	58.65	63.97	EW-Lateral-Y	NDL
20100304 JiaShan (CHY103)	FQ24(320gal)	326.2	368.14	289 | 368	32.92	39.17	NS-Lateral-Y	FCL
	FQ24(320gal)			289 | 368			NS-Lateral-Y	FCH

*Geometric mean value of horizontal PGA scaling to 320 gal.

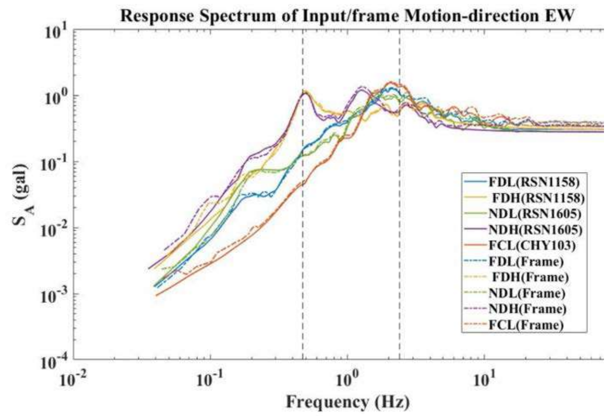

Fig. 5 Floor response spectrum in the horizontal direction.

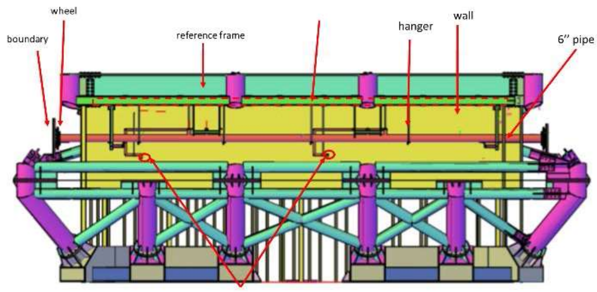

Fig. 7 Test configuration (front view).

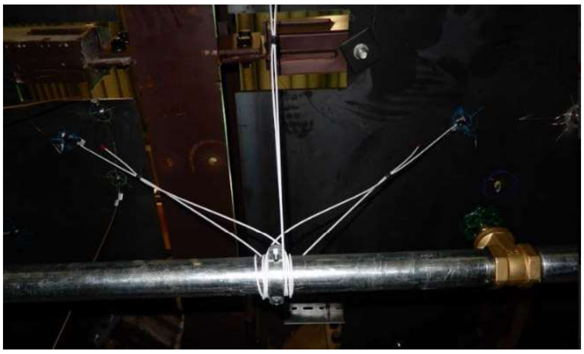

Fig. 8 Steel wire for the sprinkler head and branch.

Shaking Table Tests

The objective of this testing is to identify the failure modes of the typical sprinkler piping system in hospitals and to propose appropriate improvement strategies for higher seismic performance. As shown in Fig. 6 and Fig. 7, the test specimen was suspended in the test frame. During this test, the same damage that occurred during the earthquake event was reproduced for the original configuration with screwed fittings. Additionally, the modified configurations with the proposed seismic restraint devices, including braces, attachments for the braces, flexible hoses, and steel wires, were also tested to verify their effectiveness (Fig. 8). From the results of the resonant frequency survey, the first mode of the original configuration of the sub-system was translation along the *Y*-axis (Table 1). Braces increased the natural frequency of the piping significantly, while the steel wires and flexible hose slightly changed the natural frequencies of the entire system. The effectiveness of the devices was mainly reflected by the stress distribution of the local pipe segments.

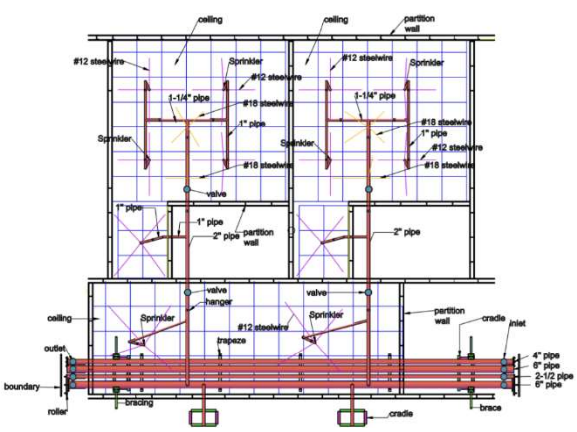

Fig. 6 Test configuration (plan view).

Conclusions

In view of the immediate need of the emergency medical services provided by hospitals after strong earthquakes, an ongoing research program on assessment and improvement strategies for a typical configuration of a sprinkler piping systems in hospitals was organized by the NCREE. Based on the shaking table test results and the original configuration of the hospital during the 2010 Jiashian earthquake, a screwed fitting of a 1" drop at the tee branch was the most vulnerable part of the damaged sprinkler piping system. Brittle failure associated with a screwed fitting and couplings was observed in the shaking table tests. The effectiveness of the three types of seismic restraint devices for a sprinkler piping system, namely braces with well-designed attachments for the main pipe, steel wires for branch lines, and flexible hoses for penetration, were also tested. Although seismic bracing can reduce the damage of adjacent architectural components, the optimum strategy to avoid leakages is to strengthen the main pipe with braces and to use flexible hoses near the tee branch to decrease both the shear and displacement demands on screwed fittings, or to use braces and steel wires to limit the movement of the main pipe and branch lines respectively. Based on the results of the finite element analysis and component tests, simulated parameters of the prototype and modified types of attachments under different loading directions were proposed for the seismic design of piping systems.

References

Ministry of the Interior (MOI), the Building Act, Taiwan, 2011.

National Fire Protection Association (NFPA), Standard for the Installation of Sprinkler Systems, NFPA 13, U.S, 2010.

G&E Engineering Systems Inc., “Fragility of Non-Structural Components: A.1 fire sprinkler systems”, FEMA P-58/BD-3.9.12, Federal Emergency Management Agency (FEMA), Washington, D.C, 2009.

Juin-Fu Chai, Jenn-Shin Hwang et al. Seismic Evaluation and Strengthened Guidelines for Hospital Buildings 2015

Su YS, Lin FR, Chai JF and Liao WI, A research on analysis of seismic demands for non-structural components of system in Mid- to High-Rise Buildings, the 14th National Conference on Structural Engineering, Taichung, Taiwan, 2018

Applied Technology Council, Quantification of Building Seismic Performance Factor, FEMA P-695, FEMA, Washington, D.C., 2009.

PEER Center, University of California, PEER NGA West database, https://ngawest2.berkeley.edu

Study of the 3D Periodic Foundation for Seismic Mitigation

Witarto[1], Cho-Yen Yang[2], Shiang-Jung Wang[3], Wang-Chuen Lin[4], Chung-Han Yu[2], Yi-Lung Mo[5], and Kuo-Chun Chang[6]

Witarto[1]、楊卓諺[2]、汪向榮[3]、林旺春[4]、游忠翰[2]、莫詒隆[5]、張國鎮[6]

Abstract

Structural vibration is an important concern for structures subjected to seismic excitations, especially for critical structures such as nuclear power plants and high technology facilities. To completely function under and after seismic excitations, structural vibration should be mitigated as much as possible. In this study, the 3D periodic foundation, which is one implementation of periodic material, is experimentally studied. This type of material possesses a frequency bandgap that could isolate or change the direction of wave propagation if the frequency content of a wave falls into that frequency bandgap. Thus, the structural vibration can be suppressed by the implementation of the proposed 3D periodic function. The seismic performance and feasibility of the 3D periodic foundation are verified by the shaking table test.

Keywords: periodic material, isolation, seismic, shaking table, experiment

Introduction

Structural isolation technologies have proven an effective means to isolate acceleration transmission to superstructures, which can reduce the responses of the superstructure. However, to obtain improved performance in acceleration, a relatively large displacement is usually required due to the long period of the isolation system. Thus, many studies have focused on the implementation of periodic material in the structural foundation as an alternative means of achieving similar control. The earliest study of periodic material sprung from the research of phononic crystals. This material can isolate or change wave propagation by appropriately designing the lattice of the phononic crystal. Seismic performance similar to an isolation system can be obtained by implementing the periodic material in the structural foundation.

Analysis and Design of the Benchmark Structure

The superstructure is a one story 2 × 1 span steel structure with a size of 3700 × 1700 × 1575 mm (Fig. 1). Additional masses of 1830 and 8368 kg mounted on the top and bottom plate, respectively, are considered in the numerical analysis. Each unit cell of the periodic foundation is composed of a cubic concrete core with an edge length equal to 32.5 cm and covered by a Polyurethane sheet with a thickness of 1.93 cm on the six surfaces (Fig. 2). All material properties used in the numerical model are listed in Table 1. From the analysis results, the first and second modes equal to 3.557 and 3.639 Hz are two translation modes in the longitudinal and lateral directions. The third mode in the torsional direction has a frequency of 4.532 Hz. The sixth mode at 12.389 Hz is the vertical model (Fig. 3). In the sweeping analysis, three points on the top of the periodic foundation and one point on the roof of the superstructure are taken as observation points (Fig. 4). The results for the frequency response function (FRF) are illustrated in Fig. 5. The S-wave is the input in the transverse horizontal direction and the P-wave is the input in the vertical direction. From Fig. 5a, attenuation zones between 5-9 and 9.8-50 Hz are observed for the three points on the top of the 3D periodic foundation, and 10-50 Hz for the roof of the superstructure under the S-wave. Similarly, Fig. 5b demonstrates the results for the P-wave, with an attenuation zone between 15-28 Hz observed for Points A and C on the top of the 3D periodic foundation. The results for Point B vary

1 PhD., University of Huston
2 Assistant Researcher, National Center for Research on Earthquake Engineering
3 Associate Professor, National Taiwan University of Science and Technology
4 Associate Researcher, National Center for Research on Earthquake Engineering
5 Professor, University of Huston
6 Professor, National Taiwan University

somewhat when compared to those of Point A and C, while still following similar trends. Meanwhile an attenuation zone for the roof of the superstructure from 17.58-50 Hz is also observed. These frequency ranges of the corresponding attenuation zones meet the capacity of the shaking table, and thus the performances of the 3D periodic foundation could be experimentally verified.

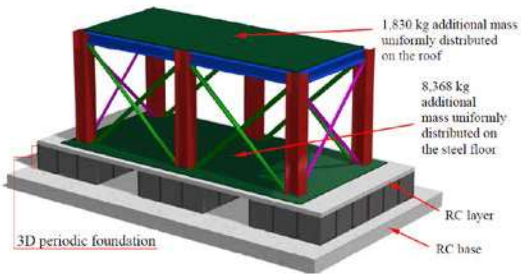

Fig. 1 Schematic diagram of the benchmark steel structure with a 3D periodic foundation.

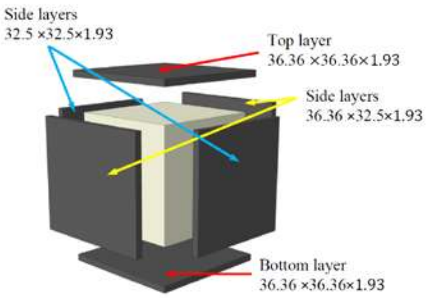

Fig. 2 Unit cell of the periodic foundation.

Table 1 Material properties for the numerical analysis.

Material	Young's modulus (MPa)	Density (kg/m^3)	Poisson's ratio
Steel	200,000	7850	0.3
Reinforced concrete	314,000	2300	0.2
Polyurethane	0.1695	1100	0.463

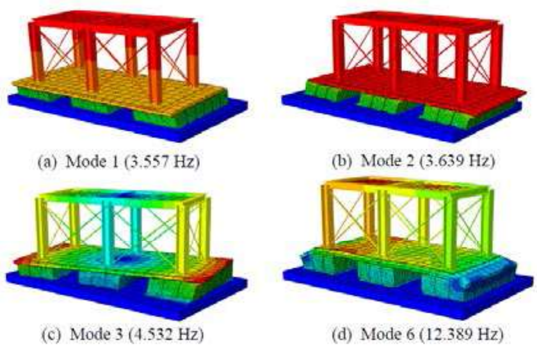

Fig. 3 Modal analysis results.

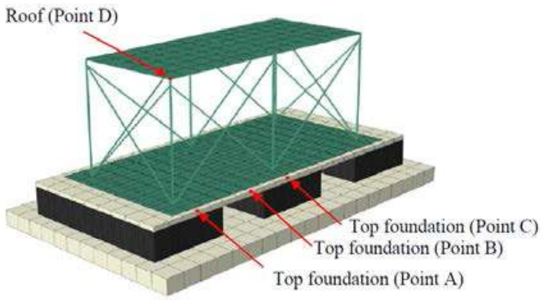

Fig. 4 FEM model of the 3D periodic foundation showing the locations of the output points.

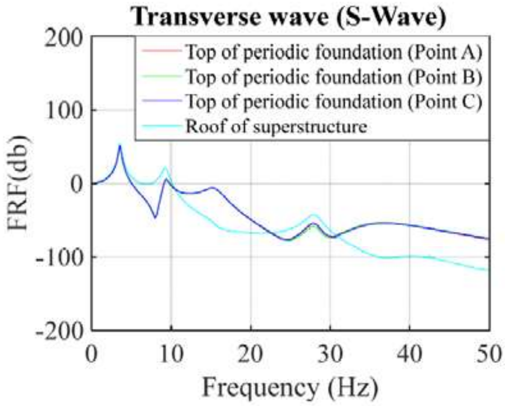

Fig. 5a Frequency response functions under the influence of S-waves.

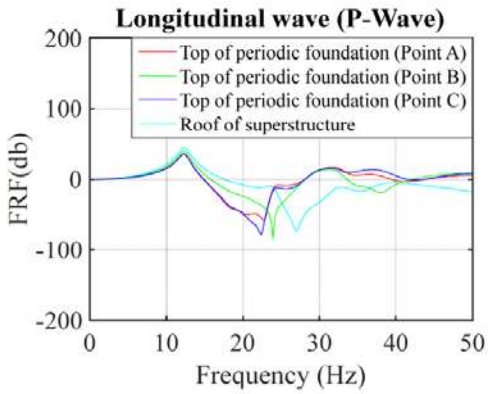

Fig. 5b Frequency response functions under the influence of P-waves.

Shaking Table Test

The setup and the sensor allocation in the shaking table test are shown in Fig. 6. Various sensors including an accelerometer, displacement transducer, and optical measurement system (NDI) were selected and installed on four corners of the specimen. For each corner, the sensors are distributed on the top and bottom plates, the periodic foundation, and the concrete base. The responses of the superstructure can be obtained from these sensors, and then the seismic performance of the 3D periodic foundation can be verified by comparing the acceleration responses measured from the experimental results. Inputs considered for the shaking table included white noise, a sinusoidal wave, sweep sine, and seismic records. For the seismic records, eight earthquakes including Anza, Bishop, Gilroy, Oroville, Loma Prieta, Imperial Valley, Northridge, and San Fernando were selected.

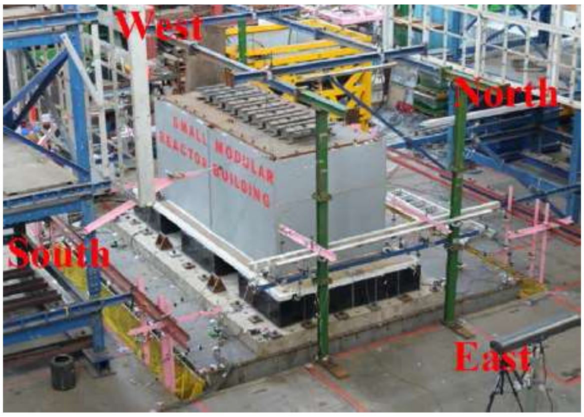

Fig. 6 Setup and sensor allocation

Experimental Results

The test results of the roof under the sweeping test were analyzed in the frequency domain. The frequency response functions of the horizontal and vertical directions and the torsional mode are shown in Fig. 7.

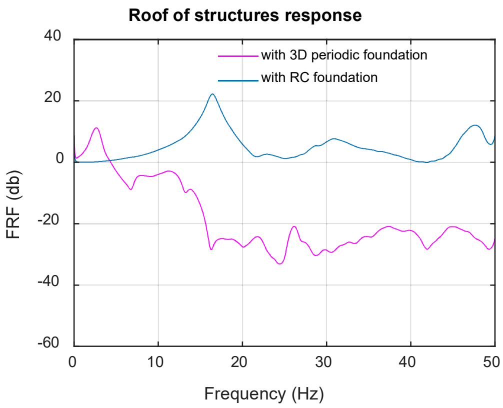

Fig. 7a Frequency response functions of the roof in the horizontal direction.

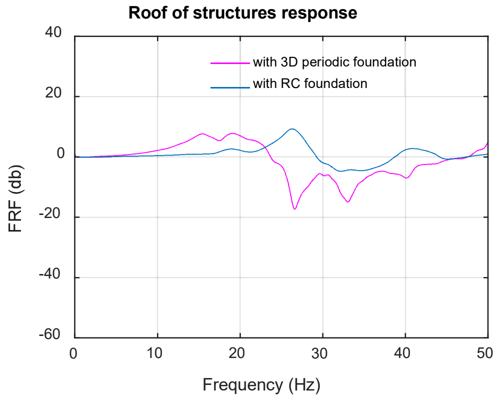

Fig. 7b Frequency response functions of the roof in the vertical direction.

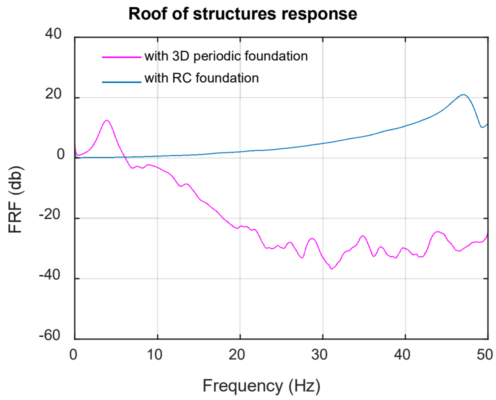

Fig. 7c Frequency response functions of the roof in the torsional mode.

Taking the case of the Oroville earthquake as an example, the input of the shaking table is normalized to 0.4 g. The maximum acceleration measured from the concrete base is 0.4154 g. The maximum acceleration at the top of the 3D periodic foundation is reduced to 0.0258 g, which is a 93.8% reduction relative to the concrete base. Similarly, the maximum acceleration at the roof of the superstructure is 0.0273 g, which is a 93.42% reduction. Thus, the mitigation of acceleration due to the 3D periodic foundation is verified (Fig. 5). From the acceleration spectrum, it is evident that the amplitudes of the roof and top of the 3D periodic foundation are both smaller than the corresponding shaking table input when the frequency falls between 5 to 50 Hz. That is, the 3D periodic foundation is quite effective within the above frequency range (Fig. 6). Alternatively, the deformation of the superstructure is also an important index. From Fig. 7, the displacement of the superstructure with the 3D periodic foundation is smaller than the superstructure with a fixed base.

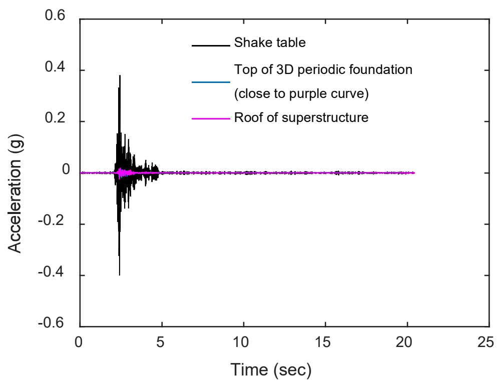

Fig. 8a Acceleration history (Oroville).

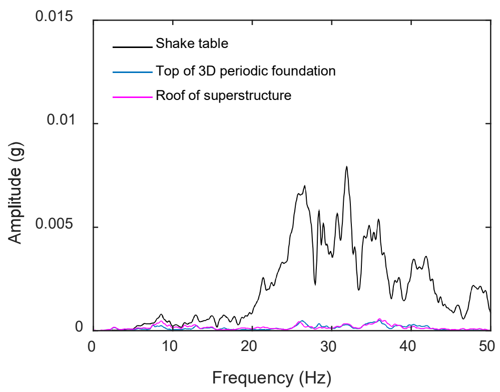

Fig. 8b Acceleration spectrum (Oroville).

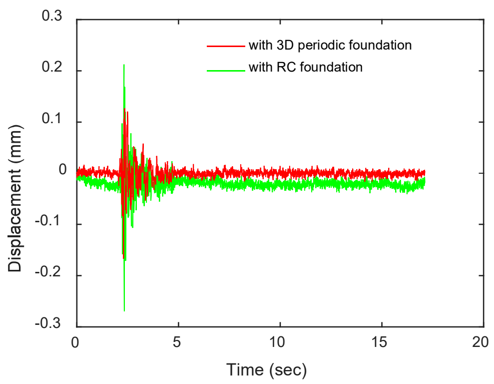

Fig. 8c Displacement history (Oroville).

Conclusions

In this study, the characteristics and the feasibility of the practical application of a 3D periodic foundation are completely verified by the shaking table test with various input ground motions. In a future study, the design of the periodic foundation and a different composition of the unit cell could be considered for obtaining improved performance.

References

Witarto Witarto, SJ Wang, CY Yang, Jiaji Wang, YL Mo, KC Chang, Yu Tang, "Three-dimensional periodic materials as seismic base isolator for nuclear infrastructure," AIP Advances 2019; 9(4): 045014. DOI: 10.1063/1.5088609.

Witarto W, Wang SJ, Yang CY, Nie X, Mo YL, Chang KC, Tang Y, Kassawara R. "Seismic isolation of small modular reactors using metamaterials," AIP Advances 2018; 8(4): 045307. DOI: 10.1063/1.5020161.

Entropy-Based Structural Health Monitoring System for Damage Detection in Multi-Bay Three-Dimensional Structures

Tzu Kang Lin[1] and Ana Gabriela Lainez[2]

林子剛 [1]、賴佳荷 [2]

Abstract

In this paper, a structural health monitoring (SHM) system based on multi-scale cross-sample entropy (MSCE) calculations was proposed for detecting damage locations in multi-bay three-dimensional structures. The location of damage was evaluated for each bay through MSCE analysis by examining the degree of dissimilarity between the response signals of vertically adjacent floors. Subsequently, the results were quantified using the damage index (DI). The performance of the proposed SHM system was determined in this study by performing a finite element analysis of a multi-bay seven-story structure. The derived results revealed that the SHM system successfully detected the damaged floors and the respective direction of damage for several cases. The proposed system provides a mechanism for the preliminary assessment of determining which bay has been more severely affected. Thus, the effectiveness and high potential of the SHM system for rapidly locating damaged areas in large and complex structures at low cost is demonstrated.

Keywords: multi-bay, three-dimensional, structural health monitoring, multi-scale, cross-sample entropy

Introduction

In 2013, Fabris *et al.* (2013) applied the Samp-En and Cross-SampEn algorithms to electroglottogram and microphone signals. Healthy patients and those with throat or vocal disorders could be identified by quantifying the degree of asynchrony between the time series results. Subsequently, structural health monitoring (SHM) systems based on the MSE and multi-scale cross-sample entropy (MSCE) algorithms, introduced by Richman *et al.* (2000), Costa *et al.* (2000), and Costa *et al.* (2005), in the field of physiology have been proposed to identify damage locations and the direction of damage for a single-bay structure (Lin *et al.*, 2015; Lin *et al.*, 2017). Vertical MSCE analysis was performed to identify the damaged floor location, and planar MSCE analysis was performed to identify the direction of the damage. The resulting MSCE curves indicated that a higher degree of synchronicity between two signals yields lower entropy values. Furthermore, time series with high complexity have correspondingly high entropy values, indicating the occurrence of damage. Considering the higher entropy values obtained for damaged floors, vertical and planar damage index (DI) values were proposed for efficiently quantifying the damage. Comparison of healthy and damaged signals revealed positive DI values for damaged floors, whereas negative DI values were observed for healthy floors. Moreover, the parameters of the sample entropy and wavelet transformation were optimized to detect the possible crack on a cantilever beam (Wimarshana *et al.*, 2017), and a cross-entropy optimization technique was applied to identify the damage of shear structure components (Guan *et al.*, 2017).

The aim of the present study was to implement the vertical MSCE analysis coupled with the vertical DI on a large and complex three-bay bi-axial numerical model to identify the damaged floors and damaged bays within the structure.

[1] Adjunct Research Fellow, National Center for Research on Earthquake Engineering / Professor, Department of Civil Engineering, National Chiao Tung University

[2] Master, Department of Civil Engineering, National Chiao Tung University

MSCE and DI

The SHM system proposed in this study relies on MSCE analysis for identifying structural damage. Furthermore, as an extended three-bay model was analyzed in this study, it was also of interest to identify the location of damaged bays. However, diagnosing the location of damage through a simple observation of the obtained MSCE curves is typically difficult. Therefore, a DI value based on the findings of Lin *et al*. (2015) and Lin *et al*. (2017) was proposed for rapidly and efficiently identifying the damaged floor, axis, and bay within the structure. For the three-bay structure described in the following section, the SHM process was applied to each bay separately to detect any possible damage, while the interaction between each bay was included in the measured signals. Thus, the following procedure was repeated three times. Two groups of curves representing the healthy and damaged conditions of the structure were then analyzed. For a biaxial structure with N floors, the MSCE curves for the x- and y-axes under healthy conditions can be expressed as matrices:

$$MSCE_{undamaged} = \begin{Bmatrix} H_1^x \\ H_2^x \\ \vdots \\ H_N^x \end{Bmatrix} \quad MSCE_{undamaged} \begin{Bmatrix} H_1^y \\ H_2^y \\ \vdots \\ H_N^y \end{Bmatrix} \tag{1}$$

Similarly, the MSCE curves for the x- and y-axes under damaged conditions are expressed as follows:

$$MSCE_{damaged} = \begin{Bmatrix} D_1^x \\ D_2^x \\ \vdots \\ D_N^x \end{Bmatrix} \quad MSCE_{damaged} \begin{Bmatrix} D_1^y \\ D_2^y \\ \vdots \\ D_N^y \end{Bmatrix} \tag{2}$$

where H and D represent the MSCE curve for the healthy and damaged conditions, respectively. The superscripts *x* and *y* represent the analyzed axes, and the subscript depicts the analyzed floor number. For example, H_N^x is the x-axis MSCE of the signal in the analyzed Nth floor and the signal of the floor beneath it under healthy conditions. This can be further expressed as follows:

$$H_N^{axis} = \{CS_E{}^1_{HNaxis}, CS_E{}^2_{HNaxis}, CS_E{}^3_{HNaxis}, \ldots, CS_E{}^\tau_{HNaxis}\} \tag{3}$$

Similarly, D_N^{axis} can be arranged as follows:

$$D_N^{axis} = \{CS_E{}^1_{DNaxis}, CS_E{}^2_{DNaxis}, CS_E{}^3_{DNaxis}, \ldots, CS_E{}^\tau_{DNaxis} \tag{4}$$

where CS_E denotes the Cross-SampEn value in each element, the superscript denotes the scale factor τ, the first superscript denotes the health condition, the second subscript denotes the analyzed floor, and the third subscript denotes the analyzed axis. Subsequently, the following formulae can be used to calculate the dual-axis DI per floor on a specific bay:

$$DI_{Nx} = \sum_{k=1}^{\tau}(CS_E{}^q_{DNx} - CS_E{}^q_{HNx}) \qquad DI_{Ny} = \sum_{k=1}^{\tau}(CS_E{}^q_{DNy} - CS_E{}^q_{HNy}) \tag{5}$$

The DI is evaluated by calculating the difference between the MSCE values of the damaged and healthy structures. Each bay of the structure has two DI values per floor: one on the x-axis and the other on the y-axis. For a specific floor, a positive DI indicates that the floor has sustained damage, whereas a negative DI indicates no damage to the floor, where the structure is associated with a more stable condition when compared to the original healthy state. As verified in previous research (Lin *et al.*, 2015), the proposed method can sustain the velocity changes over an approximately 10% to 20% noise level.

Numerical Simulation

To verify the feasibility of the SHM system proposed in this study, SAP2000 software was used to construct and analyze the three-bay, seven-story model, which is an extension of areal benchmark structure commonly used at the National Center for Research on Earthquake Engineering (NCREE), for numerical simulation. The dimensions and characteristics of the numerical model are outlined as follows: The model was a steel structure comprising seven stories and three bays on the x-axis and a single bay on the y-axis. The height of each story was 1.06 m, and the widths of the bays on the x- and y-axes were 1.32 and 0.92 m, respectively. The columns were steel plates measuring 75 × 50 mm^2. The beams were steel plates of 70 × 100 mm^2. All sides of the structure were fitted with steel bracing selected as L-shaped steel angles measuring 65 × 65 × 6 mm^3. Apart from the self-weight of the structure, an additional 500 kg mass was added per bay on each story to simulate the actual characteristics of the structure.

After the SHM database was constructed by performing the time history and modal analyses on the numerical model for each damage condition, biaxial velocity response data were extracted from the center of each floor per bay. The scenarios comprised various combinations of single-story, two-story, or multistory damage, paired with single- or multi-bay, and single- or multi-direction damage. The cases for the damage database were selected with a broad spectrum of diverse damage locations. In total, the damage conditions were classified into 12 categories and 26 cases. Numbers in the case names indicates the damaged floors; X and Y represent the damaged axes; and L, C, and R (left, center, and right) denote the damaged bay. For example, Case 9 (6X-L & 6Y-R) represents a case involving damage on the sixth floor, x-axis, left bay and sixth floor, y-axis, right bay. Figure 1 illustrates the numerical model, with the dotted lines representing the braces removed to exemplify the damaged bracing for Case 9.

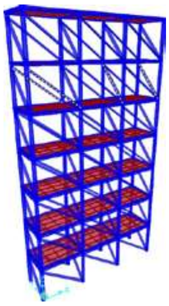

Figure 1. Three-dimensional view of the numerical model. The dotted braces represent the damaged bracing for Case 9 (6X-L & 6Y-R)

General Discussion

In this study, 26 damage cases classified into 12 categories were examined to verify the feasibility of MSCE and DI analyses for undertaking damage detection in a complex three-bay structure. The complete results are summarized in Table 1. The DI values were lower when there were more damaged floors as the structural complexity was redistributed under different damage conditions. These results were further analyzed in two stages. First, the DI results obtained for the identification of the damaged floors and damage directions were quantified through a precision and recall analysis. For the precision and recall analyses, the DI results for the X- and Y-directions were first classified into four categories: true positives (TP), representing damaged floors that have been correctly identified; false positives (FP), representing floors that have been misclassified as damaged; true negatives (TN), representing undamaged floors that have been correctly classified; and false negatives (FN), representing damaged floors that have been misclassified as undamaged. Precision and recall values were then calculated as follows:

$$\text{Precision} = \frac{TP}{TP+FP} \qquad \text{Recall} = \frac{TP}{TP+FN} \tag{5}$$

Table 1. Classification results of DI analysis

Case Number	Damage Group	Damage Case	Damage Index (X-direction)	Damage Index (Y-direction)
1	Single-story,	5X-L	OK	OK
2	single-bay,	3Y-C	OK	OK
3	single-direction	7Y-R	OK	$1F^1$
4	Single-story, single-	4XY-L	OK	OK
5	bay, multi-directional	6XY-C	$6F^2$	OK
6	Single-story, multi-	2X-L & 2X-C	$2F^2$	OK
7	bay, single-direction	5Y-L & 5Y-C & 5Y-R	OK	$5F^2$
8	Single-story, multi-	3X-R & 3Y-C	OK	OK
9	bay, multidirectional	6X-L & 6Y-R	OK	$1F^1$
10	Two-story, single-bay,	3X-L & 6X-L	OK	OK
11	single-direction	1Y-R & 5Y-R	OK	OK
12	Two-story, single-bay,	4X-C & 7Y-C	OK	OK
13	multidirectional	2XY-R & 3XY-R	OK	$1F^1$
14	Two-story,	5X-R & 7X-L	OK	OK
15	multi-bay,	2Y-C & 4Y-R	OK	$1F^1$ & $2F^2$
16	single-direction	2X-L&C, 6X-C&R	$2F^2$ & $6F^2$	OK
17	Two-story, multi-	4X-R & 2Y-L	OK	$1F^1$
18	bay, multidirectional	6XY-R & 7XY-L	OK	$1F^1$ & $2F^1$
19	Multistory, single-	3X-L & 4X-L & 6X-L	$6F^3$	OK
20	bay, single-direction	1Y-R & 4Y-R & 7Y-R	OK	OK
21	Multistory, single-	4X-L & 5Y-L & 6Y-L	OK	$1F^1$ & $2F^1$
22	bay, multidirectional	1XY-C & 3XY-C & 5XY-C	$1F^3$ & $5F^3$	$1F^3$ & $3F^2$
23	Multistory, multi-bay,	3X-L & 4X-C & 5X-R	$5F^3$	OK
24	single-direction	6Y-L & 2Y-C & 7Y-R	OK	$1F^1$ & $2F^3$
25	Multistory, multi-bay,	1X-R & 2X-R & 1Y-L	$1F^3$ & $2F^3$	OK
26	multidirectional	7XY-R & 4Y-L & 6Y-C	OK	$1F^1$ & $6F^2$

[1]Indicates that the floor has been misclassified as damaged; [2]Indicates that the damaged bay has not been successfully identified; [3]Indicates that the damaged floor has not been detected.

Damage Location

High precision results were denoted by few false positives, which represent the percentage of correctly detecting the damage to 350 locations, where a high recall result indicates few false negatives, confirming the reliability of the analyses in not missing possible damage. The combined results for both directions are summarized in Table 2. The derived precision and recall were 83% and 87%, respectively. These results indicate that 83% of the floors identified and their respective directions classified by the DI as damaged were truly damaged. As most of the damages were simulated along the X-direction, better performance of the findings was achieved along the X-direction for 100% when compared to the Y-direction, which was 73% in the study. Moreover, 87% of all actual damaged floors and their respective directions were correctly classified as damaged. The high-percentage accuracy of the findings proved that the system can reliably detect any level of damage with only a small probability of losses. The results have demonstrated the capacity of the proposed SHM system for locating the damaged floors and damage direction of a large, three-bay numerical model.

Table 2. Precision and recall analysis results (X- and Y-directions)

Direction	True Positives	False Positives	True Negatives	False Negatives	Precision	Recall
X	25	0	151	6	100%	81%
Y	30	11	139	2	73%	94%
Total	55	11	290	8	83%	87%

Damage Bay Identification

A separate analysis of the accuracy of the identification of the damaged bays was subsequently performed; therefore, the results pertaining to the damaged bays were not considered in the precision and recall analyses. Because the removal of bracings on a specific bay would inevitably affect those adjacent to it, the calculated DI values were assumed to be fairly close. The combined results for both directions are shown in Table 3; an average identification accuracy of 75% was obtained. Better performance was achieved in the Y-direction as there was only one bay located along the Y-direction. For complicated damage combinations along the X-direction, the accuracy dropped to 71%. Furthermore, the proposed system was limited when more than one bay was damaged. Therefore, these results are merely a suggestion as to which bay might have been affected more severely. With the support of the damage bay identification analyses, the proposed method may be easily extended to any complicated structure.

Table 3. Identification accuracy of damaged bays (X- and Y-directions)

Direction	Damage Instances	Correctly Identified Bay	Accuracy
X	34	24	71%
Y	34	27	79%
Total	68	51	75%

Conclusions

In this study, the feasibility of detecting damage in a complex three-bay, seven-story numerical model by SHM methods was examined. Through the proposed SHM system, damage locations are able to be rapidly and effectively detected by recording the velocity response data of the model under ambient vibrations measured from the center of each floor, before and after damage occurs, and subsequently analyzing the complexity of the signals using the MSCE method. The reliability and viability of the proposed SHM system were examined through the numerical analysis of 26 damage cases in 12 categories, representing several degrees of damage severity. The results of the analyses were examined in two stages. First, the results pertaining to the damaged floor and damage direction indicate that 83% of the floors and their respective directions were truly damaged. Furthermore, 87% of the damaged floors and their respective directions were correctly classified as damaged by the DI. Subsequently, the identification of the damaged bays was analyzed, and an identification accuracy of 75% was obtained. Identification of the damaged bays through the proposed SHM system was found to be limited, especially when multi-bay damage exists on a single floor.

The obtained results verify the feasibility and further potential of the proposed SHM system for the detection and local identification of damage in large and complex structures.

References

Richman, J.S., Moorman, J.R., (2000). Physiological time-series analysis using approximate entropy and sample entropy. *American Journal of Physiology-Heart and Circulatory Physiology*, 278, H2039–H2049.

Costa, M., Goldberger, A.L., Peng, C.K., (2002). Multiscale entropy analysis of complex physiologic time series. *Physical review letters*, 89, 068102.

Costa, M., Goldberger, A.L., Peng, C.K., (2005). Multiscale entropy analysis of biological signals. *Physical review E*, 71, 021906.

Fabris, C., De Colle, W., Sparacino, G., (2013). Voice disorders assessed by (cross-) sample entropy of electroglottogram and microphone signals. *Biomedical Signal Processing and Control*, 8, 920–926.

Lin, T.K., Liang, J.C., (2015). Application of multi-scale (cross-) sample entropy for structural health monitoring. *Smart Materials and Structures*, 24, 085003.

Lin, T.K., Tseng, T.C., Lainez, A.G., (2017). Three-dimensional structural health monitoring based on multiscale cross-sample entropy. *Earthquakes and Structures*, 12, 673–687.

Wimarshana, B., Wu, N., Wu, C., (2017). Crack identification with parametric optimization of entropy wavelet transformation. *Structural Monitoring and Maintenance*, 4, 33–52.

Guan, X.F., Wang, Y.X., He, J.J., (2017). A probabilistic damage identification method for shear structure components based on Cross-Entropy optimizations. *Entropy*, 19, 27.

Metaheuristic Optimization of Controller Design for Active Mass Dampers

Pei-Ching Chien[1], Bryan Jevon Sugiarto[2] and Kai-Yi Chien

陳沛清 [1]、張恩典 [2]、簡楷益 [2]

Abstract

The linear-quadratic regulator (LQR) solution has been applied to active structural control theory and has been extensively investigated over past decades. State feedback gains can be obtained by minimizing the cost function that contains weighted states and control inputs; however, the appropriate selection of weights mostly depends on trial and error combined with engineering experiences. In this study, a novel metaheuristic optimization algorithm named symbiotic organisms search (SOS) was applied to optimize the LQR weighting matrices with respect to different objective functions. In addition, three objective functions were proposed, which contain the root-mean-square of modal acceleration, the peak absolute modal acceleration, and the square root of the sum of squares of the modal acceleration. A 10-story shear building with an active mass damper installed on the top floor was adopted to validate the effectiveness of the proposed method.

Keywords: Active mass damper, linear-quadratic regulator, metaheuristic optimization, symbiotic organisms search

Introduction

The linear quadratic regulator (LQR) solution is one of the most commonly used controllers to achieve optimal control performance. To obtain an optimal control force, LQR works through adjusting weighted parameters used to minimize a cost function and is described as per equation (1):

$$J = \int_0^\infty \left(\mathbf{x}^T(t)\mathbf{Q}\mathbf{x}(t) + \mathbf{u}^T(t)\mathbf{R}\mathbf{u}(t)\right)dt \quad (1)$$

where **x** is the structural states; **u** is the control input; and **Q** and **R** are the weightings. However, it is difficult to tune the weighted parameters of the LQR algorithm effectively since identifying the correlation between the weighted parameters of the LQR algorithm and the structural response is not straightforward. Recently, Cheng and Prayogo proposed a new simple and powerful metaheuristic optimization called symbiotic organisms search (SOS), which surpasses the performance of other metaheuristic algorithms based on numerical benchmark function results. It was expected that tuning the LQR weighting parameters by using SOS could result in satisfactory control performance.

This study focused on the optimization of an active mass damper (AMD) controlled by an LQR. SOS was used to optimize and tune the weighting parameters of LQR. Various numerical simulations were conducted based on a benchmark 10-story shear building. The results of this study may be used as a reference for LQR controller design with metaheuristic optimization algorithms.

Optimization Algorithm

Selecting the appropriate and correct weighting matrices for LQR is usually performed by trial and error, which is based on the designer's research experience. However, this approach may not result in optimal results, which then deteriorates the structural control performance. In this study, metaheuristic optimization SOS was applied in order to obtain an improved selection of LQR weighting matrices.

SOS is a metaheuristic optimization algorithm that imitates the biological interaction between two organisms in an ecosystem (symbiosis). The three phases of SOS resemble the real-world biological interaction model, which includes mutualism, commensalism, and parasitism. The procedure of SOS

[1] Assistant Professor, National Taiwan University of Science and Technology
[2] Graduate Student, National Taiwan University of Science and Technology

is to initialize a population of organisms with random locations in the search space. Then each organisms' fitness value was evaluated based on the objective function. The flowchart for conducting SOS optimization is depicted in Figure 1.

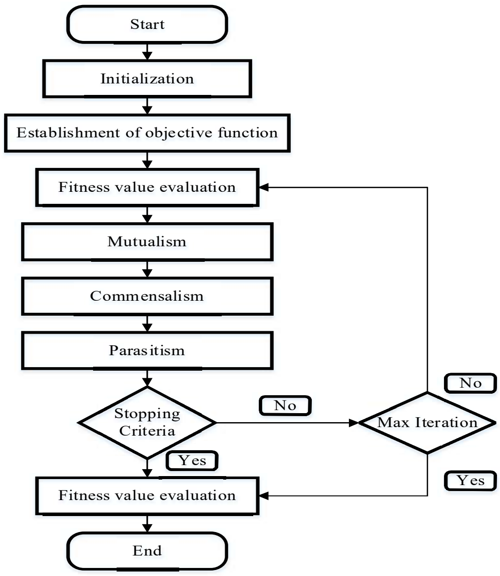

Figure 1. Symbiotic organism search flowchart

The key element in the optimization process was to define the objective function. For active structural control optimization, a meaningful and proper objective function is able to produce a satisfactory result. In this research, the optimization algorithm was performed to minimize the three objective functions, and the controller obtained from optimizing these three objective functions was then compared with each other. The three objective functions are defined as per equations (2) – (4):

$$f_1 = \max\left|\ddot{x}_{1\_\mathrm{modal}} + \ldots + \ddot{x}_{n\_\mathrm{modal}}\right| \tag{2}$$

$$f_2 = rms\left|\ddot{x}_{1\_\mathrm{modal}} + \ldots + \ddot{x}_{n\_\mathrm{modal}}\right| \tag{3}$$

$$f_3 = SRSS\left(\max\left|\ddot{x}_{1\_\mathrm{modal}}\right| + \ldots + \max\left|\ddot{x}_{n\_\mathrm{modal}}\right|\right) \tag{4}$$

The first and second objective functions were selected to minimize the maximum (MAX) and the root mean square (RMS) of the total modal absolute acceleration from the first to the n^{th} controlled mode. Whereas, the third objective function was selected to minimize the square root of the sum of the squares (SRSS) of the maximum modal absolute acceleration, from the first to the n^{th} controlled mode.

To verify the control performance of the proposed method, four performance indices proposed by Jansen and Dyke were used. These performance indices are described as per equation (5) - (8):

$$J_1 = \max\left(\frac{|x_i(t)|}{x^{\max}}\right) \tag{5}$$

$$J_2 = \max\left(\frac{|d_i(t)/h_i|}{d_n^{\max}}\right) \tag{6}$$

$$J_3 = \max\left(\frac{|\ddot{x}_{ai}(t)|}{\ddot{x}_a^{\max}}\right) \tag{7}$$

$$J_4 = \max\left(\frac{|f_i(t)|}{W}\right) \tag{8}$$

where $x_i(t)$ = the relative displacement of the i^{th} floor over the entire response, $x^{\max}$ = the uncontrolled maximum displacement, $d_i(t)$ = interstory drift of the above ground floors over the response history, h_i =height of each floor, $d_n^{\max}$ =normalized peak interstory drift in the uncontrolled response, $\ddot{x}_{ai}(t)$ = absolute accelerations of the i^{th} floor, $\ddot{x}_a^{\max}$ = peak of the uncontrolled floor acceleration, $f_i(t)$ = maximum control force of the actuator, and W =weight of the structure

Numerical Simulation

A 10-story shear building concept that was introduced in the study by Amini *et al.* was adopted for the numerical simulation. The mass and the stiffness of each story was 10 tons and 2000 kN/m, respectively. The actuator used to drive the AMD was assumed to have a force capacity of 5% of the total weight of the structure, which was equal to 50 kN. For modal control, determining the number of modes to be controlled is important. For this structural model, the total effective modal mass from the first mode to the third mode already exceeded 95%; therefore, only the first three modes were considered for control of the structure in the objective function.

The structure was excited by a band-limited white noise with a RMS of 1 m/s^2, and a bandwidth ranging from 0 Hz to 20 Hz. The simulation was conducted over a duration of 40 seconds. SOS was used to optimize the **Q** matrix, while the **R** matrix was set to a fixed value of 100. For the optimization algorithm, 1×10^{10} and 0 were used as the upper bound and lower bound values for the **Q** matrix, respectively. For the tuning process, saturation with a value of 10% of the actuator capacity, which was equal to 5 kN (0.5% of the structure weight) was used for the control force adopted for the optimization algorithm to generate a **Q** matrix that can produce control force within an expected value. If the saturation was not used in the optimization process, the value of the **Q** matrix blew up and resulted in a very large control force that may lead to saturation issues. Saturation issues occur when the expected control force exceeds the actuator capacity, thus causing the control force to behave like a step function. Another advantage of using saturation in the tuning process, is that it can reduce the search field of the optimization algorithm and reduce the simulation time. While optimizing the **Q** matrix, SOS was used to minimize the objective functions as determined in Equations (2) to (4). After the tuning process was complete, the 10% actuator capacity (5 kN) saturation was removed and changed to saturation for the 100% actuator capacity (50 kN) in order to verify the controller in real conditions. The performance of the controller was compared in terms of the control performance indicated in Equations (5) to (8). To determine the best objective function, the comparison of the optimization results are shown in Figure 2. In terms of the performance indices J1, J2, and J3, the control performance generated by the SRSS objective function was superior when compared to the RMS and MAX objective functions. From these results, it can be concluded that SRSS was the best objective function to use. The SOS convergence history with the SRSS objective function is shown in Figure 3. The uncontrolled and controlled relative displacement and absolute acceleration of the top floor of the structure are depicted in Figure 4.

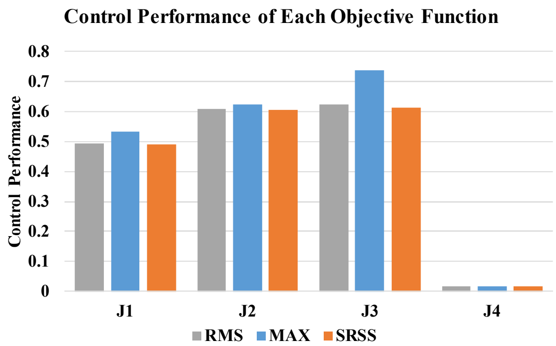

Figure 2. Performance of each objective function

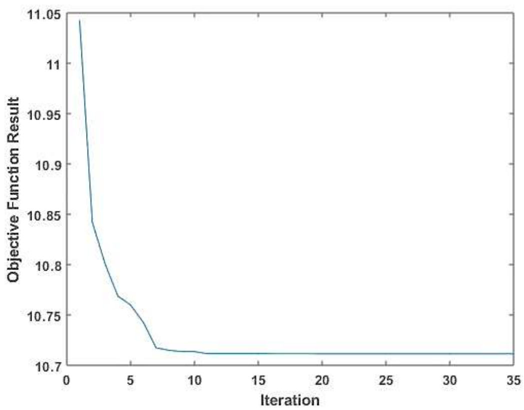

Figure 3. SOS convergence history with the SRSS objective function

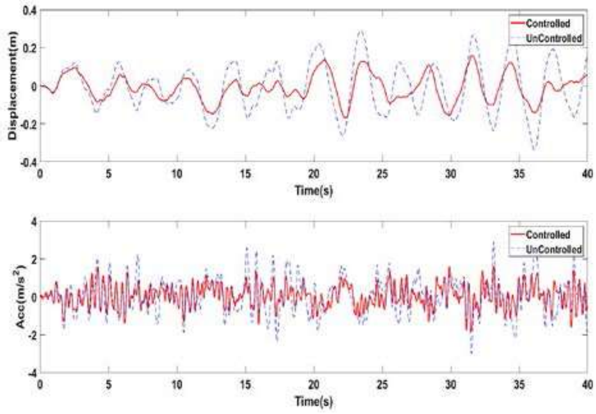

Figure 4. Relative displacement and absolute acceleration of the top floor

Comparison with Other Methods

The results obtained from the proposed method were compared with other methods cited in the paper published by Alavinasab and Moharrami. Fourteen earthquake ground excitations were used to excite the 10-story shear building in the comparison method. These methods include the variant of the **Q** matrix in LQR, which can be expressed as per equations (9) – (11).

$$Q_1 = 10^{q_i}\begin{bmatrix} \mathbf{K} & 0 \\ 0 & \mathbf{M} \end{bmatrix} \tag{9}$$

$$Q_2 = 10^{q_i}\begin{bmatrix} \mathbf{I} & 0 \\ 0 & 0 \end{bmatrix} \tag{10}$$

$$Q_3 = 10^{q_i}\begin{bmatrix} \mathbf{I} & 0 \\ 0 & \mathbf{I} \end{bmatrix} \tag{11}$$

where K= the structure stiffness matrix, M= the structure mass matrix, and R = 1 was applied to the cost function for all cases. The selection of each q_i was undertaken by trial and error until the LQR generated the same maximum average control force as that obtained from the LQR optimized by SOS subjected to the excitation of fourteen earthquakes. The control performance of method 1, method 2, and method 3 (from Equations 9 to 11) excited by the fourteen earthquakes is summarized in Figure 5. It can be seen that with the same amount of maximum control force, the control performance associated with J2 and J3 of the LQR optimized by SOS, outperforms that obtained from the other methods. However, in terms of J1, the results from method 1 to method 3 seem to have improved results when compared to the LQR optimized by SOS. These findings are reasonable since method 1 to method 3 determine the **Q** matrix with respect to the structural states, which includes the relative displacement. Moreover, method 1 to method 3 tend to suppress the relative displacement without considering other control objectives, while the proposed method gives balanced control.

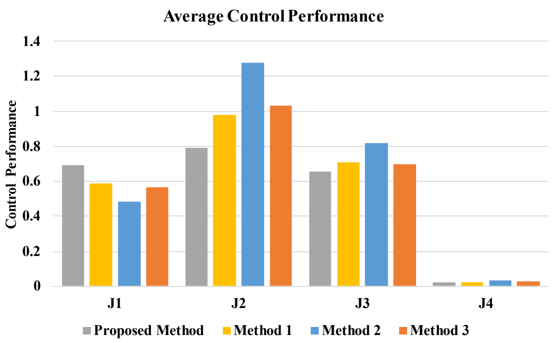

Figure 5. Comparison of control performance

Summary and Conclusions

In order to obtain a proper controller for active structural control, a novel metaheuristic optimization SOS was implemented to optimize the weighting matrices of LQR. This controller was tuned according to an objective function that aimed to reduce the SRSS of the modal absolute acceleration. The control performance of the proposed method was compared with other methods, under various earthquake excitations. The results indicated that the proposed method permanently provides superior control performance in terms of story drift and absolute acceleration reduction.

Based on the analytical results, the following conclusions are drawn:

(1) SOS performed well for optimization of the weighting matrices of LQR as it is able to obtain the global best without getting constrained by local optima. Moreover, it also converged rapidly and did not require the tuning of any optimization parameters.

(2) The best objective function for optimization was the SRSS of the modal absolute acceleration. In terms of control performance, the SRSS of the modal absolute acceleration achieved the best control performance.

(3) Tuning the controller using saturation of 10 % of the actuator force capacity was suggested in order to sustain the actuator control force such that it did not exceed the force capacity of the actuator when a larger earthquake is striking.

(4) The control performance (mostly with respect to story drift and absolute acceleration) of the proposed method was superior when compared to the control performance of the other described methods.

References

1. Abubakar, I. and Farid, B. (2013) “Generalized Den Hartog tuned mass damper system for control of vibrations in structures”, London, UL: WIT Press.

2. Alavinasab, A., Moharrami, H., and Khajepour, A. (2006) “Active control of structures using energy-based LQR method”, *Computer-Aided Civil and Infrastructure Engineering,* **21**(8), 605-611.

3. Amini, F., Hazaveh, N. K., and Rad, A. A. (2013) “Wavelet PSO-based LQR algorithm for optimal structural control using active tuned mass dampers”, *Computer-Aided Civil and Infrastructure Engineering*, **28**(7), 542-557.

4. Cheng, M. Y. and Prayogo, D. (2014) “Symbiotic Organisms Search: A new metaheuristic optimization algorithm”, *Computers & Structures*, **139**, 98-112.

Study on the Static Loading History of Steel Beam-to-Column Connections with Near-Fault Effects

Sheng-Jhih Jhuang[1], Ker-Chun Lin[2], Huang-Cheng Chen[3], and Chui-Hsin Chen[4]

莊勝智 [1]、林克強 [2]、陳奐丞 [3]、陳垂欣 [4]

Abstract

Taiwan is located on a seismic belt with many faults. Around one third of Taiwan's population lives within 10 kilometers of faults. This study aims to investigate the seismic performance of steel moment resisting frames with near-fault effects and to establish the loading history protocols of static tests with near-fault effects using nonlinear dynamic history analysis. In this study, two loading history protocols are proposed with a return period of 475 years and 2500 years for the design earthquake and the maximum considered earthquake, respectively. Using the results from Krawinkler and AISC 341-16, which considered near fault effects and far-field effects up to 4% rad, respectively, the results of four loading history protocols are compared. For the accumulated story drift angles of the loading history protocols, the three considering near-fault effects are smaller than that of AISC 341-16 with far-field effects ranging from 70% to 80%. The accumulated plastic story drift angle of the loading history protocol for a return period of 2500 years is larger than the other three. However, the largest story drift angles due to the pulse of near-faults for the two proposed loading history protocols are 6% and 6.5% rad, respectively, and are less than the 8% rad found for the loading history protocol from Krawinkler.

Keywords: near fault effect, loading history protocol of static test, beam-to-column connection, story drift angle

Introduction

Taiwan is situated in the Circum-Pacific seismic belt, and faults in the country are spread across the eastern and western plains. Approximately one-third of Taiwan's population lives within ten kilometers of a fault. Therefore, the near-fault effect of buildings is an issue that needs to be addressed urgently in domestic seismic engineering research. In the past, due to a lack of geological survey data in Taiwan, the location and distribution of faults were unclear. This resulted in the design of buildings that did not account for the characteristics of near-fault effects. In 2005 and 2011, the Construction and Planning Agency, Ministry of the Interior (CPAMI) promulgated a code entitled "Building Seismic Design Specifications and Commentaries". This code specifically formulated provision for the consideration of near-fault effects for the first type of active faults identified by the Central Geological Survey in 2000 and 2010. This provision prescribed the acceleration method for sites affected by the fault to enhance the design of the seismic force requirements of buildings.

The main purpose of the moment resisting frame (MRF) structural system is to improve the ductile capacity of the system through the inelastic deformation of the beam-end flexural plastic hinge. Therefore, it is necessary to ensure that the beam-to-column connection of the MRF can provide the necessary deformation. Previously, when the engineering industry in Taiwan used test methods to evaluate the performance of the steel beam-to-column connections, the loading history recommended in the 2002 edition of the American Institute of Steel Construction design specification (AISC 341) was generally used to carry out the testing (AISC, 2002). This continued until the 2016 edition was published (AISC, 2016), after which the loading history was of the far-field type, as shown in Figure 1. The loading

[1] Research Assistant Fellow, National Center for Research on Earthquake Engineering

[2] Research Fellow, National Center for Research on Earthquake Engineering

[3] Master, Department of Civil Engineering, National Chiao Tung University

[4] Associate Professor, Department of Civil Engineering, National Chiao Tung University

history encompasses a gradually increasing story drift angle without residual displacement. However, the deformation requirement for the beam-to-column connection of the structure is likely to depend on the seismic hazard of the location of the structure. As surface vibrations of near-fault earthquakes have high velocities and large relative displacements, the loading history near faults is likely to differ from the far-field type. The specific loading history of near-faults should therefore be related to the seismic design response spectrum of the local site.

In 2000, Krawinkler proposed a loading history with far-field effects for steel beam-to-column connection tests (see Figure 1). He also proposed a loading history that is suitable for near-fault effects (Krawinkler, 2000), as shown in Figure 2. However, Krawinkler does not describe the design seismic force requirements.

An inelastic dynamic history analysis of structures was herein carried out in accordance with ASCE 7-16. The results are used to adjust the acceleration record according to the basic vibration period of the structure and the target design acceleration spectrum. The adjustment method could adopt the acceleration spectrum matching method and amplitude scaling method. This was done in accordance with ASCE 7-16 of the American Society of Civil Engineers (ASCE), which stipulates that at least eleven sets of acceleration records are required for nonlinear dynamic analysis (ASCE, 2016).

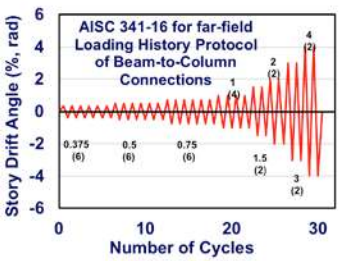

Fig. 1. Steel beam-to-column connection loading history with the far-field loading history of AISC 341-16.

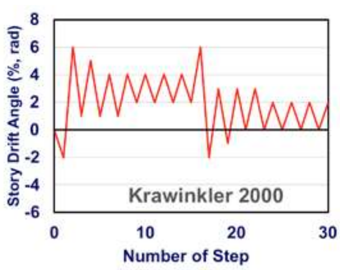

Fig. 2. Steel beam-to-column connection loading history with the near-fault effect of Krawinkler (2000).

The purpose of this study is to establish a loading history for steel beam-to-column connection tests that meets the current seismic force design requirements in Taiwan and that considers near-fault effects. Near-fault earthquake records with a nonlinear dynamic history analysis of structures have pulse velocities greater than 300 mm/s.

Establishing the Loading History of Beam-to-Column Connection with Near-Fault Effects

The structural model analyzed in this study is a 15-story steel structural MRF building. The height of the first floor is 5.1 m and the remaining floors are 3.4 m high, giving a total height building of 52.7 m. The site is assumed to be in the Hualien area, with maximum near-fault effects considered. According to the provisions of ASCE 7 on the adjustment of acceleration records, when structural modelling involves nonlinear dynamic history analysis, it is necessary to establish first an acceleration target response spectrum that conforms to the structure's site. The magnitudes of earthquakes considered include a design earthquake with a 10% exceedance probability (return period, RP: 475 yr) and a maximum consideration earthquake with a 2% exceedance probability (RP: 2500 yr) during the 50-year lifespan.

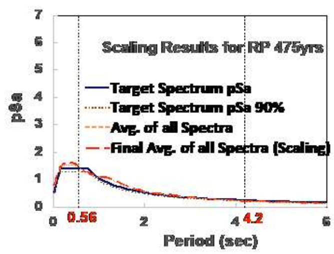

Fig. 3. Target spectrum of the 475 yr RP and the adjusted response spectrum of each record.

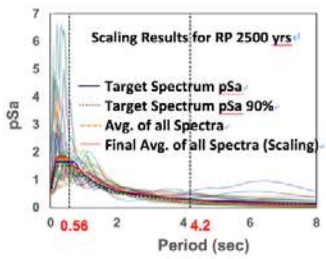

Fig. 4. Target spectrum of the 2500 yr RP and the adjusted response spectrum of each record.

As the number of recorded earthquakes in Taiwan exceeding a magnitude of 6.5 is limited, near-fault records from the PEER strong earthquake database (PEER, 2011) were used and acceleration history orthogonal to the fault direction was selected to obtain a more objective test loading history. Earthquake records were taken from thirty-four stations and the scaling method was used to adjust the acceleration history record. The target spectrum and the adjusted response spectrum of each record for a 475 yr and 2500 yr RP are plotted in Figure 3 and 4, respectively.

The structural nonlinear behavior analysis software PISA3D (Tsai et.al, 2011), developed by the NCREE, was used for the nonlinear dynamic history analysis. The main result of interest in the nonlinear history analysis is the floor drift angle. The floor in which the maximum drift angle occurred during the earthquake history was selected in the analysis, and that floor drift angle history was used as the basis for establishing the test loading history distribution of the steel beam-to-column connections. The following steps were performed to establish the loading history:

1. To reduce redundant data of the inter-story drift angle history, the rainflow method (Amzallag, et.al, 1994) was used to delete redundant data points and capture the peak value. The horizontal time axis was converted into the step axis to obtain a peak distribution graph, as shown in Figure 5.

2. The near-fault earthquake has mainly pulse characteristics, so the maximum pulse drift angle ($\delta\theta_{max}$) caused by the pulse characteristics is an important characteristic of the test loading history of the near-fault. Hence, $\delta\theta_{max}$ is turned to a positive direction to facilitate the arrangement and calculation of the inter-story drift angle distribution of each group in the subsequent steps.

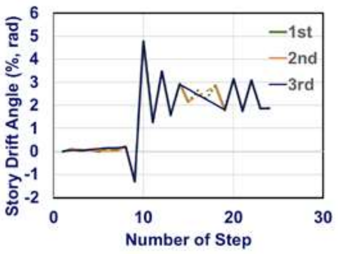

Fig. 5. Rainflow method program diagram.

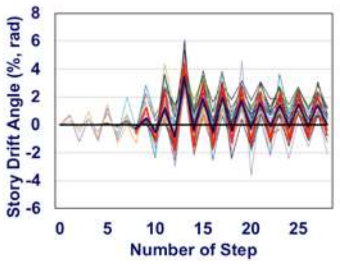

Fig. 6. Inter-story drift angle distributions were aligned with the maximum pulse for each group.

3. All inter-story drift angle distributions were aligned with $\delta\theta_{max}$ (Figure 6). The peaks before $\delta\theta_{max}$ are not distributed in each group. To obtain a more representative test loading history, the peak values that do not reach 80% of the data points were deleted. The cumulative inter-story drift angle ($\Sigma\delta\theta_i$) and its average value ($(\Sigma\delta\theta_i)_{avg}$) were calculated for each group of drift angle distributions as the basis for determining the length of the inter-story drift angle distribution in Step 5.

4. To ensure that the established test loading history of the beam-to-column connection has a sufficient safety margin, the average value ($\delta\theta_{avg}$) of the peak value of all drift angle distribution plus one standard deviation value (σ) was determined and plotted in Figure 7.

5. To conform to the actual distribution of the inter-story drift, the length of the loading history with the near-fault effect of the beam-to-column connection test was determined by the average value $(\Sigma\delta\theta_i)_{avg}$ of the distribution of the inter-story drift. This is as shown by the solid line in Figure 7, where a residual drift angle (θ_{res}) of + 0.5% rad is observed.

6. To ensure that the specimen of this history still has a sufficient safety margin in the negative direction, *X*-axis mirroring is used for reverse loading. Figure 8 (a) and (b) show the near-fault loading history of the beam-to-column connection test corresponding to the 475 yr RP and 2500 yr RP, respectively.

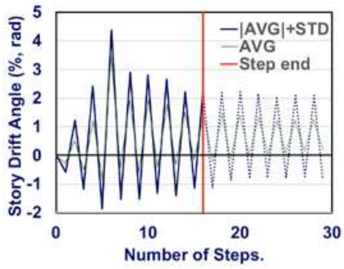

Fig. 7. The average and standard deviation of the inter-story drift angle distribution.

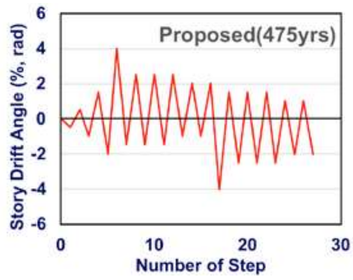

(a) 475 year RP.

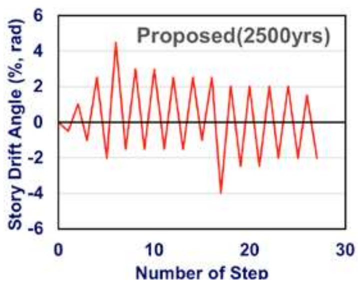

(b) 2500 year RP.

Fig. 8. Static test loading history of the proposed beam-to-column connection.

Analysis of Results

The present study proposes a procedure for estimating beam-to-column connections (or substructures) using a static test loading history that considers near-fault effects and is based on the 475 yr RP and 2500 yr RP target acceleration response spectra. The procedure is in accordance with the Taiwan building seismic design code for steel buildings, and the results are shown in Figure 8. In the present study, the cumulative inter-story drift angle $\Sigma\delta\theta_i$ and cumulative plastic inter-story drift angle $\Sigma\delta\theta_{pi}$ are used as evaluation indicators. These parameters can be compared with values suggested by Krawinkler (2000) for a near-fault static test displacement history reaching 4% rad and the AISC 341-16 (2016) static test displacement history for far-field earthquakes reaching 4% rad. The comparison of the cumulative inter-story drift angles and cumulative plastic inter-story drift angles for the four histories is shown in Figure 9. The results of this comparison can be summarized as follows:

1. The cumulative inter-story drift angle $\Sigma\delta\theta_i$ of Krawinkler is approximately the same as the proposed near-fault beam-to-column connection static test loading history of a 475 yr RP and 2500 yr RP, and both are approximately 70-80% of the AISC 341-16 far field history reaching 4% rad.

2. The cumulative plastic inter-story drift angle $\Sigma\delta\theta_{pi}$ of the proposed history of a 475 yr RP and Krawinkler is approximately 90% of the AISC 341-16 far-field history reaching 4%. However, the proposed history of a 2500 yr RP is 13% larger than the AISC 341-16 far-field history reaching 4% rad.

3. For the near-fault beam-to-column connection static test loading history, the index of $\Sigma\delta\theta_i$ and $\Sigma\delta\theta_{pi}$ of the proposed 475 yr RP history is almost the same as that found by Krawinkler. Both should belong to the same level history; $\Sigma\delta\theta_i$ and $\Sigma\delta\theta_{pi}$ of the proposed 2500 yr RP history are 17% and 24% larger than found by Krawinkler or the proposed 475 yr RP, respectively.

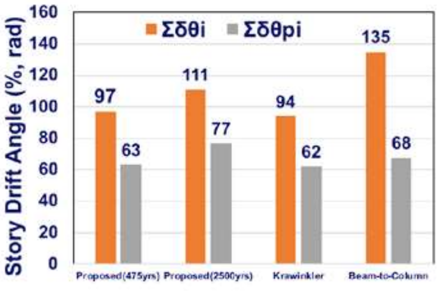

Fig. 9. Comparison of results suggested in this study, with those of Krawinkler (2000), and those obtained from AISC-341-16 (2016) reaching 4% rad.

Conclusions

The test load history recommended here is based on considerations of near-fault effects, and is estimated for return periods of 475 yr and 2500 yr. Evaluating $\Sigma\delta\theta_i$ and $\Sigma\delta\theta_{pi}$ indicates that both cases are stricter than that of Krawinkler (2000). The maximum difference of the inter-story drift angle due to a pulse is 6% and 6.5% rad, respectively, which is smaller than the 8% rad in Krawinkler yet still larger than the 4% rad obtained from the AISC 341-16 (2016) model. The results of this study shows that the four types of static test loading histories of the beam-to-column connections discussed can be evaluated by three indices: $\Sigma\delta\theta_i$, $\Sigma\delta\theta_{pi}$, and the maximum difference in inter-story drift angle caused by a pulse. As the results of the evaluated indices are different for the different models, it is recommended that full-size beam-to-column connection tests be conducted to confirm the applicability of these three indices to beam-to-column connection specimens.

References

AISC (2012), Seismic Provisions for Structural Steel Buildings (AISC 341-16), American Institute of Steel Construction, Chicago, IL.

AISC (2016), Seismic Provisions for Structural Steel Buildings (AISC 341-16), American Institute of Steel Construction, Chicago, IL.

ASCE (2016), Minimum Design Loads for Buildings and Other Structures (ASCE7-16), American Society of Civil Engineers, New York, Manual of Practice.

C. Amzallag, J.P. Gerey, J.L. Robert1 and J. Bahuaudl (1994), "Standardization of the Rainflow Counting Method for Fatigue Analysis", Volume 16, Issue 4, June 1994, Pages 287-293.

Krawinkler, H., Akshay, G., Medina, R. and Luco, M. (2000), "Development of loading histories for testing of steel beam-to-column assemblies", Rep. prepared for SAC Steel Project, Dept. for Civil and Environmental Engineering, Stanford University.

Tsai, K. C., Lin, B. Z., Chuang, M. C., and Yu, Y. J. (2011), Platform of Inelastic Structural Analysis for 3D Systems, PISA3D Standard Edition R3.2 User's Manual, National Center for Research on Earthquake Engineering, Taiwan Department of Civil Engineering, National Taiwan University.

PEER (Pacific Earthquake Engineering Research Center) (2011), PEER ground motion database. University of California, Berkeley, CA. <http://ngawest2.berkeley.edu/> (June 1, 2011).

Bond Slip Behavior of Beam Main Bars within the Reinforced Concrete of Interior Beam–Column Joints

Kai-Ning Chi[1], Ker-Chun Lin[2] and Zhi-Kuo Liu[3]

紀凱甯 [1]、林克強 [2]、劉志國 [3]

Abstract

The use of high-strength reinforced steel bars in the construction of high-rise buildings reduces the amount of steel bars required and mitigates poor construction quality caused by congested reinforcement configurations. However, in the absence of structural test verifications using bars of grade SD 550W or higher, most current seismic design provisions in concrete structure design codes stipulate that steel bars be limited to grade SD 420W. In a revision of the American Concrete Institute building code requirements (ACI 318-19), a yield strength of 550 MPa is permitted for reinforcement bars in special moment resistant frame systems. In addition, in prescribing dimensions of column members in beam–column joints, the revised code specifies that the development length of the beam reinforcement through the joint is proportional to the yield strength. This means that the minimum depth of column members should not be less than 20 or 26 times the diameter of beam bars of grade SD 420W or SD 550W, respectively. However, this provision does not consider the contribution of concrete strength, which is inconsistent with the design concept of the bond between the reinforcement bar and the concrete. To address this problem, a series of full-scale reinforced concrete (RC) internal beam–column joint seismic tests were conducted to clarify the bond performance of beam reinforcement through joints. Based on the beam–column joint seismic performance, an equation is proposed for the minimum dimensions of column members.

Keywords: high-strength reinforced steel bars, beam-column joint, development length, minimum dimensions of column members.

Introduction

For urban areas with concentrated populations, residential land is gradually lacking, and as such, high-rise residential buildings in cities are gradually becoming more common. The use of high-strength reinforced steel bars in the construction of high-rise buildings reduces the amount of steel bars required as well as mitigating against poor construction quality caused by congested reinforcement configurations. However, in the absence of structural testing for verification using bars of a grade higher than SD 420W, the seismic design provisions in ACI 318-14 (ACI, 2014) stipulate that steel bars be limited to grade SD 420W, and the domestic concrete structure design code (Ministry of the Interior Construction Agency, 2017) stipulates that the upper yield strength limit of longitudinal reinforcement for precast reinforced concrete (RC) members be increased to 490 MPa by relevant research and testing.

Since 2009, the reinforcement specifications of Grade 80 (f_y = 550 MPa) has been included in ASTM A706 (ASTM, 2009), and Grade 100 (f_y = 690 MPa) has been added to ASTM A615 (ASTM, 2015) in 2015. Based on the revision of the American reinforcement standard, the domestic standard, "CNS 560-Steel bars for concrete reinforcement," was revised in 2018 (CNS, 2018), and the SD 550W and SD 690 grades, which are seismic steel bars, were added to CNS 560. Furthermore, in a revision of the American Concrete Institute building code requirements (ACI 318-19), a yield strength of 550 MPa and 690 MPa are permitted for reinforcement bars in special moment resistant frame systems and structural wall systems, respectively. This means that the SD 550W steel bars

[1] Assistant Researcher, National Center for Research on Earthquake Engineering
[2] Research Fellow, National Center for Research on Earthquake Engineering
[3] Master Student, National Taiwan University of Science and Technology

have been included in the seismic design specifications. However, for the revision of the straight bond of the beam reinforcement through the joint, the development length of the steel bar (the depth of the column member) should be increased with the increase in the yield strength; however, this does not consider the contribution of the concrete strength.

Based on the few studies on the bond performance of high-strength beam reinforcement (f_y ≥ 550 MPa) through beam–column joints, this study will focus on the correlation between the bond performance of beam bars through internal joints and the depth of the column members. Six sets of full-size RC internal beam–column joint seismic experiments are conducted. From the results, a model is proposed for the development length of beam reinforcement through the beam–column joint.

Literature Review

Previously, the research team conducted fourteen sets of cyclic tensile loading tests on fourteen sets of reinforced concrete beams with deformed bars (Bo-Chou Liao, 2017) to simulate the bond performance of the beam bars through the RC beam–column joint. In addition to discussing the influence of many design parameters on the bond performance, the relevant design requirements and recommended formulas were also summarized. Finally, a recommended model considering axial loads for the ultimate bonding strength of the beam bars was proposed, as shown in Equation (1):

$$u_{ultimate} = 1.08\alpha_p\sqrt{f_c^{'}}$$
$$\alpha_p = 1 + 0.8\frac{N}{A_g f_c^{'}} \tag{1}$$

where $u_{ultimate}$ is the ultimate bonding strength (MPa), α_p is the axial load factor, $f_c^{'}$ is the compressive stress (MPa), N is the axial load (N), and A_g is the cross section of the member (mm^2).

Experimental Plan

In the present study, six groups of beam–column joints were tested for seismic performance. The parameters of the joints were #8 (D25) and #10 (D32) for the diameter of the beam bars, SD 420W and SD 550W for bar grades, and 42 and 70 MPa for the strength of the concrete. The design of the column depth is based on ACI 318-19 and the results of previous research on the cyclic bond performance of bars, with values of $20d_b$, $26d_b$, and $34d_b$ used here. Table 1 presents details of the design parameters for the joint specimens.

Table 1. Design parameters of the specimens.

Spec.	f_y (MPa)	$f_c^{'}$ (MPa)	Beam Bars		Column (b×h) (mm)	Column Depth (d_b)	V_{ju}/V_{jn}	$\Sigma M_{nc}/\Sigma M_{nb}$
			Top	Bot.				
JI1	420	42	2-D32	2-D32	650×650	20	0.698	1.94
JI2			2-D25	2-D25				2.14
JI3	550		4-D25	4-D25		26	0.716	2.22
JI4	420		3-D32	3-D32	500×850		0.641	2.91
JI5	550		4-D25	4-D25		34	0.697	3.18
JI6		70			650×650	26	0.539	2.42

Note: f_y is the yielding stress of the beam bars (MPa), $f_c^{'}$ is the compressive stress of the concrete (MPa), b represents the effective width of the shear resistance of the joint (mm), h is the depth of the column in the shearing direction in the joint (mm), d_b is the bar diameter, V_{ju} is the shear demand in the joint, V_{jn} is the shear capacity in the joint, and $\Sigma M_{nc}/\Sigma M_{nb}$ is the flexural strength ratio of the column and the beam.

For a moment-resisting frame system under the action of a horizontal force, the inflection point of the story usually occurs at the midpoint of the beam span and the column height. Therefore, the cross joint between the middle point of the beam and the column members in the frame is generally taken as the specimen. Figure 1 shows the configurations of the beam–column joint testing device. The axial force on the column that increases the shear strength of the joints is set to $0.075A_g f_c^{'}$ (A_g is the cross section of column). A hydraulic jack is connected to the end of each beam to apply a gradually increasing and reversing cyclic vertical load to simulate a seismic force induced by an earthquake. The displacement of the beam ends is calculated by multiplying the drift ratio of the structure by the distance from the center of the column to the beam end, as shown in Figure 2. The drift ratio at each peak is applied three times.

Fig. 1 Test setup.

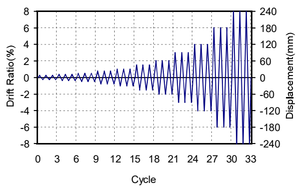

Fig. 2 Loading protocol.

Results and Discussion

Figure 3 presents the relationship between the bending moment and the drift ratio of the beam for each specimen. Comparing results for specimens JI1, JI2, and JI4 (which have SD 420W beam bars), it is evident that JI4 has improved strength and deformation over its hysteresis than JI1 and JI2. Furthermore, the unloading stiffness (which is defined in the second and fourth quadrants) of JI4 is larger than that of JI1 and JI2 at the drift ratio of 4% radian. A comparison of the results for specimens JI3, JI5, and JI6 (which have SD 550W beam bars, Table 1), indicates that JI5 and JI6 also have better hysteresis behavior in strength and deformation than JI3, and the unloading stiffness for JI5 and JI6 are higher than that of JI3. In summary, it has been shown that an increase of column depth and concrete strength can effectively improve the seismic performance of the joint. In addition, this increase can enhance the unloading stiffness in the second and fourth quadrants, and delay the occurrence of bond slips for beam bars in joint areas.

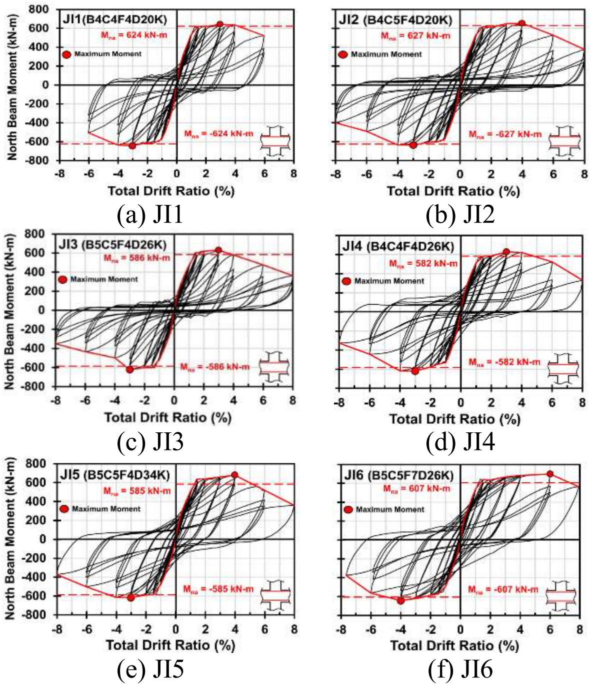

Fig. 3 Relations between the moment and the story drift of beam members.

The failure modes (defined as bond failures or plastic hinge failures) of the specimens are shown in Figure 4. For specimens with SD 420W beam bars, those with a joint depth of $20d_b$ (JI1 and JI2) have spalling and are crushed at the beam–column interface; however, there are no significant plastic hinges in the beam members. By contrast, there is a significant plastic hinge area for specimen JI4 (with a joint depth of $26d_b$), and the failure mode is plastic hinge failure. The failure modes of specimens with SD 550W beam bars indicate that the bond failure of specimen JI3 (with a joint depth of $26d_b$) is the same as for specimens JI1 and JI2, and that plastic hinge failures in beam members of specimens JI5 ($f_c{}' = 42$ MPa and joint depths of $34d_b$) and JI6 ($f_c{}' = 70$ MPa and joint depths of $26d_b$) are the same as in specimen JI4.

Discussion on Bond Slips

Generally, the bond slip of beam bars in the beam–column joint can be evaluated by the stiffness around zero displacement in the overall force–displacement hysteresis loop. The index of the bond slip K_b, which is the secant stiffness between the positive and negative directions of 0.35% radians, is defined as the third circle at 4%. The difference in the bond performance of beam bars at the joint area can be determined by comparing the average bond stiffness ratio, R_{Kb}, which is the ratio of the K_b between specimens.

Figure 5 shows that the average bond stiffness ratios (R_{Kb}) of JI1 and JI4, which have SD 420W beam bars, are 0.94 and 0.48 at 3% and 4% drift ratios, respectively. This demonstrates that the bond slip resistance for JI4 is greater than for JI1.

Figure 6 shows that the average bond stiffness ratios (R_{Kb}) of JI3 and JI5, which have SD 550W beam bars, are 0.12 and 0.16 at 3% and 4% drift ratios, respectively. Figure 7 shows that the average bond stiffness ratios (R_{Kb}) of JI3 and JI6, which have SD 550W beam bars, are 0.11 and 0.13 at 3% and 4% drift ratios, respectively. Based on the analysis results, the resistance of bond slips for JI5 and JI6 are greater than for JI3, and the resistance of JI6 is greater than for JI5.

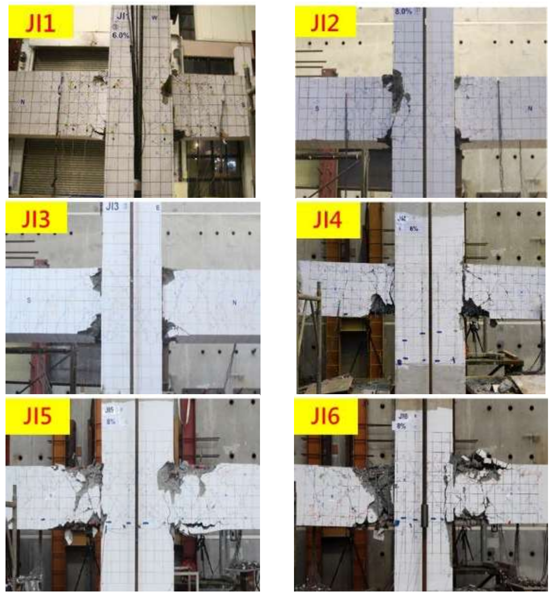

Fig. 4 Failure modes of the test specimens.

Proposed Model for the Minimum Dimensions of Column Members

The previous study (Bo-Chou Liao, 2017) proposed a model for the ultimate bond strength of beam bars under cyclic tensile loading in the beam–column joint. The recommended model for the minimum dimensions of column members is shown in Equation (2), with parameters including the ultimate bonding strength $u_{ultimate}$, the factor of axial loads α_p, the compressive stress of the concrete $f_c{}'$, the coefficient of reinforcement tensile development strength α_o, and compression development strength β.

$$\alpha_p = 1 + 0.8\frac{N}{A_g f_c'}, \quad u_{ultimate} = 1.08\alpha_p\sqrt{f_c'}$$
$$h_c \geq \left(\alpha_o + \beta\right) A_s f_y \Big/ u_{ultimate}\pi d_b \tag{2}$$

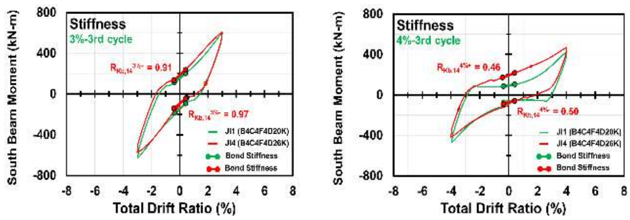

(a) Drift ratio: 3% (b) Drift ratio: 4%

Fig. 5 Comparisons of bond stiffness for JI1 and JI4.

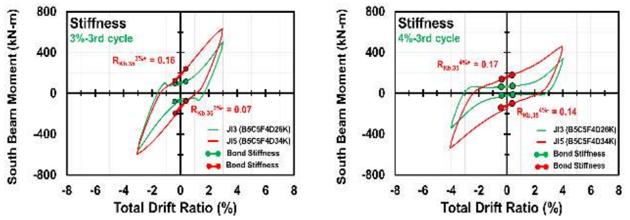

(a) Drift ratio: 3% (b) Drift ratio: 4%

Fig. 6 Comparisons of bond stiffness for JI3 and JI5.

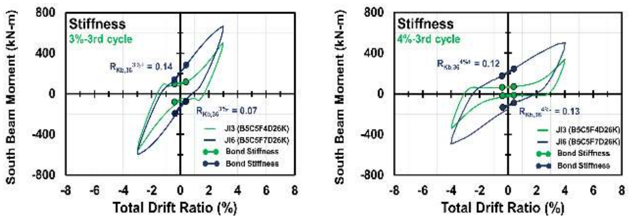

(a) Drift ratio: 3% (b) Drift ratio: 4%

Fig. 7 Comparisons of bond stiffness for JI3 and JI6.

Conclusions

For the beam bars of JI1 and JI2 with SD 420W and JI3 with SD 550W under the design concrete strength of 42 MPa and column depths of $20d_b$ and 26 d_b recommended by ACI 318-19, the bond slips of the beam bars occur when the story drift reaches 2% to 3% radians. However, the bond slips of beam bars for JI4, JI5, and JI6, which increase the depth of column member or concrete strength in the joint, can be effectively delayed to 4% radians, so that the beam members can fully develop their plastic hinge strength. This study also proposed a formulation for the minimum column depth under cyclic tensile loading of the beam reinforcement in the beam–column joint.

References

ACI Committee 318, 2014, "Building Code Requirements for Structural Concrete (ACI 318-14) and Commentary (ACI 318R-14)," American Concrete Institute (ACI), Farmington Hills, Mich.

Construction and Planning Agency Ministry of the Interior (CPAMI), 2017, "Design Specifications for Concrete Structures," Taiwan. (in Chinese)

American Society for Testing and Materials (ASTM), 2009, Standard Specification for Deformed and Plain Carbon-Steel Bars for Concrete Reinforcement, ASTM A706/A706M, ASTM International, West Conshohocken, Pennsylvania.

American Society for Testing and Materials (ASTM), 2015, Standard Specification for Low-Alloy Steel Deformed and Plain Bars for Concrete Reinforcement, ASTM A615/A615M, ASTM International, West Conshohocken, Pennsylvania.

National Standards of the Republic of China (CNS), 2018, "Steel Bars for Concrete Reinforcement," CNS 560, Bureau of Standards, Metrology and Inspection (M.O.E.A), Taiwan.

ACI Committee 318, "Building Code Requirements for Structural Concrete (ACI 318-19) and Commentary (ACI 318R-19)," American Concrete Institute (ACI), Farmington Hills, Mich., 2019.

Bo-Chou Liao, 2017, "Study on Bond Behaviors of Reinforced Concrete under Cyclic Loading," Master Thesis, Department of Civil and Construction Engineering, National Taiwan University of Science and Technology. (in Chinese)

Investigation of Isolation Systems with Geometrically Nonlinear Damping for Seismic Protection of Sensitive Equipment

Chia-Ming Chang[1], Ting-Wei Hsu[2], Shieh-Kung Huang[3], and Kung-Chun Lu[3]

張家銘 [1]、許庭維 [2]、黃謝恭 [3]、盧恭君 [3]

Abstract

Earthquakes pose risks to sensitive equipment in a structure and may sometimes result in significant economic losses. A widely utilized technique to mitigate seismic responses involves the installation of an isolation system underneath such equipment; however, excessive displacements along isolation layers may occur during severe earthquakes. It is recommended that viscous dampers be included with the isolation layer. However, this combination is only designed for earthquakes of a certain magnitude and may not be effective for small or moderate earthquake events. In this study, an isolation system with geometrically nonlinear damping is developed to mitigate the seismic responses of important equipment. For example, this system provides a better reduction in acceleration responses during small to moderate earthquakes, while excessive displacement responses can be effectively reduced during severe earthquakes. To understand the dynamic behavior of this system, a series of investigations is carried out. Considering the dynamic characteristics, the control force surface is first generated in terms of displacement and velocity to determine the contributions of the geometric nonlinearity. Moreover, this isolation system is investigated under harmonic excitation to understand its generalized frequency-domain performance. The control effectiveness of the proposed isolation system is also evaluated under non-periodic excitations, such as earthquakes, and the results are compared with those of conventional isolation systems. The results show that seismic isolation with a geometrically nonlinear viscous damper can be effective and adaptive at all levels of earthquakes.

Keywords: cable vibration, semi-active control, stay-cable, MR damper

Introduction

Earthquakes not only imperil the structures of buildings but also pose risks to sensitive equipment inside the buildings, which can result in significant losses. A number of non-structural components are susceptible to seismic excitations, such as high-precision machines and storage vessels for fragile products in high-tech factories, sensitive medical equipment and medicine cabinets in hospitals, storage vessels for dangerous chemicals in laboratories, and fragile items in museums. If these non-structural components and equipment are damaged during an earthquake, the result will be significant economic losses and possible fatalities.

To protect sensitive equipment from the threats posed by earthquakes, one of the most effective and commonly utilized techniques is seismic isolation. Instead of fixing the equipment to the floor, it can instead be placed on a platform sitting on bearings or sliders [1], allowing for the isolation of vibrations from ground motion. These platforms successfully mitigate the effects of seismic excitation; nevertheless, excessive displacement responses might be induced during earthquakes, which may lead to collisions or

[1] Adjunct Associate Researcher, National Center for Research on Earthquake Engineering
[2] Undergraduate Student, National Taiwan University
[3] Associate Researcher, National Center for Research on Earthquake Engineering

further catastrophic failures.

To address this problem, viscous dampers are recommended to be placed along the isolation platform [2, 3]. However, the combination of seismic isolation with viscous dampers may introduce other problems. For example, the force of a typical viscous damper is velocity-dependent. Viscous dampers are manufactured at the level of design-basis earthquakes. Due to the nature of viscous dampers, they may induce excessive acceleration responses in small-to-moderate earthquake events [3], and the base isolation system will therefore be ineffective. Conversely, when severe earthquakes occur, the viscous damper may also fail to control the maximum displacement responses. Because the combination of seismic isolation with viscous dampers is insufficiently adaptive to different magnitudes of earthquakes, this isolation system may only be effective against design-basis earthquakes.

In this study, an improved isolation system with a geometrically nonlinear configuration of a viscous damper is proposed to enhance the control performance of these systems under different magnitudes of earthquakes. The system is assumed to be a single-degree-of-freedom (SDOF) system in which the platform and the protected equipment are regarded together as a rigid body. In this configuration, the viscous damper is placed perpendicularly to the direction of motion of the isolation platform at the equilibrium point. This proposed isolation system provides a better reduction in acceleration during small to moderate earthquakes, while excessive displacements may be effectively controlled during severe earthquakes, thereby demonstrating adaptivity.

Mathematical Model

The proposed base isolation system with geometrically nonlinear damping is shown in Fig. 1. The equipment and isolation platform are supported by single-curvature rolling bearings and are regarded as a rigid body with mass m. The viscous damper is perpendicularly installed at the equilibrium point and has a damping coefficient C_{d} and a pin-to-pin length L. In the diagram, u denotes the horizontal displacement relative to the ground, v denotes the vertical displacement due to the single-curvature bearings, and $\ddot{x}_{\mathrm{g}}$ denotes the base excitation. The equation of motion can be written as:

$$\ddot{u} + 2\zeta_{\mathrm{i}}\omega_{\mathrm{n}}\dot{u} + \omega_{\mathrm{n}}{}^2 u$$

$$+2\zeta_{\mathrm{d}}\omega_{\mathrm{n}} \cdot \mathrm{sgn}(\dot{u}) \left|\frac{\dot{u}u}{\sqrt{u^2+L^2}}\right|^{\alpha} \frac{|u|}{\sqrt{u^2+L^2}} = -\ddot{x}_{\mathrm{g}}, \qquad (1)$$

where u is the horizontal displacement along the isolation layer, the inherent natural frequency is $\omega_{\mathrm{n}} = \sqrt{\frac{K_{\mathrm{i}}}{m}}$, the inherent damping ratio is $\zeta_{\mathrm{i}} = \frac{C_{\mathrm{i}}}{2\sqrt{mK_{\mathrm{i}}}}$, and the damping ratio of the damper is $\zeta_{\mathrm{d}} = \frac{C_{\mathrm{d}}}{2\sqrt{mK_{\mathrm{i}}}}$. Note that Eq. (1) is normalized by the mass of the isolation platform.

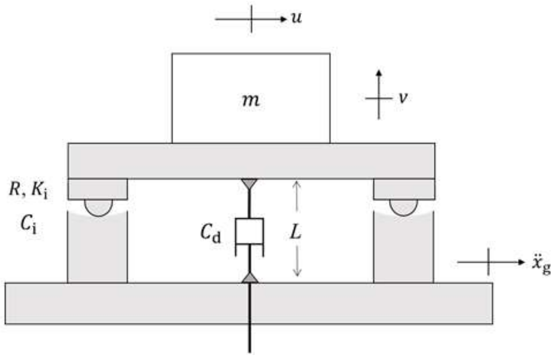

Fig. 1 Illustration of an isolation system with geometrically nonlinear damping.

Because this study focuses on geometric nonlinearity, $\alpha = 1.0$ is assumed in order to eliminate the nonlinearity of the viscous damper itself. Therefore, the effective control force normalized by the mass can be written as:

$$f_{\mathrm{ec}}(\dot{u}, u) = 2\zeta_{\mathrm{d}}\omega_{\mathrm{n}} \cdot \dot{u} \cdot \frac{u^2}{(u^2+L^2)^2}. \qquad (2)$$

Fig. 2(a) illustrates a plane with a constant slope in the $\dot{u}$ direction as the damping coefficient is normalized with the mass in a linear isolation system. In Fig. 2(b), the "valley" regions show that when the amplitude of u is within a certain range near $u = 0$, the geometric nonlinearity is significant. The amplitude of f_{ec} gradually decreases to zero as the amplitude of u decreases to zero. This range of u is defined as the range of geometric nonlinearity (GNL range). Conversely, when the amplitude of u is sufficiently larger than L, the effect of geometric nonlinearity vanishes. The f_{ec} converges to the case that this linearly viscous damper is parallel-installed. Therefore, the "plane" region of Fig. 2(b) actually coincides with the plane of Fig. 2(a) at a large amplitude of u.

(a) (b)

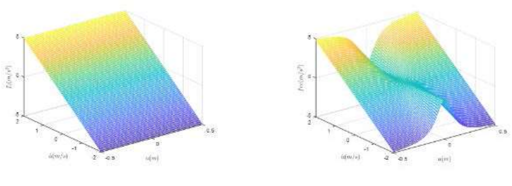

Fig. 2 (a) The control force (normalized to the mass) of a parallel-installed linearly viscous damper. (b) The effective control force index of a vertically installed linearly viscous damper. Both systems have $\omega_{\mathrm{n}} = 2\pi(0.2)$ rad/s, $\zeta_{\mathrm{d}} = 1$, and $\alpha = 1.0$, and the system with a vertically installed linearly viscous damper has $L = 0.1$ m.

Analysis of Dynamic Characteristics

The frequency content of the proposed system can identify the frequency band for adverse responses. For nonlinear systems, there is no explicitly and analytically defined frequency response function. Therefore, the averaging method can be applied to derive the frequency-amplitude relationship of the system [4].

Assume that the resulting displacement under harmonic excitation is formed by:

$$u(t) = U(t)\sin\theta(t), \tag{3}$$

where $\theta(t) = \Omega t + \phi(t)$. Then, the implicit equation for the frequency-amplitude relationship is given by:

$$\begin{gathered} 2\zeta_{\mathrm{i}}\omega_{\mathrm{n}}\Omega\, U\,\pi + A\sin\phi\,\pi \\ +8\zeta_{\mathrm{d}}\omega_{\mathrm{n}}\Omega^{\alpha}U^{2\alpha+1}G = 0, \end{gathered} \tag{4}$$

where:

$$G = \frac{\left(\left|L^2-\sqrt{L^2(L^2+U^2)}+U^2\right|\cdot\left|L^2-\sqrt{L^2(L^2+U^2)}\right|\right)^{\frac{\alpha+1}{2}}}{U^{2\alpha+1}[L^2(L^2+U^2)]^{\frac{\alpha+1}{4}}}.$$

The amplitude of the steady-state absolute acceleration is given by:

$$\ddot{\mathrm{X}}_{\mathrm{a}} = \sqrt{A^2 + \Omega^4U^2 - 2A\Omega^2U\cos\phi}. \tag{5}$$

Because U/A is known, the frequency-amplitude relationship for the normalized absolute acceleration $\ddot{\mathrm{X}}_{\mathrm{a}}/A$ can be obtained.

The frequency–amplitude relationships U/A and $\ddot{\mathrm{X}}_{\mathrm{a}}/A$ are shown in Fig. 3, in which the system parameters $\zeta_{\mathrm{i}} = 0.02$, $\omega_{\mathrm{n}} = 2\pi(0.2)$ rad/s, $\zeta_d = 1$, $\alpha = 1.0$, and $L = 0.1$ m are considered. Various frequency–amplitude relationships are observed under different levels of input excitation, such as $A = 0.05$ g, 0.3 g, and 1.0 g. In Fig. 3(a), U/A becomes smaller when A becomes larger, indicating that u responses are relatively smaller under larger input amplitudes. Nevertheless, Fig. 3(b) shows that $\ddot{\mathrm{X}}_{\mathrm{a}}/\mathrm{A}$ becomes larger as A becomes smaller at resonance and low frequencies, while $\ddot{\mathrm{X}}_{\mathrm{a}}/\mathrm{A}$ becomes smaller as A becomes smaller at most of the other frequencies, implying that the $\ddot{\mathrm{x}}_{\mathrm{a}}$ responses are relatively smaller under smaller excitations. These observations align with the findings of the former sections; for example, the displacement-dependent C_{eq} demonstrates better displacement control authority under large excitations, while this C_{eq} better mitigates under small excitations. In addition, to compare the frequency–amplitude relationship with the frequency content of earthquakes, the averaged power spectral density of eighteen modified Meinong earthquake time histories is included in these plots.

(a) (b)

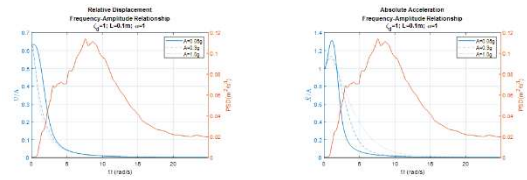

Fig. 3 (a) The frequency–amplitude relationship for the u response, U/A, and (b) the frequency–amplitude relationship for the $\ddot{x}_a$ response, $\ddot{\mathrm{X}}_{\mathrm{a}}/A$, under input amplitudes $A = 0.05$ g, 0.3 g, 1.0 g, and with system parameters $\zeta_{\mathrm{i}} = 0.02$, $\omega_{\mathrm{n}} = 2\pi(0.2)$ rad/s, $\zeta_d = 1$, $\alpha = 1.0$, and $L = 0.1$ m.

Time-Domain Performance Evaluation

To evaluate the performance of the system subjected to different levels of earthquakes, the maximum displacement response U and maximum acceleration response $\ddot{\mathrm{X}}_{\mathrm{a}}$ of the systems with $\zeta_{\mathrm{i}} = 0.02$, $\omega_{\mathrm{n}} = 2\pi(0.2)$ rad/s, and $\alpha = 1.0$ while considering different L and ζ_d against earthquakes with various peak ground accelerations (PGAs) are obtained. For comparison, U and $\ddot{\mathrm{X}}_{\mathrm{a}}$ are normalized by the corresponding PGAs, and the performance indices are denoted as U/PGA and $\ddot{\mathrm{X}}_{\mathrm{a}}/PGA$, respectively. The record of the Meinong earthquake obtained at the station CHY058 is modified to be compatible with the design spectrum and denoted as the CHY058-DBE record. This ground acceleration is scaled to different intensities with respect to PGA. Figs. 4 and 5 demonstrate the results of U/PGA and $\ddot{\mathrm{X}}_{\mathrm{a}}/PGA$. As shown in these figures, U/PGA decreases as PGA increases, while $\ddot{\mathrm{X}}_{\mathrm{a}}/PGA$ decreases as PGA decreases for the geometrically nonlinear isolation system. The results imply that the proposed system can generate smaller peak accelerations under small earthquake excitations, while smaller peak displacements are found under large earthquake excitations. Note that because the results are not proportional to the PGAs, the nonlinearity is quite significant, as shown in these figures.

(a) (b)

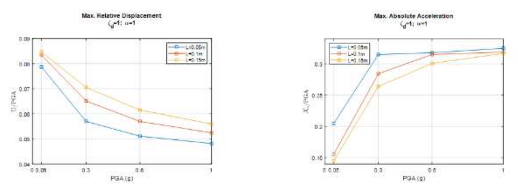

Fig. 4 The effect of L on (a) U/PGA and (b) $\ddot{\mathrm{X}}_{\mathrm{a}}/PGA$ under $PGA = 0.05$ g, 0.3 g, 0.6 g, 1.0 g with $\zeta_{\mathrm{i}} = 0.02$, $\omega_{\mathrm{n}} = 2\pi(0.2)$ rad/s, $\zeta_d = 1.0$, and $\alpha = 1.0$.

(a) (b)

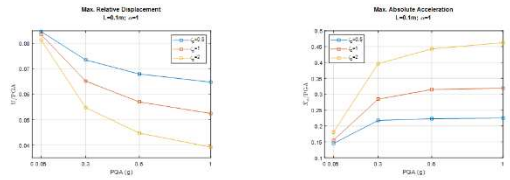

Fig. 5 The effect of ζ_d on (a) U/PGA and (b) $\ddot{X}_a/PGA$ under $PGA = 0.05$ g, 0.3 g, 0.6 g, 1.0 g with $\zeta_i = 0.02$, $\omega_n = 2\pi(0.2)$ rad/s, $\alpha = 1.0$, and $L = 0.1$ m.

The effects of L on U/PGA and $\ddot{X}_a/PGA$ under the CHY058-DBE seismic excitation with different PGAs are shown in Fig. 4. As observed in Fig. 4(a), a larger L results in larger isolation displacements under all PGAs; conversely, Fig. 4(b) shows that a larger L is beneficial for the mitigation of platform accelerations, especially under small PGAs. Similar effects of L on the responses are observed in the frequency–amplitude relationship analysis. The effects of ζ_d on U/PGA and $\ddot{X}_a/PGA$ under the CHY058-DBE excitation with different PGAs are shown in Fig. 5. As seen in Fig. 5(a), a larger ζ_d yields smaller isolation displacements; conversely, Fig. 5(b) shows that a larger ζ_d produces larger platform accelerations. In brief, the findings in this section are generally consistent with the observations of the frequency–amplitude relationship analysis.

It should be noted that the effects of ζ_d on U/PGA and $\ddot{X}_a/PGA$ are more significant under excitations with large PGAs, as seen in Fig. 5. The displacement-dependent C_{eq} accounts for such phenomena. As seen in Eq. (2), ζ_d determines the maximum value to which C_{eq} converges when the displacements are large outside of the GNL range, and the effects of ζ_d on C_{eq} increase as the displacements increase; conversely, ζ_d has minor effects on C_{eq} when the displacements are small. Therefore, the larger the PGAs of the excitations, the larger the responses, which result in more significant effects of ζ_d on U/PGA and $\ddot{X}_a/PGA$.

Conclusions

In this study, an improved isolation system with a geometrically nonlinear configuration of a viscous damper was proposed to enhance the seismic protection of equipment. The primary dynamic characteristics were also investigated and analyzed. As indicated by the results for the effective control force index, the geometric nonlinearity was significant in the defined GNL range, whose width was mainly determined by L. The geometric nonlinearity also vanished outside of the GNL range, and the effective control force index behaved similarly to the damping force (normalized to the mass) of a parallel-installed linearly viscous damper. The control force surface provided insights into the dynamic characteristics, and the instantaneous equivalent damping and stiffness indices were derived based on this surface. Because the effective control force index was a function of both displacement and velocity, the equivalent damping index had a displacement-dependent feature. The averaging method was applied to obtain the frequency–amplitude relationship of the geometrically nonlinear system, which provided a better understanding of the system in the frequency domain.

Simulations conducted using the Meinong earthquakes were carried out to verify the observations of the dynamic characteristics and the frequency–amplitude relationship, and the effects of the system parameters ζ_d and L were then investigated. Generally, the increase of ζ_d resulted in improved displacement control but worsened acceleration attenuation. The increase of L resulted in improved acceleration attenuation but worsened displacement control.

Finally, the important advantages of the geometrically nonlinear system for performance were verified. The results showed that the proposed system can better mitigate accelerations under small-to-moderate earthquakes, while the maximum displacements were effectively controlled under large earthquakes. Control adaptivity was provided by the proposed system to accommodate different magnitudes of seismic excitation, resulting in better control effectiveness compared to the conventional seismic isolation system. Moreover, this geometrically nonlinear system demonstrated an improved performance in counteracting transient inputs while effectively controlling the maximum displacement. The displacement-dependent equivalent damping index and the geometry of the control force index surface demonstrated the aforementioned advantages.

References

1. Wang, S.J., Hwang, J.S., Chang, K.C., Shiau, C.Y., Lin, W.C., Tsai, M.S., Hong, J.X. and Yang, Y.H. (2014). Sloped multi-roller isolation devices for seismic protection of equipment and facilities. Earthquake Engineering & Structural Dynamics, 43(10), 1443-1461.
2. Wolff, E. D., Ipek, C., Constantinou, M. C., & Tapan, M. (2015). Effect of viscous damping devices on the response of seismically isolated structures. Earthquake Engineering & Structural Dynamics, 44(2), 185-198.
3. Kelly, J. M. (1999). The role of damping in seismic isolation. Earthquake Engineering & Structural Dynamics, 28(1), 3-20.
4. Sun, J., Huang, X., Liu, X., Xiao, F., & Hua, H. (2013). Study on the force transmissibility of vibration isolators with geometric nonlinear damping. Nonlinear Dynamics, 74(4), 1103-1112.

Preliminary Study of the Damage Mechanisms of Hualien Harbor in the February 6, 2018 Hualien Earthquake

Yuan-Chang Deng[1] Chih-Chieh Lu[2] Jin-Hung Hwang[3]

鄧源昌 [1] 盧志杰 [2] 黃俊鴻 [3]

Abstract

After the Hualien earthquake on February 6, 2018, sand volcanoes of soil liquefaction and significant settlement were observed at gravel backfill backlands of Wharf 19–25 and the western breakwater, which significantly obstructed shipping work in Hualien Harbor. To better realize the liquefaction and settlement mechanisms of gravel backfill ground, a site with clear evidence of liquefaction and settlement was chosen at the backland of Wharf 25 for a series of tests, including a field test pit, standard penetration tests, shear wave velocity measurements, and laboratory tests. For comparison, a second site without obvious evidence of damage and close to Wharf 25 was selected for similar tests. Afterward, the testing results and seismic records for Hualien Harbor were collected to evaluate the liquefaction potential of the studied sites by using simplified methods based on the standard penetration test. Based on the field reconnaissance, testing results, analysis results, and existing completion drawings, the causes of the significant settlement of Wharf 25 are preliminarily deduced from the liquefaction at the shallow loose gravel and the densification effect of deeper reclaimed ripraps due to the strong ground vibration.

Keywords: 20180206 Hualien Earthquake, Hualien Harbor, liquefaction, gravel soil

Introduction

At 23:50:42.6 (UTC+8) on February 6, 2018, an Mw = 6.4 earthquake (according to the U.S. Geological Survey) occurred in offshore of Hualien County, Taiwan. The epicenter was at 24.1° North and 121.73° East, which is approximately 18.3 km from the Hualien County Government, and the focus of the earthquake was located 6.31 km beneath its epicenter. Peak ground accelerations (PGA) greater than 400 gal were observed at some locations, such as the Hualien weather station (HWA019). In the aftermath of the earthquake, the geotechnical division of the National Center for Research on Earthquake Engineering (NCREE) in Taiwan deployed a survey team for field reconnaissance. The evident seismic settlement induced by liquefaction in gravel backfill backlands of Hualien Harbor was found to be significant. The geotechnical damage including settlement, soil liquefaction, and road surface failure was mainly observed at the backlands of Wharf 19–25 and the western breakwater in the outer port area of Hualien Harbor. Among the damage zones, the junction area of the wharf and the backland of Wharf 25 were worse than neighboring areas. Serious cracks were observed, and the settlement at the backland was up to 50–60 cm (Hsu et al., 2018; Ko et al., 2018).

A site with clear evidence of liquefaction and settlement at the backland of Wharf 25 was chosen for a series of tests including a field test pit, standard penetration tests, shear wave velocity measurements, and laboratory tests. For comparison, a different site without obvious evidence of damage close to the liquefied site was selected to perform similar tests. Due to space limitations, the wave velocity measurement test results and related analysis will not be introduced here. Afterward, the testing results and seismic records of Hualien Harbor station were collected to evaluate the liquefaction potential of the studied sites using simplified methods based on the standard penetration test (SPT). Based on the field reconnaissance, testing results, analysis results, and existing completion drawings, the causes of the significant settlement at Wharf 25 after the Hualien earthquake are preliminarily clarified for future earthquake disaster mitigation policies of the the Hualien Harbor Port Authority.

Field Investigation Configuration

Based on the field reconnaissance at Hualien

[1] Project Assistant Researcher, National Center for Research on Earthquake Engineering
[2] Associate Researcher, National Center for Research on Earthquake Engineering
[3] Professor, Department of Civil Engineering, National Central University

Harbor after the February 6, 2018, Hualien earthquake, a site was chosen with evident liquefaction in the backland of Wharf 25 (hereinafter referred to as "Site L"), which had the most serious settlement compared with neighboring backlands, for a series of tests, including a field test pit, standard penetration tests, shear wave velocity measurements, and laboratory tests. For comparison, a site 35 m from Site L, which was not observed to have evidence of liquefaction (hereinafter referred to as "Site N") was selected to undergo similar tests. The field investigation configuration is shown in Fig. 1. Due to space limitations, the wave velocity measurement configuration will not be introduced in this article.

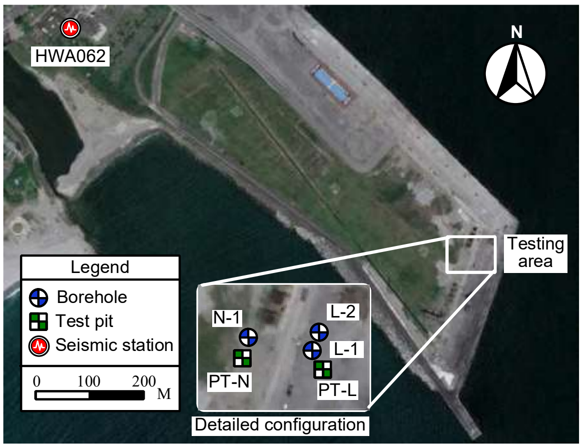

Fig 1. Field boreholes and pit configurations of the surface liquefaction (L) site and the control site (N).

The locations of the geotechnical borings and test pits are shown in Fig. 1. The two boreholes at Site L are denoted as L-1 and L-2, respectively, and the borehole at Site N is denoted as N-1. The drilling depths were approximately 24 m. Considering the restoration schedule for the port area, the boreholes in both areas were constructed by percussion drill. The test pit at Site L is denoted as PT-L, with a size of 2.5 in length and width and 2.2 m in height. The pit at Site N is denoted as PT-N, which is 2.5 m in width, height, and length. Field sieve analyses and field density tests were conducted in the pits. Based on the test results, the liquefaction mechanism of the Hualien Harbor in the Hualien earthquake is explored.

Field Investigation Result

The results from PT-L show that the deposits range from ground level GL = 0 to −2.2 m and are poorly graded gravel with silt and sand (GP-GM) and well-graded gravel with sand (GW). The maximum gravel particle size is 130, 80, and 50 cm in length, width, and height respectively. D_{50} ranges 6.07–10.45 mm, and the average D_{50} is 8.64 mm. D_{10} ranges 0.14–0.28 mm, with an average of 0.23 mm. The results from PT-N show that the deposits range from GL = 0 to −2.5 m and are silty gravel with sand (GM) and poorly graded sand with gravel (SP). The maximum gravel particle size is 24, 17, 9 cm, in length, width, and height, respectively. The yielded D_{50} ranges 2.75–4.05 mm, and the average D_{50} is 3.55 mm. D_{10} ranges 0.04–0.68 mm, with an average of 0.43 mm. The average and maximum grain size at Site L are larger than that at Site N. Less gravel is present at Site N than Site L. The wet unit weight of the gravel soil is 19.1–20.4 kN/m^3 at Site L and 18.1–25.0 kN/m^3 at Site N.

The design profile of Wharf 25 in Hualien Harbor (Chen et al., 2000) and the borehole logs of L-1 and N-1 are shown in Fig. 2. The SPT-N profiles of Sites L and N are shown in Fig. 3. The shallow deposits (GL = 0 to −7 m) at Sites L and N consist of an uneven distribution of backfill gravel with sand layers. The deposits (GL = −7 to −17.6 m) at Site L consist of backfill rubble, while the deposits at Site N consist of loose backfill gravel with sand layers. The deposits below 17.6 m at Site L and N are original strata. Due to particle sedimentation effects, the original ground at Site L, which is closer to the water, is alternations of sand and clay soil. In contrast, the original ground of Site N, which is farther from the edge of the water, is gravel soil.

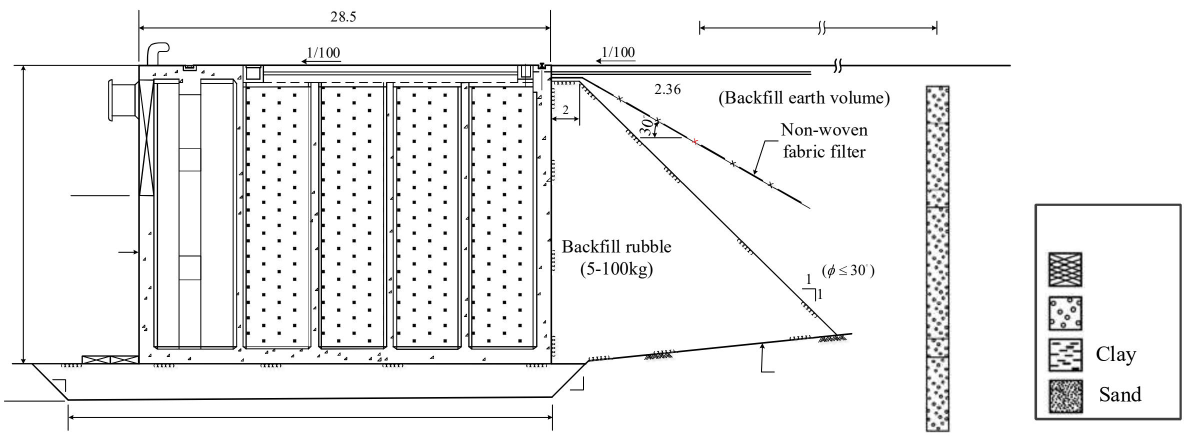

Fig. 2. Design profile of Wharf 25 in Hualien Harbor (Chen et al., 2000) and the boring logs.

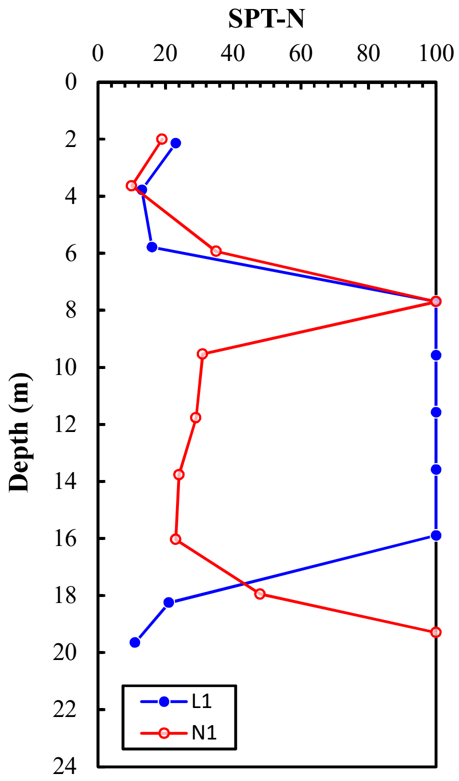

Fig 3. SPT-N profiles at Sites L and N.

Simplified Soil Liquefaction Evaluation

To discuss the soil liquefaction mechanism of the backland of Wharf 25 during the Hualien earthquake, the SPT-based NCEER method (Youd and Idriss, 1997), and HBF method (Hwang et al., 2012) were adopted to analyze soil liquefaction potential and to calculate the liquefaction potential index (LPI) proposed by Iwasaki et al. (1978), Iwasaki et al. (1982), and Iwasaki et al. (1984).

The geotechnical parameters of soil layers in liquefaction assessments are based on the results of geological investigations. The analysis of the groundwater tables was performed at 1 m below the ground surface according to the tidal level records of Wharf 25 in Hualien Harbor in the Hualien earthquake. The horizontal maximum surface acceleration of 0.21 g is based on the EW acceleration history at the HWA062 seismic station, as depicted in Fig. 4.

In the simplified soil liquefaction evaluation, soil with a factor of safety (FS) less than one is regarded as liquefied. The FS against soil liquefaction of Sites L and N as calculated by the SPT-N-based methods are shown in Fig. 5, and the LPI are shown in Table 1. From Fig. 5 and Table 1, the liquefaction potential of Site L is low as the FS at each depth as calculated by the NCEER and HBF methods is larger than one, and the corresponding LPIs are equal to zero. The minimum FS of Site L as calculated by the two methods occurs in loose gravel layers at GL = −3.78 m (NCEER FS: 1.22, HBF FS: 1.12). The overall FS profile analyzed by the NCEER method is similar to the one analyzed by the HBF method at Site L.

The minimum FS of Site N as calculated by the two methods occurs in loose gravel layers at GL = −3.64 m (NCEER FS: 0.95, HBF FS: 1.0). However, the liquefaction potential of Site N is low as the FS at the others depths as calculated by the NCEER and the HBF methods are larger than one, and the corresponding LPIs are therefore less than five. The overall FS profile analyzed by the NCEER method is similar to the one analyzed by the HBF method at Site N.

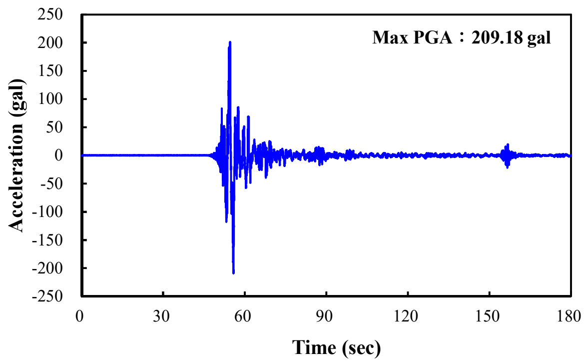

Fig. 4. Acceleration history in the East–West direction recorded at the HWA062 seismic station.

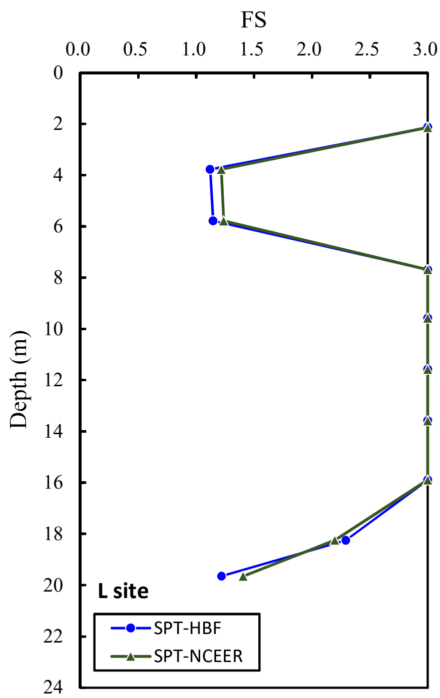

Fig. 5. Liquefaction potential at Site L from the SPT-N method.

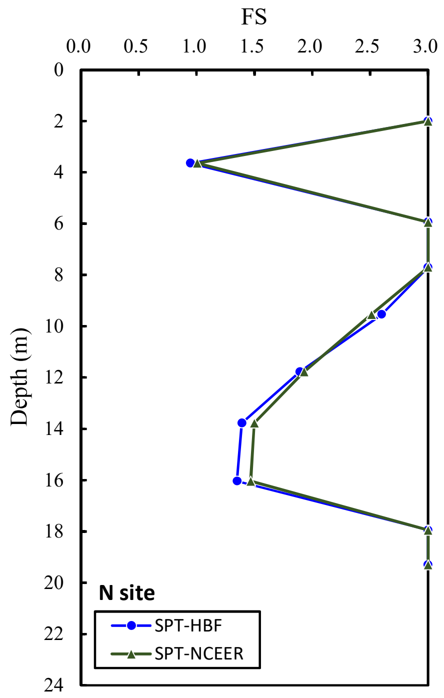

Fig. 6. Liquefaction potential at Site N from the SPT-N method.

Table 1. LPI evaluation results of the studied sites.

Site	SPT-based methods	
	NCEER	HBF
L	0	0
N	0	1.0

Based on the field investigation and analysis results, the liquefaction of shallow loose gravel layers would occur at Site N. The liquefaction issue may have seriously obstructed shipping work in Hualien Harbor.

Conclusions

The results of the post-disaster field reconnaissance infer that the seismic damage at Wharf 25 in Hualien Harbor from the Hualien earthquake was caused by soil liquefaction and post-earthquake densification. Moreover, the main liquefaction layers consist of loose backfill gravel within 5 m of the ground surface based on the supplementary geological investigation and analysis results. The shallow loose backfill gravel layers close to the concrete caisson may not be compacted effectively, especially the junction of the wharf and backline area.

.

References

Chen, S.H., Chen, C.C., Wang, C.C., Hu, T.M. (2000). Harbor engineering database – Hualien harbor, Institute of Transportation, Taiwan.

Hwang, J.H., Chen, C.H., and Jaung, C.H., “Calibrating the model uncertainty of the HBF simplified method for assessing liquefaction potential of soils”, Sino-Geotechnics, 133, 2012, pp.77-86. (in Chinese)

Hsu, S.Y., Yang. H.C., Lu, C.C., Hwang, Y.W., Liu, C.H., Ko. Y.Y., and Hwang, J.H., “The reconnaissance on seismic settlement of Hualien Harbor and soil liquefactions in the 0206 Hualien Earthquake”, Sino-Geotechnics, 156, 2018, pp. 65-76. (in Chinese)

Iwasaki, T., Arakawa, T., and Tokida, K., “Simplified procedures for assessing soil liquefaction during earthquakes”, In: Proceedings of the conference on soil dynamics and earthquake engineering, Southampton, 1982, pp. 925–939.

Iwasaki, T., Arakawa, T., and Tokida, K., “Simplified procedures for assessing soil liquefaction during earthquakes”, Int J Soil Dyn Earthq Eng, 3, 1984, pp. 49-58.

Iwasaki, T., Tatsuoka, F., Tokida, K., Yasuda, S. (1978). “A practical method for assessing soil liquefaction potential based on case studies at various sites in Japan,” Proceedings of the 2nd international conference on microzonation for safer construction—research and application, San Francisco, CA, 885–896

Ko. Y.Y., Hsu, S.Y., Yang. H.C., Lu, C.C., Hwang, Y.W., Liu, C.H., Hwang, J.H. (2018). “Soil liquefaction and ground Settlements in February 6, 2018 Hualien, Taiwan Earthquake,” Seismological Research Letters, 90(1), 51-59.

Youd, T.L. and Idriss, I.M., Proceedings of the NCEER workshop on evaluation of liquefaction resistance of soils, Technical Report NCEER-97-0022, 1997.

Preliminary Study of the Liquefaction Potential of Gravelly Soils using Shaking Table Tests

Kuan-Yu Chen[1], Chia-Han Chen[2], Hsuan-Chih Yang[2] and Jin-Hung Hwang[3]

陳冠羽 [1] 陳家漢 [2] 楊炫智 [2] 黃俊鴻 [3]

Abstract

In recent years, damages to ports filled with gravelly sandy soils due to earthquake-induced liquefaction have been observed and received considerable attention in geotechnical engineering. In order to study the liquefaction behavior and dynamic characteristics of sand–gravel composites, a series of 1 g shaking table tests are performed using a large-scale biaxial laminar shear box filled with gravelly sandy soils sampled from the Port of Hualien in Taiwan, as a case study for its failure during the Hualien earthquake on 6 February, 2018. Specimens are prepared using the wet pluviation technique in order to simulate the in-situ conditions of the sand–gravel composites in the wharf area. For input motions, the records of the Hualien earthquake with varying amplitudes are applied, as well as white noises and sinusoidal sweeps for further comparison. Instrument sensors including accelerometers, piezometers, and linear displacement transducers are used to record the accelerations, pore water pressure responses, and displacements of the soil specimen during the dynamic tests. According to the results, if the seismic loading is large enough the excess pore water pressure would be significantly increased and lead to the gravelly soils liquefy.

Keywords: gravelly soils, soil liquefaction, large-scale laminar shear box, shaking table tests

Introduction

Earthquake-induced liquefaction occurring at ports with gravelly sandy fills is often accompanied by severe damage, such as CentrePort in Wellington, New Zealand, during the 2016 Kaikoura earthquake and Port Island in Hyogo-Ken Prefecture, Japan, during the 1995 Nanbu earthquake. In 2018, an earthquake occurred in Hualien, Taiwan, resulting in severe damage to the Port of Hualien. There were significant ground settlements and considerable surface cracks induced in the backland of several gravity-type wharves. These were accompanied by the eruption of a mixture of sands and gravels from some surface cracks. These effects have been surveyed in the field and have been extensively discussed in the literature.

Some studies have been conducted using cyclic triaxial tests to investigate the liquefaction potential and dynamic properties of sand–gravel composites. However, large-scale experiments with durations similar to real earthquakes to investigate the responses of gravelly sandy soils have not yet been carried out. Therefore, in this study, a large-scale biaxial laminar shear box filled with approximately 10 tons of gravelly sandy soil samples from wharf No.25 of the Port of Hualien was used to perform a series of 1 g shaking table tests. The liquefaction behavior and dynamic characteristics of these sand–gravel composites were investigated. Finally, the test results are demonstrated and discussed.

Experiment Design

In order to simulate the site conditions of the aforementioned wharf area, the gravel samples were used to construct the specimen. Because of the size of the shear box and other limitations of the laboratory testing equipment, the gravel was sieved to remove particles exceeding 19 mm (¾ inch) in diameter. Sieve analysis was performed and the resulting grain-size distribution curves of the tested materials are shown in Fig. 1. The proportions of different particle sizes of the specimens were gravel content 41%, sand content 55%, and fine content 4%. Other basic properties of the specimens are given in Table 1. For shaking table tests, each soil specimen was 1.88 m (L) × 1.88 m (W) × 1.20 m (H) and placed in a laminar box developed at

[1] Assistant Research Fellow, National Center for Research on Earthquake Engineering
[2] Associate Research Fellow, National Center for Research on Earthquake Engineering
[3] Professor, Department of Civil Engineering, National Central University

the National Center for Research on Earthquake Engineering (NCREE) in Taiwan. To simulate the conditions of gravel fill in a harbor area, the wet pluviation method was applied to the specimens. Before the dynamic event, the specimens had a relative density of $D_r = 37\%$.

The apparatus is fitted with three types of sensors: precision accelerometers, piezometers, and linear displacement transducers (LDT). Accelerometers and piezometers were installed at different depths and positions inside the specimen and these were used to measure the horizontal accelerations and pore water pressure response of the soil during the dynamic test. In addition, the LDTs and accelerometers were installed at individual layers on the frames of the laminar box to measure the horizontal displacement of the frames, surface settlement of the specimen, and the acceleration response during lateral movements of the soil. These observations were used to estimate the average shear strain of the soil layers during the test. The movement mechanism of the biaxial laminar box is shown in Fig. 2(a). A schematic illustration of the apparatus sensors is shown in Fig. 2(b). Fig. 3 shows the soil specimen in the laminar box on the shaking table.

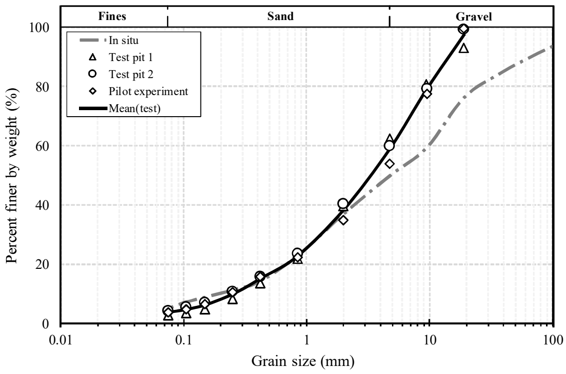

Fig. 1. Grain-size distribution curves for tested materials.

Table 1. Physical properties of sand–gravel composites.

D_{max} (mm)	19.0
D_{50} (mm)	3.58
C_u	19.48
$G_{s,avg}$	2.70
e_{min}	0.14
e_{max}	0.50

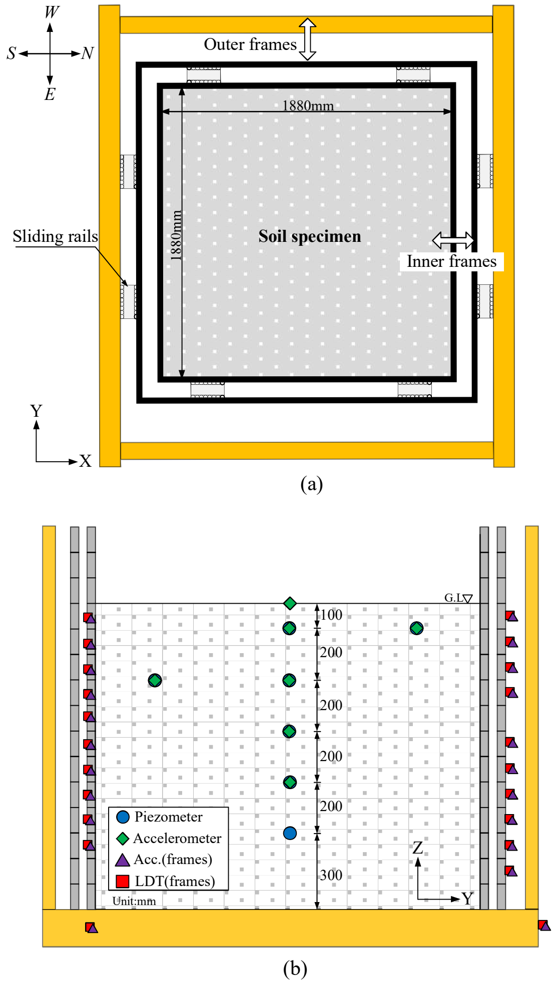

Fig. 2. Schematic illustration of the biaxial laminar shear box: (a) plan view of the movement mechanism of the laminar box and (b) cross-section of the positions of the sensing apparatus.

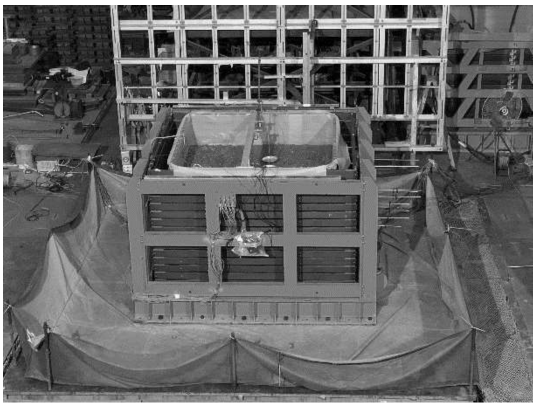

Fig. 3. Gravelly soil specimen in the laminar box on the shaking table.

The input motions were applied to the shear box in the Y-direction through the shaking table to simulate the motion of soil layers subjected to seismic loading. The historical earthquake records of the 2018 Hualien earthquake were used. Records from station HWA062 in the east–west direction (Y-direction in Fig. 2(a)) were adopted as input motions because that station is close to the Port of Hualien. The maximum acceleration amplitudes of the input motions were 0.1, 0.2, and 0.4 g. Input motions represented by white noise and a sinusoidal sweep were also applied to identify the dominant frequency and dynamic properties of the soil. The acceleration amplitude and bandwidth of the white noise were respectively 0.02 g and 50 Hz, and for the sinusoidal sweep they were 0.02 g and 30 Hz. The sequence of experimental procedures for the input motion is as follows: (1) white-noise excitation, (2) sinusoidal sweep, and (3) historical earthquake records.

Test Results

1. Predominant frequency

In this study, a white-noise sweep was performed before each event to identify the predominant frequency of the gravelly soil specimen. Using the horizontal accelerations at the surface and the bottom of the soil under the white-noise sweep, the transfer function could be established using a fast Fourier transform (FFT), as shown in Fig. 4. The predominant frequency of the gravelly specimen was found to be approximately 10.5 Hz. The results of the sinusoidal sweep excitation indicated that the resonance frequency was approximately 10.6 Hz, which was very similar to the predominant frequency determined from white-noise excitation.

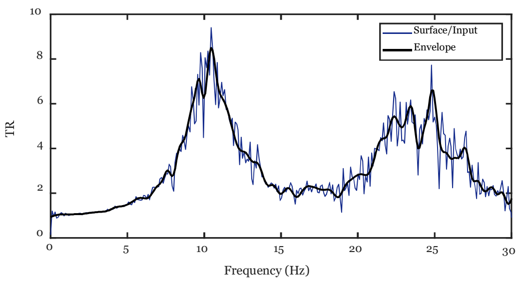

Fig. 4. Predominant frequency of the specimen

2. Seismic response

The acceleration responses of the specimen and the input motion during a seismic loading of 0.2 g are shown in Fig. 5. The figure shows that the acceleration response of the soil surface is dramatic when some of the soil layers develop a state of initial liquefaction (at times of 2.6 s). Further experimentation showed that, if the input seismic loading is larger, then the acceleration amplitude of the ground surface is significantly increased and delayed.

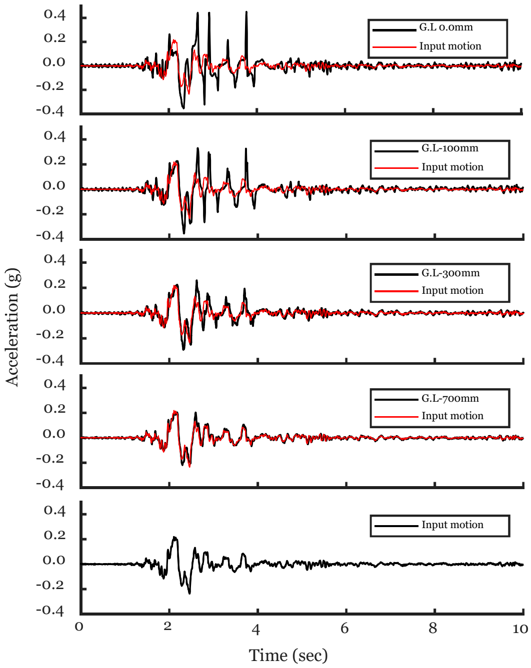

Fig. 5. The acceleration responses of the ground surface and the input motions (A_{max} = 0.2 g).

3. Excess pore water pressure

The excess pore pressure responses of the gravel specimen to seismic motion with an acceleration of 0.2 g are shown in Fig. 6 for different depths below the surface of the specimen. They show that the excess pore water pressure increases significantly during an earthquake event, leading to liquefaction of the gravelly soil. The figure shows that the depths of the liquefied layers are 300–700 mm below the soil surface under the dynamic loading conditions of this experiment.

The excess pore water pressure is negative at times of 2–3 s, which is interpreted to be caused by shear dilation behavior of the gravelly soils. The excess pore water pressure ratio reaches greater than 1.0, and this may reflect settlement of the sensor during the liquefaction. It can be seen that, during the dynamic loading, the gravelly specimen quickly accumulated excess pore water pressure until soil liquefaction occurred. After that, the excess pore water pressure dissipated gradually with time.

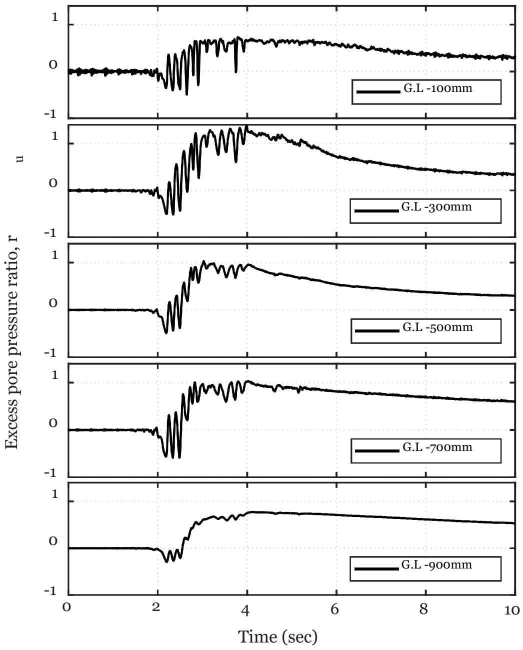

Fig. 6. Excess pore pressure response of sand–gravel composites during seismic motion with an acceleration of 0.2 g.

Conclusions

The initial test results are summarized as follows:

1. The pore water pressure changes are insignificant for remolded gravelly soil samples of loose relative density when the maximum acceleration of the earthquake event is 0.1 g. During seismic loading with an acceleration of 0.2 g, the excess pore water pressure was significantly increased and lead to some parts of the gravelly deposit liquefy.

2. During seismic loading with an acceleration of 0.2 g, the acceleration response of the soil surface is dramatic and some parts of soil layers develop a state of initial liquefaction (at times of 2.6 s). The acceleration response of the specimen surface was amplified and delayed.

References

Ko, Y. Y., Hsu, S. Y., Yang, H. C., Lu, C. C., Hwang, Y. W., Liu, C. H., and Hwang, J. H. (2018). “Soil Liquefaction and Ground Settlements in 6 February 2018 Hualien, Taiwan, Earthquake,” Seismological Research Letters., 90 (1), 51-59.

Ueng, T. S., Chen, M. H., Wang, M. H. and Chen, M. H. (2006). “A Large Biaxial Shear Box for Shaking Table Test on Saturated Sand,” Geotechnical Testing Journal., 29(1), 1-8.

Evans, M. D. and Zhou, S. (1995). “Liquefaction Behavior of Sand-Gravel Composites,” J. Geotechnical Engineering. ASCE., 121(3), 287-298.

Hatanaka, M., Uchida, A. and Uhara, J. (1997). “Liquefaction Characteristics of a Gravelly Fill Liquefied during the 1995 Hyogo-Ken Nanbu Earthquake,” Soils and Foundations. JGS., 37(3), 107-115.

Amini, F. and Sama, K.M. (1999). “Behavior of Stratified Sand-Silt-Gravel Composites under Seismic Liquefaction Conditions,” Soil Dynamics and Earthquake Engineering., 18(6), 445-455.

Evans, M. D., Seed, H. B. and Seed, R. B. (1992). “Membrane Compliance and Liquefaction of Sliced Gravel Specimens,” J. Geotechnical. Engineering. ASCE., 118(6), 856-872.

Evans, M. D. (1993). “Liquefaction and Dynamic Properties of Gravelly Soils,” Transactions on the Built Environment. WIT Press. ISSN 1743-3509., 3, 317-331.

Wong, R.T., Seed, H. B. and Chan, C. K. (1975). “Cyclic Loading Liquefaction of Gravelly Soils,” J. Geotechnical Engineering. ASCE., 101(6), 571-583.

Vertical Loading Analysis of Large-Diameter Monopiles using 3D Numerical Model

Teng-Ruei You[1] and Jung-Hung Huang[2]

游騰瑞 [1]、黃俊鴻 [2]

Abstract

Offshore wind power has been a flourishing industry for over ten years and is the fastest-growing renewable energy source in the world. Underwater infrastructure is fundamentally important for building offshore wind turbines (OWTs). Large-diameter monopiles are widely used foundations for OWTs and such piles usually acquire large internal soil plugs during installation. In this study, three-dimensional finite-difference analyses were performed to estimate the static vertical load-carrying capacity of a monopile embedded in the substratum at a real site. The soil plug was shown to have a large effect on frictional resistance and vertical loading capacity. P-S curve showed frictional resistance by soil plug was increasing gradually without yielding but frictional resistance by soil strata wasn't. This appears to be caused by compression of the soil plug during vertical loading and also inflicted t-z curve out of synchronization. The effect of soil plug should be evaluated in monopile structure design.

Keywords: large-diameter monopile, vertical loading capacity, FLAC3D, soil plug

Introduction

Energy generated by offshore wind turbines has been one of the most promising and rapidly growing sources of renewable energy in recent years around the world. Because offshore winds are steadier and stronger than winds in onshore environments and because of decreasing construction costs, offshore wind energy is gradually becoming mainstream. Good design and construction are essential to overcome environmental problems associated with various types of underwater infrastructure, including monopiles, gravity-based structures, steel jackets, suction caissons, and anchored floating systems. Of these, large-diameter monopiles driven into the seabed are the most widely used foundation system for offshore wind turbines. Depending on the power of the wind turbine, large-diameter monopiles vary from 3 m to 8 m in diameter. Their design has been guided by experience gained in construction of offshore oil and gas platforms, for which there are regulation codes, *e.g.* the American Petroleum Institute (API, 2002) and Det Norske Veritas (DNV, 2016). However, these guidelines are semi-empirical and based on *in-situ* tests on piles with diameters less than 2 m. This may not be appropriate for the large-diameters required by wind turbines, whose characteristics such as skin friction (t-z) load transfer curves or lateral bearing (p-y) relationships may differ substantially.

Large-diameter monopiles are usually filled with large soil plugs, which develop as the piles are driven into sea floor. The behavior of the piles must be influenced by characteristics of the soil plug during vertical or lateral loading, but existing guidelines do not take into account these two effects. This study addresses this problem by considering the design of an actual base structure of an offshore wind turbine. The capacity and behavior of the monopile and plug under vertical loading are analyzed using a three-dimensional finite-differential program (FLAC3D). The results are used to show that the effect of the soil plug cannot be ignored in structural design.

Case Information and Numerical Model

This case under study is an 8 MW wind turbine situated offshore of Miaoli City, Taiwan, where the water depth is 24.5 m. The underwater infrastructure consists of a large-diameter monopile embedded in a layered soil deposit, for which borehole data are available. The embedded length of pile is 42 m and its

[1] Assistant Research, National Center for Research on Earthquake Engineering
[2] Professor, National Central University

diameter is 8 m. Each monopile is different, having a unique diameter and different wall thickness, because the design of the moment of pile depends on environmental factors and the power of the turbine. A simplified specification for the pile was adopted in this study for use in three-dimensional numerical analysis using FLAC3D.

Fig. 1. shows the configuration of the monopile and the sedimentary deposit in which it is embedded. The sediment consists of layers of clay, silty sand, sandstone, and conglomerate with gravel. The soil deposit in the numerical model is built from a simplified blow count (N-value) derived from an *in-situ* standard penetration test (SPT). N-values could only be obtained to a depth of 16.5 m below the seabed because this is the limit of the SPT test (Fig. 1). The soil layers below the depth of 16.5 m are those given by the developer, which were obtained from borehole data used for designing the foundation. The layer bearing the tip of the pile is conglomerate with gravel and this is assumed to extend to the basal boundary of the numerical model.

Fig. 2 shows the three-dimensional numerical model used for the vertical bearing capacity analysis. It is assumed that a soil plug exists inside the pile and the same soil layers occur inside and outside the pile (Liu *et al*., 2009). The total length of the pile is 44 m so that it extends 2 m above the seabed, and this provides a convenient coupling for applying the vertical load. The bottom boundary of the model is 80 m wide, which is approximately twice the embedded length of the pile (L_p) and sufficient to meet the requirements of vertical loading analysis. The vertical load was applied in stages when the unbalanced force ratio was smaller than 10^{-7} until the load-displacement (or P-S) curve reached a plateau. Soil inside and outside the pile determines the behavior of the interface between the pile and its surroundings. Parameters characterizing the interface were assumed using an empirical formula provided by FLAC3D, which depends on the bulk modulus and shear modulus of each layer.

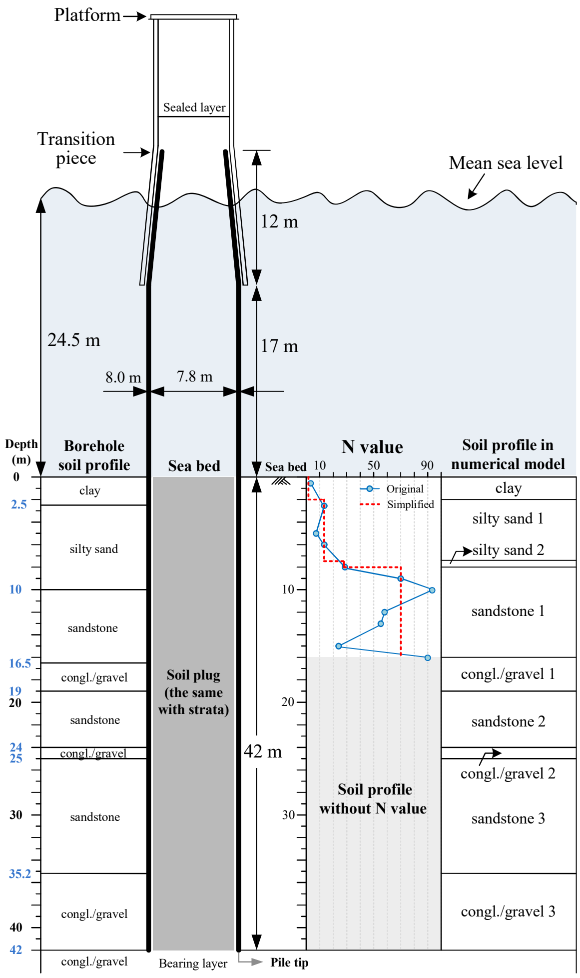

Fig. 1. Distribution of soil layers (left and right) and configuration of the monopile (center left). Results of SPT tests to a depth of 16.5 m are shown in center right.

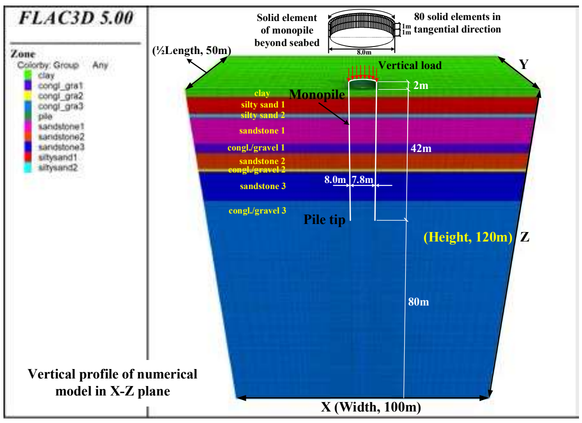

Fig. 2. Three-dimensional numerical model used for vertical load bearing capacity analysis showing the position and dimensions of the monopile and the sedimentary layering

Vertical Load Bearing Capacity

Fig. 3. shows the vertical loading-displacement curve, which is known as a P-S curve, for the modeled monopile structure. Typical P-S curves are of three types that include nonlinear relationship with yielding plateau, nonlinear relationship with gradual increasing after yield and nonlinear relationship ending with yield cause of pile failure. The maximum curvature of such P-S curves is usually used to define the yield point, which is the point at which the vertical bearing capacity of pile is attenuated. In this research, only frictional load bearing of the outside of the pile reveals an obvious yield point but this does not show in the P-S curve. Frictional bearing of the outside of the pile conforms to typical P-S curves, but this is not the case for the soil plug. Therefore, frictional load bearing associated with the soil plug results in a special form of the P-S curve in this research. The yield point indicated by the load bearing behavior is different from the $0.1D_p$ Terzaghi rule because of the large diameter of the monopile. In this case, $0.1D_p$ is 0.8 m (if D_P is the diameter of the pile) and this is larger than the pile settlement, which is 6.5 cm under a vertical load of 12360 tons. It is thus demonstrated that P-S curves for large-diameter and small-diameter monopiles are quite different.

The frictional bearing capacity of the soil plug contributes significantly to the P-S curve and even dominates it. It increases almost linearly up to a load on pile head of 7000 tons and is larger than the friction of soil strata at loads. There is a reduction in this trend over settlement of 2.5cm but no clear plateau is reached. Resistance of the pile tip has no obvious effect during vertical loading because the extruding effect of the pile and large frictional resistance of the soil plug induce small displacement of the pile tip. The frictional bearing capacity of the soil plug contributes about 2/3 of total bearing capacity.

Fig. 4. shows contours of horizontal stress in an X-Z plane through the center of the pile under a vertical load of 11330 tons. At this stage, frictional resistance of the outside of the pile contributes one-third of the total vertical load bearing capacity and has attained a plateau. Frictional resistance of the soil plug contributes the other two-thirds and it increases gradually with increasing vertical load, but more slowly during later than early loading. Frictional resistance of the soil plug does not appear to reach a yield point and the reason for this may be compression of the soil plug by the pile. The downward force of the pile extrudes the soil plug, which cannot spread laterally, thus inducing high vertical stresses in the lower section of soil plug. The constraining effect also leads to high horizontal stresses and large normal stresses at the interface. The result is a cone-shaped stress concentration outside of tip of the pile (Fig. 4). The soil plug in the lower section of the pile therefore provides large frictional resistance in the late stage of vertical loading.

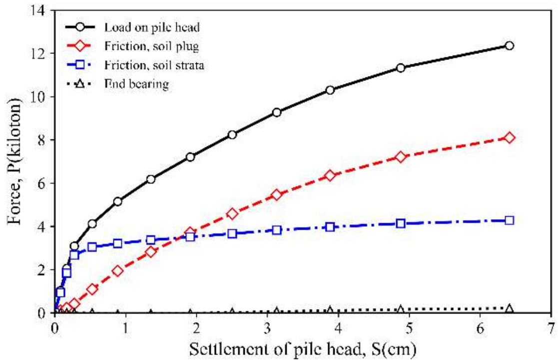

Fig. 3. P-S curves showing results of the numerical analysis of loading of the monopile

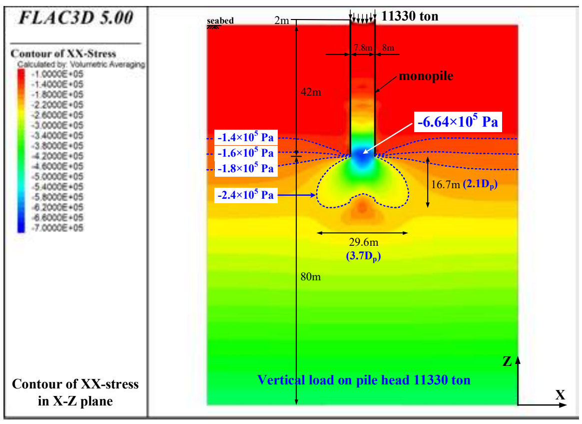

Fig. 4. Contours of horizontal stress in the X-Z plane through the monopile and sediments. Note the difference in behavior of the sediments inside and outside the pile

The t-z Curves

Skin friction (t-z) load transfer curves are important tools for analyzing the vertical bearing capacity of monopiles. These curves were designed as guidelines by DNV (2016) and API (2002). The following discussion is a comparison of the results derived from the 3D numerical model analysis and designed guidelines.

Fig. 5 shows the t-z curve at 1 m depth in the uppermost clay layer, which had an undrained shear strength of 9.81 kPa and a submerged unit weight of 9.78 kN/m^3. In accordance with the API rule, α was set at 0.5 and the maximum frictional stress was set at 0.5 t/m^2. The same soil properties were used for the total stress α method of DNV; r_f was set at 0.9 and α was set at 0.5 for $s_u/p_0' \leq 1.0$, which influenced the yield point in the t-z curve. The t-z curve calculated according to the API guideline reached yielding within a value of 0.01 for S/D and then decreased to between 0.7 and 0.9

of the maximum frictional stress. It is possible that pile diameter (D_p) makes a big difference when dealing with large and small diameter piles, and this may explain the very small S/D ratio in the t-z curve. On the other hand, the result may be affected by a difference in behavior of the soil plug and the soil outside the pile. The displacement (S) of the soil inside and outside the pile is different at the same stage of vertical loading, and it is difficult to model these effects simultaneously.

The initial negative frictional stress was due to equilibrium procedure of geological stresses. The real geo-stress was difficult to evaluate and equilibrium between original parameters and the actual state of the interface may have been carried out automatically. This could induce faster settlement of soil than the pile so that negative frictional stress occurred. Estimating appropriate stress conditions in the soil plug and surrounding ground after the pile is installed was a difficult issue, and the effect of unequal displacement on the t-z curves is an issue for further research.

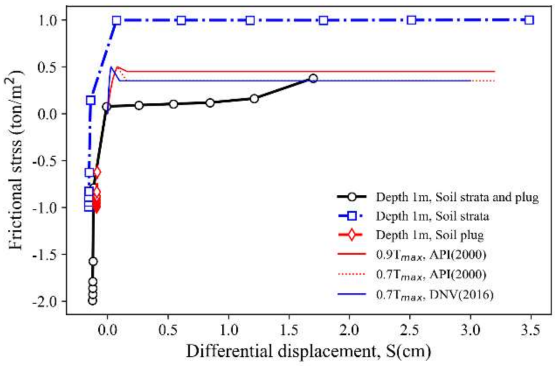

Fig. 5. The t-z curve at a depth of 1 m.

Fig. 6 shows the t-z curve at 4 m depth. The sediment at this depth is silty sand, which had a cohesion of 1 kPa and a frictional angle of 31 degrees. The yield point using the API guideline occurred at a differential displacement of 0.1 inch and this was not influenced by any parameter. It meant that yield occurred at very small differential displacements like frictional behavior of soil strata. But frictional behavior of soil plug didn't yield. Average differential displacement of soil strata and plug between pile was used to calculate summated t-z curve which was not conventional. Friction between the outer soil and the pile was normal, which resulted in conventional behavior and yielding at small differential displacement. However, the soil plug did not behave according to accepted guidelines. Friction between the soil plug and the pile appears to be almost negligible, with the result that differential displacements are very small; this may be caused by large lateral stress due to compression of the plug.

The results summarized in Figs 5 and 6 suggest that the vertical load bearing capacity may not be in a controlled state in large-diameter monopiles and that the influence of the soil plug cannot be ignored in designing monopile structures.

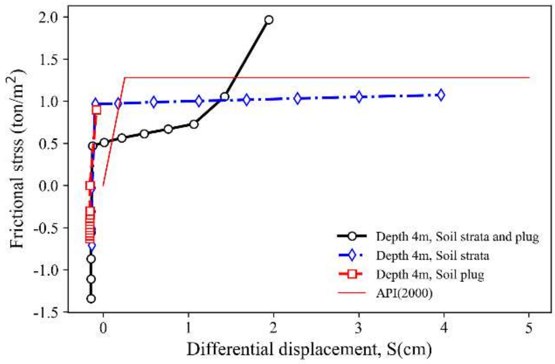

Fig. 6. The t-z curve at a depth of 4 m.

Conclusions

In this study, 3D numerical modelling was conducted to analyze the vertical load bearing capacity and behavior of a large-diameter monopile. It is clear that the soil plug is a big issue in large-diameter monopiles. Compression of the soil plug has an important effect on the overall frictional resistance as the vertical load is increased. The frictional resistance of soil plug is twice the frictional resistance associated with soil outside the pile in the final stage of loading to 12360 tons. It is also significant that the t-z curve is influenced by the soil plug because of its frictional behavior and should be considered in designation of vertical bearing pile.

References

API (American Petroleum Institute). (2000), Recommended practice for planning, designing and constructing fixed offshore platforms, 21st Ed., Washington, DC.

Liu, R., Yan, S. W., and Li, Z. H. (2009), Soil plug effect prediction and pile driveability analysis for large-diameter steel piles in ocean engineering. China Ocean Eng., 23(1), 107-118.

DNV (2016), "Design of Offshore Wind Turbine Structures." Det Norske Veritas., DNV-OS-J101.

Cue'llar, P. (2011), Pile Foundations for Offshore Wind Turbines: Numerical and Experimental Investigations on the Behaviour under Short-Term and Long-Term Cyclic Loading. Ph. D. thesis, BAM, Bundesanstalt fr Material for schung undprfung, Berlin.

Merphy G., Igoe D., Doherty P. and Gavin K. (2018), 3D FEM approach for laterally loaded monopile design Computers and Geotechnics, Volume

Shallow Crustal Velocity Structures along the Deformation front of the Taiwan Orogen Revealed by Ambient Seismic Noise

Yu-Chih Huang[1], Che-Min Lin[2], Hung-Hao Hsieh[3], Kuo-Liang Wen[4] and Chau-Huei Chen[5]

黃有志 [1]、林哲民 [2]、謝宏灝 [3]、溫國樑 [4]、陳朝輝 [5]

Abstract

Taiwan is located at a convergent plate boundary on the Circum-Pacific seismic belt, accompanied by high seismicity and complex tectonics. The Western Coastal Plain and Western Foothills are located along the deformation front of the Taiwan orogen. This area includes highly active faults and a complex seismogenic structure that have historically caused significant damage. The densely populated cities are situated on thick alluvium and threatened by seismic-wave amplification and soil liquefaction. A temporary seismic network had been operated by the National Center for Research on Earthquake Engineering (NCREE) between 2006 and 2010, with 48 broadband seismometers and an average interstation distance of ~10 km, set up to monitor the seismicity surrounding the three Science Parks to further study the characteristics of ground motion and fault activity. Since the basic theorem of ambient seismic noise analysis has been verified, investigations of subsurface velocity structures have provided important constraints in various parts of the world, with routine data processing occurring over the past decade. In this study, the quality of data of the daily vertical component was preliminarily assessed to calculate the cross-correlation function (CCF) for each station pair in the 1–15 s period band. The daily CCFs were stacked to retain coherent signals for acquiring Rayleigh-wave phase-velocity dispersion curves. Tomography was applied to construct 1–10 s Rayleigh-wave phase-velocity maps with 0.04° grid spacing. Lateral velocity variations showed dramatic patterns among different geologic provinces. Shallow crustal S-wave velocity (Vs) structures will be obtained for further comparison with data on active faults, seismogenic structures, groundwater distribution, etc. The Vs structures will also help to construct strong ground motions, which is particularly important for seismic hazard mitigation of the densely populated metropolitan areas in western Taiwan.

Keywords: Taiwan orogen, ambient seismic noise, velocity structures

Motivation and Seismic Data

Taiwan is located at a complex convergent plate boundary zone where the Eurasian plate interacts with the Philippine Sea plate, accompanied by high seismicity and complex tectonics (Tsai et al., 1977; Tsai, 1986). According to observations from long-term Global Positioning System (GPS) data, major crustal deformations are concentrated along the suture zones of the Longitudinal Valley and deformation front of the Taiwan orogeny (Hsu et al., 2009; Ching et al., 2011). Active faults and complex seismogenic structures have been observed and have historically caused serious damage in this area. Densely populated cities on the Western Coastal Plain are situated on thick alluvium and are threatened by seismic-wave amplification and soil liquefaction (Kuo et al., 2015).

Although there are numerous studies of seismic velocity structures at different scales and regions in

[1] Associate Researcher, National Center for Research on Earthquake Engineering
[2] Researcher, National Center for Research on Earthquake Engineering
[3] Assistant Researcher, National Center for Research on Earthquake Engineering
[4] Professor, National Central University
[5] Professor, National Chung Cheng University

Taiwan, poor lateral resolution is typically present in the shallow crust and Western Coastal Plain due to uneven distribution of seismic sources and stations. For the surface alluvium, more detailed velocity structures and site parameters (e.g., Vs30, Z1.0) could be studied and summarized with microtremor surveys, suspension P-S logging, receiver function analysis, etc. (NCREE; http://egdt.ncree.org.tw/news_eng.htm). In addition, Central Geological Survey (CGS) announced the evaluations of soil liquefaction potential from integrated geological and engineering drilling data (https://www.liquid.net.tw/CGS/Web/Map.aspx). In summary, there are still no proper high-resolution seismic velocity structures at depths of a few kilometers to combine the current local-scale models with large-scale crustal models in Taiwan.

Since the basic theorem of ambient seismic noise analysis has been verified, the investigations of subsurface velocity structures have provided important constraints in various parts of the world over the past decade. From 2006 through 2010, a temporary seismic network operated by the NCREE with 48 Güralp CMG-6TD broadband seismometers was employed for monitoring the seismicity and ground motion in three Science Parks. The deployment started from Hsinchu Science Park and operated for ~5 years. Then the network was deployed to Southern Taiwan Science Park, operating for ~4 years, and finally the Central Taiwan Science Park integrated the whole network from Hsinchu to Tainan County and operated for ~2 years. The network was ~220 km in the longitudinal direction and ~70 km in the transverse direction, with an average interstation distance of ~10 km. Based on the observations of the network, the seismicity of active faults can be determined, with these parameters important for the assessment of hazards and numerical simulations for potential seismic risks (Fig. 1; Lin et al., 2010).

In the present study, we applied routine data processing to obtain shallow crustal velocity structures along the deformation front of the Taiwan orogen, analyzing the daily vertical component of continuously recorded ambient seismic noise signals. The results can be further compared with the available data on active faults, seismogenic structures, groundwater distribution, etc.

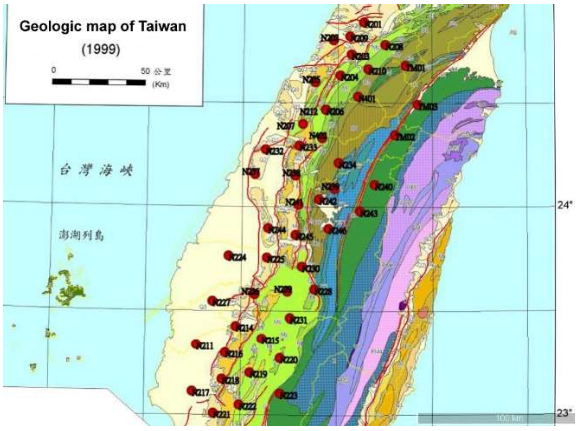

Fig. 1. The temporary broadband seismic network in three Science Parks operated by the NCREE.

Methods and Data Processing

Ambient seismic noise is caused by a variety of factors, such as human activities, atmospheric pressure changes, interaction of ocean waves with the coast and seafloor, and other factors in the natural environment. Ambient seismic noise contains diffuse wavefields with passive structural signals, which could be enhanced after long-term stacking. The particle motion is similar to surface wave propagation, hence exhibiting dispersion properties related to underground velocity structures.

The underground velocity structures can be obtained from the cross-correlation of station pairs with simultaneous and continuous ambient seismic noise signals (Weaver, 2005). The depth range of an obtained velocity structure is positively related to the aperture of the seismic network, and its lateral resolution is positively related to the density of path coverage. The study region will have high lateral resolution if the seismic stations are densely and homogeneously distributed. Besides, it is unnecessary to spend significant amounts of time waiting for sufficient seismic records, and furthermore, this method avoids inhomogeneous source distributions from affecting the lateral resolution, such as travel-time tomography. Thus, this method can provide good results for velocity structures in areas with relatively low seismicity.

Figure 2 shows the data analysis procedure for ambient seismic noise in this study. First, baseline corrections of the seismograms were performed and the quality of data on the daily vertical component was preliminarily assessed. After data preparation, the daily CCFs were derived using one-bit cross-correlation and spectral whitening for enhancing the spectral energy of ambient seismic noise. Hence, while calculating CCFs, the continuous recordings are simply used without removing earthquake signals. The basic concepts of these two methods have been verified and regularly utilized for research on ambient seismic noise to obtain high signal-to-noise ratio (SNR) CCFs (Cupillard and Capdeville, 2010). The time domain empirical Green's function (TDEGF) in the 1–15 s period band is further obtained from the time-derivative of the CCF.

After long-term stacking daily CCFs, a relatively stable and representative CCF for each station pair can be derived. The phase image analysis and far-field approximation methods were employed to measure the Rayleigh-wave phase-velocity dispersion curves from the TDEGF for each station pair (Yao et al., 2006). Phase-image analysis enables selection of an appropriate dispersion curve and interstation distances are required to be at least twice the wavelength of the propagating surface waves. Before constructing Rayleigh-wave phase-velocity maps, checkerboard resolution test (CRT) models at different scales were used to assess the lateral resolution of the obtained phase velocities. Then, the tomographic method was applied to construct phase-velocity maps for periods of 1–10 s. The shallow-crust Vs structures were then constructed from the obtained phase-velocity maps.

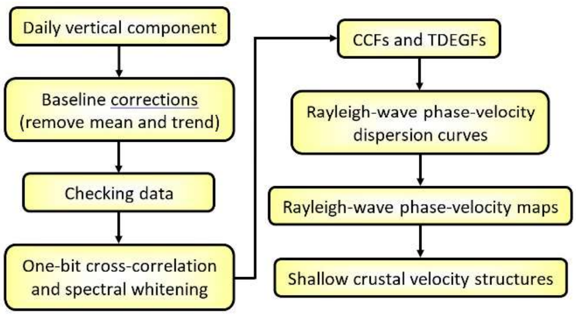

Fig. 2. Data processing in the ambient seismic noise analysis in this study.

Preliminary Results

Daily CCFs were calculated with a 200 s lag time in the 1–15 s period band for all station pairs. Figure 3 presents examples of the calculated daily and stacked monthly CCFs for two station pairs. The station pair N203-N208 has a small interstation distance of 18 km and demonstrates a high consistency and SNR of its daily CCFs. In contrast, the interstation distance for N203-N219 is large at 178 km, with this station pair demonstrating a relatively low consistency and SNR of its daily CCFs. Nevertheless, after long-term stacking of monthly CCFs, the representative CCF of station pair N203-N219 can still be obtained.

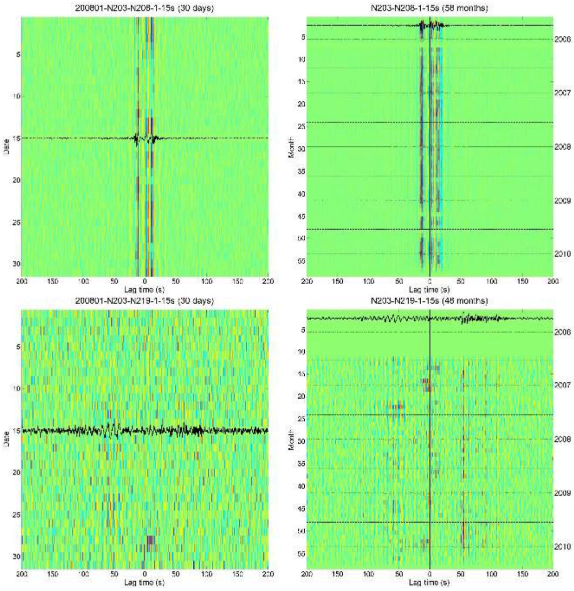

Fig. 3. Examples of 1–15 s CCFs for two station pairs with short interstation distances (above: N203-N208) and long interstation distances (below: N203-N219); daily (left: in January 2008) and monthly CCFs (right: between 2006 and 2010). The solid black lines indicate the averages of the daily and monthly CCFs.

Figure 4 presents the stacked monthly 1–15 s CCFs with varying interstation distance for all station pairs. The main Rayleigh-wave signals propagate with an average apparent velocity of 2.5 km/s. Figure 5 shows the measured 1–12 s Rayleigh-wave phase-velocity dispersion curves along with their averages and standard deviations. The averages vary from 1.95 km/s at 1 s to 3.27 km/s at 12 s. The measured Rayleigh-wave phase-velocity dispersion curves are compared in Figure 6 for six selected station pairs transecting different portions of the study region with approximate interstation distances of 50 km. The phase velocities were relatively high around Hsinchu Science Park (N205–TM01 and N207–TM02). The lowest phase velocities appeared in the west of Southern Taiwan Science Park (N221–N227) and exhibited a variance of ~1 km/s.

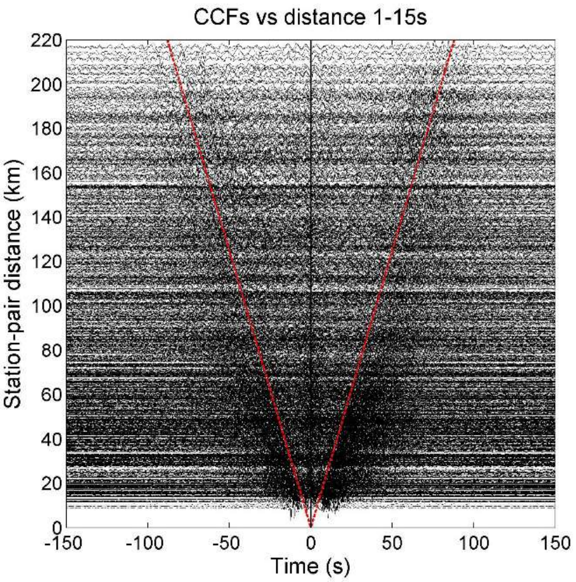

Fig. 4. Stacked monthly 1–15 s CCFs versus interstation distance for all station pairs. Red dashed lines mark the TDEGF signals with an apparent velocity of 2.5 km/s.

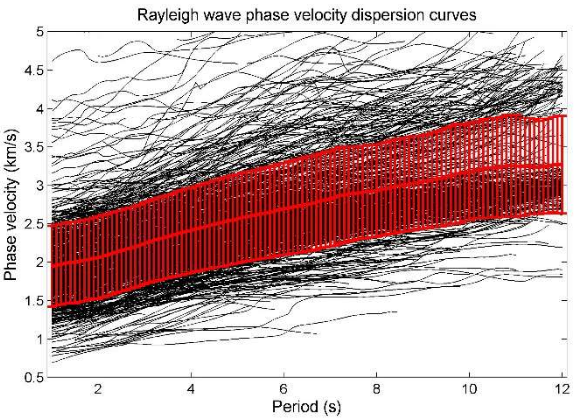

Fig. 5. Measured 1–12-s Rayleigh-wave phase-velocity dispersion curves. Black lines indicate individual dispersion curves and the red lines are the averages with the respective standard deviations.

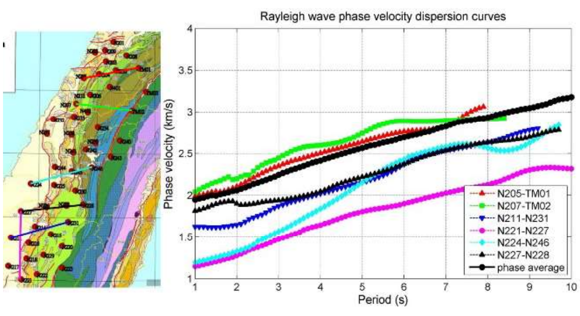

Fig. 6. Comparison of six measured Rayleigh-wave phase-velocity dispersion curves with interstation distances of ~50 km. The solid black line with circle markers represents the average Rayleigh-wave phase-velocity dispersion curve shown in Fig. 5.

Figure 7 displays four CRT input models with a velocity contrast of 1.5 ± 0.2 km/s for 0.25°, 0.125°, 0.1°, and 0.075° anomalies with 0.1°, 0.05°, 0.04°, and 0.03° grid spacing, respectively. The recovery results indicated that, apart from some margins and the 0.075° anomaly, most of the study region was recovered. Therefore, grid spacing of 0.04° was applied for the construction of 1–10 s Rayleigh-wave phase-velocity maps in the region of 120.20–121.48°E and 22.98–24.90°N. This resulted in 33 grid points in the longitudinal direction and 49 grid points in the latitudinal direction. Figure 8 shows Rayleigh-wave phase-velocity maps with individual velocity ranges for three arbitrarily selected periods. The predominant lateral velocity variations showed dramatic patterns among different geologic provinces.

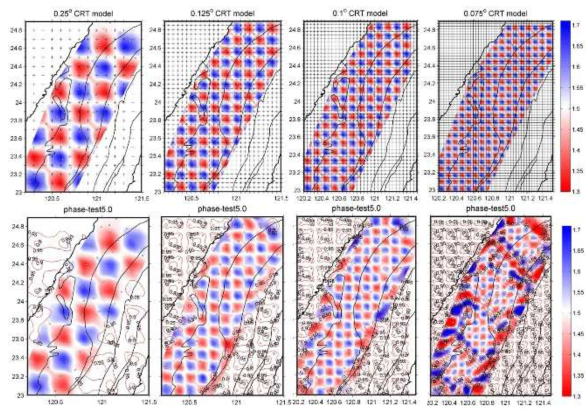

Fig. 7. Four CRT input models (above) and example recovery results at 5 s (below).

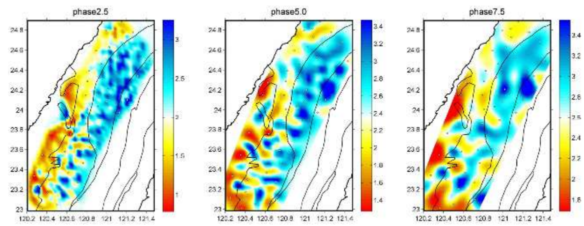

Fig. 8. Rayleigh-wave phase-velocity maps at periods of 2.5 s, 5.0 s and 7.5 s.

Future Studies

In the near future, the shallow crustal Vs structures along the deformation front of the Taiwan orogen will be further investigated, with future two-dimensional and three-dimensional modeling of the structures. The obtained shallow crustal Vs structures could help to construct strong ground motions, which are particularly important for seismic hazard mitigation of the densely populated metropolitan areas in western Taiwan.

References

Ching, K. E., Hsieh, M. L., Johnson, K. M., Chen, K. H., Rau, R. J., and Yang, M. (2011), "Modern vertical deformation rates and mountain building in Taiwan from precise leveling measurements and continuous GPS observations, 2000-2008", *J. Geophys. Res.* 116, B08406.

Cupillard, P., and Capdeville, Y. (2010), "On the amplitude of surface waves obtained by noise correlation and the capability to recover the attenuation: a numerical approach", *Geophys. J. Int.* 181, 1687-1700.

Hsu, Y. J., Yu, S. B., Simons, M., Kuo, L. C., and Chen, H. Y. (2009), "Interseismic crustal deformation in the Taiwan plate boundary zone revealed by GPS observations, seismicity, and earthquake focal mechanisms", *Tectonophys.* 479, 4-18.

Kuo, C. H., Chen, C. T., Wen, K. L., Lin, C. M., Hsieh, H. H. (2015), "Investigation of Shallow S-wave Velocity Profile-Western Plain of Taiwan", NCREE-15-005, NCREE, Taipei. (In Chinese)

Lin, C. M., Chang, T. M., Wen, K. L., Hsieh, H. H., Chen, A. B., Chang, L. C., and Kuo, C. H. (2010), "Micro-Earthquake Monitoring of Science Parks in Taiwan", NCREE-10-020, NCREE, Taipei. (In Chinese)

Tsai, Y. B. (1986), "Seismotectonics of Taiwan", *Tectonophys.* 125, 17-37.

Tsai, Y. B., Teng, T. L., Chiu, J. M., and Liu, H. L. (1977), "Tectonic implica- tions of the seismicity in the Taiwan region", *Mem. Geol. Soc. China* 2, 13-41.

Weaver, R. L. (2005), "Information from seismic noise", *Science* 307, 1568-1569.

Yao, H., van der Hilst, R. D., and de Hoop, M. V. (2006), "Surface-wave array tomography in SE Tibet from ambient seismic noise and two-station analysis - I. Phase velocity maps", *Geophys. J. Int.* 166, 732-744.

Radon Monitoring for Earthquake Precursory and Mud Volcano Studies in Taiwan

Vivek Walia[1], Shih-Jung Lin[2], Arvind Kumar[3]and Ching-Chou Fu[4]

Abstract

In this study, data from various stations are examined synoptically to evaluate earthquake precursory signals against the backdrop of rainfall and other environmental factors. During the observation period of 2019, about 26 earthquakes of magnitude ≥ 5 were recorded, and out of these, 9 earthquakes met the defined selection criteria and were tested in the proposed model. Some mud volcanoes in the Kaohsiung (Mao-Tao-San) and Pingtung (Wan-Dan) areas were selected. Based on the observed data of eruption and water radon at Mao-Tao-Sen, we propose that the radon variations of well no. 2 and well no. 3(B) show opposite trends and can be used as a behavior model for the area. It will also help in understanding the relationship of radon data with tectonic activities in the region.

Keywords: Earthquake Precursory, Mud volcano, Soil-gas, Water, Radon, Southern Taiwan

Introduction

Taiwan is situated within a complicated tectonic setting. It is situated on a focused boundary between the Eurasian Plate and the Philippine Sea Plate. In the Southern Part, the Eurasian Plate is subducting under the Philippine Sea Plate. In the Northern area, the Philippine Sea Plate is surrounded by the Ryukyu Trench and is subducting to a lower place than the Eurasian Plate. At the back of the Ryukyu Trench, the widening of the Okinawa Trough has matured. These collisions are generally considered to be the main source of tectonic stress in the region and are thus densely faulted and seismically active. A detailed study of these active faults will provide information about the activity of these faults, which may greatly help to reduce the damage when unavoidable large earthquakes occur. Soil-gas geochemistry and its spatial–temporal variations has been used for monitoring seismic activities, volcanic activity, environmental research, mapping of fault zones, geological traces, etc. for decades (Kumar et al., 2013; Walia et al., 2013). There have been various studies on the measurements of radon concentration in soil and gas emanating from the ground along active faults, which may provide useful signals before seismic events (Walia et al., 2009; Yang et al. 2011). Studies on diffuse degassing from the sub-surface have clearly shown that the gases can escape toward the surface by diffusion, advection, and dispersion as they are transported by rising hot fluids and migrate along preferential pathways such as fractures and faults.

Natural gas release, hot springs, hydrothermal exercise, and mud volcanoes are present in various tectonic fields of Taiwan. A number of mud volcanoes were additionally acclaimed in Taiwan on-land (Shih 1967) and offshore (Chow et al. 2001). Shih (1967) discovered that there have been sixty-four live mud volcanoes in seventeen land spaces. To find the fluid sources in mud volcanoes and mud pools, gas compositions and isotopic measurements were utilized. Although active mud volcanoes emit methane-prevailing gases, some gases have shown unexpected carbon dioxide-dominated and/or nitrogen-excess compositions. This suggests that there are various sources for the gas compositions of mud volcanoes in Taiwan (Yang et al. 2004). Volcanic exertions have altered human life to a large extent, as well as small extent, numerous times. Learning the warning signs of volcanic eruptions is still ongoing and it is a difficult challenge: seismic tremor and gas emissions for instance have been linked to future eruptive activity in some studies. However, the mechanisms at this time are not totally known.

[1] Research Fellow, National Center for Research on Earthquake Engineering, walia@ncree.narl.org.tw
[2] Assistant Research Fellow, National Center for Research on Earthquake Engineering, sjlin@ncree.narl.org.tw
[3]Associate Research Fellow, National Center for Research on Earthquake Engineering, kumar@ncree.narl.org.tw
[4] Associate Research Fellow,Institute of Earth Sciences, Academia Sinica, ccfu@earth.sinica.edu.tw

In recent years, we focused on temporal geochemical variations of soil-gas composition at established geochemical observatories along different faults (Fig.1) in the Hsinchu (HC) (i.e., along Hsincheng fault), Tainan (HH) (along Hsinhua Fault), and Ilan (at Jaosi (JS)) regions of Taiwan. This is done to determine the correlation of enhanced concentrations of radon with the seismic activity in the region from data generated during the observation period and test the efficiency of the proposed tectonic setting based model (Walia et al., 2013). This is being done along with some preliminary investigations in the Taipei region from an appropriate site at an established geochemical monitoring station along the Shan-Chiao fault in Northern Taiwan. However, in the last two years we also focused on the soil-gas and water geochemistry of some selected mud volcanoes in the Pingtung and Kaohsiung (Fig. 2) regions to understand the mechanism of the eruption and the relationship between the mud volcanoes eruption cycle and gas composition variations. Two mud volcanoes were selected for this study; the Wan-Dan (WD) mud volcano in Pingtung and the Mao-Tao-San (MTS) mud volcano in Kaohsiung. The selected mud volcanoes are located above the mud diaper system in southern Taiwan.

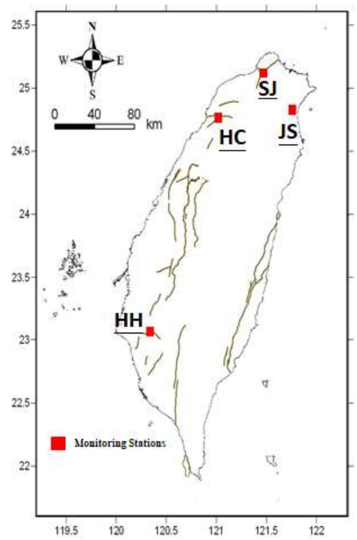

Fig.1. Map showing distribution of monitoring stations.

Methodology

To carry out the investigation, temporal soil-gas composition variations were measured regularly at the above-mentioned continuous earthquake monitoring stations established using RTM2100 (SARAD) for radon and thoron measurement. To carry out the investigation for the selected mud volcanoes, three different sampling techniques have been used to collect samples in and around the mud volcanoes. Soil-gas samples (taken at a depth of one meter) and dissolved gases were also collected from the mud volcanic sites (or nearby) for radon gas analyses. Soil-gas samples and dissolved gas from the mud pool/ground water were also analyzed for radon concentration using DURRIDGE RAD7 (Solid-state nuclear track detector) for field surveys and bi-weekly monitoring (see previous reports). The Nuclear Track technique using the Solid State Nuclear Track Detectors has also been used at some chosen sites in and around the mud volcanic areas. In this passive technique, LR-115 alpha detector films have been used. Semiautomatic methodology has been used for counting the tracks formed in the film detectors. The computed tracks per cm^2 in the films were converted to kBq/m^3 using the calibration factor calculated within the earlier study (Kumar et al. 2013).

(A)

(B)

Fig.2: Selected mud volcanoes in southwest Taiwan for the present study: (A) Wan-dan mud volcano (B) Mao-Tao-San mud volcano.

Results and Discussions

Earthquake Precursory Monitoring

As per present practice, the data from various stations are examined synoptically to evaluate earthquake precursory signals against the backdrop of rainfall and other environmental factors. Various guidelines are developed to identify the nature of the precursory signals almost in real-time. Data from various monitoring stations are automatically uploaded to the web service that provides the data management/exhibition to the database with less response time.

In addition to the monitoring station data, seismic parameters (i.e., magnitude/location/depth of the event, the intensity/epicentral distance at a monitoring station etc.) and meteorological parameter data are uploaded from the Central Weather Bureau of Taiwan (www.cwb.gov.tw) simultaneously. This is helpful in increasing the efficiency of earthquake prediction studies. Figs. 3–6 shows data that have been retrieved from established continuous monitoring stations and have been correlated. During the observation period (Jan. to Dec. 2019), 26 earthquakes with magnitude ≥ 5 were recorded. Only nine qualified under the defined criteria. Of these, seven earthquakes have shown precursory signals and two have not shown precursory signals. This can be due to many possible reasons (e.g., no data due to instrument problem/Typhoon /heavy rain etc.).

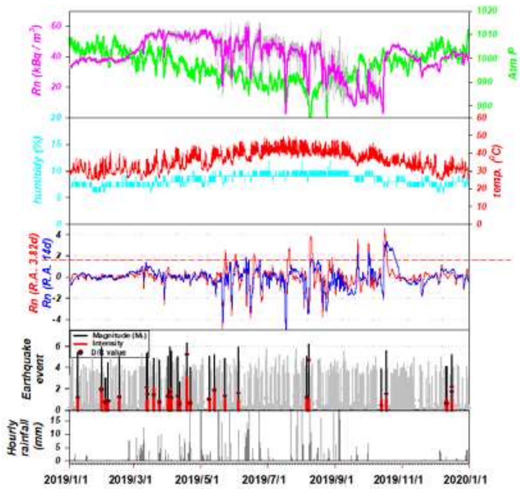

Fig. 3: Variations of radon data at HC monitoring stations and their correlation with earthquakes.

Mud Volcanoes Monitoring

Two mud volcanoes were selected for the present study (Fig. 2). Bi-weekly sampling was carried out at selected sites at/near both mud volcano eruption locations. At MTS, two sites for soil-gas testing and three boreholes for water samples were selected for bi-weekly monitoring. At WD, two sites (WD1 & WD2) for soil-gas testing and one site (WD1) for water samples were selected to study their characterization and eruption mechanism. The MTS mud volcano almost has a fixed eruption location, while the WD mud volcano eruption site changed with each eruption. Water samples have been collected and analyzed bi-weekly for radon gas as well as for other physical parameters at three wells at MTS (Fig. 2B). Radon values for the MTS water samples ranged from 38 Bq/m^3 to 9.9 kBq/m^3 in 2019. Both MTS1 and MTS3 soil-gas samples have recorded comparatively

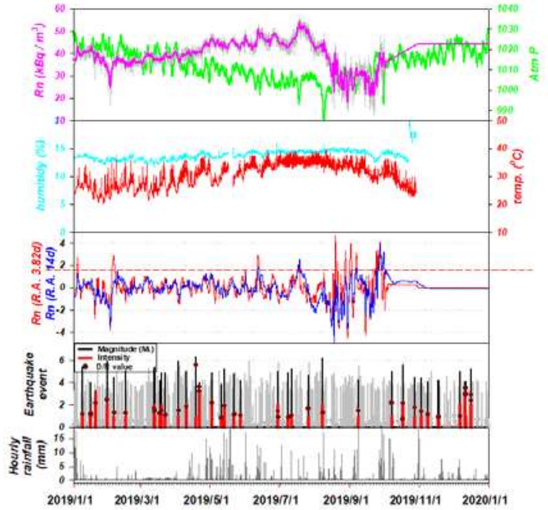

Fig. 4: Variations of radon data at JS monitoring stations and their correlation with earthquakes.

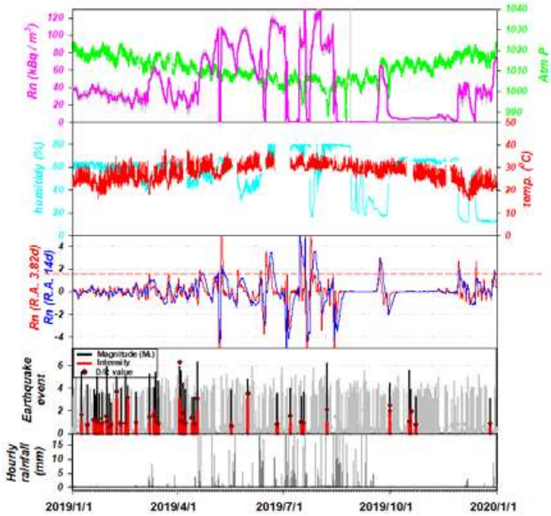

Fig. 5: Variations of radon data at HH monitoring stations and their correlation with earthquakes.

higher values of radon ranging 6.4–54.9 kBq/m^3 and 14.4–-42.5 kBq/m^3, respectively, in 2019. Figs. 7 and 8 show the water radon and soil-gas radon data recorded bi-weekly at the MTS area of south Taiwan along with volcanic eruption in 2019. This study shows that anomalous radon values have been observed before some volcanic eruptions during the study's period. Based on the eruption and radon observed data, we have proposed that radon variations of well no. 2 and well no. 3 (B) show opposite trends to each other (see the previous reports) and can be used as a behavior model for the area.

We also monitored the radon data in water and in soil (using active and passive methods) in the WD region (Fig. 2B). We recorded the radon concentration in the soil biweekly at two points, WD1 and WD2, using RAD 7 as well as LR115 films, whereas radon in water is monitored in the tap water near to point WD1. Figure 9 shows the radon data recorded in the soil-gas at WD1, WD2 and recorded data from the

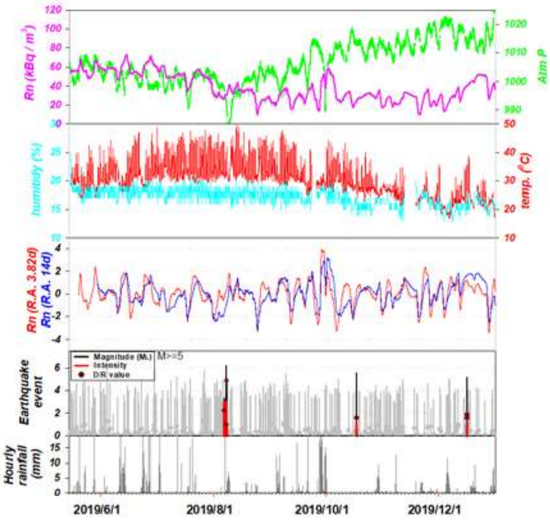

Fig. 6: Variations of radon data at SJ monitoring stations and their correlation with earthquakes.

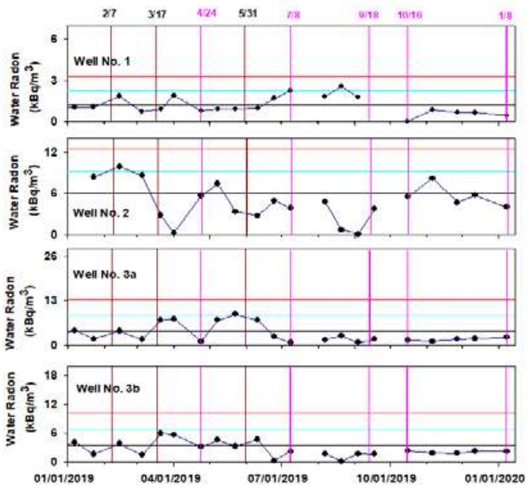

Fig. 7: Bi-weekly water radon data recorded in different wells at Mai-Tao-San area of south Taiwan along with mud volcanic eruption.

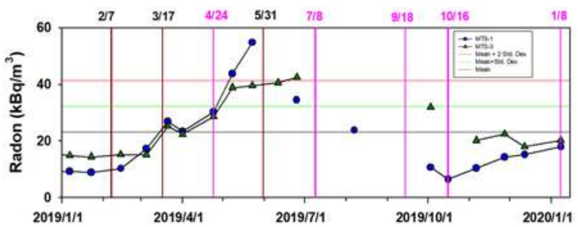

Fig. 8: Bi-weekly soil-gas radon data recorded in different wells at Mai-Tao-San area of south Taiwan along with mud volcanic eruption.

water samples in the WD regions during 2019. An increase in radon concentrations in both soil-gas as well as water samples have been noted before a few eruptions in WD1, whereas soil-gas samples have not shown any correlation with the eruption cycle in WD2. This study will also help in understanding the tectonic activities in the region.

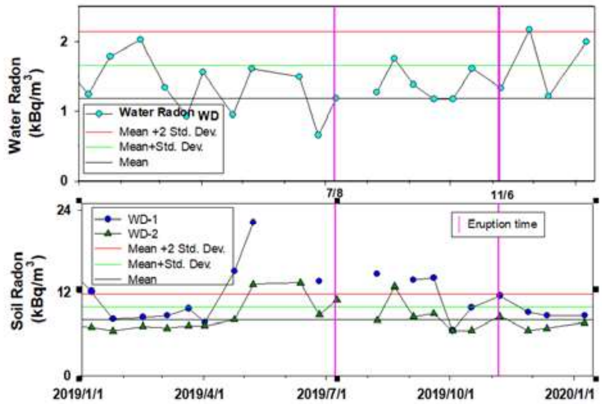

Fig. 9: Bi-weekly radon data recorded in soil-gas and water samples at Wan-dan area of south Taiwan along with mud volcanic eruption.

References

Chow. J., Lee, J.S., Liu, C.S., Lee, B.D., Watkins, J.S., (2001). A submarine canyon as the cause of a mud volcano: Liuchieuyu Island in Taiwan. Mar Geol., 176,55–63.

Kumar A, Walia V, Yang TF, Hsien C-H, Lin S-J, Eappen KP, Arora BR (2013) Radon-thoron monitoring in Tatun volcanic areas of northern Taiwan using LR-115 alpha track detector technique: pre calibration and installation. Acta Geophys 61(4):958–976.

Shih, T.T., (1967). A survey of the active mud volcanoes in Taiwan and a study of their types and the character of the mud. Petrol Geol. Taiwan, 5, 259–311.

Walia, V., Yang, T.F., Lin, S.J., Hong, WL., Fu, C.C., Wen, K-L.,Chen, C-H. (2009). “Geochemical variation of soil-gas composition for fault and earthquake precursory studies along Hsincheng fault in NW Taiwan”. *Appl. Radiat. Isotopes, 67, 1855-1863*.

Walia V, Yang TF, Lin S-J, Kumar A, Fu CC, Chiu J-M, Chang H-H, Wen K-L, Chen C-H (2013) Temporal variation of soil gas compositions for earthquake surveillance in Taiwan. Radiat Meas 50:154–159.

Yang, T.F., Wen, H.-Y., Fu, C.-C., Lee, H.-F., Lan, T.F., Chen, A.-T., Hong, W.-L., Lin, S.-J., Walia, V., (2011). “Soil radon flux and concentrations in hydrothermal area of the Tatun Volcano Group, Northern Taiwan”. *Geochem. J.*, 45, 483-490.

Yang, T.F., Yeh, G-H., Fu, C-C., Wang, C-C., Lan, T.F., Lee, H-F., Chen, C-H., Walia, V., Sung Q-C., (2004). Composition and exhalation flux of gases from mud volcanoes in Taiwan. Environmental Geology, 46, 1003–11..

Parametric Study on the Seismic Responses of Simply-supported Bridges Crossing Fault-rupture Zones

Hsiao-Hui Hung[1] and Chang-Wei Huang[2]

洪曉慧 [1]、黃仲偉 [2]

Abstract

The main objectives of this paper were to investigate the effect of fault-crossing on the seismic performance of simply supported bridges, and to identify key parameters that may influence the responses. The considered parameters included the friction coefficient of the rubber bearing supports, the distance between the superstructure and the transverse seismic stoppers, and the fault crossing angle with respect to the axis of the bridge. Non-linear time history analyses with multi-support input was adopted to perform this analysis. The ground motion records adopted were the recorded accelerograms collected during Hualien earthquake that occurred on February 6, 2018 in Taiwan. For comparison purposes, the corresponding case without fault-crossing considerations was also analyzed. The analysis results showed that neglecting to consider the effect of fault crossing led to significant underestimation of the torsional forces operating at the column bases and the relative displacement between neighboring girders for simply supported bridges. In addition, different bearing friction coefficients and different gap distances provided by the seismic stoppers was associated with different behaviors by the bridge.

Keywords: multi-support displacement input, bridge crossing faults, fault offset

Introduction

Taiwan is located within a compressive tectonic boundary occurring between the Eurasian Plate and the Philippine Sea Plate, where active faults are densely distributed. According to investigations conducted by the Central Geological Survey in Taiwan (MOEA, 2012), there are a total of 33 active faults located in Taiwan. Thus, bridges constructed in Taiwan are unable to completely avoid the threat from surface rupture faults. Previous reconnaissance reports produced after earthquake events have confirmed that the impact of the large pulse like velocity combined with the fault offsets arising from the fault rupture could cause more damage to the bridges than the far field earthquake impacts. As shown through the damage to bridges observed from recent earthquakes, including the 1999 Chi-Chi earthquake in Taiwan, 1999 Kocaeli earthquake and Duzce earthquake in Turkey, and the 2008 Wenchuan earthquake in China, many bridges that were located across fault lines were severely damaged as a consequence of the fault rupture. Recently, some bridges also sustained damage due to an apparent slip of the Milun fault observed during the 0206 Hualien earthquake that occurred offshore of the north of Hualien City on 6 February 2018 (Sung, et al. 2018). Evidently, the fault-crossing effect experienced by bridges has become a vital issue on the seismic responses of bridges that are located in the fault-rupture zone worldwide.

It is not always possible to avoid building bridges that cross earthquake fault zones in regions with a dense network of active faults, such as Taiwan. Accordingly, it is most likely that a large number of bridges have been unintentionally built across potentially active fault rupture zones around the world. These bridges all face a threat from damage due to differential ground displacement occurring across the fault line during large earthquake events. However, the international standards relating to design or seismic evaluation guidelines for bridges crossing faults is currently lacking. To have confidence when revising the relevant design codes and seismic evaluation processes for bridges crossing fault-rupture zones, a more in-depth understanding of the effect of fault ruptures on the response of bridges has to be gained. Therefore, the main objectives of the present paper are to parametrically investigate the effects of fault crossing on the seismic performance of bridges.

[1] Research Fellow, National Center for Research on Earthquake Engineering
[2] Associate Professor, Department of Civil Engineering, Chung Yuan Christian University

Nonlinear time history analyses with multiple-support inputs were adopted to perform this analysis. The ground motion records employed during this study were the actual recorded accelerogram data collected during 0206 Hualien earthquake. For comparison purposes, the corresponding case of bridges that were not associated with fault crossing was also investigated to highlight the effect of fault crossing on the bridge behavior.

Problem Description

In Taiwan, many of the existing bridges are multiple-span, simply-supported girder bridges. A simply supported bridge is the type of bridge that is most susceptible to span collapse when subjected to a cross-fault earthquake. For this reason, the target bridges selected for this study were multiple-span, simply-supported bridges with different design details.

A hypothetical bridge crossing a strike-slip fault was considered in the current study as shown in Figure 1, the bridge was a multiple-span, simply-supported bridge with an equal span length of 40 m and an equal pier height of 10 m. For simplicity, only 3 spans with a total length of 120 m were simulated, but the effect of the neighboring span was also taken into account by adding the tributary mass of a half span on top of P1 and P4. The superstructure of the bridge consisted of a concrete deck on top of four PCI girders, with the superstructure mass equaling 22 ton/m throughout. The piers were circular RC columns with a diameter of 2.5 m. All of the piers possessed the same reinforcement details with 74-D32 longitudinal reinforcing bars and were transversely reinforced with 19 mm bar hoops spaced at 8 cm.

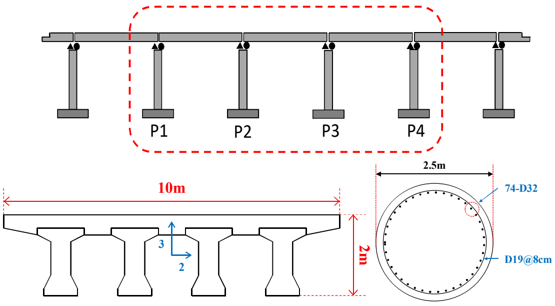

Figure 1. Schematic of the hypothetical bridge

The ground motions adopted in current study were adopted from the real earthquake records collected at station HWA019 during the Hualien earthquake as shown in Figure 2, where Figures (a) and (b) show the time history of the ground velocity and displacement along the north-south (N+) direction and east-west (E+) direction, respectively. As illustrated in the figures, the records exhibited significant near fault earthquake characteristics as they were associated with relatively large peak ground velocities. In addition, pulse-like ground motions affected by forward directivity and permanent translation can also be observed in the data. For the records collected along the N+ direction, a permanent ground displacement of 40 cm due to fault rupture can be observed. For the E+ direction, a large long period pulse of motion caused by rupture directivity effects is also noted. These records demonstrate typical behavior associated with a strike slip fault, where the records along the E+ direction represent the horizontal component perpendicular to the strike of the fault, while the records along the N+ direction represent the horizontal component parallel to the fault.

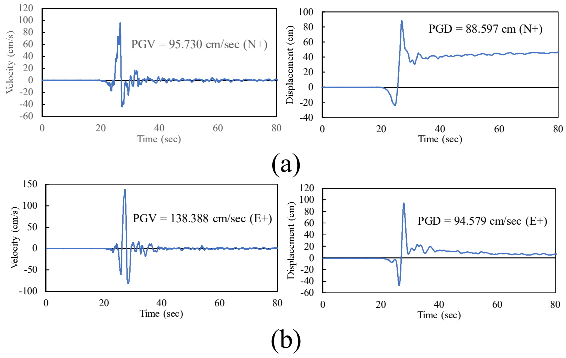

Figure 2. Input ground motions HWA019 (a) North-South direction (N+); (b) East-West direction (E+)

In the current parametric study, a hypothetical left-lateral strike-slip fault was assumed, with the vertical strike-slip fault assumed to have a north-south orientation. As such, along the direction parallel to the fault line, the ground motions in the N+ direction, as illustrated in Figure 2, were applied on opposite sides of the fault in opposite directions. Along the direction normal to the fault line, the ground motions in the E+ direction were applied on both sides of the fault line but in the same direction. Accordingly, it was not only the permanent ground displacements in the fault-parallel direction due to earthquake faulting that were applied in the present study, but the long-period pulses in the fault-normal direction due to rupture directivity were also taken into account. To investigate the effect of the fault direction on the seismic responses of the impacted bridges, the fault line was assumed to run at an angle of θ° with respect to the axis of the hypothetical bridge, and the surface fault rupture was assumed to cross the bridge between piers P2 and P3, as shown in Figure 3. In the current study, the axis of the bridges was assumed to be along the global x-axis. For ease of description, a local coordinate system for axes 1 and 2, which were parallel and normal to the fault line, respectively, was also defined.

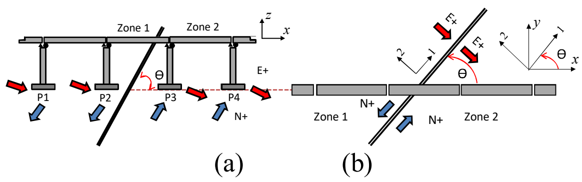

Fig. 3. Fault orientation for ground motion simulation (a) side view; (b) top view

Analytical Model

The selected bridge was analyzed using the structural analysis software Sap2000N. The simulation model is schematically shown in Figure 4, where both the girders and piers were modeled by elastic beam column elements. However, the plastic hinged areas located at the column bases were simulated using fiber elements to take into account its plastic behavior. The rubber bearing supports were modeled using friction isolators with different friction coefficients, and the seismic stoppers positioned beside the girders to provide transverse restraint were simulated using nonlinear link elements with an ultimate strength of 1.5 R_d (6510kN), according to design code, where R_d is the reaction force generated in the bearing support due to the dead load of the superstructure. There was a gap between the seismic stopper and the girder, where the gap was simulated by gap elements with different gap distances. In this study, it was assumed that only the transverse seismic stoppers were provided, and there was no restraint along the longitudinal direction. To consider the fault dislocation behavior associated with the ground motions, nonlinear time history analysis using multiple-support displacement excitation as input motions was conducted. During the analysis, the ground displacements as shown in Figure 2 were applied to each bridge pier base along the directions defined in Figure 3.

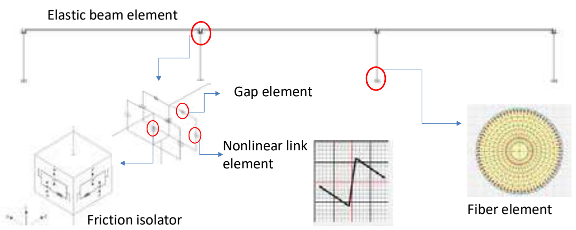

Figure 4. Schematic illustration of the simulation models

Parametric Study and Discussion

Bridges crossing fault-rupture zones experience ground offset across the fault line and hence also experience spatially varying ground motions. To investigate the effect of fault crossing on the seismic responses of simply supported bridges, a parametric study using nonlinear time history analyses with multiple-support displacement inputs was conducted. Three parameters were considered, which included the friction coefficient of the bearing, gap distance between the girders and seismic stoppers, and the orientation of the fault line. The mechanical responses calculated in this investigation included pier base reactions, hinge rotation at the plastic hinge zone, and the relative displacement between neighboring superstructures. Unless otherwise mentioned, for the current parametric analysis, the friction coefficient μ for each bearing was assumed to be 0.1. The gap distance between transverse seismic stoppers and girders was assumed to be 20 cm, and the fault line was assumed to be perpendicular to the axis of bridge, i.e., θ = 90°. Since the fault line was assumed to pass through the target bridge between piers P2 and P3, only the responses at P2 and P3 were presented in current paper for simplicity.

The analysis results obtained for the effect of the friction coefficient μ of the bearings on the maximum response of base shear, base torsion and hinge rotation angle obtained at pier base is shown in Figure 5. The hinge rotation, which indicates deformation demand in the column, was obtained from the rotation of the fiber element hinge at the column base. All the responses shown in Figure 5 are the maximum responses obtained from the time history analysis. The friction coefficients in this study included μ= 0.02, 0.1, 0.2, and 0.8. For the base shear shown in Figure 5 (a), V1 and V2 represent the shear forces experienced along the local axes 1 and 2, respectively. Because θ was assumed to be 90° for the current case, V2 and V1 in Figure 5 represent the shear force along the longitudinal and transverse directions of the bridge, respectively. As observed from the results, for the base shear acting along the longitudinal direction, where no restraint was provided, the shear response V2 increased significantly with the increasing friction coefficient because the friction forces transmitted by the bearing to the substructures also increased with the increasing friction coefficient. For the same reason, the hinge rotations of the plastic hinge zone around the y-axis exhibited a similar trend. Conversely, for the shear force acting along the transverse direction (V1), where a transverse restraint was located, the responses increased with an increase in the friction coefficient when the friction coefficient was equal or higher than 0.1. For the case of μ = 0.02, as the girder would collide with the seismic stoppers, and the resulting impact force due to the collision would also transmit to the substructure through the seismic stoppers, the corresponding responses observed were higher than those for μ = 0.1. The base torsional forces and the hinge rotation around the x-axis are given in Figure 5 (b) and (c), respectively, and also show a similar trend due to the same reason.

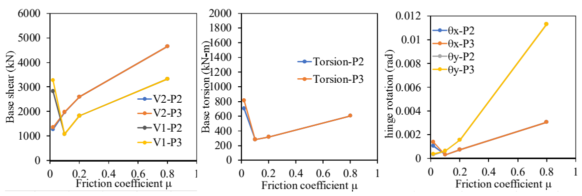

(a) (b) (c)

Figure 5. Effect of friction coefficient on the responses of: (a) base shear; (b) base torsion; (c) hinge rotation.

The effect of the gap distance between the girders and the seismic stoppers on the seismic responses of bridge was calculated and shown in Figure 6. The gap distance modelled varied from 0 to 40 cm. As expected, because the seismic stoppers were located in the transverse direction only, the gap distance had almost no effect on the shear forces acting along the longitudinal direction (V2). On the other hand, the effect of the gap distance on the shear forces acting along the transverse direction (V1) and the torsional forces was not found to function in a monotonic way. It was found that the maximum response occurred when the gap distance was equal to 5 or 10 cm. The response then declined with a decreasing gap distance when the gap distance was smaller than 5 cm. This observation was probably due to the impact forces arising from the collision between the girder and seismic stopper reducing as the gap distance decreased. Figure 6 also shows that the minimum response was observed for a gap distance of 40 cm. This observation is due to when the gap distance is as high as 40 cm, the girder did not collide with the seismic stopper under the modelled earthquake motions, and hence the inertial force of the superstructure induced by the earthquake excitation would only transmit to the substructure via the friction force of the rubber bearings.

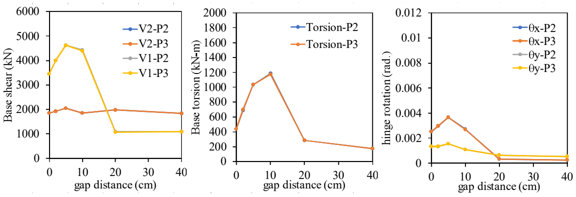

(a) (b) (c)

Figure 6. Effect of gap distance on the responses of: (a) Base shear; (b) Base torsion; (c) hinge rotation

Figure 7 shows the effect of the fault line orientation on the different responses. The direction of the fault line with respect to the axis of the bridge was varied from 0° to 180°. The case of θ = 0° and 180° represented the case where fault crossing was absent and replicated near fault conditions. Figure 7 (a) shows the base shear measured along the local axes 1 and 2, which were parallel and normal to the fault line, respectively. It was found that the response of P2 and P3 were almost symmetric to each other when θ = 90°. The shear force that was acting transverse to the fault line (V2) increased with increasing θ when θ > 90° and with decreasing θ when θ < 90°. Conversely, for the shear force acting parallel to the fault line (V1), the influence of fault direction was not as significant. The effect of fault line direction on the torsional forces shown in Figure 7 (b) exhibited similar trends to V2, where the torsional forces increased dramatically with increasing θ when θ > 90° and decreasing θ when θ < 90°. However, for the case of θ = 0° and 180°, which represents the case absent of fault crossing but with near fault consideration, the torsional forces at the column base were very limited. The effect of fault direction on the hinge rotation was also symmetric to θ = 90°. As the fault line was more inclined to the axis of the bridge, the hinge rotation angle increased. Figure 7 (d) shows the maximum relative displacement between neighboring girders along the longitudinal direction. It was found that for the bridges associated with fault crossing, the increase in the fault direction θ would lead to a decrease in the relative displacement, where when θ > 90°, the relative displacement became a negative value. This finding indicates that the neighboring girders collided with and squeezed each other. On the contrary, when θ < 90°, the relative displacement became a positive value, which suggests that the neighboring girders moved away from each other, and it is most likely that the girder would unseat from the substructure if the displacement exceeded the support length. By further comparing the results for the bridges modelled with and without fault crossing as shown in Figure 7, it can be noted that the influence of the fault crossing on the response of the bridge is mainly experienced in the torsional forces and relative displacement between neighboring girders in the longitudinal direction of the bridge. On the other hand, the influence of the fault crossing on the shear forces and hinge rotation angle was not that significant.

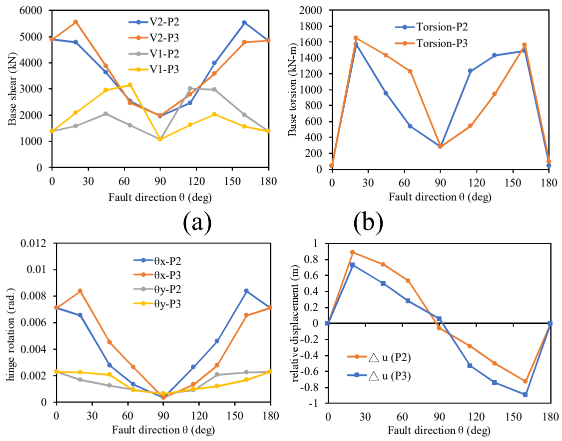

(c) (d)

Figure 7. Effect of fault line orientation on the responses of: (a) Base shear; (b) Base torsion; (c) hinge rotation; (d) relative displacement between neighboring girders along the longitudinal direction

Conclusion

In this study, rigorous nonlinear response history analyses were performed to parametrically investigate the effect of fault crossing on simply supported bridges. The seismic responses of bridges subjected to spatially uniform rather than spatially varying ground motions were also analyzed and compared. From this parametric study, several key parameters that affect the bridges responses were identified and discussed. The results also show that the boundary condition of the bearings has a significant effect on the response of simply-supported bridges in the event of an earthquake, and therefore the simulation of bearing systems should be as realistic as possible.

Study of the Near-Fault Effect on the Sloshing Mode of Storage Liquid in Tanks

Juin-Fu Chai[1], Fan-Ru Lin[2], Liang Shen[3], Wei-Hung Hsu[4], Zhi-Yu Lai[4] and Tzu-Chieh Chien[4]

柴駿甫 [1]、林凡茹 [2]、沈亮 [3]、徐瑋鴻 [4]、賴姿妤 [4]、簡子婕 [4]

Abstract

The long period velocity pulse is recognized as one of the characteristics of near-fault ground motions, and hence the response of vibration modes with lower frequencies will be amplified due to the effects of resonance. In general, the sloshing frequency of storage liquid in tanks is low and the period is similar to the pulse period of near-fault ground motions. Compared to far-field ground motions, the induced slosh height will be amplified significantly by the near-fault ground motions due to the resonant excitation. Therefore, it is worth considering the near-fault effect on the sloshing mode of liquid stored in tanks. This study aims to describe the test setup, the selection and processing of input motions including the original near-fault ground motions, the extracted velocity pulse or extracted band-pass signals for resonance analysis, and the impulse motion for free vibration. In addition, the experimental results are compared with the code-specified values as determined by the industrial standards and guidelines for general seismic conditions. It is expected that based on the test results, a more proper prediction equation can be proposed for the seismic design and evaluation of the spent fuel pool in nuclear power plants.

Keywords: sloshing mode; near-fault ground motions; spent fuel pool

Introduction

This study aims to investigate the dynamic behavior of the sloshing mode and to discuss the resonance phenomenon caused by the lower frequency content of near-fault ground motions on water contained in relatively stiff rectangular tanks in nuclear power plants.

Considering that the fundamental frequencies of plant buildings in horizontal directions are mainly above 5 Hz and the locations of spent fuel pools (SFPs) are at or near ground levels, the seismic response of the top portion of the fluid content in such a tank is mainly controlled by the sloshing mode at low frequencies, which might be resonant with low-frequency content of ground motion. Under the same zero period acceleration (0.67g) as depicted in Fig. 1, the 5% damped spectral acceleration values at the sloshing frequency of the near-fault ground motions recorded in the 1999 Chi-Chi earthquake are higher than the value of the NUREG/CR-0098 design spectrum [4]. To examine the rationality of the evaluation equations provided by the design guidelines, a series of shaking table tests were executed to discuss possible parameters that might influence the sloshing frequency f_c and slosh height h_s. In this study, the test plan including the design of the tank specimen and input motion is described in detail. The preliminary analysis results are presented for comparison with the code-specified values.

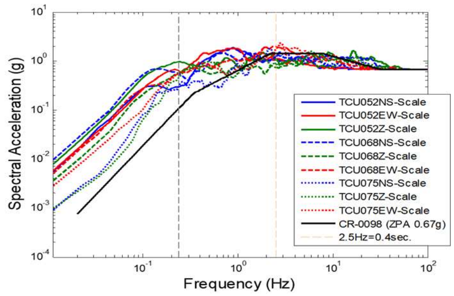

Fig. 1 – Response spectrum of the near-fault ground motions.

Design of the Tank Specimens

To investigate the sloshing behaviors of tanks with different dimensions, the rectangular tank set was

---

[1] Research Fellow and Deputy Director General, National Center for Research on Earthquake Engineering

[2] Associate Researcher, National Center for Research on Earthquake Engineering

[3] Graduated Student, National Taiwan University of Science and Technology

[4] Assistant Researcher, National Center for Research on Earthquake Engineering

designed with an inside width of 0.5 m and a length of 1.0 m, while the square tank set had an inside length of 1.0 m. The square tank set and the length of the rectangular tank set were for H_L/L = 0.5, and the width of the rectangular tank set was for H_L/L = 1.0. Both the square and rectangular tank sets with equal water levels were subjected to the same input motion simultaneously. By comparing the measured slosh height for the square and rectangular tank sets, the effect of adjacent orthogonal side length can be clearly compared. Furthermore, there were two testing tanks with different heights prepared for each tank set. The two tanks, with equal water level, were subjected to the same input motion simultaneously, such that the slosh height could be measured for the higher tank, and the volume of water splashing out of the tank could be estimated from the lower tank.

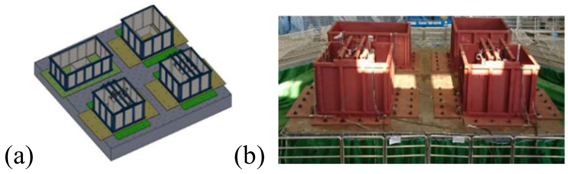

Fig. 2 – Specimens of the scaled tanks: (a) numerical models, and (b) test configuration.

Input Motion of the Shaking Table Tests

The shaking table is designed to simulate near-fault ground motions with frequency contents in the range of 0.1 to 30 Hz. In this study, the largest scale of input motions are limited by the capacity of the stroke or velocity of the shaking table. As shown in Fig. 3, to investigate the basic dynamic characteristics and seismic behavior of the contained water, the test types and respective input motions were designed as below:

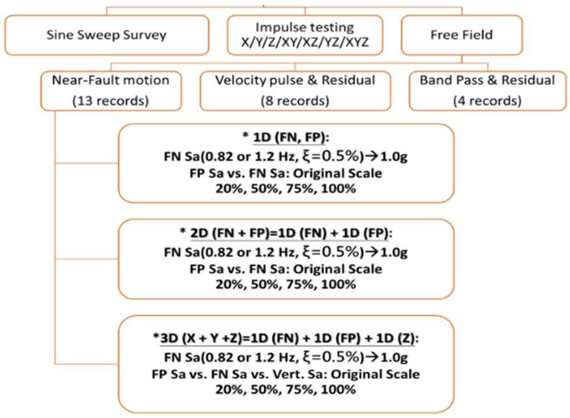

Fig. 3 – Categories of input motions.

1. System-identification tests: Sine-sweep survey and impulse tests were adopted in this study. The purpose of the sine-sweep survey is to obtain a more distinct modal shape of the water surface. Both kinds of input motions are designed to excite equal responses for each tested contained water with a sloshing frequency in the range from 0.3 Hz to 2 Hz. The spectral acceleration values of the impulse motion in the range from 0.3 to 2 Hz are approximately 0.14g.

2. Near-fault ground motion tests: Referring to the definition proposed by Baker [5], 91 near-fault motions with pulse-like properties were first selected from 3551 records stored in the PEER NGA West database [6]. The database provides the period of the velocity pulse T_p through wavelet analysis and the period of the peak spectral velocity T_{Sv} of the fault-normal (FN) component of each ground motion. Based on the designed water level (0.5 m) and tank dimensions, the sloshing frequencies can be predicted as 0.84 Hz for the direction with a length of 1.0 m. As shown in Fig. 4, to observe possible effects caused by a resonant response or a long-period velocity pulse on slosh height, thirteen records of seven earthquake events were selected from 91 records based on the comparison of T_p and T_{Sv} values.

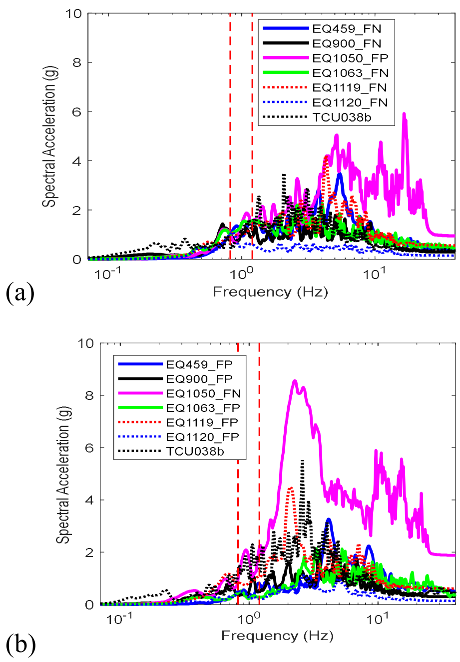

Fig. 4 – Normalized near-fault ground motions for square tanks in the (a) X and (b) Y directions.

3. Velocity-pulse (VP) and residual motion (RVP) tests: To clarify the effects of a velocity pulse at a resonant or non-resonant frequency on slosh height for comparison to the original near-fault ground motion test results, the velocity pulses and residual motions were extracted from RSN 451, RSN 459, RSN 900, RSN 1550, and RSN 1063 using the wavelet analysis MATLAB code provided by Baker [5]. To further study the influence of long-period energy on sloshing behavior, RSN 900 and 1550 were selected due to their remarkable long-period pulse characteristics

in three components. Taking RSN 900 as an example (Fig. 5), the FN and FP velocity pulses (depicted as red lines) of RSN 900 were extracted with T_p values of 7.637 s and 2.685 s, respectively. Meanwhile, the residual motions (depicted as black lines) keep other frequency content including the sloshing frequency of 0.8 Hz to 1.2 Hz and the T_{sv} of 0.7 Hz. By comparing the slosh heights resulting from the original near-fault ground motion, velocity-pulse, or residual motions, the contribution from the long-period pulse energy or resonant response to the sloshing behavior can be clarified.

(a)

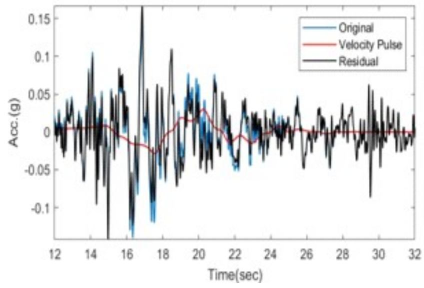

(b)

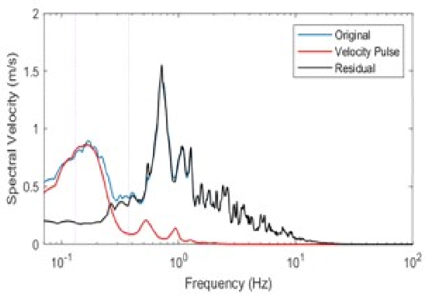

Fig. 5 – (a) Acceleration time histories and (b) velocity response spectra of RSN 900 in the FN direction.

4. Band-pass and residual motion tests: In addition to the wavelet analysis of velocity time histories, a band-pass frequency analysis for the accelerations of RSN 900 and 1550 were also derived in the frequency range of 0.730 Hz to 1.324 Hz.

Test Configuration

During the shaking-table tests, accelerometers and magnetostrictive linear-position sensors (Temposonic transducers) were used to record the responses of the tank specimens and their water contents. Four ± 5g tri-axial accelerometers were arranged on the steel bottom plate and the top of the square and rectangular tank walls, respectively, to record the acceleration response of the tank specimens. As shown in Fig. 6, nineteen displacement transducers were used for water level sensing applications. Four action cameras for each tank were attached directly on the top of the tank walls to record the entire test process of the movement of the water surface. The video records were also used to observe the sloshing and waving condition of the water surface and to ensure the accuracy of the water level measurements from the transducers by observing the achieved water levels noted by the attached waterproofed rulers.

(a)

(b)

Fig. 6 – Instrument configuration for the (a) rectangular and (b) square tanks.

Preliminary Test Results

1. Frequency

From the measured data of the acceleration of the tank specimens, the tank frequencies are above 30 Hz and are much higher than the frequency content of the input motions and the sloshing frequencies of the contained water. This implies that the effect of the impulsive mode might be neglected in the analysis of the dynamic behavior of the sloshing modes. On the other hand, Fig. 7 shows the relationship between the measured sloshing frequency and H_L/L. The dashed lines are the theoretical sloshing frequencies. The blue and black lines depict the relationship between the experimental sloshing frequency and H_L/L ratio under horizontal impulse motions. From Fig. 7, it can be seen that the experimental sloshing frequencies are quite close to but slightly higher than the theoretical values.

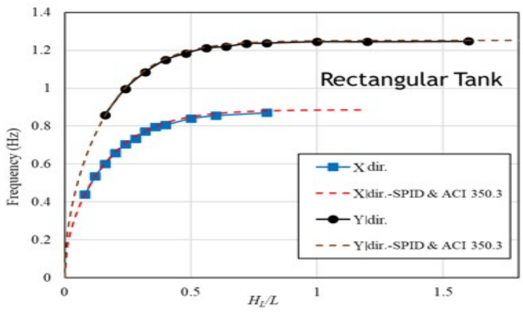

Fig. 7 – The relationship between sloshing frequencies and H_L/L for the stored waters in tanks.

2. Slosh height

Fig. 8 depicts the test results under uniaxial excitation. The abscissa of each point represents the input spectral acceleration at the convective frequency according to the test conditions (H_L = 0.5 m and L = 0.5 m or 1.0 m), while the ordinate represents the ratio of the measured slosh height to the value evaluated by SPID [2]. Spectral acceleration was calculated for a damping ratio of 0.35%. In addition, the measured slosh heights and those evaluated by SPID [2] and Chen [3] are also compared in Fig. 9. It can be seen from Fig. 8 and Fig. 9 that the evaluated results per SPID [2] are conservative for most test cases. However, it is still evident that in some cases the slosh height recorded experimentally greatly exceeds the theoretical prediction. According to the test results, other factors of influence might be further considered under strong input motions.

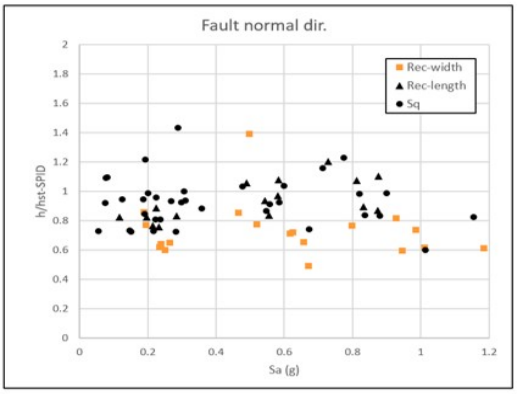

Fig. 8 – Ratio of the slosh height and evaluated height per SPID [2] in the FN (left) direction.

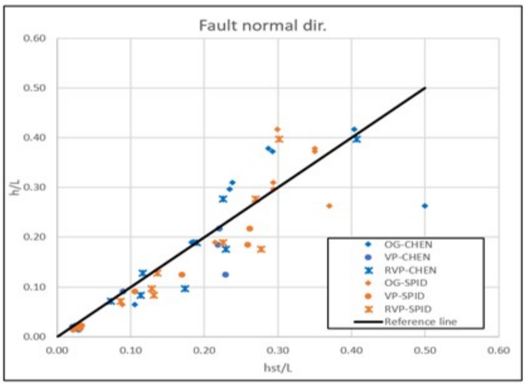

Fig. 9 – Relationship between the ratio of the measured slosh height to side length (h/L) and ratio of the evaluated value to side length (h_{st}/L) per SPID [2] and Chen [3] in the FN (left) direction.

Conclusions

The purpose of this experiment was to estimate the slosh height and the associated total volume of water splashing out of the tank under near-fault ground motions. Seven near-fault ground motions were selected to discuss the effects of resonant response and velocity pulse, and a total of 180 seismic tests were executed. Furthermore, the validity of the evaluation method for the frequency and slosh height and designated damping ratio value of the sloshing mode provided by SPID [2] and ACI350.3-06 [1] were discussed based on the results of the system identification tests. From the preliminary test results and a previous study for circular tanks [7], it can be seen that the evaluation of convective frequency is quite accurate under free vibration. However, the observed damping ratio decreased dramatically for a depth of stored water-to-length ratio H_L/L greater than 20 cm. The value of the damping ratio converged to approximately 0.35%, which is smaller than the value of 0.5% specified in ACI350.3-06 [1].

Alternatively, although SPID [2] is conservative for most of the test cases, the slosh height under two-dimensional input motion might exceed the predicted values per SPID [2]. Thus, it is recommended that the evaluation method for slosh height considers other possible factors of influence, and this will be discussed in the future study.

References

[1]. ACI Committee 350.3-06, *Seismic Design of Liquid-Containing Concrete Structures and Commentary*, American Concrete Institute, Farmington Hills, MI, 2010.

[2]. EPRI, Seismic Evaluation Guidance- Screening, Prioritization, and Implementation Details (SPID) for the Resolution of Fukushima Near-Term Task Force Recommendation 2.1: Seismic,

EPRI Report 1025287, 2013.

[3]. W. Chen, M. A. Haroun & F. Liu, Large amplitude liquid sloshing in seismically excited tanks, Earthquake Engineering and Structural Dynamics, Vol.25, Issue7, pp. 653-669, July 1996.

[4]. Newmark N. M. & Hall W. J., *Development of Criteria for Seismic Review of Selected Nuclear Power Plants*, Technical Report NUREG/CR-0098, U.S. NRC, May 1978.

[5]. Jack W. Baker, *Quantitative Classification of Near-Fault Ground Motions*, Bulletin of the Seismological Society of America, Vol. 97, No. 5, pp. 1486–1501, October 2007.

[6]. PEER Center, University of California, PEER NGA West database, https://ngawest2.berkeley.edu/

[7]. J.-F. Chai, F.-R. Lin, W.-H. Hsu, T.-C. Chien, Z.-Y. Lai, Z.-Y. Lin, *experimental study of near-fault effect on sloshing mode of storage liquid in tanks*, PVP2019- 93388, Proceedings of the ASME 2019, San Antonio, TX, USA.

Analytical Study of Effects of Near-Fault Ground Motion on Seismically Isolated Structures

Wang-Chuen Lin[1], Jenn-Shin Hwang[2], Cho-Yen Yang[3], Chung-Han Yu[4] and Shiang-Jung Wang[5]

林旺春[1]、黃震興[2]、楊卓諺[3]、游忠翰[4]、汪向榮[5]

Abstract

The concept of seismic isolation design is accepted as an effective method for the seismic mitigation of structures. However, in Taiwan, an earthquake prone island, many sites are located in near-fault zones. The recorded seismic waves have near-fault characteristics such as velocity pulses and displacement pulses. These seismic waves may cause excessive displacement demand on the isolation system, and transmit significant acceleration to the superstructure. Consequently, the design of seismically isolated structures located in near-fault areas is challenging.

The objective of the study is to develop a suitable design strategy for an isolation system to resist near-field ground motion. The code-specified procedure is examined for their appropriateness of designing seismic isolation system against near-fault ground motions. A design procedure is proposed for the isolation system composed of lead-rubber bearings and viscous dampers. Results show that the proposed procedure can lead to controllable maximum displacement of the isolation system and an acceptable acceleration transmitted to the superstructure.

Keywords: Near-fault ground motion; Seismic isolated system; Lead-rubber bearing; Viscous damper.

Introduction

Seismic isolation technology has been regarded as one of the most effective strategies to enhance the safety and functionality of buildings, infrastructure, and equipment. However, seismically isolated structures located on soft ground, such as the Taipei basin, and near-fault areas is challenging. Because the recorded seismic waves of soft ground and basin have a long period, they cause a large displacement response of the isolation system. The recorded seismic waves of near-fault ground motions have marked characteristics such as velocity pulses and displacement pulses. The main difference between near-fault ground motion and far-field ground motion is that the velocity of near-fault ground motion has accompanying pulses with long periods (Somerville et al., 1997). These seismic waves of near-fault ground motion may cause excessive displacement demand on the isolation system and transmit significant acceleration to the superstructure (Hall et al., 1995) (Heaton et al., 1995) (Kasalanati and Constantinou, 1999) (Kelly, 1999).

In 2007, Jack.W. Baker (2007) proposed a method, based on wavelet analysis, to quantitatively identify velocity pulses of near-fault ground motion. In 2014, Shahi and Baker (2014) developed a more reliable method by optimizing some criteria to extract the largest velocity pulse from the given near-fault ground motion. The proposed algorithm was then used to classify each record in the NGA-West2 database and a total of 244 near-fault ground motion records were identified. These records have been used as the basis for the study of the effects of near-fault ground motion on civil infrastructure.

For the purpose of designing an isolation system against near-fault ground motions, the current isolation

[1] Associate Researcher, National Center for Research on Earthquake Engineering, wclin@ncree.narl.org.tw
[2] Courtesy Researcher, National Center for Research on Earthquake Engineering, jshwang@ncree.narl.org.tw
[3] Assistant Researcher, National Center for Research on Earthquake Engineering, cyyang@ncree.narl.org.tw
[4] Assistant Researcher, National Center for Research on Earthquake Engineering, chyu@ncree.narl.org.tw
[5] Courtesy Researcher, National Center for Research on Earthquake Engineering, sjwang@ncree.narl.org.tw

design specifications generated from the equivalent linear analysis are examined for their accuracy and appropriateness in predicting seismic responses of isolation systems subject to near-fault ground motion. Maximum seismic responses obtained from various equivalent linear models using linear dynamic analysis are compared with those determined by nonlinear dynamic analysis.

Selection of Ground Motions

To investigate the characteristics of near-fault ground motions, this study uses the following two approaches for determining near-fault earthquakes with significant maximum incremental velocity: (1) When two obvious velocity values passing through zero do not have any clear peak values, the recorded earthquake histories possess clear maximum incremental velocity. Otherwise, the velocity histories do not pass the zero value between two obvious peak values, and the peak values have the same direction. (2) When between two obvious peak values, velocity histories passing the zero value have clear peak values it can be concluded that they do not have clear maximum incremental velocity. As stated above, this study also adopts the method from Shahi and Baker (2014) to define near-fault earthquakes for analysis and discussion.

Based on the results of the selected approaches, seven recorded near-fault earthquake histories are selected, including TCU052 and TCU102 of strong ground motion stations in the E–W direction during the 1999 Taiwan Chi-Chi Earthquake, HWA014, HWA019, and MND016 of strong ground motion stations in the E–W direction during the 2018 Hualien Earthquake, Bam of strong ground motion station during the 2003 Bam Earthquake as well as Rinaldi of strong ground motion station during the 1994 Northridge Earthquake (see Table 1). Three far-field earthquake histories are selected, namely the 1940 El Centro earthquake as well as TCU074 and TCU089 of strong ground motion stations in the E–W direction during the 1999 Taiwan Chi-Chi Earthquake, as shown in Table 2.

Table 1. Information on near-fault ground motions

Station	Direction	PGA (g)	PGV (cm/s)	Incremental Velocity (cm/s)	Duration (s)
TCU052	EW	0.36	174.6	260.72	33.705–35.31
TCU102	EW	0.31	87.4	159.22	35.895–36.96
HWA014	EW	0.32	146.5	251.83	25–26.145
HWA019	EW	0.41	138.4	220.54	27.29–28.47
MND016	EW	0.31	133.6	212.11	26.52–27.815
Bam	L	0.81	124.1	182.55	17.175–17.85
Rinaldi	228	0.87	148.0	245.66	2.45–2.86

Table 2. Information on far-field ground motion

Station	Direction	PGA (g)	PGV (cm/s)
El Centro	NS	0.28	30.93
TCU074	EW	0.60	70.6

Proposed procedure for the isolation system design

As shown in Figure 1, the proposed design procedure is provided for the isolation system composed of lead-rubber bearings and viscous dampers in this study. Based on the fact that the weight (*W*) of the structure above the isolation interface is 500tf, and on TCU052 of strong ground motion stations in the E–W direction during the 1999 Taiwan Chi-Chi Earthquake, 0.05W of the characteristic strength (Q_d) of the lead-rubber bearings and 40% of effective damping ratio (ξ_e) of the isolation system were taken as an example. The calculation formulas and detailed procedure are as follows.

1. Assuming that the natural period (*T*) is 1 s and the strain hardening ratio (α_b) is 0.05, the parameters of the isolation system can be calculated as follows:

$$K_u = \frac{4\pi^2 W}{T^2 g} = 4.024W \tag{1}$$

$$K_d = \alpha_b \times K_u = 0.2012W \tag{2}$$

$$F_y = \frac{Q_d}{(1-\alpha_b)} = 0.053W \tag{3}$$

$$D_y = \frac{F_y}{K_u} = 0.013 \quad \text{m} \tag{4}$$

2. The 5% damped acceleration response spectra of the TCU052 of recorded earthquake history are used for design and analysis.
3. Assuming that the effective damping ratio (ξ_e) is 40% and the design displacement (D_d) is 0.3 m in the first iteration by adopting an iterative method.
4. The maximum force (F_d) at the corresponding design displacement (D_d), the effective stiffness (K_{eff}), the effective period (T_{eff}), the effective damping ratio (ξ_b) of lead-rubber bearings and the design spectral response acceleration (S_{aD}) can be calculated as follows.

$$F_d = Q_d + K_d \times D_d = 0.11W \tag{5}$$

$$K_{eff} = \frac{F_d^+ + F_d^-}{D_d^+ + D_d^-} = 0.37W \tag{6}$$

$$T_{eff} = 2\pi\sqrt{\frac{W}{K_{eff}\, g}} = 3.31\,\text{s} \tag{7}$$

$$S_{aD} = 0.413 \tag{8}$$

$$\xi_b = \frac{4Q_d(D_d - D_y)}{2\pi E_s} = 0.276 \tag{9}$$

5. Based on the value of effective damping ratio (ξ_e), the damping factor (B_1) can be obtained and the new design displacement (D_d) can be computed by an iterative method. Repeating steps 4 and 5 as necessary, the more accurate design displacement (D_d) can be converged and found.

$$D_d = \frac{g}{4\pi^2 B_1} S_{aD} T_{eff}^2 = 0.662 \quad \text{m} \tag{10}$$

6. Checking the design displacement (D_d) as a practical design value, the updated maximum force (F_d) at the corresponding design displacement can be calculated. If the design displacement (D_d) is not a reasonable value, the design should be restarted from step 3.
7. Assuming that the nonlinear exponent (α_d) of the nonlinear viscous dampers is 0.3, the damping coefficient (C_d) can be computed as below:

$$C_d = \frac{(2\pi)^{3-\alpha} T_{eff}^{\alpha-2} \xi_d}{\lambda D_d^{\alpha-1}} \frac{W}{g} \text{ m} = 37.9\text{tf-(s/m)}^{0.3} \tag{11}$$

The final parameters of the isolation system can be obtained by an iterative method.

Therefore, the characteristic strength (Q_d) from $0.03W$ to $0.09W$ with an increment of $0.02W$ and effective damping ratio from 30% to 60% with an increment of 10% are designed in this study. The yielding displacements are calculated to be 0.8, 1.3, 1.8, and 2.4 cm, respectively.

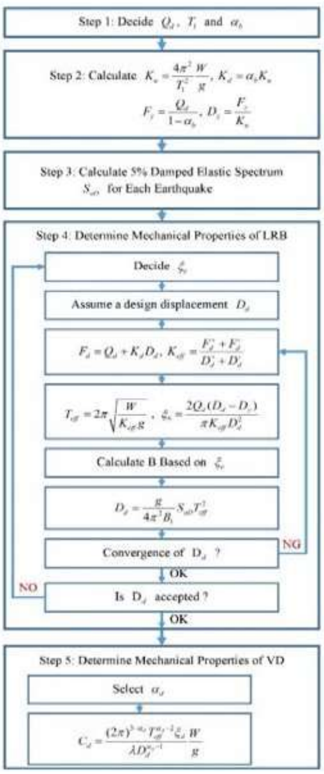

Figure 1. Proposed procedure for the isolation system design composed of lead-rubber bearings and viscous dampers.

Analytical Study and Discussion

Taking the design and analysis results of TCU052 and HWA019 of strong ground motion stations as an example, the parameters and responses of the isolation system are illustrated in Tables 3 and 4. It can be seen that the displacement responses of the isolation system composed of lead-rubber bearings and viscous dampers from the dynamic analysis results are less than the displacement responses from the static analysis results. However, the displacement responses of the isolation system without viscous dampers from the dynamic analysis results are more than the displacement responses from the static analysis results.

For the same characteristic strength, the isolation system with viscous dampers can effectively suppress the displacement responses due to the increase in the equivalent damping ratio. Therefore, the isolation system with viscous dampers will not increase the transmission horizontal force greatly and the transmission horizontal force is also decreased. It is revealed that the force of the viscous dampers will increase as the damping ratio increases.

Tables 3 and 4 show that when the effective damping ratio is 40%, the displacement responses from the dynamic analysis are predicted effectively by the design displacement from the static analysis. However, it is also evident that when the effective damping ratio is increased, the displacement responses from the dynamic analysis are much smaller than the design displacement from the static analysis due to the increase of the damper force.

Table 3. Design results for recorded earthquake histories of TCU052

Q_d (tf)	ξ_e (%)	D_d (cm)	F_{max} (W)	T_{eff} (s)	ξ_b (%)	ξ_d (%)	C_d $(tf \cdot (sec/m)^{0.3})$	D_{dyn} (cm)	F_{dyn} (g)	$F_{LRB,dyn}$ (W)	$F_{VD,dyn}$ (W)
0.03W		147.8	0.33	4.26	5.8			160.3	0.35	0.35	
	30	81.9	0.23	4.11	9.7	20.3	31.7	90.7	0.26	0.21	0.07
	40	77.1	0.24	4.09	10.2	29.8	45.0	75.3	0.25	0.18	0.09
	50	74.4	0.25	4.08	10.5	39.5	58.4	61.0	0.24	0.15	0.12
	60	74.4	0.27	4.08	10.5	49.5	73.2	47.2	0.23	0.13	0.14
0.05W		92.5	0.24	3.97	13.3			123.8	0.30	0.30	
	30	74.8	0.22	3.87	15.6	14.4	23.4	91.5	0.26	0.23	0.05
	40	71.6	0.24	3.85	16.1	23.9	37.9	73.9	0.25	0.20	0.08
	50	69.5	0.25	3.84	16.5	33.5	52.3	58.3	0.24	0.17	0.10
	60	69.5	0.27	3.84	16.5	43.5	67.9	43.7	0.23	0.14	0.12
0.07W		82.1	0.24	3.75	18.5			112.7	0.30	0.30	
	30	72.9	0.23	3.68	20.0	10.0	17.4	89.2	0.27	0.25	0.04
	40	69.6	0.25	3.65	20.7	19.3	32.9	70.4	0.26	0.21	0.07
	50	67.4	0.26	3.63	21.1	28.9	48.6	53.4	0.24	0.18	0.09
	60	67.4	0.28	3.63	21.1	38.9	65.4	38.3	0.24	0.15	0.12
0.09W		75.6	0.24	3.54	22.9			101.9	0.29	0.29	
	30	70.9	0.24	3.50	23.8	6.2	11.5	86.8	0.28	0.26	0.02
	40	67.7	0.26	3.47	24.5	15.5	28.2	66.6	0.26	0.22	0.06
	50	65.5	0.27	3.45	24.9	25.1	45.1	48.7	0.25	0.19	0.09
	60	65.5	0.30	3.45	24.9	35.1	63.1	33.5	0.24	0.16	0.11

As mentioned above, it is evident that the effect of viscous damping is not estimated adequately from the damping factor (B_1) in the static design procedure. By contrast, results show that the proposed procedure for the isolation system composed of lead-rubber bearings and viscous dampers can provide controllable maximum displacement of the isolation system and an acceptable acceleration transmitted to the superstructure to resist near-field ground motion. Hence, this study suggests that the design procedure can be applied in engineering practice.

Table 4. Design results for recorded earthquake histories of HWA019

Q_d (tf)	ξ_e (%)	D_d (cm)	F_{max} (W)	T_{eff} (s)	ξ_b (%)	ξ_d (%)	C_d $(tf \cdot (sec/m)^{0.3})$	D_{dyn} (cm)	F_{dyn} (g)	$F_{LRB,dyn}$ (W)	$F_{VD,dyn}$ (W)
0.03W		149.0	0.33	4.26	5.8			165.1	0.36	0.36	
	30	96.2	0.26	4.16	8.5	21.5	36.8	104.2	0.29	0.24	0.09
	40	92.3	0.28	4.15	8.8	31.2	52.1	82.0	0.27	0.20	0.12
	50	89.8	0.29	4.14	9.0	41.0	67.4	63.5	0.26	0.16	0.15
	60	89.8	0.32	4.14	9.0	51.0	83.9	48.3	0.26	0.13	0.18
0.05W		125.4	0.30	4.09	10.4			157.9	0.37	0.37	
	30	98.1	0.28	3.99	12.7	17.3	32.2	99.7	0.30	0.25	0.08
	40	94.1	0.30	3.98	13.1	26.9	48.9	75.5	0.27	0.20	0.11
	50	91.5	0.31	3.97	13.4	36.6	65.5	56.7	0.26	0.16	0.14
	60	91.5	0.34	3.97	13.4	46.6	83.4	42.4	0.26	0.14	0.17
0.07W		118.6	0.31	3.93	14.2			147.0	0.37	0.37	
	30	99.3	0.30	3.85	16.2	13.8	27.6	95.1	0.30	0.26	0.07
	40	95.4	0.32	3.83	16.7	23.3	45.6	69.1	0.27	0.21	0.10
	50	92.8	0.34	3.81	17.0	33.0	64.0	50.1	0.27	0.17	0.14
	60	92.8	0.37	3.81	17.0	43.0	83.3	37.3	0.28	0.14	0.17
0.09W		112.8	0.32	3.78	17.7			131.1	0.35	0.35	
	30	100.1	0.32	3.72	19.2	10.8	23.0	89.7	0.30	0.27	0.05
	40	96.2	0.33	3.69	19.7	20.3	42.6	61.9	0.27	0.21	0.09
	50	93.5	0.36	3.68	20.1	29.9	61.8	44.2	0.27	0.18	0.13
	60	93.5	0.39	3.68	20.1	39.9	82.5	33.5	0.29	0.16	0.16

Conclusions

Results show that the isolation system composed of lead-rubber bearings and nonlinear viscous dampers can not only effectively suppress extremely large displacement of the isolation system subjected to near-fault ground motion but also achieve acceptable maximum displacement responses in practical applications.

Therefore, in order to achieve the expected seismic-resistance performance provided by the isolation design to structures located in the near-fault area, this study suggests adopting nonlinear viscous dampers within the isolation system and the use of a smaller characteristic strength (Q_d) and a larger effective damping ratio to apply earthquake reduction effects rapidly and achieve controllable maximum displacement responses.

The analysis results show that the difference between the displacement responses of the dynamic analysis results and the design displacement of the static analysis results is significant in some case studies. Therefore, the damping factor (B_1) from the design code procedure should be adjusted accordingly and the design displacement of isolation systems composed of lead-rubber bearings and viscous dampers must be reduced by the nonlinear dynamic analysis procedure.

References

Hall, J. F., Heaton, T. H., Halling, M. W. and Wald, D. J. "Near-Source Ground Motion and Its Effects on Flexible Buildings," EERI Earthquake Spectra, Vol. 11, No. 4, 1995.

Heaton, T. H., Hall, J. F., Wald, D. J. and Halling, M. W. "Response of High-Rise and Base-Isolated Buildings to a Hypothetical Mw 7.0 Blind Thrust Earthquake," Science Vol. 267, pp. 206-217, 1995.

Jack W. Baker, "Quantitative Classification of Near-Fault Ground Motions Using Wavelet Analysis," Bulletin of the Seismological Society of America, Vol. 97, No. 5, pp. 1486–1501, 2007.

Kasalanati, A. and Constantinou, M. C., Experimental Study of Bridge Elastomeric and Other Isolation and Energy Dissipation Systems with Emphasis on Uplift Prevention and High Velocity Near-Source Seismic Excitation, MCEER Report, MCEER-99-004, SUNY, Buffalo, 1999.

Kelly, J. M. "The role of damping in seismic isolation," Earthquake Engineering & Structural Dynamics, Vol. 28 Issue 1, pp. 3-20, 1999

Shahi, S. K., and Baker, J. W. (2014), "An Efficient Algorithm to Identify Strong-Velocity Pulses in Multicomponent Ground Motions." Bulletin of the Seismological Society of America, Vol. 104, No.5, pp. 2456-2466.

Somerville, P. G., N. F. Smith, R. W. Graves, and N. A. Abrahamson. "Modification of empirical strong ground motion attenuation relations to include the amplitude and duration effects of rupture directivity," Seismological. Research. Letters. 68, no. 1, 199–222. 1997.

Seismic Failure Modes and Assessment of Underground Pipelines

Hsuan-Chih Yang [1] and Wei-Kuang Chang[2]

楊炫智 [1]、張為光 [2]

Abstract

Taiwan is located at the junction of the Eurasian and the Philippine plates in the Pacific Rim seismic zone, where disastrous earthquakes have repeatedly occurred. As a result, Taiwan has a rich geography, with mountains, forests, basins, plains, and bay shores. It also has geological conditions such as alluvium and backfill that are prone to soil liquefaction. When earthquake disasters occur, they are accompanied by immense social shocks and economic losses. For example, a magnitude 6.6 earthquake in the Meinong area of Kaohsiung on February 6, 2016 caused many buildings to collapse and be destroyed in the Tainan area. At the same time, the soil liquefaction caused building subsidence in many places, and many water supplies were also interrupted by water bursts due to the earthquake and the collapse of Weiguan Building. Additionally, natural gas systems are also decompressed to avoid secondary disasters. During the 1999 Chi-Chi earthquake, additional major disasters occurred such as subgrade cracking and lateral shifting due to soil liquefaction, underground pipe rupture and floating, and subsidence along wharves. Few studies have investigated underground pipeline earthquake risk assessment. The seismic design of underground pipelines and their failure modes requires careful evaluation and consideration to avoid disasters. Furthermore, this also enables the assessment of damage and loss caused by an earthquake to the pipeline, which can be used as a reference for disaster prevention, emergency response, or post-disaster recovery.

Keywords: Underground pipeline, Failure mode, Seismic assessment

Introduction

Many important lifeline systems in Taiwan are buried pipes due to innate local factors such as location and topographical conditions. Although geologically fragile areas have been avoided during design and construction to decrease the seismic risk, some buried lines still inevitably pass through earthquake faults, soil liquefaction, and landslide sensitive areas. Ground movements, soil damage and soil liquefaction that occur during strong earthquakes cause damage to underground pipelines. For example, the 1964 Niigata earthquake in Japan caused severe soil liquefaction and subsequent building subsidence and failure of underground oil pipes.

The seismic performance of underground pipelines in metropolitan areas requires review due to their complex nature and age. Once a main pipeline is ruptured or damaged, it will cause inconvenience to the people in the disaster area and may even cause an explosion. The Chi-Chi earthquake in 1999 caused significant damage to important lifeline systems in Taiwan. The fault displacement caused buckling and fracture failure of the 2000 mm diameter pipeline of the Fengyuan water treatment plant in Taichung, with the extent of the damaged natural gas pipeline reaching 827,527 meters. Furthermore, the Northridge earthquake caused the rupture of the gas system and fire damage resulting in huge economic loss.

Due to uncertainty in pipeline distribution and location and varying geological conditions in different regions, pipelines built in different years may have different probabilities of damage under different earthquake scales. Therefore, assessing seismic behavior and reinforcement of the underground pipelines are urgently required.

[1] Associate Researcher, National Center for Research on Earthquake Engineering, hcyang@narlabs.org.tw.

[2] Associate Researcher, National Center for Research on Earthquake Engineering, wkchang@narlabs.org.tw

Underground Pipeline Failure Modes

Due to the wide range of pipeline types, different materials and joints can be used according to their different functions, temperatures, fluids, flows, pressures, etc. Generally, different classifications can be given according to functions, fluid conditions, materials, production methods, and structural styles. In Taiwan, cast iron pipes, steel pipes, plastic pipes, cement pipes, etc., are commonly used. However, damage resulting from earthquakes may occur regardless of the pipeline material used.

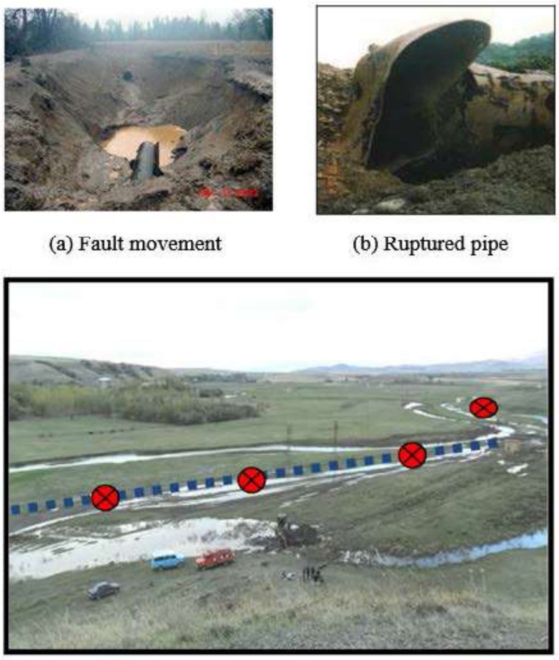
(a) Fault movement (b) Ruptured pipe

(c) Liquefaction and landslide

Figure 1. Damaged underground pipelines.

Many cases of underground pipeline damage can be found in earthquake disasters in Taiwan and abroad, as shown in Figure 1. The modes of pipeline damage caused by earthquakes can be divided into three categories:

1. Fault displacement:

   When fault movement occurs in an earthquake, the pipeline is sheared, pulled, squeezed to fracture, folds, or suffers joint damage. The leakage of the pipeline contents can easily cause secondary disasters and serious environmental pollution.

2. Soil liquefaction:

   The 1964 Niigata earthquake in Japan caused damage to underground oil pipelines with diameters between 100 to 300 mm, with a frequency of damage of 0.97 times/km. The leaked oil burned on the water surface, eventually causing more than 1,000 deaths.

3. Landslide phenomenon

   A giant landslide (1.1 × 108 m^3) was caused by the magnitude 6.9 earthquake in Ecuador in 1987. A 660 mm crude oil pipeline ruptured and the damaged length was 40 km, causing an economic loss of USD 850 million.

According to the damage modes of the pipeline, damage can be divided into pipeline fracture (pulling, shearing, and bending), pipe joint detachment, and pipeline buckling. Pipeline breaks or joint damage is due to the soil being pulled, sheared, or a lost support. Pipeline buckling occurs when a weak interlayer or liquefaction region is sandwiched in the pipeline path, which is pushed on both sides, and buckling occurs in a weak medium region. Ground deformation or displacement can cause more damage to the pipeline as compared with seismic acceleration. Therefore, the ground deformation can be divided into two parts. The first part is the ground strain, which is caused by the propagation of seismic waves, and does not result in permanent large deformations. The second part is ground displacement, which is usually caused by faults, soil liquefaction, subsidence, and slope slip. In addition to the above conditions, there is also indirect damage to pipelines after earthquakes, such as in the connection between the pipeline and the structure, floods, explosions, fires, or damage to the pipeline support equipment. Figure 2 shows statistics of pipeline damage in the United States after an earthquake. There is a positive relationship between the peak ground velocity and the pipeline failure rate.

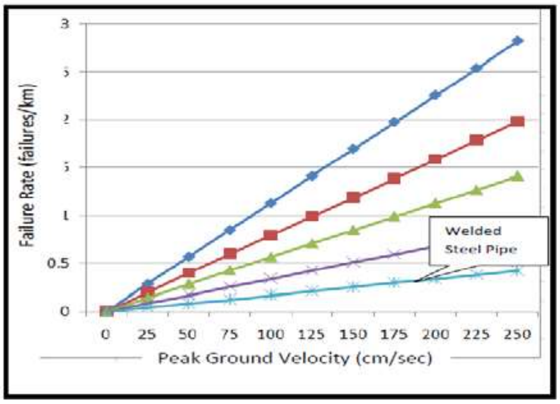

Figure 2. The failure rate versus peak ground velocity [ALA (2001)].

Underground Pipeline Seismic Design and Assessment

Taiwan's seismic data and related codes are continuously updated and adjusted with annual surveys and studies. Therefore, early pipeline seismic design may no longer meet today's seismic requirements. The structural materials may have become fragile due to aging and corrosion after many years. To ensure that new and existing pipelines are protected from future seismic hazards, local design codes and seismic assessment methods must be developed as soon as possible.

1. Seismic design

The seismic design codes of domestic pipelines are still mainly based on the seismic design codes of buildings. Three types of earthquake levels and seismic design goals are mainly considered. In addition, in the code a coefficient “I” is used for each type of building that will amplify the designed seismic level. Generally, the value of “I” in the building is 1, and the value of “I” for storing explosive items such as petroleum will be taken as 1.5.

Pipelines are usually designed with reference to foreign pipeline codes. ASME B31 in the American Society of Mechanical Engineers (ASME) pressure pipeline code is the most commonly used reference design specification. This code also reduces the corresponding stress under the state of the pipeline and different design stresses, as shown in Table 1.

Table 1. ASME B31 pipeline yield stress.

Location	Internal and External Pressure Stress, S_x	Allowable Expansion Stress, S_E	Additive Longitudinal Stress, S_L	Sum of Longitudinal Stresses From Sustained and Occasional Loads	Equivalent Combined Stress, S_{eq}	Effective Stress for Casing or Uncased Pipe at Road or Railroad Crossings
Restrained pipeline	$0.72(E)S_y$	$0.90S_y$	$0.90S_y$ [Note (1)]	$0.90S_y$	$0.90S_y$	$0.90S_y$ [Note (2)]
Unrestrained pipeline	$0.72(E)S_y$	S_A [Note (3)]	$0.75S_y$ [Note (1)]	$0.80S_y$	n/a	$0.90S_y$ [Note (2)]
Riser and platform piping on inland navigable waters	$0.60(E)S_y$	$0.80S_y$	$0.80S_y$	$0.90S_y$	n/a	n/a

GENERAL NOTES:
(a) S_y = specified minimum yield strength of pipe material, psi (MPa)
(b) E = weld joint factor (see Table 403.2.1-1)
(c) In the setting of design factors, due consideration has been given to and allowance has been made for the underthickness tolerance and maximum allowable depth of imperfections provided for in the specifications approved by the Code.
(d) S_L in the table above is the maximum allowable value for unrestrained piping calculated in accordance with para. 402.6.2. The maximum value of S_L for restrained pipe is calculated in accordance with para. 402.6.1.
(e) See para. 403.10 for allowable stresses of used pipe.

NOTES:
(1) Beam-bending stresses shall be included in the longitudinal stress for those portions of the restrained or unrestrained line that are supported aboveground.
(2) Effective stress is the sum of the stress caused by temperature change and from circumferential, longitudinal, and radial stresses from internal design pressure and external loads in pipe installed under railroads or highways.
(3) See para. 403.3.2.

2. Seismic assessment

The design examination meeting at the design stage provides a pipeline stress analysis report in accordance with the regulations and owner specifications. The pipeline stress analysis report will include the pipeline supports that need to be set due to seismic requirements. After the construction and installation of underground pipelines, the seismic assessment will not be carried out, including the impact of faults or soil liquefaction on underground pipelines. The process is divided into three stages:

(1) Preliminary assessment: As a simple, fast, and subjective assessment, which is more conservative and rough, a checklist is used to score whether there is any doubt about earthquake resistance. It is based on the pipeline information, site environment, structural form, pipeline status, capacity demand ratio, and matching site survey. However, since the underground pipeline is deep in the soil, the assessment of the current situation needs to be performed by non-destructive testing.

(2) Detailed assessment, simple model:

This is the second stage of seismic assessment, in which the seismic performance is checked separately by the standard seismic design calculation method. The formulae of the ASME B31.4 modified seismic design guidelines for liquid pipeline systems using the static and elastic analysis methods are used for evaluation. The static model mainly considers the influence of wave propagation, liquefaction (differential subsidence), fault displacement, stress in the pipe, and thermal changes on the pipeline. The displacement of the pipeline is not taken into account, and the allowable stress is used for calculation and analysis only. The stress analysis must consider radial stress, longitudinal stress, shear stress, and equivalent stress, and must include all relevant permanent, temporary, and seismic load induced effects. In addition to considering permanent effects, it must be carried out for different seismic load combinations. Figures 3 and 4 show simplified analysis models considering pipelines passing through faults and soil liquefaction, respectively.

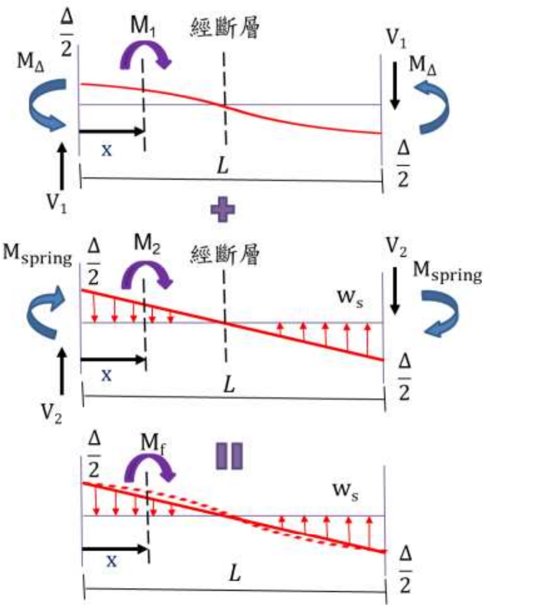

Figure 3. Simplified analysis models of a pipeline passing through a fault.

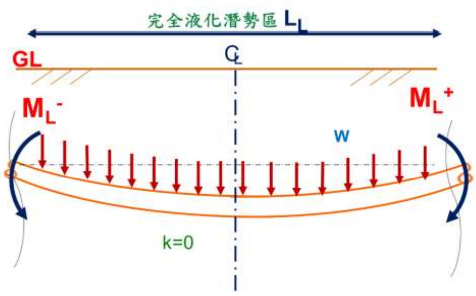

Figure 4. Simplified analysis models of a pipeline at a liquefaction area.

Seismic Reinforcement of Underground Pipelines

At present, most underground pipelines are designed for seismic resistance in accordance with building seismic design codes only at the design process. There is no seismic evaluation and monitoring during the operation phase. Therefore, the pipeline can be reinforced by the following methods:

1. Improving seismic assessment in standards for underground oil pipelines

   After the great Hanshin earthquake in Japan in 1995, Japan reviewed and revised relevant seismic design codes for various pipeline seismic design standards. The seismic standards of Japan are mainly divided into two grades "A "and "B" to consider the use of the facility, importance, earthquake scale and frequency, and other conditions for seismic assessment. The geological conditions in Taiwan are poor. The importance of the facility and the geographical characteristics of the area should be considered. For pipeline facilities in areas with liquefaction potential and fault margins, the seismic design standards should be appropriately raised to reduce the damage to pipeline facilities after earthquakes and to prevent system paralysis.

2. Using the earthquake-resistant pipes and joints

   Ductile cast iron pipe (DIP) and steel pipe (SP) joints with higher seismic resistance can be considered. The anti-deformation devices are added to the joints to absorb large displacements and improve the phenomenon of joints failing after earthquakes. Seismic-resistant materials such as welded steel pipes, flexible pipes, low-pressure screw joint steel pipes, etc., can be used, which are optimal for earthquake resistance.

3. Increase the site condition

   Depending on the equipment configuration, appropriate site improvement methods should be adopted to enhance the structural foundation's resistance to uneven subsidence. Soft sand backfill can also be used to increase the flexibility of the pipeline.

4. Earthquake monitoring and system control

   Underground pipeline facilities are likely to cause large-scale damage after a strong earthquake. A suitable earthquake monitoring system can be used to transmit seismic information rapidly to a control center, where the scope and extent of the disaster can be determined for reference by decision makers to take emergency measures.

Conclusion

After the 1999 Chi-Chi earthquake in Taiwan, attention has been focused on the seismic resistance of underground pipelines. However, they are often forgotten over time, as the pipelines are deep in the soil. Most pipelines have no subsequent seismic assessment and reinforcement schemes after the completion of the design phase. This will expose the underground pipelines to a very high risk of damage due to an earthquake. Future research should consider the seismic performance of underground pipelines and their evaluation methods.

Reference

1. ALA, American Lifelines Alliance, Seismic fragility formulations for water systems, 2001.
2. ASME-B31.4, “Pipeline transportation systems for liquid hydrocarbons and other liquids”, An American National Standard, (2009)
3. Chenna Rajaram, Srikanth Terala, Ajay Pratap Singh, Kapil Mohan, Bal Krishna Rastogi, Pradeep Kumar Ramancharla,” Vulnerability Assessment of Buried Pipelines: A Case Study”, Frontiers in Geotechnical Engineering (FGE) Report No: IIIT/TR/2014/-1, (2014)
4. Donald Ballantyne,”M7.8 Southern San Andreas Fault Earthquake Scenario: Oil and Gas Pipelines”, MMI Engineering (2008)

A Review of the Earthquake Experiences of Water Supply Systems in Taiwan and Lessons Learnt for Hazard Mitigation

Gee-Yu Liu[1]

劉季宇 [1]

Abstract

This study reviewed the experiences of water supply systems surrounding three major earthquakes in Taiwan, namely the 1999 Chi-Chi earthquake in central Taiwan, 2016 Meinong earthquake in southern Taiwan, and 2018 Hualien offshore earthquake in eastern Taiwan. The major findings and lessons learnt for hazard mitigation from these earthquakes are summarized. Some of the actions taken to respond to the noted challenges are also summarized.

Keywords: water supply system, earthquake experiences, hazard mitigation

Introduction

Taiwan is located on the circum-Pacific seismic belt, one of the most earthquake-prone areas in the world. Evidence indicates that the widespread disruption of the water supply in this area, which has occurred in the past in the presence of major earthquakes, will occur again in future earthquake events. Therefore, it is very important to learn from past earthquake experiences, through which future seismic hazard mitigation plans can be implemented more adequately. Taiwan has been struck by numerous earthquakes in the past two decades, among which three events have great significance in terms of the damage that occurred in water supply systems. The 1999 Chi-Chi earthquake (ML7.3) was the deadliest and most devastating earthquake in history. Widespread disruption of the water supply occurred in central Taiwan and lasted for more than one month due to the severe damage of the water systems. The less devastating 2016 Meinong earthquake (ML6.6) and 2018 Hualien earthquake (ML6.2) also caused substantial damage to the water systems in the affected areas, respectively. The earthquake experiences, findings, and lessons learnt from these events will be summarized in the following sections.

1999 Chi-Chi Earthquake

In terms of recorded history, the 1999 Chi-Chi earthquake is the largest inland seismic event to have occurred in Taiwan. The ML7.3 main shock occurred on 21 September at 01:47 local time. It caused widespread damage to buildings, roadway and highway systems, and other infrastructure, resulting in 2,415 deaths, 29 missing persons, and 11,305 injured persons.

Regarding the water systems, as many as 3,826 instances of damage to the pipelines were recorded, among which 351 occurred in pipes with diameters between 300 and 2,600 mm (TWC, 2000). One of the most significant instances of damage occurred near the Feng-Yuan First Water Treatment Plant, as depicted in Figure 1. It is a 2,000-mm steel pipe and the only common outlet of the Feng-Yuan First and Second Water Treatment Plants, which provided 70% of the water demand from 740 thousand customers in the Taichung metropolitan area before the earthquake. It was bent at a 90-degree angle and buckled by the offset of the Chelungpu fault rupture. It is now kept at the Water Park in Taipei for permanent exhibition.

In addition, dozens of water supply facilities in central Taiwan were damaged. Figure 2 depicts some of the affected water tanks (distribution reservoirs) and water pipe bridges, in which extensive or complete damage was caused by the fault offset.

The lessons learnt from this event may be summarized as follows:

1. This event is the first in Taiwan that raised

[1] Research Fellow, National Center for Research on Earthquake Engineering, karl@ncree.narl.org.tw

concerns about the high seismic exposure of water pipes and facilities. Many of these pipes encounter a fault crossing or are in the vicinity of one. Similarly, many are located at sites of high susceptibility towards liquefaction. They were installed or built as a result of the rapid growth of the water demand following the rapid economic development of earlier years, without much consideration for seismic effects.

2. The greater Taichung metropolitan area was then the third (now the second) largest urban area. It relies on the water supplied from (1) the Liyutan Reservoir and Liyutan Water Treatment Plants, and (2) the Shih-Gang Reservoir and the two Feng-Yuan Water Treatment Plants, with the latter providing a larger share. In this earthquake event, the latter completely failed, while the former fortunately remained nearly intact and was capable of producing more clear water than before earthquake. Such redundancy in a large urban area is crucial as it secures the minimum water supply required against "the Big One".

Figure 1 A 2,000-mm steel pipe damaged at the Chelungpu fault crossing near the Feng-Yuan Water Treatment Plants in the 1999 Chi-Chi earthquake.

Figure 2 Water facilities damaged in the 1999 Chi-Chi earthquake (courtesy of TWC).

2016 Meinong Earthquake

On February 6, 2016, at 03:57 local time, an ML6.6 earthquake occurred in the Meinong District of Kaohsiung City in southern Taiwan. The epicenter was located at 120.54 E and 22.92 N. The rupture process of this event was very complex. At least two asperities were identified on the fault plane. The rupture mainly developed in the down-dip direction and propagated toward the northwest. Analysis results further indicate that the strong ground shaking that was observed was caused by a combination of three effects: (1) rupture directivity, (2) the source radiation pattern, and (3) sedimentary amplification (Lee et al., 2016).

The earthquake caused substantial damage to water pipelines in Tainan, especially in its southern region (Liu et al., 2016). The 2,000-mm transmission pipeline conveying water from the Nanhua Water Treatment Plant was damaged at three sites, denoted as 1, 2, and 3 in Figure 3. It is the largest and most critical pipeline supplying water to the downtown area. These instances of damage caused an initial outage of the entire system.

The damage at Site 1 occurred in a pipeline of 1,205-meter steel double-skinned pipe segments filled with cement. They were installed by a pipe jacking method, segment by segment, at a depth of 8 meters. There were many breaks along the pipeline in the annular welds at the collars where two segment pipes from opposite sides met. Although it was very time consuming, deep excavations (Figure 4) and pipe repairs from the inside of the pipes were applied. Site 2 is located at the west end of Kei-Yun Bridge on Provincial Highway 20, where a pipe slip-out occurred at a special joint between a concrete pipeline and a welded steel pipeline from a nearby water pipe bridge.

It was quickly repaired without any difficulty. Site 3 is located in front of the Weiguan Jinlong Building (Figure 5). A pre-stressed concrete pipe (PSCP) that was around one hundred meters long was severely damaged by the collapse of this building. In addition, an adjacent steel pipe lying at a right angle to the concrete pipe was evenly torn apart for 30 cm along the annular weld. This is presumed to be a result of the ground displacement that occurred during the collapse. The required repair work cannot commence until the completion of a search and rescue operation.

Considering smaller pipelines, thousands of cases of damage have been reported, mostly in customer pipelines. Notably, clusters of damage towards pipes were identified in the Guan-miao and Yuh-ching districts. However, widespread soil liquefaction unexpectedly occurred in the An-nan and Sin-shin districts. This caused numerous damage cases to residential buildings and water pipes.

The lessons learnt from this event may be summarized as follows:

1. The 2,000-mm transmission pipeline conveying water from the Nanhua Water Treatment Plant was not functional until February 24, 18 days after the earthquake event. Fortunately, another 1,750-mm pipeline, depicted in Figure 3, was not damaged and served as a timely backup for water transmission to downtown Tainan. Had this pipeline not been available, the consequences of this event would be unimaginable.
2. The damage and delay of repair work at Site 3 due to the tragic collapse of the Weiguan Jinlong Building was accidental. Otherwise, the damage at Site 1 may have been preventable. Both good pipe selection and proper installation to ensure the feasibility of quick repairs are crucial.

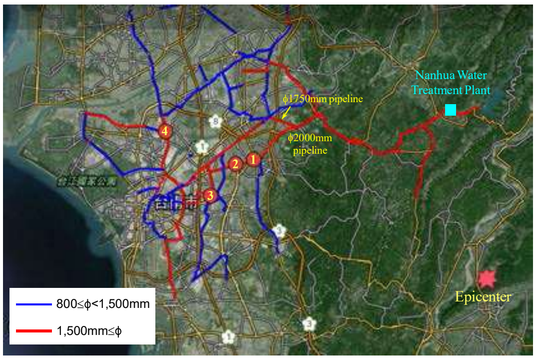

Figure 3 Water pipeline network in Tainan and locations of major damage that occurred in the 2016 Meinong earthquake.

Figure 4 Deep excavations required to reach the damaged pipe segments at Site 1, as indicated in Figure 3.

Figure 5 The location of the damaged transmission pipes near the collapsed Weiguan Jinlong Building, depicted as Site 3 in Figure 3.

2018 Hualien Offshore Earthquake

On February 6, 2018, at 22:50 local time, an ML6.2 offshore earthquake occurred in Hualien, eastern Taiwan. The epicenter was located at 121.73 E and 24.10 N. A fault-to-fault jumping rupture was identified via source inversion. It indicated that the initial rupture started from a north-south striking fault dipping into the west and propagated to the south with a high rupture speed. The rupture then jumped to the shallower east-dipping Milun fault. Slip on the Milun fault was slow and continued for more than 10 seconds, which produced the largest asperity near Hualien City. The rupture jumped again to the Lingding fault. Therefore, the movement on the Milun and Lingding faults was passive (Lee et al., 2019).

The earthquake caused damage to the pipelines of the local water system, leaving 40,000 households without water (Liu et al., 2019). As depicted in Figure 6, such pipeline damage was scattered along the Milun fault zone. The water supply system was quickly reinstated due to the repair of damage to large pipelines, of which some were apparently a result of ground deformation due to fault offsets, as depicted in Figure 7. This event also addresses the safety concerns associated with water pipes mounted on roadway bridges. Strong shaking apparently contributed to the damage to the pipes on the Shangji Bridge, as depicted in Figure 8. This would not have occurred if the pipes had been mounted adequately.

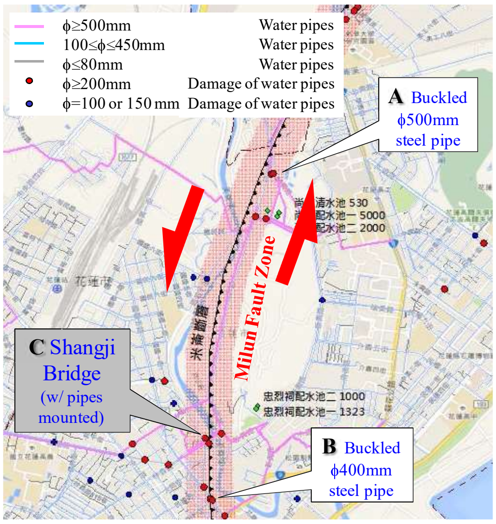

Figure 6 The location of the Milun fault zone and some of the water pipe damages resulting from the 2018 Hualien earthquake.

The lessons learnt from this event may be summarized as follows:

1. The issue of the seismic resistance of pipelines that cross faults or are in the vicinity of a fault is once again addressed.

2. The damage to pipes mounted on roadway bridges that occurred due to this earthquake appears to be avoidable. The adequate design and detailing of pipe installation may be easily achieved such that the pipes are capable of surviving severe ground shaking events. Of course, the survival of such pipes also depends on the safety of the roadway bridges themselves. Whenever a roadway bridge failure is expected to occur in a worst-case scenario, countermeasures should be implemented to secure the water supply if the pipes on such a bridge are crucial.

Figure 7 The buckled 500-mm (above) and 400-mm (below) steel pipes in the 2018 Hualien earthquake (courtesy of TWC).

Figure 8 The damage to a 600-mm pipe mounted on the Shangji Bridge in the 2018 Hualien earthquake (courtesy of TWC).

Response to the Challenges

Immediately after the Chi-Chi earthquake, seismic design codes for buildings in Taiwan were revised. They have since been revised several additional times considering state-of-the-art research findings from seismic hazard analyses, site effects, basin effects in Taipei, and near-fault amplification effects. Significant advances in research and field investigations of active faults in Taiwan have also been achieved since the Chi-Chi earthquake. The Central Geological Survey (CGS), MOEA, the authority of geo hazards, has published the active fault map and associated reports. As widespread liquefaction occurred unexpectedly in the Meinong earthquake, the government and general public in Taiwan have become aware of the threat of such a hazard. As a result, the Construction and Planning Agency (CPA), MOI launched the “Home Security Plan” in the selected cities and counties with liquefiable areas. One of its missions is to develop liquefaction hazard maps with increased resolutions for urban planning and hazard mitigation. These measures help to secure the seismic safety of not only the general building stocks, but also the water pipelines and facilities that are newly constructed in Taiwan.

To mitigate hazardous effects resulting from earthquakes, water authorities and utilities in Taiwan have been collaborating with NCREE for years to develop the required knowledge and database. Software Twater for the seismic risk assessment of water supply systems has been developed and implemented by NCREE. Twater is capable of simulating the damage to pipelines and facilities in a water system, a reduction in their functionalities, and water outages given an earthquake scenario. Recently, Twater has been employed to analyze the seismic performance of water systems in Kaohsiung (TWC, 2018). According to the results of these simulations, the weaknesses in water systems can be identified for future seismic improvements.

References

1. Lee, S.-J., Yeh, T.-Y., and Lin, Y.-Y., 2016. “Anomalously Large Ground Motion in the 2016 ML 6.6 Meinong, Taiwan, Earthquake: A Synergy Effect of Source Rupture and Site Amplification,” Seismological Research Letters, 87(6), pp. 1319-26.
2. Lee, S.-J., Lin, T.-C., Liu, T.-Y., and Wong, T.-P., 2019. “Fault-to-Fault Jumping Rupture of the 2018 Mw 6.4 Hualien Earthquake in Eastern Taiwan,” Seismological Research Letters, 90(1), pp. 30-39.
3. Liu, G.-Y. et al., 2016. Performance of Water Systems during the Meinong M6.6 Earthquake, Proc. 13th National Confer, Structural Eng. / 3rd National Confer. Earthquake Eng., Paper No. 2312, Aug. 24-26, Taoyuan (in Chinese).
4. Liu, G.-Y. et al., 2018. Water System Performance in the 2018 Hualien Taiwan Earthquake, Proc. 14th National Confer, Struct. Eng. / 4th National Confer. Earthquake Eng., Paper No. 24008, Nov. 6-8, Taichung (in Chinese).
5. TWC, 2000. Emergency Response and Restoration of Water Systems in 921 Chi-Chi Earthquake, Taichung (in Chinese).
6. TWC, 2018. “Seismic Hazard Exposure and Risk Assessment of Water Supply Systems in Kaohsiung Metropolitan Area,” TWC Research Report, Taichung, Taiwan, 2018 (in Chinese).

Online Model Updating for Advanced Hybrid Simulations

Ming-Chieh Chuang [1], Kung-Juin Wang[2], Keh-Chyuan Tsai[3], Ching-Yi Tsai[4], and You-Jin Zhon[5]

莊明介 [1]、王孔君 [2]、蔡克銓 [3]、鍾侑津 [4]、蔡青宜 [5]

Abstract

Hybrid simulations allow for the integration of numerical and physical substructures, such that the interactions between them can be considered in a seismic performance assessment. As a result, hybrid simulations can provide a cost-effective alternative to the shaking table test. However, conventional hybrid simulations are often restricted by the limited number of available facilities and specimens. Some structural elements that are similar to or the same as the physical substructures (PS) to be examined must be modeled in hybrid simulations. Therefore, the advantages and applicability of hybrid simulations diminish as a result of inaccurate modeling of the numerical substructures (NSs). To address the aforementioned issue, the researchers at Taiwan's National Center for Research on Earthquake Engineering (NCREE) have developed the techniques of online model updating (OMU) to overcome such issues in hybrid simulations. The NCREE researchers proposed the gradient-based parameter identification (PI) method for OMU. The novelty of the proposed gradient-based PI method is to identify certain components of parameters during the identification stages for different stress states, leading to a reduction in the number of design variables to be determined. The time consumed in computing the gradients can be reduced accordingly to improve the identification efficiency of the system. In this study, the proposed PI method is applied to the OMU schemes of the hybrid simulations of a steel panel damper (SPD) substructure conducted using a multi-axial testing system at the NCREE in 2017. In the hybrid simulations, the structure under investigation is a three-dimensional, six-story moment-resisting frame (MRF) with four SPDs installed on each story. In these advanced hybrid simulations with OMU, only one SPD is represented as the PS, namely the SPD specimen. The remainder of the SPDs and MRF are represented as the NS. It was found that through the proposed PI method for OMU, the proper parameter values of the constitutive model representing the experimentally measured force versus the deformation relationships of the PS can be identified effectively. Using the identified parameter values, the constitutive models of relevant SPD elements in the NS can be rectified online during the hybrid simulations. The accuracy of the hybrid simulations can be improved accordingly. The OMU technologies noted above have been upgraded and utilized in the recent hybrid simulations of an SPD substructure. These tests were successfully conducted using actuators mounted on a reaction wall and strong floor at the NCREE in 2019. The hybrid simulations of the SPD substructures demonstrate the effectiveness and benefits of OMU for advancing hybrid simulations and empowering testing facilities.

Keywords: Parameter identification, online model updating, hybrid simulation, optimization, steel panel damper

[1] Associate Researcher, National Center for Research on Earthquake Engineering
[2] Technologist, National Center for Research on Earthquake Engineering
[3] Professor, Department of Civil Engineering, National Taiwan University
[4] Postdoctoral Fellow, Department of Civil Engineering, National Taiwan University
[5] Graduate Student, Department of Civil Engineering, National Taiwan University

Introduction

In a hybrid simulation (HS), the target structure can be divided into components whose behavior can be modelled numerically with confidence and those that should be tested physically. Therefore, the target structure under investigation can be partitioned into multiple substructures. These substructures can be divided into two categories including the numerical substructure (NS) and the physical substructure (PS). Hybrid simulations allow the numerical and physical substructures to be integrated such that the interactions between them can be considered in the evaluation of seismic performance. As a result, hybrid simulations can provide a cost-effective alternative to the shaking table test for investigating large-scale target structures.

In general, multi-story seismic-resistant buildings are often equipped with many dampers. Distributed damage or plasticity can be expected when the building is subjected to a high-intensity earthquake. In a conventional hybrid simulation, several PSs corresponding to the dampers are required to investigate the seismic behavior of such a structure with distributed plasticity developing on the dampers (Fig. 1). However, the strategy of using several PSs in a conventional hybrid simulation is usually restricted, owing to the limited availability of experimental facilities and specimens. Fig. 2 shows an example of a hybrid simulation in which only one damper is presented as a PS. The remainder of the target structure, comprising a moment-resisting frame (MRF) and three dampers, is numerically modeled as an NS while the hybrid simulation is conducted. However, challenges arise in modeling the nonlinear behavior of the dampers in the NS. Clearly, improper numerical modeling of the dampers will jeopardize the accuracy of the hybrid simulation. Therefore, the applicability of hybrid simulations is not ideal.

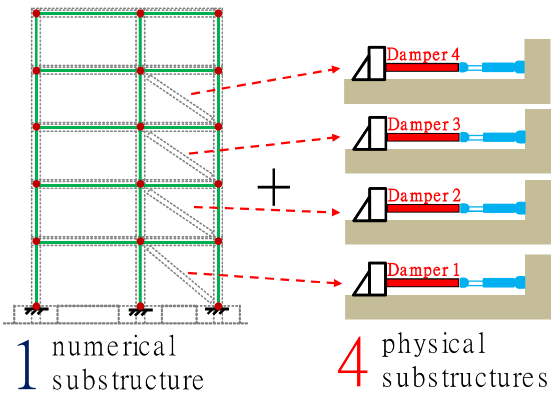

Fig. 1. HS with 1NS and 4PSs

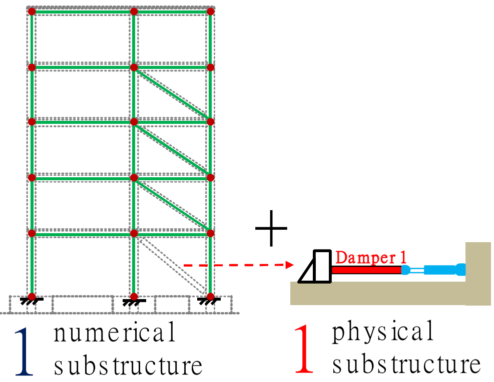

Fig. 2. HS with 1NS and 1PS

To address these problems, the NCREE researchers (Chuang et al., 2018; Wang et al., 2019) of Taiwan's National Center for Research on Earthquake Engineering (NCREE) developed online model updating (OMU) for advancing such hybrid simulations. Through advanced hybrid simulation with OMU technologies, the proper parameter values of the constitutive model used to represent damper behavior can be calibrated or identified online using the measured experimental data of the PS. With the identified parameter values, the constitutive models of relevant damper elements in the NS can be rectified online during the hybrid simulation. Based on recent research (Chuang et al., 2018) and experiments (Wang et al., 2019) conducted in NCREE, this paper presents an advanced hybrid simulation with OMU and demonstrates the effectiveness and benefits of using OMU via actual hybrid simulations on a steel panel damper (SPD) substructure.

Advanced Hybrid Simulations of a Six-Story SPD-MRF

An SPD (Tsai et al., 2018) is an energy dissipation device that promotes the shear yielding mechanism of a steel wide-flange section to dissipate the earthquake-induced input energy. To experimentally investigate the performances of an SPD and an MRF equipped with SPDs during seismic events, NCREE researchers conducted a series of hybrid simulations performed on an SPD specimen by using a multi-axial testing system (MATS) (Fig. 3) (Wang et al., 2019). In the series of hybrid simulations with OMU (Fig. 4), the target structure under investigation adopted a three-dimensional six-story moment resisting frame (MRF) equipped with 24 SPDs. There are four SPDs installed at each story. The details of the six-story SPD-MRF have been documented by Tsai et al. (2018).

According to the results from a series of nonlinear response history analyses conducted on the same six-story SPD-MRF (Tsai et al., 2018), it can be found that the 3rd story SPDs exhibit the most nonlinearity during the selected seismic excitations. Therefore, the northwest 3rd story SPD (Wang et al., 2018) is chosen as the physical specimen. However, only the north-west SPD installed on the 3rd story was tested as a PS in the hybrid simulation, as shown in Fig. 4. Because the SPD-MRF is a symmetric-plane building, the other three SPDs on the same story were modeled by using the duplicated PS responses via the RecdexElement objects (Wang et al., 2019). Clearly, the remaining 20 SPDs will inevitably be numerically represented as a part of the NS.

Fig. 3. The multi-axial testing system (MATS)

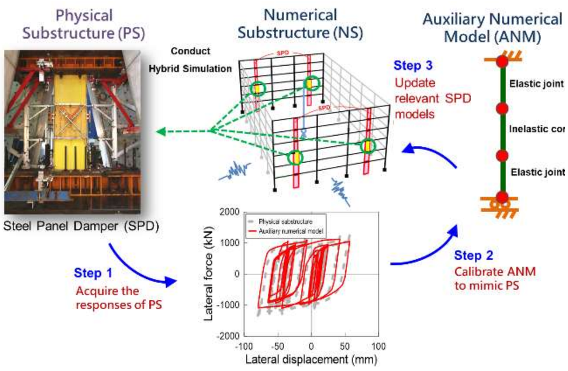

Fig. 4. Advanced hybrid simulation with online model updating in 2017

To numerically simulate the nonlinear behavior of the SPD for the NS or auxiliary numerical model (ANM) (Fig. 4), the three-segment SPD, which comprises one inelastic core (IC) and two elastic joints (EJs), is represented using three beam-column elements. The two-surface plasticity model (Dafalias and Popov, 1975) (Fig. 5) that combines isotropic and kinematic hardening effects is the constitutive model adopted for the beam-column element used for the IC segment. Fortunately, PISA3D (Lin et al., 2009), the nonlinear structural analysis program developed by the NCREE researchers, provides both the beam-column element and the two-surface model, which is called the hardening material model in PISA3D. Hence, PISA3D was utilized to construct the SPD analytical model for the SPDs of the NS and ANM of the hybrid simulations with OMU in this study.

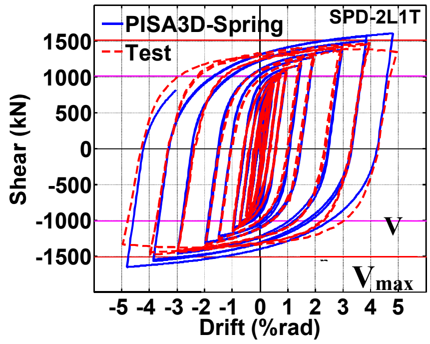

Fig. 5. Experimental and PISA3D numerical SPD shear vs. drift ratio relationships for the SPD specimen SPD-2L1T (Tsai et al., 2018)

By using the proposed parameter identification (PI) method (Chuang et al., 2018), the proper parameter values of the two-surface models of the ICs of the ANM, which can numerically represent the PS, can be identified. Through the OMU technologies, the parameter values of the two-surface models of the ICs of these relevant SPDs of the NS could be updated using the aforementioned parameter values identified during the hybrid simulation. The proposed gradient-based PI method was verified in the previous study (Chuang et al., 2018), and employed in the actual hybrid simulations of the SPD-MRF for efficiently performing the OMU.

Results of the Advanced Hybrid Simulations with OMU

Fig. 6 shows a portion of the time history of the normalized identified values of the four hardening material model parameters. It should be noted that the normalized values all remain at 1.0 prior to around the 1100th step. In other words, the PI operation was not triggered until the experiment progressed to around the 1100th step, when the ANM numerically representing the SPD specimen started to experience inelastic responses. At this moment, as can be clearly seen in Fig. 6, the values of Hiso1+ and Hiso2+ began to vary while the values of Hkin1 and Hkin2 remained unchanged. This suggests that the involved plasticity at this moment is of the isotropic hardening state. Kinematic hardening did not occur until around the 1137th step. It is also evident that at any time instance, the PI operation is either not triggered (the SPD specimen is in the elastic range) or is working on either isotropic or kinematic hardening parameters only.

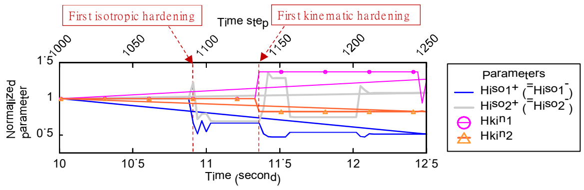

Fig. 6. Results of the parameter identification using the proposed gradient-based method

In short, a novelty of the proposed gradient-based PI method (Chuang et al., 2018) is proposed to identify certain components of parameters during the identification stages for different stress states, thereby reducing of the number of design variables to be determined. The time consumed in computing the gradients can be reduced accordingly to improve the identification efficiency. Fig. 7 compares the experimental results with the ANM hysteresis of the simulation results, which is obtained by using parameter values that are continuously identified from the test results. It is evident that the proposed gradient-based PI method can significantly improve the accuracy of the ANM to model the SPD hysteresis.

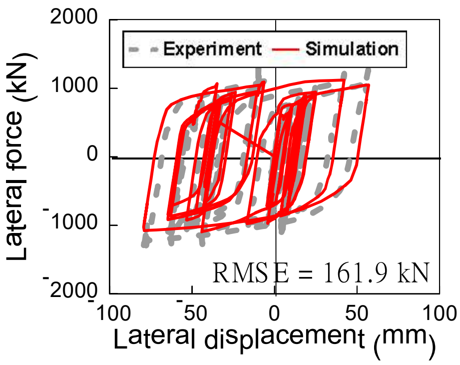

Fig. 7. Shear vs. drift ratio relationships for the PS and the ANM

Moreover, OMU technologies have been utilized in the hybrid simulations conducted using the configuration of the reaction wall and strong floor with actuators at the NCREE in 2019 (Fig. 8). In the series of hybrid simulations, the SPDs are constructed with low-yield-strength (LYS) steel in the target structure under investigation. With OMU, the researchers can utilize an SPD made of LYS steel (LYS-SPD) as a PS to conduct a hybrid simulation. The performance of the LYS-SPD and the MRF equipped with LYS-SPDs during seismic events can be experimentally investigated. Again, the hybrid simulations verified and demonstrated the effectiveness and benefits of the OMU technologies with the developed techniques for advanced hybrid simulations.

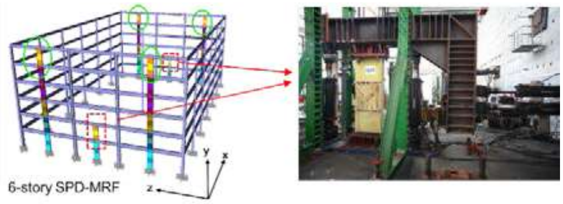

Fig. 8. Advanced hybrid simulation with online model updating in 2019

Conclusions

Considering an OMU scheme, a novelty of the proposed gradient-based PI method is to adjust components of the parameters along the identification stages of different stress states, thereby resulting in a reduction in the number of design variables to be determined. The consumed time can be reduced accordingly to improve the parameter identification efficiency. The hybrid simulations of the SPD substructures demonstrated the effectiveness and benefits of OMU for advancing hybrid simulations and empowering testing facilities. By taking advantage of advanced experimental technologies, the NCREE will enable the earthquake engineering community to boldly explore new technological frontiers.

References

Chuang MC, Hsieh SH, Tsai KC, Li CH, Wang KJ, Wu AC. (2018). Parameter identification for on-line model updating in hybrid simulations using a gradient-based method. *Earthquake Engineering and Structural Dynamics*, **47**(2): 269-293.

Dafalias YF, Popov, EP. (1975). A model of nonlinearly hardening materials for complex loading. *Acta Mechanica*, **21**(3): 173-192.

Lin BZ, Chuang MC, Tsai KC. (2009). Object-oriented development and application of a nonlinear structural analysis framework. *Advances in Engineering Software*, **40**(1): 66-82.

Tsai KC, Hsu CH, Li CH, Chin PY. (2018). Experimental and analytical investigations of steel panel dampers for seismic applications in steel moment frames. *Earthquake Engineering and Structural Dynamics*, **47**(6): 1416-1439.

Wang KJ, Chuang MC, Tsai KC, Li CH, Chin PY, Chueh SY. (2019). Hybrid testing with model updating on steel panel damper substructures using a multi-axial testing system. *Earthquake Engineering and Structural Dynamics*, **48**(3): 347-365.

Simulation of a Cyclic Loading Test of Reinforced Concrete Column with Plastic Damage

Wei-Tze Chang[1]

張慰慈 [1]

Abstract

Reinforced Concrete (RC) is one of the most common engineering materials. However, the complex mechanical properties of this material are not easily predicted when the continuity between the reinforced steel bars and concrete is broken due to microcracks in the plastic deformation region. Therefore, the continuity-based theory is applicable only in a limited range of failure. Finite Element Analysis (FEA) with Concrete Damaged Plastic (CDP) model was applied to simulate cyclic loading tests of RC column in this paper. It has been shown that the FEA with CDP model can predict the failure region of concrete and its hysteresis loop of lateral force-displacement when the drift ratio is smaller than 2%, which can be used to study more detailed plastic behaviors of RC components.

Keywords: Reinforced concrete column, cyclic loading, plastic failure, concrete damaged plastic model

Background

Reinforced Concrete (RC) is a composite material in which steel bars, net, planes, or fibers are added to concrete material. Utilizing the advantages of the economy of concrete and the high tensile strength of steel, RC is currently one of the most common engineering materials. The coefficients of thermal expansion for steel and concrete are similar such that they are easy to work with together under normal conditions. However, the plastic deformation region of concrete material is more difficult to work with. The closer the compressive stress is to the extreme strength, the more microcracks form in the structural components, thereby making it more difficult to utilize reinforced steel with concrete. Under these conditions, the continuity between the reinforced steel and concrete cannot be guaranteed. The resulting complex mechanical behaviors are much more difficult to predict.

We can construct material properties and the variation of geometric shapes using the theory of micro-mechanics. It is also possible to determine the macroscale mechanical properties of RC components until failure using this approach. However, this approach requires considerable computational power. A single RC component takes several days to analyze using the micro-mechanical approach. It is more time-consuming to model an entire building. Therefore, modelling an RC component with a continuum-based numerical approach by ignoring the discontinuous properties at a microscale can be a more economical approach for assessing real engineering problems with limited cracking.

Concrete Damaged Plastic Model

Finite Element Analysis (FEA) is a mature numerical analysis approach based on continuum theory. The core concept of FEA is to divide a space into small, finite regions with their own Partial Differential Equations (PDEs). Every PDE can be transformed into Algebraic Equations (AEs) and solved using the algebraic method by a computer. After eighty-years of development, FEA can be performed using various related computer software programs and is widely applied in structural mechanics, thermodynamics, fluid dynamics, and electromagnetic analysis. For these reasons, we chose to use FEA for the modelling of RC components.

Concrete Damaged Plastic (CDP) model is a mature numerical model in FEA that is used for modelling concrete material (Lubliner, *et al.*, 1989).

[1] Research Fellow, National Center for Research on Earthquake Engineering

The phenomenon of strength reduction of damaged concrete is illustrated through experimental observation. The stress-strain curve of concrete increases linearly with a constant slope provided by the Young's modulus (E_c) in elastic region. After that, the slope (E_c*) decreases, i.e., $E_c* < E_c$. The unloading pathway also follows the slope E_c*. The E_c* value will decrease continuously as the degree of damage increases. The relationship between E_c and E_c* can be written as:

$$E_c^* = (1 - d_c)E_c \tag{1}$$

in which d_c indicates the discount rate of compressive strength and is smaller than 1 ($0 < d_c < 1$).

The tensile strength also has the same relationship:

$$E_t^* = (1 - d_t)E_t \tag{2}$$

in which E_t, E_t*, and d_t indicate the elastic tensile Young's modulus, plastic tensile Young's modulus, and discount rate of tensile Young's modulus, respectively. We can define several different d_c and d_t values for different stress-strain stages of concrete.

Simulated Example

A square RC column with a cross-section of 30 by 30 cm and a height of 2.6 m was studied in this paper. This column has eight main bars and 22 hoop bars in total. The main bar provides tensile strength to the structure rather than concrete. The hoop bars are used to protect the central concrete without serious separation during external loading (Figs. 1 and 2). The bottom of the column was fixed on the ground and lateral cyclic loading was applied to the top of the column by controlling its displacement (Fig. 3). The designed CDP model is shown in Fig. 4. For simplifying the model of the reinforced steel, its stress-strain curve was set as shown in Fig. 5.

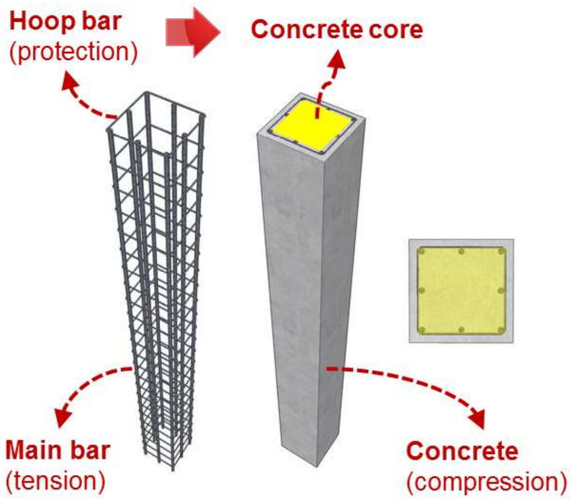

Fig. 1. The main bar provides tensile strength rather than concrete. The hoop bars are used to protect the central concrete without serious separation during external loading.

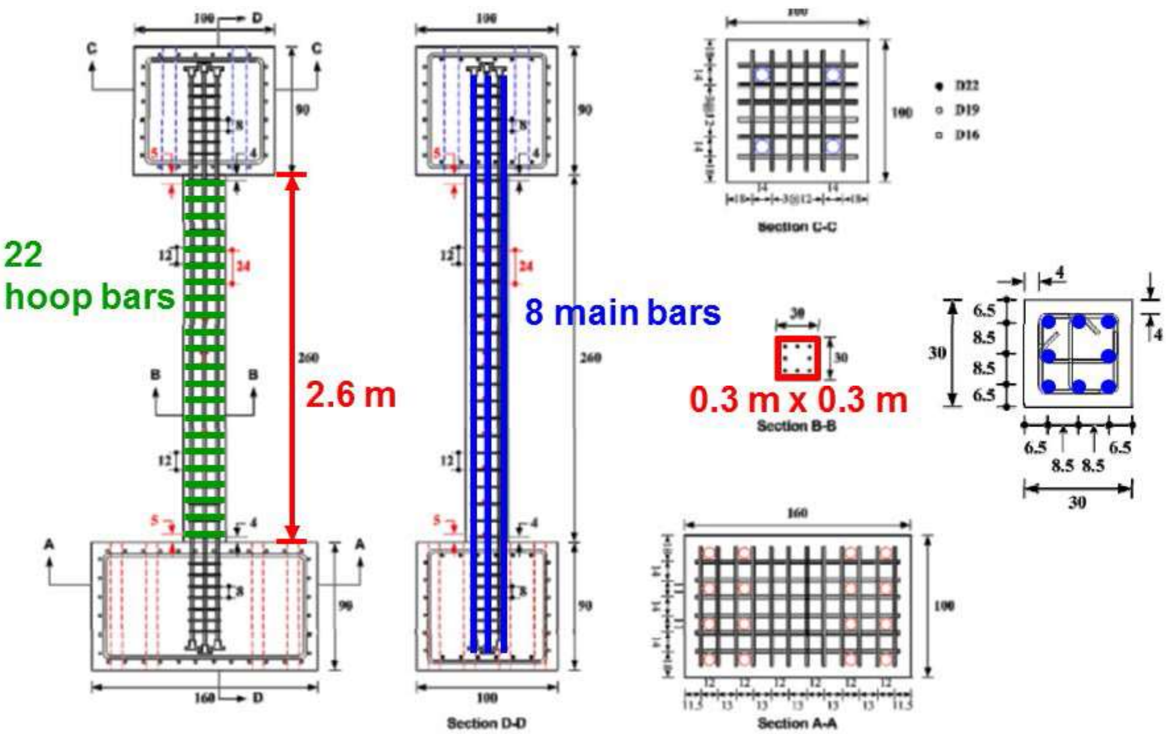

Fig. 2. Detailed specifications of the RC column studied in this paper

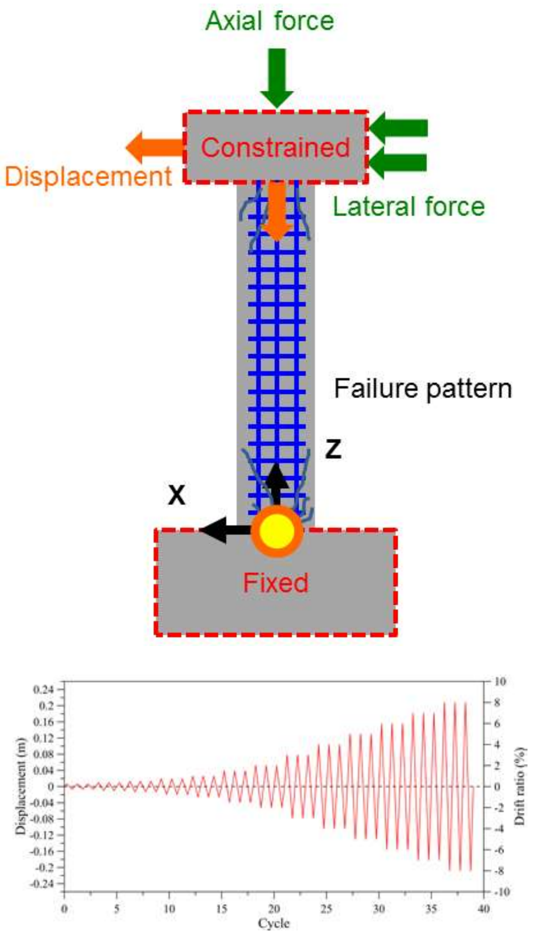

(a)

(b)

Fig. 3. Setup of the RC column studied in this paper: (a) experimental settings; (b) the lateral cyclic displacement

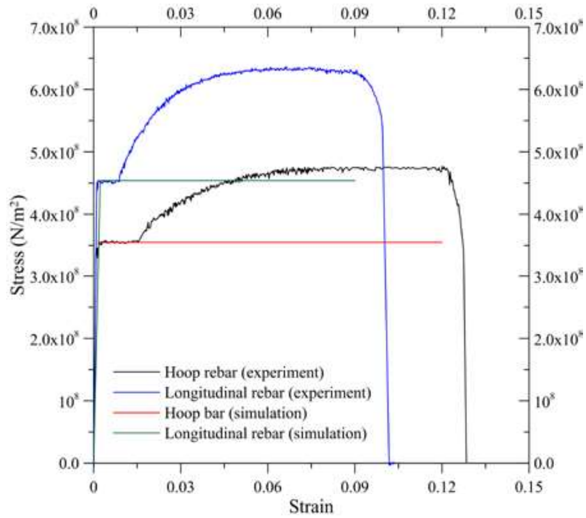

Fig. 5. Simulated and real stress-strain curves of the reinforced steel studied in this paper

In total, 4,160 solid elements, as well as 520 and 880 beam-column elements, were used for modelling the concrete, main bars, and hoop bars in the RC column examined in this study, respectively. The relationship between the reinforced steel and concrete is the stringer mode, which uses common FEA nodes between the solid and beam-column elements (Fig. 6). Furthermore, damage to the core concrete inside the hoop bars was limited to a certain degree to avoid the total failure of the RC column, i.e., the lower bound of d_c and d_t is not zero.

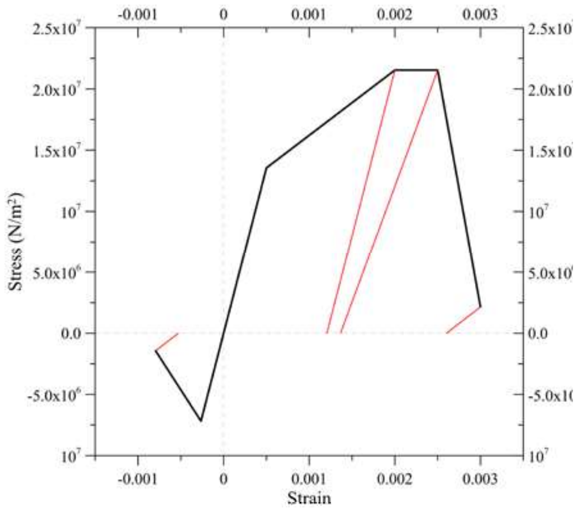

Fig. 4. The simulated stress-strain curve of the CDP model studied in this paper

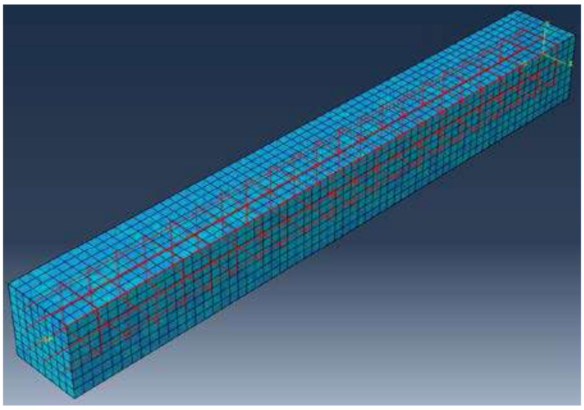

Fig. 6. In total, 4,160 solid elements, as well as 520 and 880 beam-column elements, were used for modelling the concrete, main bars, and hoop bars in the RC column examined in this study, respectively. The relationship between the reinforced steel and concrete is the stringer mode, which uses common FEA nodes between the solid and beam-column elements.

Results and Discussion

The simulated hysteresis loop of the lateral force to the displacement is shown in Fig. 7. The red and green lines indicate the experimental and simulated results, respectively. Before the drift ratio reaches 0.5% (i.e., a displacement of 1.3 cm relative to the total height, 2.6 m), the proposed approach can determine the phenomenon of strength reduction of the damaged concrete (Fig. 7a). When the drift ratio reaches 2% (i.e., a displacement of 5.2 cm relative to the total height, 2.6 m), the error between the simulated and experimental results increases. Although the simulated hysteresis loop is plumper than the experimental curve, this approach is still able to determine the maximum stress and strain values. Furthermore, the damage degree of the simulated RC column shows the damage-propagation progress. It is obvious that the damaged region is located on the outside region of the ends of the column, which appears as a "hinge" shape (Fig. 8). That is the so-called "plastic hinge" referred to in engineering practices.

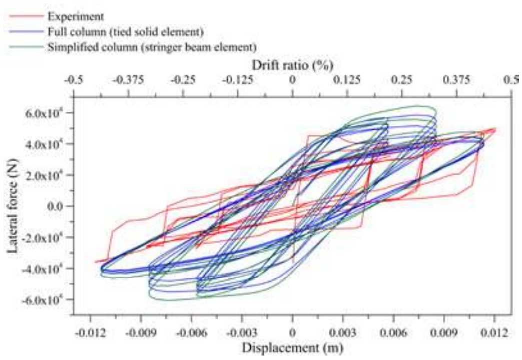

(a)

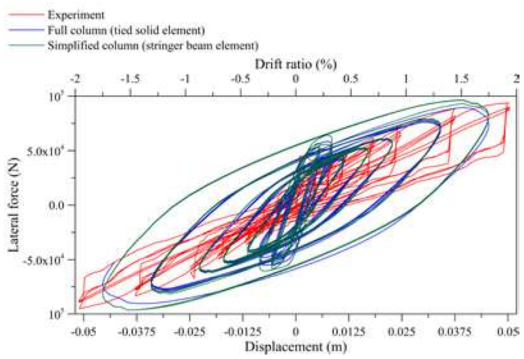

(b)

Fig. 7. Simulated hysteresis loop of the lateral force to the displacement with different drift ratios: (a) 0.5%; (b) 2%.

Conclusion

This study applied Finite Element Analysis (FEA) with Concrete Damaged Plastic (CDP) model to simulate the dynamic behavior of a Reinforced Concrete (RC) column during a cyclic loading test. With a limited degree of damage of the concrete material, the lateral force-displacement curve and damage-propagation progress can be predicted successfully using this method. More detailed information can be found in the conference papers released in 2018 (Chang, 2018a; Chang, 2018b).

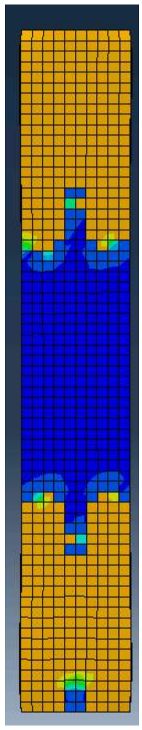

(a) 1% (b) 2%

Fig. 8. Damage-propagation progress of the RC column studied in this paper

References

Chang, W.-T., "Applying Concrete Damaged Plastic Model on Failure of Reinforced Concrete Material," Second International Conference on Mechanics (ICM 2018), jointing conferences of the Twelfth Asian Computational Fluid Dynamics Conference (ACFD), the Twenty-fifth National Computational Fluid Dynamics Conference (NCFD) and the Fourth Association of Computational Mechanics Taiwan Conference (ACMT), Yilan, Taiwan, October 15-18, 2018a, Paper No. 211.

Chang, W.-T. "Study of Failure of Reinforced Concrete Material with Concrete Damaged Plastic Model," Thirteenth World Congress in Computational Mechanics and Second Pan American Congress on Applied Mechanics (WCCMXII & PANACM II), New York, United States, July 22-27, 2018b, Paper No. 2021015.

Lubliner, J., Oliver, J., Oller, S., and Oñate, E. "A Plastic-Damage Model for Concrete, International Journal of Solids and Structures, 25, 1989, pp. 299-326.

Feasibility Study on the Real-Time Hybrid Simulation of a Building Mass Damper System using a Shaking Table

Pei-Ching Chien[1], Meng-Wei Dong[2] and Po-Chang Chen

陳沛清[1]、董孟洧[2]、陳柏彰[2]

Abstract

A building mass damper (BMD) system, which incorporates the concept of a tuned mass damper into a mid-story isolation system, has been proposed to control the seismic response of both a superstructure and substructure. The effectiveness of the BMD system may only be verified via shaking table testing with limited design parameters in which the superstructure and substructure must remain elastic such that repeated tests can be conducted. Therefore, real-time hybrid simulations (RTHSs) may provide an alternative method for evaluating the seismic performances of BMD systems subjected to earthquake ground motions. In this study, a BMD system is separated into a numerical substructure and a physical substructure. The physical substructure includes the control layer and the superstructure of the BMD system installed on a seismic shake table, while the substructure is numerically simulated. The stability margin is represented as a mass ratio relating the physical substructure to the numerical substructure. The results can provide valuable information for conducting parametric studies of BMD systems via RTHSs in the future.

Keywords: Building mass damper, real-time hybrid simulation, stability margin, mass ratio

Introduction

A building mass damper (BMD) system, which combines the advantages of seismic isolation and tuned mass damper design, has been previously proposed and studied. A BMD system is composed of a substructure, a control layer, and a superstructure. Conventionally, the mass of the superstructure above the control layer can be designed as a tuned mass, becoming an energy absorber to suppress the response of the substructure. In the past, the substructure and superstructure were emulated by steel specimens. The control layer was represented by sets of viscous dampers and elastomeric bearings; therefore, the structural parameters could be varied by replacing various viscous dampers and elastomeric bearings. However, the shaking table test was not repeatable as long as the steel structure behaved nonlinearly. As a result, real-time hybrid simulation (RTHS) may provide a powerful approach to investigate the seismic responses of BMD systems wherein nonlinear behavior may occur.

RTHS, which combines experimental testing with numerical simulation, is an advanced and effective method used to evaluate structural responses when subjected to dynamic excitation. In general, a structure is separated into a numerical substructure and a physical substructure in an RTHS. Considering BMD substructuring, the physical substructure includes the superstructure (SUP) and the control layer (CL), while the substructure (SUB) is numerically simulated. The interfacial degrees of freedom between the physical and numerical substructures are represented by a seismic shake table. In this study, stability analysis is conducted to realize the feasibility of conducting a parametric study of BMD systems via RTHS using a seismic shake table.

BMD Mathematic Model

In the design process, a BMD system is represented by a simplified three degrees-of-freedom (3DOF) lumped mass structural model, which is composed of a superstructure, a control layer, and a substructure, as shown in Fig. 1. The equation of motion of the 3DOF BMD system is expressed as:

$$\mathbf{M}\ddot{\mathbf{u}}(t)+\mathbf{C}\dot{\mathbf{u}}(t)+\mathbf{K}\mathbf{u}(t)=-\mathbf{M}\mathbf{l}\ddot{u}_g(t) \qquad (1)$$

where **M**, **C**, and **K** are the mass, damping, and stiffness matrices, respectively; **u** is the relative displacement vector; and **l** is a vector with all elements

[1] Assistant Professor, National Taiwan University of Science and Technology
[2] Graduate Student, National Taiwan University of Science and Technology

equal to 1. In this study, a 2-story steel specimen was used as the physical substructure of a 3-DOF BMD system. The steel specimen was single bay with widths of 1.1 and 1.5 m in the longitudinal and lateral directions, respectively. Each floor was 1.1-m high and each slab was 20-mm thick. The columns were all wide flanges with a sectional dimension of 100 × 100 × 6 × 8 mm. The beams were 100 × 50 × 5 × 5 mm channels. Four elastomeric bearings with diameters of 180 mm and two linear fluid viscous dampers were installed on the control layer. One set of steel blocks with a total mass of 500 N-s^2/m was installed regularly on each floor to simulate the mass. After considering the additional mass contributed by the beams and columns, the total lumped mass at the superstructure and control layer was 800 N-s^2/m and 760 N-s^2/m, respectively. The natural frequency of each mode can be obtained by conducting system identification. Table 1 shows the identified damping coefficient and stiffness of each floor. Figure 2 illustrates the experimental setup of the physical substructure.

Table 1 Structural properties of the physical substructure

Floor	Mass (N-s^2/m)	Stiffness (N/m)	Damping coefficient (N-s/m)
CL	760	2,495,320	3,330
SUP	800	4,941,700	78

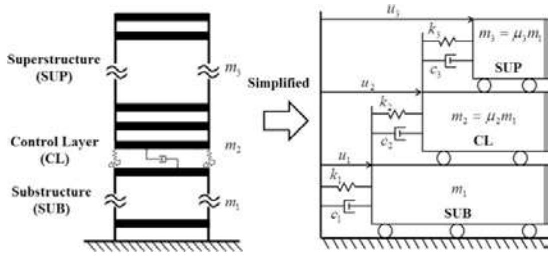

Fig. 1 Simplified 3DOF structure model of a BMD system

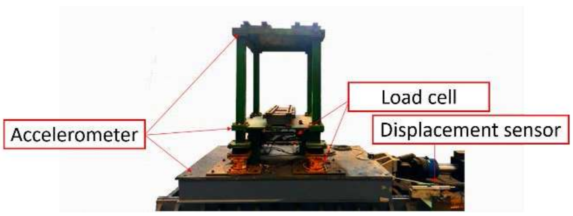

Fig. 2 Experimental setup

Stability Analysis

In this study, the RTHS of a BMD system forms a closed loop between the numerical substructure, seismic shake table, and physical substructure. The ground acceleration is input into the numerical substructure and the transmitted absolute acceleration at the interfacial degree of freedom must be reproduced by the shake table. The shear force of the physical substructure is then measured and fed back to the numerical substructure and completes the RTHS closed loop. The RTHS stability can be investigated by solving the characteristic equation of the closed-loop transfer function, as indicated in Fig. 3. The interactions between the physical and numerical substructures represent the transmitted shear force, which is related to the mass of the physical substructure. As a result, the mass ratio ρ is adopted as a stability parameter for the RTHS of BMD systems, which is defined as:

$$\rho = \frac{m_P}{m_N + m_P}, 0 \le \rho \le 1 \qquad (2)$$

where m_P and m_N are the effective modal mass of the first mode of the physical and numerical substructures, respectively. According to the system identification results, the stiffness of the control layer was set to 0.5 times that of the superstructure. It was assumed that the first modal frequency of the physical substructure was about 0.5 times the natural frequency of the numerical substructure. To consider the dynamics of the seismic shake table in the stability analysis, system identification of the shaking table was conducted. Figure 4 shows the identified transfer function from the shaking table displacement command to the measured displacement.

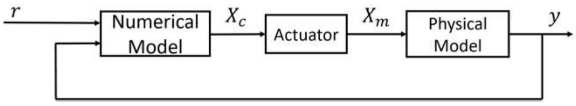

Fig. 3 Block diagram of the RTHS loop

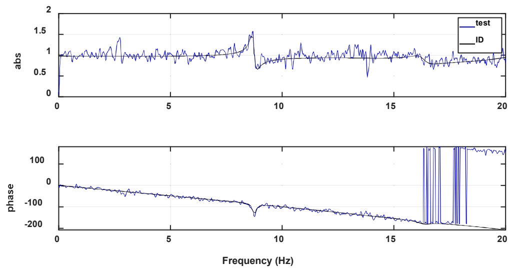

Fig. 4 System identification of the seismic shake table

The closed-loop stability analysis results of the BMD system considering the dynamics of the seismic shake table are shown in Figure 5. In addition, when delay compensation of the RTHS is applied, the best tracking performance demonstrates that the base shear of the physical substructure is a one-step delay without a magnitude error. Generally, a step size is 5 ms in the RTHS because of the sampling frequency of measured earthquake ground acceleration time histories. The closed-loop stability analysis results of the BMD system with a one-step delay are shown in Figure 6. The blue region represents the allowable mass ratio that is able to achieve a stable RTHS, while the remainder is the unstable region. Accordingly, if the BMD system from a previous study is adopted for the RTHS, such as an 8-story BMD system (Wang et al. 2018), the mass ratio is very close to the stability margin under the condition that the delay is only one step without a magnitude error. Therefore, it is very difficult to conduct an RTHS using the shake table for this 8-story case. Alternatively, a 3-story BMD system was used as a demonstrative example of the RTHS for BMD systems in the study.

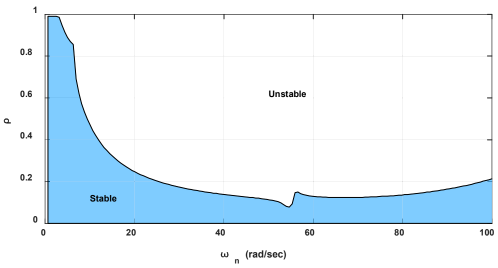

Fig. 5 Stability region of the RTHS on a BMD system considering the dynamics of the shake table

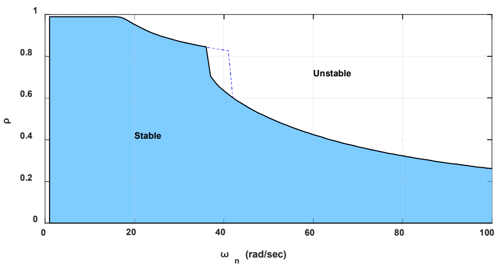

Fig. 6 Stability region of the RTHS on a BMD system with perfect delay compensation

Real-Time Hybrid Simulation

The physical substructure was installed on a uni-axial shake table in the structural laboratory of the National Center for Research on Earthquake Engineering (NCREE). The uni-axial shake table was operated by using a FlexTest GT controller manufactured by the MTS Systems Corporation with a well-tuned PID controller. The maximum stroke and force capacity of the actuator were ±250 mm and ±500 kN, respectively. Two displacement transducers were installed in the longitudinal direction of the shake table. Furthermore, three accelerometers were installed on the shake table and each floor of the physical substructure to measure the absolute accelerations. Four load cells with a measurable force of 200 kN were installed underneath the four elastomeric bearings in the control layer. A dSPACE MicroLabBox was adopted to run the numerical substructure and delay compensation.

In the demonstrative RTHS, the Kobe earthquake ground acceleration with a peak ground acceleration normalized to 0.1 g was used as the excitation. The RTHS results are compared with the numerical simulations, as shown in Figure 7, demonstrating that the root-mean-square error between the RTHS and numerical simulation was approximately 50% to 60%. This was due to the amplified frequency components above 16 Hz, as shown in Figure 8. This amplification could be due to the application of delay compensation. However, even after a band-pass filter with a passing frequency range of 15-20 Hz was applied before the compensated command was sent to the PID controller of the shake table, the amplification was not eliminated. The amplification could be due to a mechanical problem involving the entire hydraulic system of the shake table. As a result, the base shear from the physical substructure was modified in order to reduce the effects of transmitted acceleration with the amplified frequency components.

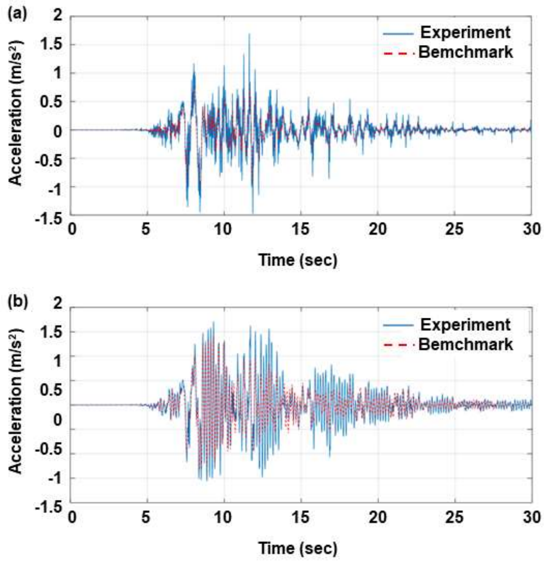

Fig. 7 Acceleration time histories of the RTHS and numerical simulation: (a) SUB (b) CL

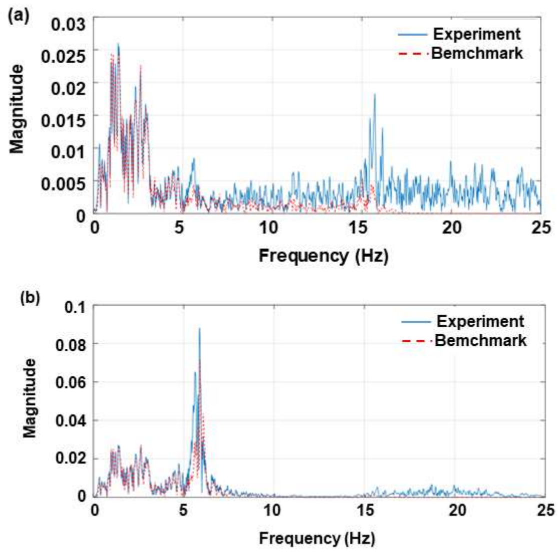

Fig. 8 Frequency domain of the acceleration in the RTHS and numerical simulation: (a) SUB (b) CL

Summary and Conclusions

It is expected that RTHS could provide an effective alternative for investigating the seismic performance of a BMD system with various structural parameters. During an RTHS, the substructure can be simulated numerically while the control layer and superstructure can be tested physically on a seismic shake table. The RTHS stability analysis was conducted in this study by solving the characteristic equation of the closed-loop transfer function of the RTHS, which considered the dynamics of a seismic shake table. The stability was represented as an allowable mass ratio related to the first modal mass of the physical substructure and the numerical substructure. The stability margin restricts the potential applications of the RTHS of a BMD system for parametric studies. Nevertheless, an RTHS of a 3DOF BMD system was conducted as a demonstrative example. The results show that it is feasible to successfully complete the RTHS of a BMD system as long as appropriate delay compensations are applied and mechanical conditions are well-maintained.

References

1. Nakashima, M., Hiroto K., and Eiji T. (1992) “Development of real-time pseudo dynamic testing”, Earthquake Engineering and Structural Dynamics 21(1): 79-92.
2. Schellenberg, A. H., Tracy C. B., and Stephen A. M. (2017) “Hybrid shake table testing method: Theory, implementation and application to midlevel isolation”, Structural Control and Health Monitoring 24(5): e1915.
3. Wang, S. J., Lee, B. H., Chuang, W. C., and Chang, K. C. (2018) “Optimum dynamic characteristic control approach for building mass damper design”, Earthquake Engineering and Structural Dynamics 47(4): 872-888.

Structural Control-Deep Learning Applied to Acceleration Control of a Shaking Table

Jeffery Hsieh[1], James Chang[2], June-Shan Chen[3], Pei-Chin Chen[4]

謝伯徽 [1]、張心寧 [2]、陳俊杉 [3]、陳沛清 [4]

Abstract

With the increasing complexity of equipment systems, determining their seismic resistance capacity simply through simulation is challenging. However, it is possible to directly test their capacity by a seismic shaking table. Due to the interactions between the shaking table and the specimen, controlling the shaking table becomes difficult, resulting in inaccurate reproduction of the history of acceleration response. To solve this problem, many scholars have used single-axis shaking table tests and have proposed new theories of control. However, significant opportunities for improvement of existing methods remain. Deep learning algorithms have the inherent capacity to model nonlinearity in dynamic systems. Therefore, the implementation of deep learning with respect to controlling a shaking table can improve the acceleration reproduction and thus are expected to facilitate development of new control methods.

Keywords: control system, deep learning

Introduction

A seismic simulation shaking table is one of the most important test equipment in seismic engineering research; it is used to reproduce the history of earthquake acceleration or an artificial earthquake history. The total weight of the shaking table and the specimen is often greater than the maximum output force of the actuator, causing control–structure interaction (CSI) to occur frequently during shaking table tests, especially under the condition of damage or a nonlinear seismic response; CSI makes the control of the shaking table more difficult. In the past decade, in addition to the traditional Proportional-Integration-Derivative (PID) and Three-Variable Control method (TVC) methods, as well as methods such as adaptive inverse control (AIC) and minimal control synthesis (MCS) of the non-stationary system dynamics have also been incorporated to improve the acceleration control performance. However, so far, these control methods still have considerable room for improvement. Therefore, we aim to use deep learning to obtain a model to calculate the appropriate control commands and improve the accuracy of the reproduced acceleration of the shaking table without changing the existing system architecture.

Literature Review

As the seismic simulation shaking table is a nonlinear system, neither the PID nor the TVC controllers can accurately reproduce the acceleration under this condition. There is still much room for improvement. Spencer and Yang used the transfer function iterative method to develop non-linear and inverse function models of the input and output of the shaking table, and used iterative correction command signals in the offline state to achieve higher acceleration reproduction.

Another common shaking table control method used in the industry is AIC, which is a feedforward control compensation technology used to correct poor control performance caused by the existing control

[1] Master Graduate. Dept. of Civil and Environment Engineering of National Taiwan University.
[2] Research Assistant. Dept. of Civil and Environment Engineering of National Taiwan University.
[3] Professor. Dept. of Civil and Environment Engineering of National Taiwan University.
[4] Assistant Professor. Dept. of Construction Engineering of National Taiwan University of Science and Technology.

architecture gain and phase irregularities. It sufficiently compensates for the deficiencies of the TVC control methods. AIC measures the dynamic response of the shaker system directly and changes relevant parameters in time to adapt it to the time-varying dynamic system. The core principle of AIC lies in the use of vibration table control.

The inverse function of the dynamic characteristics of the architecture and the vibration table cancel each other, making the control command the same as the actual measured value. However, the perfect inverse function cannot be obtained, so the ideal model under this architecture has a causality delay. Due to this delay effect, the inverse function can be obtained smoothly.

However, if the dynamic characteristics of the entire system change drastically, such as the collapse of the test members, both AIC and iterative methods will cause significant acceleration errors. To address this highly nonlinear situation, many scholars have used high-order control theory to discuss related issues. Stoten's self-adaptive MCS for the control of the vibration table is suitable for time-varying systems; its disadvantage is that inappropriate gain values may cause oscillations or instability of the system.

Yang et al. used sliding mode control for nonlinear control to confirm its stability with Lyapunov's rule; this approach can compensate for the uncertainty of the numerical model of the shaker. Nakata proposed an acceleration trajectory tracking method to stabilize the shaking table system and prevent it from drifting.

The vibration controller is placed on the upper opening in the original control structure. Usually, the current is used as the signal carrier, and the controller is directly designed to generate the servo valve control command. However, an external loop controller can also be designed to improve the existing performance of the seismic simulation shaker. Phillips used multi-metric feedback to control the performance of the shaker.

Specimen Installation

A deep learning model needs a large amount of data to tune model parameters for achieving predicted results that match closely to experimental results. In the present study, two hundred records of actual seismic ground accelerations are used as training data.

The specimen used in the study and shown in Fig. 1, is a three-story steel structure with a length of 45 cm, a width of 50 cm, and a total height of 80 cm. The thickness of each floor is 4 cm, the column size of the second floor is 5 mm × 50 mm × 227 mm, and the column size of the third floor is 5 mm × 50 mm × 202 mm. The first three natural frequencies are 5.6, 16.7, 24.2 Hz, respectively; and the total weight of the specimen is 200 kg.

Small Laboratory Shaking Table Test

This study began at the end of 2019 in a small laboratory-scale shaker. Nearly two hundred sets of ground acceleration data collected from various stations in Taiwan were used as the input. The measured quantities include one axis of acceleration response at all floors, displacement of the shaking table, and the differential pressures from cylinders in the actuator. Fig. 2 shows one set of tests (921 CHY027; north–south direction)

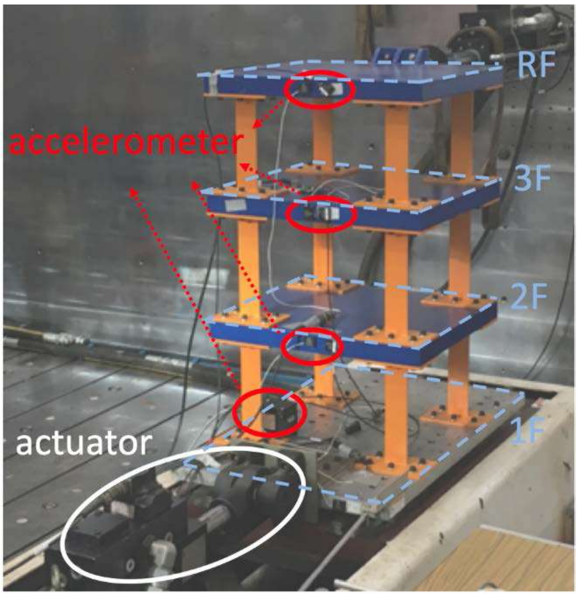

Fig 1. Three-story steel structure specimen with the shaking table.

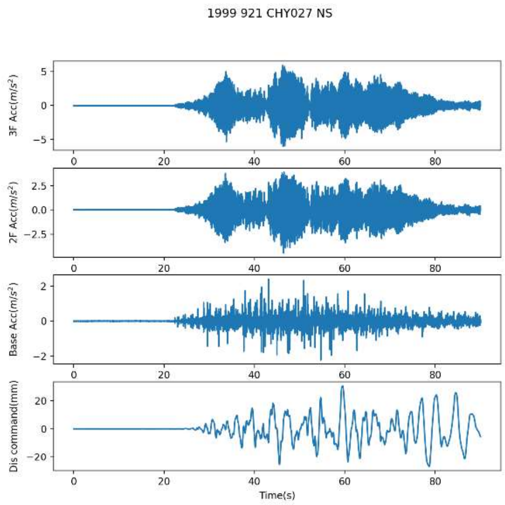

Fig. 2 History of acceleration response and displacement commands for each floor of the steel structure with the shaking table test (921 CHY060 100 gal).

Deep Learning Model

The goal of a well-trained deep learning model is to obtain the shaped displacement trajectory commands, which excite the specimen to reproduce the desired acceleration response. This is treated as time-series prediction. Therefore, a recurrent neural network (RNN) was used to uncover the hidden system dynamics. The architecture of the RNN is shown in Fig. 3. Its system state and system output are given by

$$s_{\tau+1} = \sigma(As_\tau + Bu_\tau) \qquad (1)$$

and

$$y_\tau = Cs_\tau. \qquad (2)$$

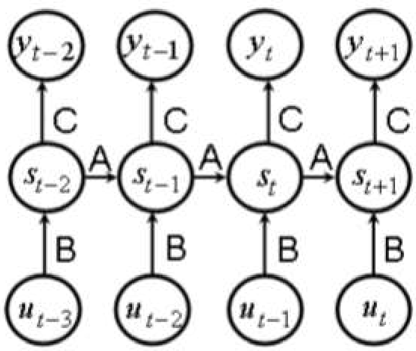

Fig. 3. Topology of the RNN.

$s_\tau, u_\tau, and\ \ y_\tau$ are the system state, system input, and system output. σ is a nonlinear transformation to model the nonlinearity in the transfer function.

The RNN uses only s_t as the memory, and it is prone to fade off in transitions of state. The Long Short-Term Memory Network (LSTM) model is used to address this problem. LSTM has a special memory cell, which retains the long-term past data to calculate the current system state and system output as follows:

$$i_t = \sigma(x_t U^i + h_{t-1} W^i) \qquad \text{Eq. (1)}$$

$$f_t = \sigma(x_t U^f + h_{t-1} W^f) \qquad \text{Eq. (2)}$$

$$o_t = \sigma(x_t U^o + h_{t-1} W^o) \qquad \text{Eq. (3)}$$

$$\tilde{C}_t = tanh(x_t U^g + h_{t-1} W^g) \qquad \text{Eq. (4)}$$

$$C_t = \sigma(f_t * C_{t-1} + i_t \tilde{C}_t) \qquad \text{Eq. (5)}$$

$$h_t = tanh(C_t) * o_t. \qquad \text{Eq. (6)}$$

The model calculates various ratios of the input and internal states to model the nonlinearity by performing a nonlinear transformation of x_t and h_t, where input h_t is the state of the system at each time step. The nonlinear operations between x_t and h_t can be used to simulate the behavior of nonlinear systems. C_t is the memory unit of the system and retains the effect of the previous inputs from the system, which is then used to calculate the future output. The structure of the model is shown in Fig. 4 (source: https://colah.github.io/posts/2015-08-Understanding-LSTMs).

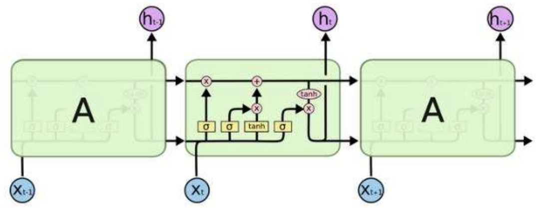

Fig. 4. LSTM architecture.

Training Process

After appropriate preprocessing, the data were divided into training, validation, and test sets. The validation data set was used to determine the complexity of the model and parameters used in optimization processes, which include the depth of the model, the size of the vector expressing the state of the system, the nonlinear transformation function, and the learning rate. The parameter space was randomly searched to obtain the parameters that are most suitable for this data set. The model was optimized using the training data set; then, we simultaneously observed whether the error rate on the training data set and the validation data set continues to decline, so as to determine whether the best state of the model is obtained. Then, the test data set was used to evaluate the performance of this model.

The recent test results are shown in Fig. 5. It is seen that the model captures the trend of the signal of the test, but cannot accurately predict high-frequency signals. This inaccuracy may be caused by the uneven distribution of catalogs in the seismic source. Therefore, the source of the earthquake must be further analyzed and the accuracy of the model should be improved.

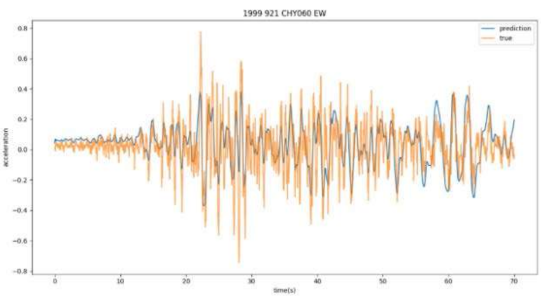

Fig. 5. Test results (921 CHY060).

Conclusions

This study used deep learning with data obtained from a uniaxial small-scale shaking table test to calculate the target control commands. Once the accuracy of the history of the acceleration response is improved, the model will be transferred to a large-scale earthquake simulation shaking table with six degrees-of-freedom to obtain actual results.

References

Chen P-C, Lai C-T, Tsai K-C. A control framework for uniaxial shaking table considering tracking performance and system robustness. Struct Control Monit. 2017;24:e2015. https://doi.org/10.1002/stc.2015

Chen P-C, Kek M-K,Hu Y-W, Lai C-T. Statistical reference values for control performance assessment of seismic shake table testing. Earthquakes and Structures, Vol. 15, No. 6 (2018) 595-603.

Filiatrault A, Kremmidas S, Seible F, Clark AJ, Nowak R, Thoen BK. Upgrade of first generation uniaxial seismic simulation system with second generation real-time three-variable digital control system. Proceedings of the Twelfth World Conference on Earthquake Engineering, Auckland, New Zealand, February 2000.

Nowak, R.F., D.A. Kunsner, R.L. Larson and B.K. Thoen (2000). Utilizing modern digital signal processing for improvement of large scale shaking table performance. Proceedings of 12th World Conference on Earthquake Engineering 2035, 1-8

S. J. Dyke, B. F. Spencer, P. Quast, M. K. Sain. Role of Control-Structure Interaction in protective system design. ASCE Journal of Engineering Mechanics, Vol. 121, No. 2, Feb. 1995 pp. 322–338.

Tagawa, Y. and Kajiwara, K. (2007), “Controller development for the E-Defense shaking table”, Inst. Mech. Eng., Part I: J. Syst. Control Eng., 221(2), 171-181.

Zhang, R., Chen, Z., Chen, Su., Zheng, J., Buyukozturk, O., Sun, H. (2019), “Deep long short-term memory networks for nonlinear structural seismic response prediction”, Computers & Structures, Vol. 220, pp. 55-68

Zimmermann, H.G., Tietz,C., & Grothmann,R. (2012). Forecasting with recurrent neural networks: 12 tricks. In G. Montavon, G. B. Orr, & K.-R. Müller (Eds.), Lecture notes in computer science: Vol. 7700. Neural networks: tricks of the trade(2nd ed.)(pp.687–707). Springer

Development of a Seismic Impact Assessment for a Road Network in Taiwan

Cheng-Tao Yang1、 Chi-Hao Lin2、Wei-Hsueh Huang3、Yi-Jie Chuang3

楊承道[1]、 林祺皓[2]、黃為學[3]、莊奕婕[3]

Abstract

This study uses a small regional road network as an example to introduce the recent development in the seismic impact assessment of a road network (ROSA). ROSA is utilized to evaluate the impact on the traffic between two areas when part of the road network is damaged and the road is blocked due to an earthquake. Since roads not only maintain human daily life and economic activities but also play an important role in emergency rescue and evacuation, it is important to evaluate the seismic retrofits of road networks. Furthermore, through ROSA, the risk of seismic blockage of road components and the impact of regional traffic can be identified; consequently, ROSA offers strategies and helps in pre-earthquake disaster prevention planning for the road network.

Keywords: seismic impact assessment, road network, earthquake disaster

Introduction

If a road network is damaged from a severe earthquake and is blocked, not only is the rescue in stricken areas hindered, the daily life and economic activities in unstricken areas are affected as well. Because the impact is extensive, the seismic assessment of a road network (ROSA) needs to reasonably quantify the damage in terms of economic losses to effectively evaluate the impact of earthquakes on a road network. ROSA is a multidisciplinary integrated technology that combines the characteristics of seismic risk, transportation demand, balance of the network, seismic resistance of road components, and distribution of the road network to determine the risks from earthquake damage to roadway systems (REDARS2) (Werner et al., 2006).

REDARS2 is a tool to analyze seismic risk for highways. It primarily comprises four modules. (1) Hazards (potential indicator of earthquake disaster), a module that evaluates ground vibration, soil liquefaction, and fault ruptures that are accompanied with earthquakes, which possibly result in permanent surface deformations. (2) Components (earthquake loss estimation), which estimates the degree of damage, repair time and cost, and traffic conditions of each infrastructure component, such as pavements, bridges, and tunnels, due to earthquake disasters (for example, whether speed limits of vehicles need to be lowered or the road partially or fully closed before bridges are repaired). (3) Systems (road network analysis), utilized to assess whether the efficiency of the road network declines owing to the impact of an earthquake disaster, such as, for instance, whether a certain bridge within a road network is damaged and needs to be closed, which results in increased travel time and distance. (4) Economic (economic losses), which calculates different kinds of economic losses such as maintenance cost, travel cancellation, and delay of vehicles that are required for the infrastructure of the road network after the earthquake.

The Taiwan Earthquake Loss Estimation System (TELES) (Yeh et al., 2006), developed by the National Center for Research on Earthquake Engineering (NCREE), is currently available for estimating the probability of damage and loss for roads and bridges after earthquake disasters in Taiwan. The relatively mature techniques include three modules, Hazards, Components, and Economic, which are similar to REDARS2. With these techniques, we are now developing the System Module to develop a seismic impact assessment on daily traffic whose road network is damaged.

When a road component is damaged, it leads to a transportation impact on the road network. This can be observed in several ways, such as vehicles having to detour, which results in increased travel distance and an economic loss. Consequently, the overall travel time of all the vehicles in the damaged road network would

[1] Associate Researcher, National Center for Research on Earthquake Engineering, Taipei, Taiwan
[2] Assistance Researcher, National Center for Research on Earthquake Engineering, Taipei, Taiwan
[3] Research Assistance, National Center for Research on Earthquake Engineering, Taipei, Taiwan

be increased relative to the undamaged road network. Note that the wasted travel time caused by detouring is related to the level and quantity of damage to road components. The damage level can be roughly divided into (1) slight damage, meaning that vehicles can still access the network at lower speeds and on narrowed roads, and (2) severe damage such as falling bridges, bridge collapse, etc., meaning that the bridges need to be closed and the traffic is blocked. Through the System Module, the daily transportation demand can be redistributed to the part of the damaged road network after an earthquake, and the total delay of travel time can be accessed on the basis of the desired methodology, such as user equilibrium or system optimum assignment. Through converting time and driving loss to a monetary value, the increase in travel time and distance can be converted to equivalent currency to quantify the impact of earthquake losses on a road network.

For TELES, two functions must be have up-to-date data: (1) travel demand analysis of the regional road network and (2) route assignment. The former aims to determine how the residents living in the regional road network utilize this transportation network on weekdays, with an Origin-Destination (OD) matrix established for which residents would go from a certain origin to a certain destination, while the latter assigns all the reasonable Origin-Destination routes to estimate the required travel time for all the vehicles. In this study, a small regional road network in Taiwan is taken as an example to introduce the under-development technology, which is shown in the second section. The relevant theory and results of the road network analysis are illustrated in the third section, and finally, the concluding remarks are given.

Study Region

Figure 1 shows the target study region. This small regional road network includes Banqiao District, New Taipei City, and Wanhua District, Taipei City, which are separated by the Tamsui River. Furthermore, these two cities are connected by four bridges above the Tamsui River.

Figure 1. Schematic diagram of the connecting bridges between Banqiao and Wanhua District.

Table 1 demonstrates the vehicles driven from Banqiao District to Wanhua District during the morning rush hour (7:30 a.m. to 9:30 a.m.) on each bridge (from the data of traffic flow in Taipei City in 2018).

Table 1. Vehicles from traveling from Banqiao to Wanhua District in the morning rush hour.

	PCU
Bridge 1	10436
Bridge 2	2174
Bridge 3	6296
Bridge 4	4176

As displayed in Figure 2, Banqiao District includes 126 tracts while Wanhua District includes 36 tracts; moreover, the dots in the picture represent the centroid of tracts. Here, it is hypothesized that these two regions are completely separated from other regions. All the vehicles departing from one of the centroids of these 126 tracts choose one of the four bridges and drive to the centroid of the 36 tracts in Wanhua District. After establishing the OD Matrix of Banqiao and Wanhua Districts, the overall required travel time for vehicles from Banqiao to Wanhua Districts during rush hour could be calculated based on route assignment. Subsequently, it is assumed that one of the four bridges is damaged during the earthquake. To estimate the impact of bridge blockage on regional traffic, the damaged bridge can be removed from the road network and the route assignment can be restarted to access the overall required travel time.

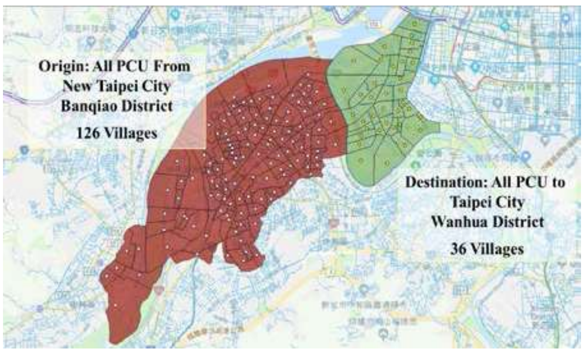

Figure 2. Centroids of tracts within Banqiao and Wanhua Districts.

Methodology

OD MATRIX

The establishment of the OD Matrix is based on the result of traffic observations on road network links and estimations under reasonable assumptions. The following are hypothesized:

- First, all the vehicles on these four bridges are departing from one of the 126 tracts in the Banqiao District, choosing one of the four bridges, and driving to one of the tracts in Wanhua District in their morning commutes.
- Second, the ratio of vehicles departing from each tract is distributed proportionally to the ratio of residential floor area in each tract in Banqiao District.
- Third, the ratio of vehicles arriving at each tract is distributed proportionally to the ratio of commercial floor area in each tract in Wanhua District.
- Fourth, the commuters choose the quickest path from their home to their work place.

Under these assumed circumstances, each of the possible OD pairs is matched together iteratively to estimate the OD matrix of these two areas for the morning commute.

Route Assignment (User-optimized equilibrium)

Figure 4 shows the road network of the study region. In the present study, the path of each trip or O-D Pair is chosen assuming all the vehicles choose the path that has the least travel time from the origin to the destination. If the origin were the same as the destination, choosing a different path would lead to equivalent travel time. Regardless of problems due to road capacity, if the increase in vehicles would result in congestion and increase in the travel time on the road, all the travel times in the network are allocated and the overall travel time of all vehicles in the network are estimated. From this, the total travel cost of the undamaged study region can be obtained. Afterwards, it is assumed that one of the four bridges may be damaged when an earthquake strikes. If the damaged bridge is removed from the road network and the route assignment is restarted, the overall required travel time of the damaged road network could be determined. Finally, the impact of each damaged bridge on the road network can be acquired by comparing the increased time in traffic.

Case Study

Table 2 demonstrates the overall traffic time of the study region during the morning commute for an undamaged and a partially damaged road network. Since the study region is only a small area and only traffic in one-direction is considered (from Banqiao to Wanhua District), the overall traffic times cannot be used as the data of the real road network; however, the increased travel time due to the damage of the individual bridge can be compared to understand the importance of the area. As shown in Table 2, Bridge 1 has the greatest impact on the area if it is damaged, while the impact of Bridge 2 is much smaller than other bridges.

Table 2. Overall traffic time of the undamaged and partially damaged road network.

Scenario	System cost (total travel time)
Undamaged road network	220,440 min
Bridge 1 is damaged	227,959 min (+7519)
Bridge 2 is damaged	220,528 min (+88)
Bridge 3 is damaged	222,280 min (+1840)
Bridge 4 is damaged	224,247 min (+3808)

Conclusions

The estimation of the impact on traffic of a damaged road network from earthquakes needs to consider the damage state and the OD matrix of the road components as input parameters. The OD matrix expresses the demand of residents in the road network for weekday travel. In this study, the government’s open source data (the traffic flow of the road network links) and the use of regional building data (ratio allocation of both the distribution of the residential floor area and the commercial floor area) are utilized for estimating the OD matrix between two regions. However, the legitimacy of the method for establishing the OD matrix needs to be confirmed in future research. Through route assignment, different traffic times between undamaged and damaged road networks can be calculated and compared, and thus the cost of increased travel time in a damaged road network can be evaluated. Overall, this developing technology can assess the impact on road networks under seismic hazards with the help of an already developed tool (assessment for the loss of damaged highways and bridges) from the NCREE. This technology can assist the department of road management in road planning for rescue and evacuation, seismic strengthening of road components, and alternative road planning after earthquakes.

References

Werner, S. D., Taylor, C. E., Cho, S., Lavoie, J. P., Huyck, C. K., Eitzel, C., ... & Eguchi, R. T. (2006). Redars 2 methodology and software for seismic risk analysis of highway systems (No. MCEER-06-SP08).

Yeh, C. H., Loh, C. H., & Tsai, K. C. (2006). Overview of Taiwan earthquake loss estimation system. Natural hazards, 37(1-2), 23-37.

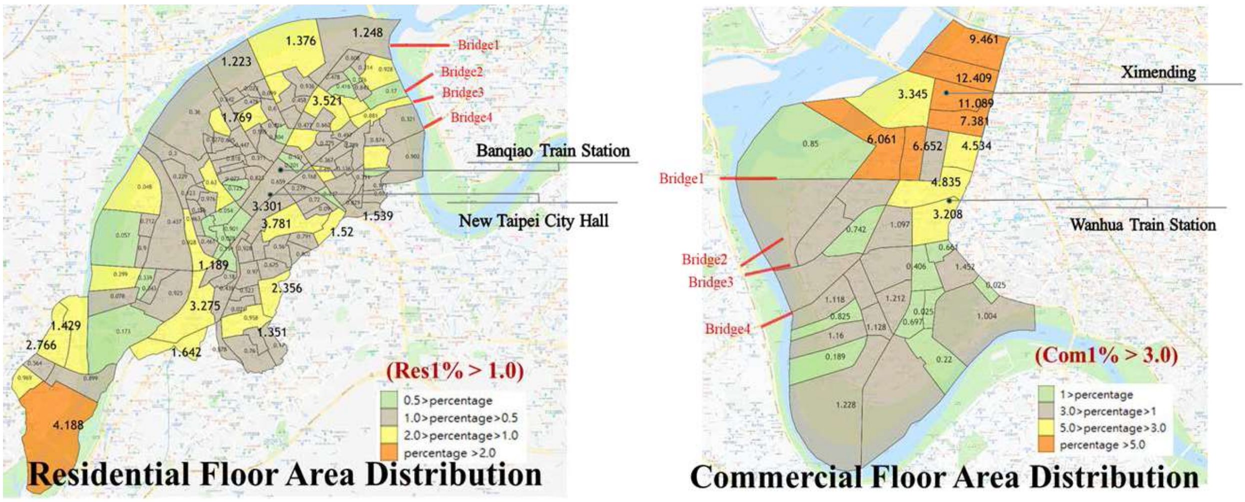

Figure 3. The ratio of residential/commercial floor area distribution in each tract in Banqiao and Wanhua Districts.

Figure 4. The road network of the study region.

Simulation Analysis on the Post-Earthquake Congestion of an Emergency Department

You-Xuan Lin[1] and Chi-Hao Lin[1]

林祐萱 [1]、林祺皓 [1]

Abstract

After a massive earthquake, the supply of medical services may fall short of the rising demand for treatment, leading to congestion in an emergency department (ED). In 2018, a 6.2 magnitude earthquake shook Hualien, on the eastern coast of Taiwan. A local hospital reported that an influx of patients with minor to moderate injuries congested the ED. Moreover, according to the official after-event summary report, over 90% of casualties fall in the categories of minor/moderate levels. These reports indicate that a sudden increase of patients with earthquake-induced injuries that are relatively minor is a critical problem that needs to be tackled. In this study, we used discrete event simulation (DES) to investigate the state of an ED confronted with surging patient arrivals after massive earthquakes. The arrival rates of patients in our simulation were based on data from Chile. SimPy, a Python DES library, is utilized to perform the simulation with a patient flow model. The simulation is operated under the assumption that all equipment and resources are intact and functional. We discuss the influences of earthquake-induced low-acuity casualties on the performance of an ED in terms of (1) patient sojourn time, *i.e.*, the period from arrival to exit, and (2) the total recovery time of an ED.

Keywords: resilience, queuing, patient flow, discrete event simulation, emergency department

Introduction

Resilience refers to the ability of a community in the face of a disaster to "resist, absorb, accommodate, adapt to, transform and recover from the effects of a hazard in a timely and efficient manner (United Nations International Strategy for Disaster Reduction, 2009)." To put it simply, a resilient community is one that mitigates the impact of a disaster as much as possible and resumes its normal state as quickly as possible. Of the vital factors that determine resilience, hospital emergency departments (ED), whose function is to offer emergency healthcare and accommodate patients, play a critical role in minimizing fatalities and relieving the suffering of victims.

A sudden increase in the demand for medical care after a mass-casualty incident may put limited emergency healthcare resources under pressure and diminish the effectiveness of patient care. The earthquake that occurred on February 6, 2018, in Hualien in eastern Taiwan is an example. A local hospital reported that within two hours after the earthquake, more than 100 patients arrived and the ED was congested by patients queuing for medical care. Of all the patients, minor and moderate injuries were the majority. The official after-event summary report (Ministry of Interior, 2019) provides more detail: over 90% of patients belonged to acuity levels 3 to 5 (AL3–AL5). While relatively less serious and less urgent, these patients still posed a threat to ED congestion due to the large number.

A flood of patients into EDs after an earthquake may risk collapsing the emergency healthcare service, thus causing less effective healthcare and even unnecessary loss of life. A failure to contain the impact of an earthquake then violates the basic principle of resilience. To address the overcrowding problem, this study focuses exclusively on AL3 to AL5 patients, which are assumed to be the primary cause of post-earthquake congestion.

Foreseeing possible situations that an ED may confront is one way to avoid the worst-case scenarios. To assist in accomplishing this, an ED performance measure that reflects effectiveness of patient treatment has been proposed, *i.e.*, the patient sojourn time (ST).

[1] Assistant Researcher, National Center for Research on Earthquake Engineering

With the use of ST, we can estimate the response of an ED to different volumes of patients by conducting repeated simulations.

In this study, discrete event simulation (DES) was conducted to simulate the operation of an ED. The experiences of patients during the course of a visit in an ED were modeled as a series of events (or medical services). Queuing behaviors between these events were modeled by setting a limited number of resource units for each event and specifying the time each event takes to complete. 300 runs of simulations were carried out for each of the five different scenarios: one for a normal number of patients and four for increased numbers of casualties. By comparing the post-earthquake ST and the regular ST, the relationship between the growth of patient numbers and the rise of ST can be evaluated.

While it is obvious that when demand grows but supply remains constant, the demand-supply imbalance in medical treatment will lead to ED congestion, the disastrous situations that could result are seldom contemplated or quantitatively evaluated. It is not possible to build a resilient community unless people are prepared for worst-case scenarios and know what actions to take to address them. The findings of this study are expected to provide reliable references for policymakers and practitioners in relevant fields to formulate response measures for emergency medical treatments after earthquakes and other mass-casualty incidents. This will improve the resilience of a society. The sojourn time measure, ST, and simulation model also offer a valuable foundation for future studies on ED congestion.

Model of Patient Flow and Parameter Settings

The DES was conducted with the help of a Python library, SimPy (Lünsdorf and Scherfke, 2003) and designed to simulate patient flow in an ED. Based on the assessments of Favier *et al.* (2019) and Côté (1999), with some modifications to better approximate the nature of EDs in Taiwan, the routes that different types of patients may take through an ED were mapped, as shown in Fig. 1.

When patients arrive, they are first triaged and then wait for doctors' consultation and treatment. After being treated and following instructions, the patients' paths diverge as indicated in Fig. 1: (1) leaving the ED immediately after treatment, (2) staying under observation, and (3) undergoing further examination and being kept under observation for a while. 'Discharge' here means that patients are no longer receiving emergency medical attention; they may be admitted as inpatients, transferred to other institutions, or sent home to recover.

Based on data from Chile, Favier *et al.* (2019) proposed the estimated proportions of different triage categories that would be assigned to one of the above three paths. This study primarily adopted their estimations, but some changes were made. For example, in their paper, a proportion of AL5 patients would leave directly without being treated at all. This would be unacceptable in Taiwan, so that portion of patients were reallocated to Paths 1 and 2.

The distribution of patients in different acuity levels and the percentages assigned to different paths are listed in Table 1. Of all the patients arriving after an earthquake, 52% would be categorized as acuity level 3, 32% acuity level 4, 5% acuity level 5, with the remaining 11% acuity levels 1 and 2 combined. Since this study focuses exclusively on the queuing behaviors of minor and moderate acuity levels (AL3–AL5), the 11% of patients in AL1 and AL2 are assigned to a fourth route (Path 4, Fig. 1), which is assumed to utilize a separate reservoir of resources and is not considered in this study. The percentage of AL3 and AL4 patients directed to Paths 2 and 3 were assumed to be the same: 76% would take Path 2 and the 24% Path 3. As for AL5 patients, 75% were assumed to take Path 1 and 25% Path 2.

Considering the fact that, after an earthquake, patients arrive at the ED in a pattern different from that on normal days, we directly borrowed the data from Favier *et al*. (2019), which was derived by estimating both the total patient numbers generated by earthquakes of different intensities and the time distribution of the injured patients reaching the ED after a given earthquake. As shown in Fig. 2, instead of being fixed, the arrival rates fluctuate with the passage of time after an earthquake strikes. The arrival rates in the five scenarios used for simulation in this study include one in the normal situation and four after earthquakes of different intensities. However, it should be noted that the seismic intensities in the figure mainly serve as convenient tags to help distinguish between different patient volumes. The casualty numbers would vary if only one parameter (*e.g.*, distance to the epicenter) is changed even with the same intensity. This study is primarily concerned with the increase of patient numbers above that of normal days and how it influences the ST, rather than the characteristics of a particular seismic event.

The simulation program is designed to generate patients at the rates designated in Fig. 2. As one patient is generated, he/she will be moved forward along the assigned route to accept medical services and this occupies one unit of resource. The time for each medical service and the resource number are two input parameters that need to be set in the program. It is supposed that the service time for each medical service follows a certain statistical distribution. The time each patient has to spend on one service is determined by random sampling from the corresponding distribution. The statistical distributions of each service and resource numbers are based on previous studies (Favier *et al.*, 2019; Côté, 1999) with some adjustments made after initial testing, shown in Table 3. The resource numbers of each service are presented in Table 2. The resource number for Observation is set to infinite in that the space for patients to rest can be any vacant space, such as benches in the hall.

To ensure that the parameter settings for the simulation model were realistic, they were checked against real ED operations. To start with, according to a monthly survey in October 2012, the distribution of patients seeking emergency medical care from hospitals in the Tainan Metropolitan Region (southern Taiwan) was as follows: AL1 and AL2 patients constituted 10% of all the patients, AL3 patients 59%, AL4 patients 28%, and AL5 patients 3% (Kao *et al.*, 2015). While not exactly the same, the percentages of patient visits set in our simulation (see Table 1) deviate little from the survey.

On the other hand, to confirm that the resource number and service time of each medical service were reasonably set, we compared the simulation results with the real census data. According to a survey by the Joint Commission of Taiwan (as cited in the Ministry of Health and Welfare, 2013), the treatment waiting times for AL3, AL4, and AL5 patients was, on average, below 10 minutes in all EDs in Taiwan, indicating that these types of patients are exempt from ED congestion. Similarly, in our simulation model, each AL3–AL5 patient approximately waits for 9 minutes before receiving treatment on normal days. The result indicates that the model can reproduce real ED operations.

The simulation for each scenario was repeated 300 times in total to average out effects of outliers during sampling. The length of each run varied from 12 to 20 days depending on the time needed to recover from the seismic effects. The first six days were kept constant, with the first two days representing the pre-earthquake situation and the following four days generating the rush of earthquake-induced patients. The subsequent days varied for different scenarios to allow complete displays of recovery, which for some cases was lengthy.

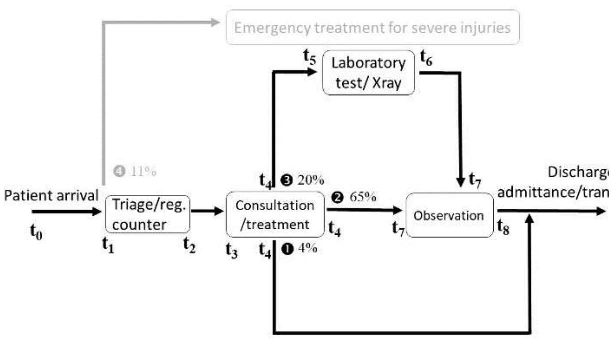

Fig. 1. Patient flow in an ED.

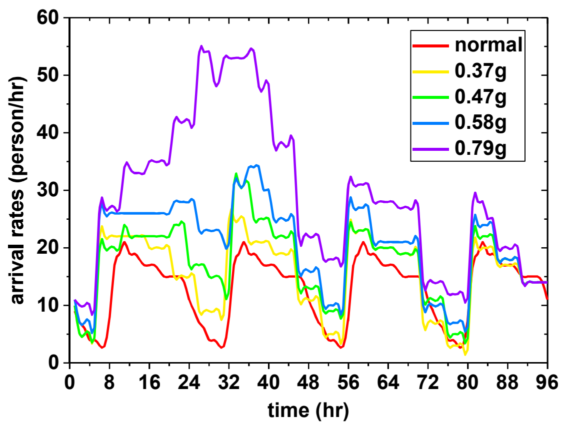

Fig. 2. Patient arrival rates within four days after earthquakes of different intensities (peak ground acceleration)

Table 1. Proportions of acuity levels and paths.

Level / Path	AL3	AL4	AL5	AL1+AL2	ALL
	52%	32%	5%	11%	100%
Path 1	0%	0%	75%	0%	[a]4%
Path 2	76%	76%	25%	0%	[b]65%
Path 3	24%	24%	0%	0%	[c]20%
Path 4	0%	0%	0%	100%	[d]11%
	100%	100%	100%	100%	100%

Table 2. Resource numbers of each service.

Service	Quantity	Source
Triage/registration	1	Favier *et al.* (2019)
Consultation/treatment	13	Favier *et al.* (2019)
Lab /X-ray	6	Obtained by testing
Observation	∞	Obtained by testing

Table 3. Distribution of service times.

	Statistical Distribution	Source
Triage/registration	*Gamma(4.5, 0.7)	Favier *et al.* (2019)
Consultation/ treatment	*Tri(15, 45, 90)	Favier *et al.* (2019)
Observation	*Tri(0, 15, 60)	Modified from Favier *et al.* (2019)
Lab/X-ray	*Tri(30, 75, 120)	Favier *et al.* (2019)

* in minutes

Preliminary Results

Preliminary results, as given in Table 4, show that when the number of patients is increased by a factor of 1.4, this causes at most a four-fold increase in sojourn time, and the queuing pattern can return to normal immediately after the earthquake-related patient arrivals terminate (*i.e.*, on the 5th day after the earthquake in our simulation). However, if 2.3 times more patients arrive at the ED during the first four days after the earthquake, then the sojourn time increases by as much as 36 times the normal value. The corresponding recovery would take 6 more days to complete after the rush.

Table 4. Preliminary results of the DES.

Growth ratio of patient number	Growth ratio of sojourn time	Extra days for recovery
1.4	4	0
2.3	36	6

Conclusion

We used the DES to investigate the state of an ED confronted with surging patient arrivals after massive earthquakes. If the growth ratio of patient numbers is greater than 1.5, then the patient sojourn time and the total recovery time increase sharply. In the future, we will summarize the queueing patterns with two regression equations to represent the influence of patient surge on post-earthquake congestion derived from the simulation. One describes the relationship between changes in the number of patients and sojourn time. The other, addresses the relationship between changes in the number of patients and total recovery time.

References

United Nations International Strategy for Disaster Reduction. 2009. *2009 UNISDR Terminology on Disaster Risk Reduction*. Retrieved from https://www.preventionweb.net/files/7817_UNISDRTerminologyEnglish.pdf

Shiu, M.N. 2013. Emergency Department Overcrowding Analysis and Countermeasures. Department of Medical Affairs. Ministry of Health and Welfare. Retrieved from https://www.mohw.gov.tw/dl-3079-d8ff7291-e302-4a8f-a2a5-8208c4a1ada2.html

Favier, P., Poulos, A., Vásquez, J.A., Aguirre, P. and de la Llera, J.C. 2019. Seismic risk assessment of an emergency department of a Chilean hospital using a patient-oriented performance model, Earthquake Spectra, 35(2), 489-512.

Côté, M.J. 1999. Patient flow and resource utilization in an outpatient clinic, Socio-Economic Planning Sciences, 33, 231-245.

Müller, K. and Vignaux, T. 2003. SimPy: Simulating Systems in Python, ONLamp.com Python Devcenter.

Ministry of the Interior. 2019. Summary report by central emergency operation center for 0206 Hualien Earthquake.

Kao, C.Y., Yang, J.C. and Lin C.H. 2015. The impact of ambulance and patient diversion on crowdedness of multiple emergency departments in a region, PLoS ONE, 10(12): 1-14.

An Application of Shaking Table and Laminar Shear Box: 1/25 Offshore Wind Turbine Model Test

Shen-Haw Ju[1], Bai-Yi Huang[2], Chia-Han Chen[3], Sheng-Huoo Ni[1] Kuang-Yen Liu[4], Yung-Yen Ko[5], Shang-Yi Hsu[3], Yu-Wen Chang[3], Lyan-Ywan Lu[1], Ging-Long Lin[6]

朱聖浩 1、黃百誼 2、陳家漢 3、倪勝火 1、劉光晏 4、柯永彥 5、許尚逸 3、張瑜文 3、盧煉元 1、林錦隆 6

Abstract

The first offshore wind farm in Taiwan started commercial operation at the end of 2019. The Taiwanese government aims to increase the installed capacity of offshore wind power up to 5.7 GW by 2025 as there are abundant wind resources on the west coast of Taiwan. However, natural hazards such as typhoons and earthquakes are a constant threat. It is important to ensure the safety of wind turbines and their supporting structures. Therefore, a 1/25 scale model of an offshore wind turbine with a jacket foundation was tested in NCREE Tainan Laboratory. The tested model includes wind turbine tower, and a jacket-and-pipe foundation, which was installed in the shear box filled with water and sand to simulate seabed environment. It was excited by white noise, sinusoidal excitation, and near-fault artificial earthquakes. The analysis of testing data is still underway, and expected results include structure–soil interaction, soil liquefaction, and shock absorption technique for wind turbine with jacket foundation.

Keywords: Shaking table, laminar shear box, offshore wind turbine, soil liquefaction, water pluviation, TMD.

Introduction

In the past, Taiwan relied on imports to meet its energy needs. These include oil, coal, natural gas, and nuclear energy. However, the national energy policy aimed to replace nuclear energy with renewable energy. There are abundant wind resources on the west coast of Taiwan. Among the sources of renewable energy, solar energy, hydroelectricity, geothermal energy, and wind power (especially offshore wind power), are the most promising. Hence constructing offshore wind farms is now a major policy endeavor in Taiwan. By the end of 2019, the first offshore wind farm had started commercial operation. However, there is a constant threat from natural hazards such as typhoons or earthquakes. Therefore, it is important to ensure the safety of wind turbines and their supporting structures.

Gravity-type, monopile–type, and jacket-type foundations are commonly used in wind turbine supporting structures worldwide. Gravity-type and monopile-type foundations are easy to manufacture and install. The monopile type are the most commonly used foundation for wind turbines. Earthquakes occur frequently in Taiwan. Meanwhile, soil liquefaction may also occur in saturated soil environments like seabed, reducing the supporting force on piles or foundations. Compared to other foundation types, gravity-type foundation is so sensitive to soil condition that soil liquefaction may cause differential settlement. By contrast, the size of a monopile type foundation needs to be increased to reduce the impact of soil liquefaction, which leads to an increase of both cost and installation difficulty. Jacket-type foundation consists of multiple piles, a jacket with braces, and a transition piece. High redundancy and stiffness lower

[1] Professor, Department of Civil Engineering, National Cheng Kung University
[2] Assistant Researcher, National Center for Research on Earthquake Engineering,
[3] Associate Researcher, National Center for Research on Earthquake Engineering
[4] Associate Professor, Department of Civil Engineering, National Cheng Kung University
[5] Assistant Professor, Department of Civil Engineering, National Cheng Kung University
[6] Assistant Professor, Construction Engineering, National Kaohsiung University of Science and Technology

its soil dependency. Considering the economy and efficiency, jacket-type foundation is more suitable for wind turbine supporting structures than other structures in Taiwan.

Instruments

In order to simulate the dynamic response of a wind turbine and its supporting structure, the earthquake simulator, or the shaking table, is introduced. The long-stroke and high-speed shaking table in NCREE Tainan laboratory can move along the x, y, and z axes translationally and rotationally with a payload of up to 250 tons. The outstanding capacity of this shaking table makes it possible to experiment on a large-scale structural model suffering near-fault ground motion.

The test platform for underwater foundation and ground (shear box for short) is designed to simulate the dynamic behavior of underwater or underground soil layers in half space. The shear box consists of a 3-m high rigid wall and a 5 m × 5 m base, and two sets of layered stacked frame system with linear guideways. The inner and outer frames can move horizontally with 35 and 65 center meter strokes, respectively, and a rubber seal is installed inside the inner frame to provide water tightness and a flexible boundary. The area of the inner frame is 2.5 × 2.5 m^2, so that the shear box has a capacity of 2.5 × 2.5 × 3 m^3. The applications of shear box include seismic response of soil, soil–structure interaction, and soil liquefaction, etc.

To prepare the saturated soil specimen, water pluviation method was introduced in this test. The sand pluviation instrument is a sand container with a perforated bottom plate. The gate of the bottom plate can be opened or closed remotely. Once the sand pluviation instrument is placed at the top of the shear box filled with water, the gate is opened and sand is dropped into the shear box. After the sand is deposited uniformly, the saturated soil ground specimen is prepared.

Specimen Preparations

Considering the seabed condition of the offshore wind farm outside Changhua County, a saturated soft soil layer was taken as the underwater ground specimen. To prepare the ground specimen, the procedure of water pluviation method is shown in Figure 1.

Based on the properties of NREL 5-MW baseline wind turbine (NREL, 2009) and the jacket structure proposed by Ju et al. (2019), the design of the upper structure is shown in Figure 2. The wind turbine and its supporting structure were minified by a factor of 1/25 to fit in the shear box. Assuming that the material proprieties are the same, and the mass of the model is 1/625 of the original, the stiffness and natural frequency relations between the model and the original are shown in equations (1) and (2).

$$K_{\text{model}} = \frac{EI_{\text{model}}}{L_{\text{model}}} = \frac{25 \cdot EI_{\text{original}}}{625 \cdot L_{\text{original}}} = \frac{K_{\text{original}}}{25} \tag{1}$$

$$\omega_{\text{model}} = \sqrt{\frac{K_{\text{model}}}{M_{\text{model}}}} = \sqrt{\frac{625 \cdot K_{\text{original}}}{25 \cdot M_{\text{original}}}} = 5 \cdot \omega_{\text{original}} \tag{2}$$

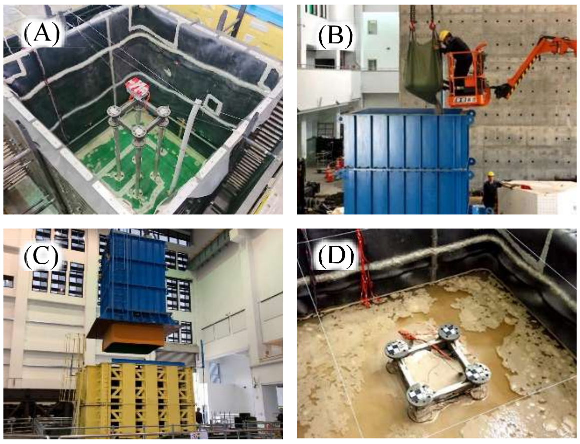

Fig. 1. (A) Piles are attached to the bottom of the shear box in advance, and the sensors inside the ground specimen are also pre-allocated (B) Well-graded silica sand is put into the sand pluviation instrument (C) The instrument is placed above the shear box filled with water and sand is poured inside the instrument in the shear box. (D) After the sand is deposited uniformly, the saturated soil underwater ground specimen is prepared.

The total height of the whole model is 8 m with the 2 m long piles. The jacket structure consists of 4 columns and the x-bracing system, and connects to the piles and the transition piece at its bottom and top, respectively. The transition piece is a section to conjunct the foundation structure and the 3 m high tower. Above the tower, three metal blocks with a total mass of 900 kg, are attached at the top of the model to simulate the mass of the wind turbine nacelle and the rotor.

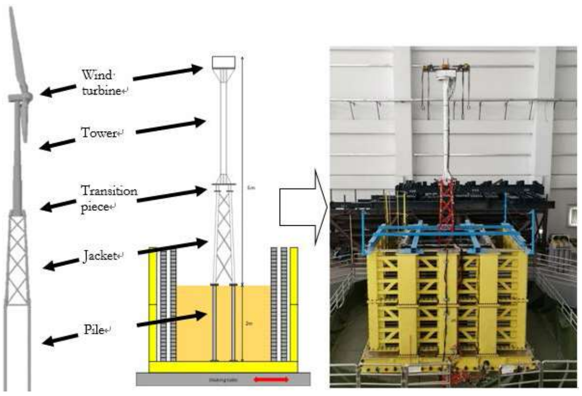

Fig. 2. Design of 1/25 scale model of offshore wind turbine with jacket foundation.

Input Motion and Outcomes

The white noise base excitations implemented in this test are controlled by specifying the RMS of the acceleration to be 0.01 g. The bandwidth is between 0.1 and 30 Hz due to the performance limitation of the shaking table. Figure 3 shows the acceleration response at the top of the model under one of the applied white noise base excitations. According to system identification method, the natural frequency of the model is approximately 1.14 Hz.

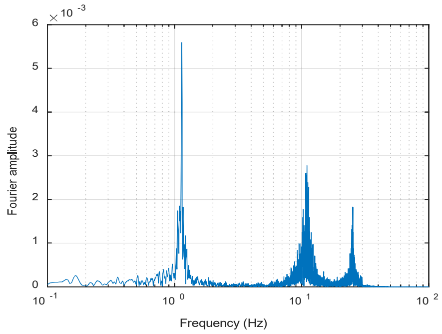

Fig. 3. Fourier spectrum of the acceleration response at the top of the model excited by white noise.

Sinusoidal excitations, all with a frequency of 2 Hz, are implemented in this test. Meanwhile, the amplitude increases from 0.03g to 0.075g. Figure 4 shows the time histories of pore water pressures at different elevations and the corresponding base excitations.

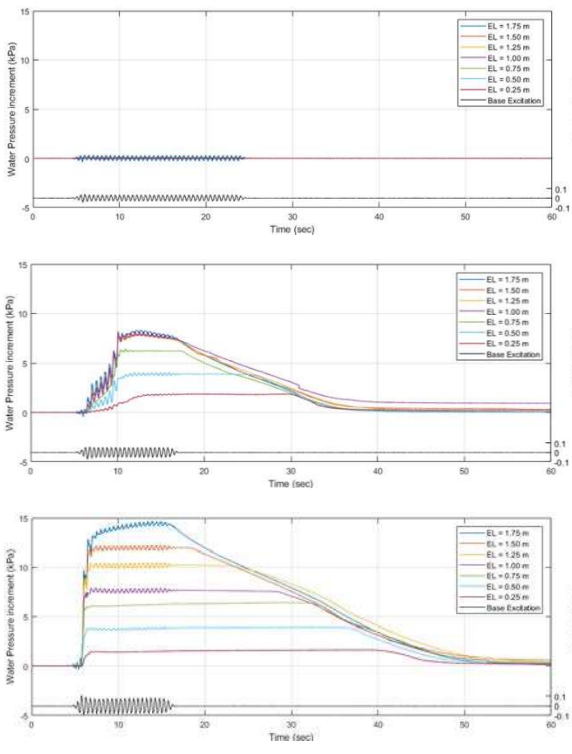

Fig. 4. Pore water pressure increment time histories with varying amplitudes of Sinusoidal excitation and elevations.

Two types of earthquake ground motions were implemented in this experiment. The first one was a typical near-fault ground motion record acquired during the 2018 Hua-Lien earthquake, and the second one is ordinary ground motion record acquired during the 1999 Chi-Chi earthquake.

Equation (2) indicates that the natural frequency of the model is five times that of the prototype. According to the law of similarity, the sampling rate of ground motion needs to be five times higher than the original record to simulate the acceleration response of the prototype. By reducing the time step to 1/5 of the original record and normalizing the ZPA to 0.1 g, the input near-fault ground motion is shown in Figure 5.

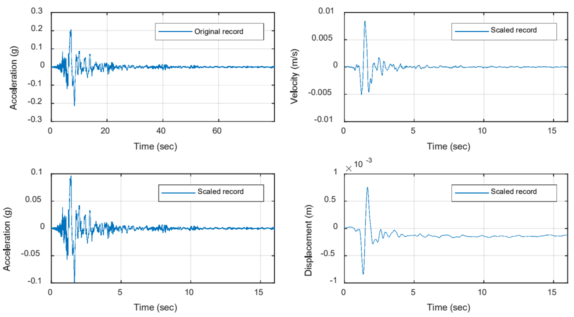

Fig. 5. Original and scaled records of near-fault ground motion record acquired during the 2018 Hua-Lien earthquake. The velocity and displacement time history reveal the nature of near-fault ground motion, which is characterized by intense speed and displacement pluses.

By contrast, based on the geological survey data of the offshore wind farm located outside Changhua County and the probabilistic seismic hazard analysis results, the uniform hazard response spectra (475-year return period UHRS with 5% damping ratio) are shown in Figure 6.

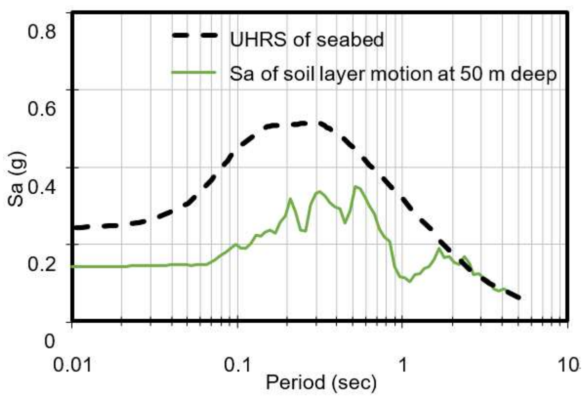

Fig. 6. Considering the dynamic response of the soil layer at target site, the response spectrum of the artificial ground motion 50 m under the seabed is shown as the solid line.

The target UHRS represents the design spectrum of the site on the seabed. However, the shaking table is under the 2 m thick ground specimen; hence, the reference base of the input ground motion is 50 m under the seabed (Figure 7). In order to meet the UHRS, the response spectrum of the conducted artificial ground motion should meet the solid line shown in Figure 6, which is obtained by simulating the dynamic response of the soil specimen.

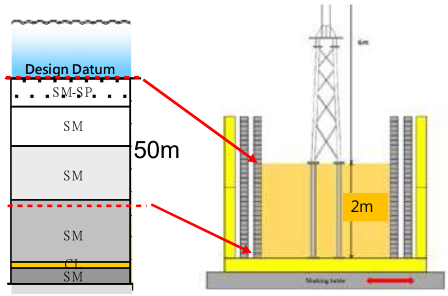

Fig. 7. Reference base of input ground motion for shaking table was 50 m deep under the seabed.

By adjusting the original seed ground motion record shown in Figure 8 (A), the artificial earthquake conducted in this test is shown in Figure 8 (B). The response spectrum of the artificial earthquake was compatible with the green line in Figure 6, and the response spectrum of the motion at the top of the soil specimen was assumed to meet the target UHRS.

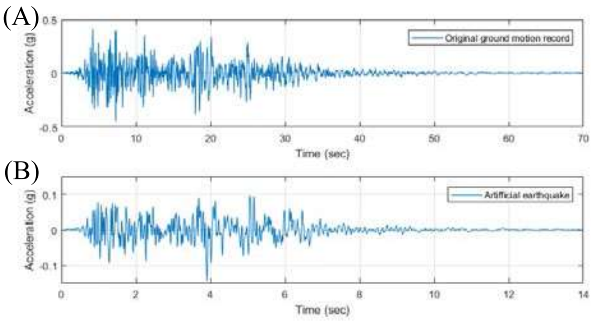

Fig. 8. (A) Original ground motion record adopted as seed. (B) Spectrum compatible artificial earthquake conducted in this test. The response spectrum of the motion at the top of the soil specimen was assumed to meet target UHRS.

Shock Absorption Technique

The maxima of absolute lateral displacements under various excitations are shown in Figure 9. The results indicate that the dynamic responses of the turbine supporting structure under near-fault earthquake were much larger than those under ordinary ground motion. In other words, the threat of near-fault earthquakes is larger than ordinary earthquakes. Therefore, the performance of passive tuned mass damper (TMD) was examined in this test.

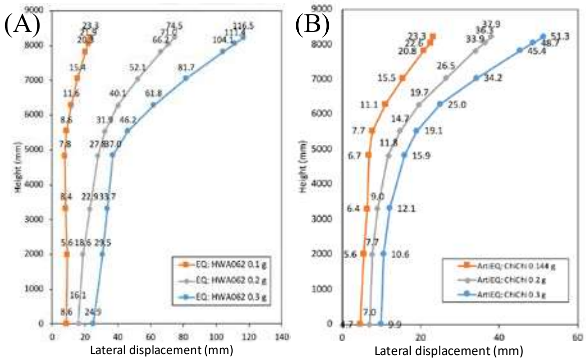

Fig. 9. Maxima of lateral displacements under (A) near-fault and (B) artificial earthquake.

The design formula for the parameters of the TMD was proposed by Lin et al. (1994). The seismic responses at the top of the model under the near-fault ground motion are shown in Figure 10. The dynamic response decays rapidly after the main shock, and the peak response drops approximately 10% with TMD.

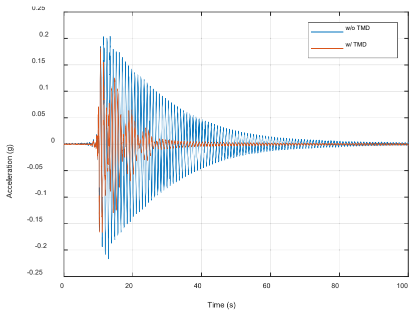

Fig. 10. Dynamic response with active and inactive TMD.

Conclusions

This experiment demonstrated the capability of NCREE Tainan Laboratory to implement dynamic tests on large-scale wind turbine supporting structures and ground specimens. Furthermore, it is possible to examine the dynamic response of wind turbine supporting structure suffering composite load by cooperating with domestic and international researching facilities or companies in the future.

References

Jonkman, J., Butterfield, S., Musial, W., & Scott, G. (2009). *Definition of a 5-MW Reference Wind Turbine for Offshore System* Development, National Renewable Energy Laboratory, USA.

Ju, S. H., Su, F. C., Ke, Y. P. & Xie, M. H. (2019). “Fatigue design of offshore wind turbine jacket-type structures using a parallel scheme,” *Renewable Energy*, 136, 69-78

Lin, C. C., Hu, C. M., Wang, J. F., Hu, R. Y. (1994). “Vibration Control Effectiveness of Passive Tuned Mass Dampers,” *Journal of the Chinese Institute of Engineers*, 17, No. 3, 367-376

Introduction of the Multi-Axial Seismic Test System

Bai-Yi Huang[1], Chin-Ta Lai[2], Juin-Fu Cai[3], Fan-Ru Lin[4]

黃百誼[1]、賴晉達[2]、柴駿甫[3]、林凡茹[4]

Abstract

The multi-axial seismic test system (MAST) in the NCREE Tainan Laboratory is designed for conducting dynamic tests on non-structural components, such as supporting structural elements or critical components of offshore wind turbines. The MAST system consists of a hydraulic-powered 6-DOF shaking table, controller, and data acquisition unit. The table motion is able to reproduce the floor responses of the location of the equipment. The table size of the MAST system is 2.2 by 2.2 m, and the payload has a maximum of 3,500 kg. The 6 actuators of the MAST system are arranged using the Stewart platform-based layout, and the max strokes of the X, Y, and Z axes are 240, 217, and 200 mm, respectively. The peak velocities of the horizontal and vertical axes are 2 and 1.65 m/s, respectively. With a fully loaded specimen, the peak accelerations of the horizontal and vertical axes are 5.5 *g* and 14 *g*. The optimum working frequency of the MAST system is from 0.1 to 60 Hz. Considering these outstanding specifications, the MAST system is compatible with GR-63-CORE or other seismic test regulations for non-structural components. The system has already been assembled and tested, and it will be available soon.

Keywords: multi-axial seismic test system, shaking table, non-structural component test.

Introduction

To achieve the goal of a nuclear-free society, the Taiwanese government aims to replace nuclear energy with renewable energy. There are abundant wind resources on the west coast of Taiwan. According to domestic energy policies, wind power (especially offshore wind power) is the most promising renewable energy resource. However, natural hazards such as typhoons or earthquakes threaten the feasibility of effectively utilizing such a resource. It is therefore important to ensure the safety of wind turbines and their supporting structures.

Wind power involves the use of wind to turn a rotor, driving electric generators to generate power. Critical components such as the convertor or controller inside the nacelle serve to keep wind turbines functional. Therefore, not only the seismic resistance of the wind turbine supporting structure, but also the non-structural components must be testified. However, the dynamic responses and weights of non-structural components are very different from the structure. The floor responses are also usually much larger than the ground motion. Therefore, the shaking table designed for structural testing is not very compatible with non-structural component tests.

Hardware of the MAST System

To examine the seismic resistance of a non-structural component, a hydraulic-powered 6-DOF shaking table (shown in Figure 1) was equipped in the Tainan Laboratory. The optimum working frequency range of the shaking table is from 0.1 to 60 Hz, and the payload has a maximum of 3,500 kg.

The shaking table consists of a rigid table, 6 actuators with a 3 stage servovalve, inline accumulators, a base plate, and a hydraulic service manifold (HSM). The rigid table has a weight of 15.5 t, and the area is 2.2 m by 2.2 m. There are M12 x P1.75 bolt holes distributed uniformly with a spacing of 10 cm on the table to mount specimens.

Underneath the rigid table, there are 6 hydraulic

[1] Assistant Researcher, National Center for Research on Earthquake Engineering
[2] Assistant Researcher, National Center for Research on Earthquake Engineering
[3] Research Fellow and Deputy Director General, National Center for Research on Earthquake Engineering
[4] Associate Researcher, National Center for Research on Earthquake Engineering

actuators arranged by the Stewart platform-based layout (D. Stewart, 1965). Compared to the structural shaking table tests utilized in the Taipei and Tainan Laboratory, the Stewart platform-based layout adopts the smallest amount of 6 actuators to achieve 6-DOF table motion, thus, the space required for this system is reduced.

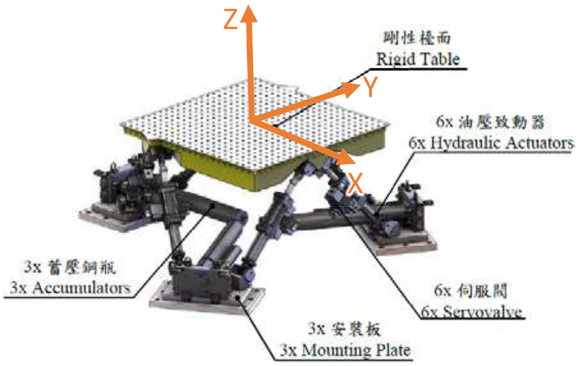

(a) Design scheme of the MAST system.

(b) Shaking table and HSM.

Fig. 1. Overview of the MAST system hardware.

The MTS model 244.20S actuator adopted in the MAST system is shown in Figure 2. It is a double-ended one-piece piston rod actuator with a rated force of 196 kN, and the stroke is plus and minus 158 mm. Due to the layout of the actuators, the peak strokes of the X, Y, and Z axes are plus and minus 240, 217, and 200 mm, respectively.

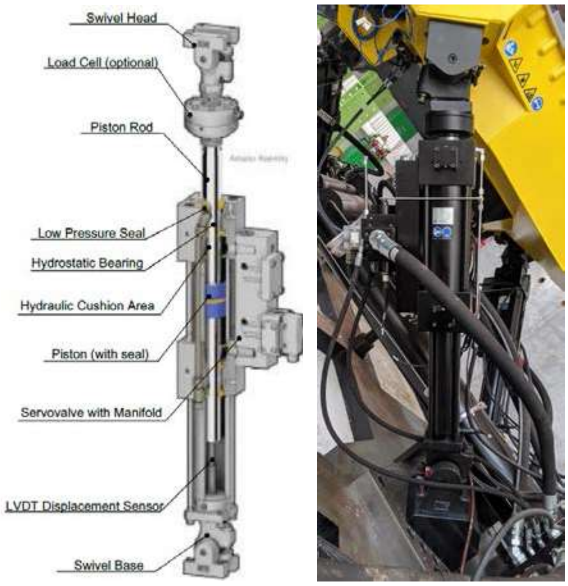

Fig. 2. Actuator and its profile.

Uniaxial Sinusoidal Motion Test

The uniaxial sinusoidal motion performance curve of the MAST system is shown in Figure 3. The curve can be separated into 3 stages: displacement-sensitive (low frequency), velocity-sensitive, and acceleration-sensitive (high frequency). The system performance is limited by the displacement in the low frequency range, and the real peak displacement of the horizontal axis mentioned before is above the performance curve. Conversely, the limitation and frequency range of the acceleration-sensitive stage varies with the payload.

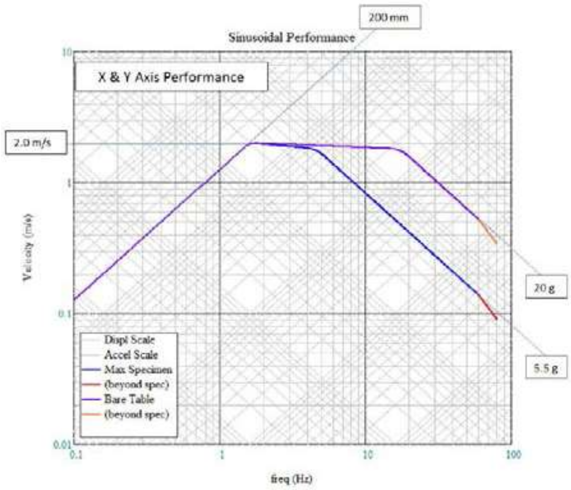

(a) Horizontal axis.

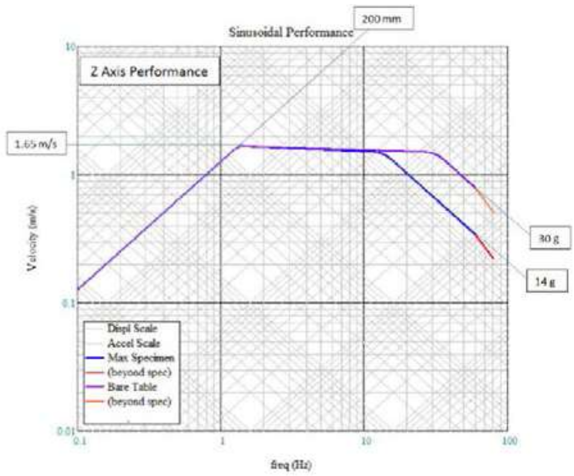

(b) Vertical axis.

Fig. 3. Performance curve of the MAST system.

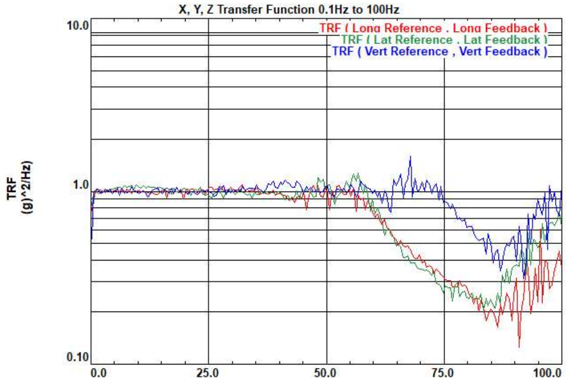

(a) Bare table.

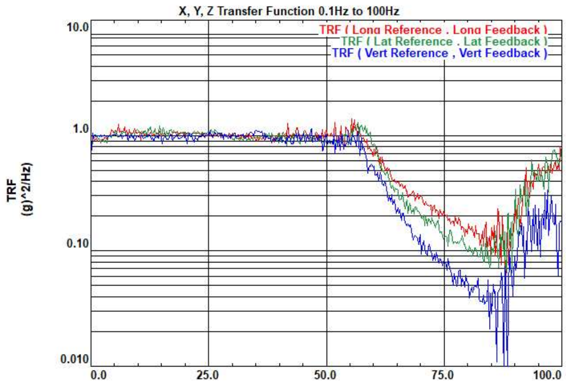

(b) Fully loaded.

Fig. 4. FRF of the MAST system.

Because of the Stewart platform-based layout, the peak velocity of the vertical axis is lower and the peak acceleration is much higher than that of the horizontal axis. The peak performance of the MAST system is shown in Table 1. Notice that each value in the table represents only the uniaxial sinusoidal motion performance of the MAST system, and the peak displacement, velocity, or acceleration values may not be achieved simultaneously.

Table 1. Peak performance of the MAST system.

Axis	Disp. ±mm	Vel. ±m/s	Accel. ± *g*'s	
			Bare table	Fully loaded
X	240	2.00	20	5.5
Y	217	2.00	20	5.5
Z	200	1.65	30	14

Frequency Response Function

The frequency response function (FRF) represents the relationship between the control command and system response. Tuning the FRF is a common way to improve the control of such a system. By adopting wide band white noise as an input signal, the FRF is shown in Figure 4, which is obtained by calculating the ratio of the Fourier amplitude between the system response over input signal. It should be noted that the FRF shown in Figure 4 is uncompensated, which indicates that the FRF can be optimized via compensation.

The amplitude of the FRF is approximately 1 through the optimum working frequency, and the error level is less than 2 dB. Beyond the working frequency, there is an anti-resonance frequency of 85 Hz. Therefore, the FRF has a local minimum around 85 Hz. This implies that the controlling performance of this system is poor and compensation is difficult around this frequency range.

Waveform Test

The GR-63-Core (Telcordia Technologies Inc., 2017) is a widely adopted testing regulation for network equipment-building systems (NEBSs). The criteria and test methods for earthquake environments are introduced in Sections 4.4.1 and 5.4.1. According to the seismic hazard zones in the US, the spectral floor accelerations of the required response spectra (RRS) are shown in Table 2.

Table 2. Spectral acceleration of RRS (g)

Freq. (Hz)	0.3	0.6	1	2	5	15	50
Zone 1 & 2	0.2	2.0	-	-	2.0	0.6	0.6
Zone 3	0.2	2.0	3.0	-	3.0	1.0	1.0
Zone 4	0.2	2.0	-	5.0	5.0	1.6	1.6

This project demonstrated the waveform performance of the MAST system by implementing the GR-63-Core zone 4 earthquake test. It is required that the test response spectrum (TRS) of the table motion captured by the accelerometer must meet or exceed the RRS in the range from 1.0 to 50 Hz and should not exceed the RRS by more than 30% in the frequency range of 1 to 7 Hz at specified frequencies. The TRS is derived by using an assumed damping level of 2%.

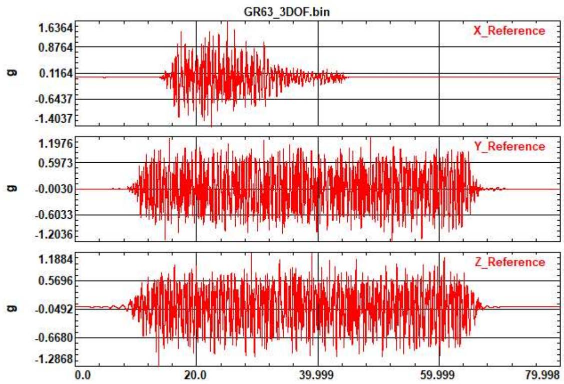

Fig. 5. Tri-axial waveform test results.

The test waveforms or control signals performed in this section are shown in Figure 5. The first waveform for the X axis is provided by Telcordia, and the remainder of the waveforms are synthesized by this project. The response spectra of the control signals are shown in Figure 6, and all of the spectra satisfied the requirements mentioned above.

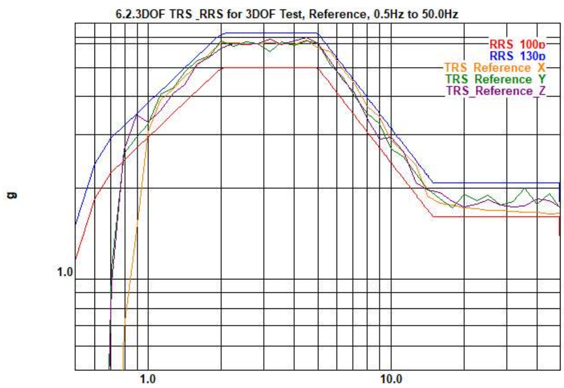

Fig. 6. Response spectra of the control signals.

According to the FRF, the MAST system is able to accurately reproduce the control signal as table motion within the optimum working frequency. The TRS of the table motion with a fully-loaded specimen are shown in Figure 7 and all of the requirements are satisfied. This implies that the MAST system is capable of conducting dynamic tests on non-structural components.

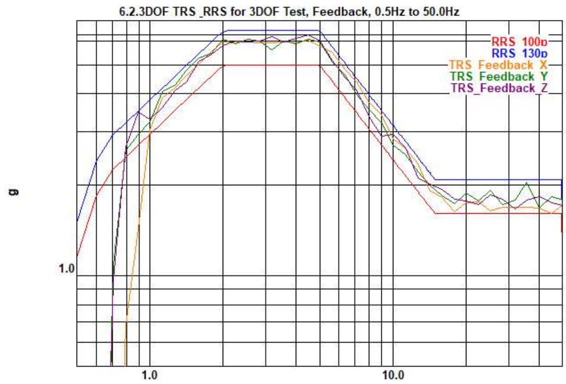

Fig. 7. TRS of the test waveforms.

Conclusions

To examine and verify the dynamic performance and seismic resistance of critical components of wind turbines or those of non-structural components, a multi-axial seismic test system was established in the NCREE Tainan Laboratory. The performance of the MAST system was also validated to be able to conduct the GR-63-Core zone 4 waveform test.

With the MAST system, the Tainan Laboratory will collaborate with various industries, research facilities and Smart Green Energy Science City to establish a research and design hub for the improvement of the seismic resistance of the supporting structures and critical components of wind turbines.

References

Stewart, D. (1965). “A Platform with Six Degrees of Freedom”. Proceedings of the Institution of Mechanical Engineers, 180(1), pp. 371–386.

Telcordia Technologies Inc., (2017). “NEBS™ Requirements: Physical Protection”, GR-63-CORE Issue 5.

Hybrid Earthquake Early Warning Services

Meng-Huang Gu[1] and Pei-Yang Lin[2]

古孟晃[1]、林沛暘[2]

Abstract

The objective of this project is to develop the relevant marketing of an earthquake early warning services (EEWS). The implementation is based on the hybrid earthquake early warning systems of schools, to reinforce fundamental infrastructure, to construct multiple communication channels of the service, to cooperate with domestic industries for the development of applications, to build a demonstration case for educational marketing, to integrate upstream, midstream, and downstream technologies, and to assist the industry in the integration and export to overseas markets. Currently, the project is focused on exploiting the applications of hybrid earthquake early warning services and promoting its use in disaster prevention in relevant industries. Depending on multiple applications of the example earthquake early warning system and demonstration cases, domestic manufacturers may cooperate for the development of disaster prevention industries. By cooperating with the industry and based on multiple applications of the example earthquake early warning service, the maintenance roots and commercial model of the EEWS is established. With this plan, we will attract domestic manufacturers to join the development works for related disaster prevention industry applications, subsequently creating the new domestic disaster prevention industry market and finally exporting EEWS to overseas markets.

Keywords: earthquake early warning, monitoring, disaster prevention

Introduction

The goal of this project is to solve problems in the development of the earthquake early warning services (EEWS) for industry, such as insufficient warning time, high costs, excessive construction costs, less application of EEWS, a lack of connection to industry. The NCREE has established a complete application case of hybrid EEWS. Therefore, the project based on the hybrid EEWS is focused on several key items: to strengthen fundamental infrastructure, to establish multiple alarm channels, to cooperate with domestic industries for the developments of related applications, to construct the related example systems, to integrate technologies, and to help industries export the EEWS for overseas markets. In this project, the expected results are as follows:

(1) Providing an EEWS integrated from the regional type and on-site type EEWS, which can reduce blind spots and help users in obtaining a faster and more accurate EEWS

(2) Demonstration of the example EEWS, which can provide a variety of earthquake disaster prevention application services (devices, systems, services)

(3) To reduce the cost threshold for constructing the EEWS

(4) Increasing the number end users of the EEWS

(5) Assisting in the rapid development of the earthquake disaster prevention industry.

In addition, for assisting in the development of the industry, this project designed the EEWS platform to develop cloud services and related application demonstrations with those who desire to join the disaster prevention industry for EEWS applications. Finally, this project will also integrate the upstream, middle stream, and downstream technologies of the EEWS with the domestic industry, and exports to overseas to increase the industrial development value.

[1] Associate Research Fellow, National Center for Research on Earthquake Engineering
[2] Research Fellow, National Center for Research on Earthquake Engineering

Development of Applications for a Hybrid EEWS

The hybrid EEWS applications were focused on cooperation with industry manufacturers to provide a home experience program based on the hybrid EEWS, which included the smart home devices that can receive EEWS info, provide sounds and lighting warnings, and can shut down gas valves automatically before the earthquake hits. Furthermore, the project cooperated with equipment vendors to provide the relevant services for use by emergency responders.

Application of the Hybrid EEWS

After the construction of the on-site EEWS station, this project hopes to popularize the related services. In 2019, the project was performed in cooperation with government units to apply the EEWS in different fields and applications, according to different requirements. The relevant applications are listed as follows.

(1) Example of hybrid EEWS for social housing: NARL cooperated with the Office of Housing Development of the Taoyaun City Government to incorporate the complete EEWS solution for their social housing. There were several independent lighting and sound warning devices installed inside of 222 houses and 10 offices. In addition, earthquake-resistant table were also provided in houses with two or three bedrooms for user refuge after the EEWS warning. Furthermore, explanations of use were also provided for users after installation of the EEWS devices.

(2) Example of hybrid EEWS for large exhibition space: In this example, the NARL cooperated with the National Taiwan Sport University to demo the example EEWS in their stadium. Prior to implementation, the emergency response and related devices were focused on fire disasters. In this application, considering that the stadium is typically used for large events, the EEWS lighting and sound warning systems were combined with an automatic evacuation guidance service for strong earthquakes.

(3) Example of hybrid EEWS for an office: In this example, the NARL cooperated with the secretariat of the Tainan City Government and the Lingya District Office of Kaohsiung City to provide the EEWS applications. In the office of the secretariat of the Tainan City Government, the lighting and sound warning were combined with earthquake-resistant OA office furniture. In the Lingya District Office of Kaohsiung City, not only were the warning devices used for users, they were also linked with digital signage to help propagate the EEWS warning info. The system could also be linked with the visible system to help the administrator to directly understand the situation.

(4) Example of hybrid EEWS for hospital: The NARL cooperated with the Yunlin branch of the National Taiwan University hospital campuses in Douliou and Huwei to install the on-site EEWS station and to provide special EEWS info and the EEWS warning for operating rooms and emergency rooms by special lighting and sounds.

(5) Advanced example of hybrid EEWS for a science park: In this example, the NARL cooperated with the National Chiao Tung University to install a structural health monitoring system in their six buildings. In addition, multiple linked on-site EEWS stations were also installed to test the performance with the hope that the relevant EEWS info can provide use for the advanced users in science parks.

(6) Example of hybrid EEWS for kindergarten: In this example, the NARL cooperated with the Kaohsiung municipal Cianjin Kindergarten to combine the EEWS info with digital multimedia signage for warning the educators and students.

(7) Home Experience Program: The NARL linked the EEWS info directly with the home devices. The participating volunteers can obtain the EEWS info from multiple devices such as lighting, sounds, and gas interruption services. This program not only allows people to use the system directly at home but can also be used to obtain relevant suggestions after program completion for fixing the unexpected bugs.

Fig. 1. Devices for social housing and an earthquake-resistant table.

Fig. 2. Warning and evacuation guidance device of the stadium.

Fig. 4. Application of the EEWS for an office.

Fig. 5. Example of digital signage and linking with the hybrid EEWS.

Fig. 6. Example EEWS for a hospital.

Operation of the Hybrid EEWS Platform

According to the industry requirements, this project planned and implemented multiple user applications. Based on these and past experiences, relevant examples, and recommendations over the past few years to defend the service providers. In this project, the communication protocols were designed by using the published transportation interfaces and related protocols. Then, the protocols were published for service providers in Taiwan to develop the related receiving module. This is based on the architecture of the IoT for connecting with the logistics, high-tech factories, police services, hospitals, etc. to implement the real-time linking and controls automatically depending on the peak ground acceleration (PGA). Furthermore, the protocols also help the service providers to connect to the users directly for reducing the load on the platform to increase efficiency.

Popularization for the Earthquake Disaster Prevention Industry

(1) Exhibitions: There were six exhibitions proposed in this year, such as at the Central Weather Bureau, Lanyang Museum, IDEER 2019, National Science and Technology Museum, Future tech and Information Technology Month, etc. Through the above exhibitions covering different topics, the hybrid EEWS was proposed for the disaster prevention industry and more than 30000 participants joined in the related promotion.

(2) Hybrid EEWS Industry briefing: there were two industry briefing held in March and December 2019. Many service providers joined the discussion.

(3) Earthquake scenario experience car: There are six-axis earthquake simulator installed inside this car, combined with a video link and related smart home devices to provide different earthquake scenarios for users. Users not only can obtain the essential information on an earthquake but also can understand the related application from smart home devices.

Fig. 8. Promotion at the Central Weather Bureau.

Fig. 9. Promotion at the Lanyang Museum.

Fig. 10. Promotion at the National Science and Technology Museum.

Fig. 11. Promotion at Future tech.

Fig. 12. Promotion at Information Technology Month.

Capacity-Based Inelastic Displacement Spectra for Reinforced Concrete Bridge Columns

Ping-Hsiung Wang[1], Kuo-Chun Chang[2], and Yu-Chen Ou[2]

王柄雄 [1]、張國鎮 [2]、歐昱辰 [2]

Abstract

Capacity-based inelastic displacement spectra that comprise an inelastic displacement ratio (C_R) spectrum and the corresponding damage index (DI) spectrum are proposed in this study to aid seismic design and evaluation of reinforced concrete (RC) bridges. Nonlinear time history analyses of SDOF systems are conducted using a versatile smooth hysteretic model when subjected to far-field and near-fault ground motions. It is demonstrated that the Park and Ang's damage index can be a good indicator for assessing the actual visible damage condition of column regardless of its loading history, providing a better insight into the seismic performance of bridges. The computed spectra for near-fault ground motions show that as the magnitude of pulse period ranges increases from NF1 (0.5 - 2.5 s) to NF2 (2.5 - 5.5 s), the spectral ordinates of the C_R and DI spectra increase moderately. In contrast, the computed spectra do not show much difference between NF2 and NF3 (5.5 - 10.5 s) when the period of vibration $T_n \leq 1.5$ s, after which the spectral ordinates of NF3 tend to increase obviously whereas those of NF2 decrease with increasing T_n. Moreover, when relative strength ratio R = 5.0, nearly all of the practical design scenarios could not survive NF3.

Keywords: Reinforced concrete, bridge column, inelastic displacement, damage index, far-field, near-fault

Introduction

To aid seismic evaluation of new designed or existing bridges, various analysis methods are available according to the seismicity, regularity, complexity, and importance of bridges. The seismic retrofitting manual for highway structures (part 1-bridges) published by Federal Highway Administration (FHWA 2006) provided three major evaluation methods for the upper level earthquake (return period of around 1000 years). The AASHTO (American Association of State Highway and Transportation Officials) guide specification for seismic bridge design (2011) suggested similar analysis methods to those of FHWA (2006) except for its D1 method. In addition, the R_d factor in the D1 method was modified as a function of displacement ductility demand instead of relative strength ratio (or strength reduction factor) and then used to magnify the elastically analyzed displacement demand in the D2 method. The Caltrans Seismic Design Criteria (SDC 2013) adopted a similar method to the AASHTO's method (2011), but it did not use the R_d factor to estimate the seismic demand. Later on, the Caltrans seismic design specifications for steel bridges (2016) retrieved the use of the same R_d factor as AASHTO (2011). On the other hand, the Eurocode 8 (2005) on design of structures for earthquake resistance (part 2: bridges) used the same R_d factor as the D1 method of FHWA (2006) to compute the design seismic displacement of bridges. Accordingly, it can be found that current seismic design and evaluation of bridges tends towards the well-known displacement coefficient method (FEMA 273, 1997).

The key element of the displacement coefficient method is the displacement coefficient (namely the R_d factor or referred to as inelastic displacement ratio, hereafter) that allows maximum inelastic displacement of a system to be estimated from its maximum elastic displacement. Many researchers have focused on this area based on statistical study on nonlinear time history analyses of SDOF systems subjected to a suite of earthquake ground motions. The authors recently

[1] Assistant Technologist, National Center for Research on Earthquake Engineering
[2] Professor, Department of Civil Engineering, National Taiwan University

proposed a versatile smooth hysteretic model (SHM; Wang et al. 2017) that can realistically simulate the seismic behaviors of reinforced concrete bridge columns with the effects of various design parameters. Most importantly, it was demonstrated that the damage index proposed by Park and Ang (1985) can be used to accurately predict the onset of strength deterioration. Furthermore, it was found in this research that the damage index can be a good indicator for assessing the actual visible damage conditions of column regardless of its loading history. Therefore, seismic analysis via this model can obtain not only the maximum responses of a column but also its damage condition under a given ground motion, providing a better insight into its seismic performance.

The objective of this paper is to statistically compute the inelastic displacement ratio and the corresponding damage index (i.e., the so-called capacity-based inelastic displacement spectra) of a SDOF system using the proposed smooth hysteretic model with the effects of various design parameters of RC bridge columns when subjected to both far-field and near-fault ground motions. The computed spectra are then used to evaluate the well-known formulae for inelastic displacement ratio, and new formulae for the capacity-based spectra as a function of period of vibration, relative strength ratio, and various design parameters of columns are presented for far-field and near-fault ground motions.

Smooth Hysteresis Model

The smooth hysteretic model (SHM) used to perform the nonlinear time history analysis of SDOF system is proposed by Wang et al. (2017). The model is based on the Bouc-Wen model (1976) with significant modification to consider hysteretic rules for damage accumulation and path dependence of RC bridge columns. To consider strength deterioration, the model utilizes the damage index (DI as defined in Eq. 1) proposed by Park and Ang (1985) to initiate strength deterioration until DI is accumulated to a threshold value DI_o.

$$DI = \frac{\delta_m}{\delta_u} + \lambda \frac{\int dE}{F_y \delta_u} \tag{1}$$

where δ_m is the maximum displacement of column; δ_u is the ultimate displacement capacity of column under monotonic loading; $\int dE$ is the accumulated hysteretic energy dissipation; F_y is the yield force; and λ is a parameter to correlate hysteretic energy dissipation to damage, which can be calculated by setting DI equal to one at the ultimate state of column when the strength of column drops to 80% of its peak value.

It was proved in Wang et al. (2017) that the damage index can accurately predict the onset of strength deterioration regardless of the loading history a column was subject to. Furthermore, it was found in this research (Figure 1) that the damage index can also be correlated well with the actual damage conditions of column. In the figure, four column specimens having identical design parameters were subjected to very different loading histories. Specimens COC and CLC underwent monotonically increasing cyclic loadings with one cycle and many cycles at each drift level, respectively, while Specimen CMC suffered monotonically increasing cyclic loading which was accompanied with monotonically decreasing as well as irregular cyclic loadings. In Specimen CPC, pseudo-dynamic loading test was conducted using three consecutive ground motion records with long duration characteristics, which was followed by extra cyclic loading test using two cycles of 6% drift ratio to exhaust the column. Figures 1(b1) to 1(b4) show the damage conditions of the four columns when their damage indices were accumulated to around 0.69 (DI_o) corresponding to the onset of strength deterioration. The four columns show similar damage states with spalling of cover concrete and slight buckling of longitudinal reinforcements. Figures 1(c1) to 1(c4) further show the damage conditions of the four columns at DI close to 1.0 that corresponds to 20% strength loss. Again, similar damage conditions can be seen in the four columns with significant crushing of confined concrete, severe buckling of longitudinal reinforcements, and severe loosening of transverse reinforcements at 135- and 90-degree hooks. Therefore, the DI can be a good indicator for assessing the actual damage conditions of column regardless of its loading history, which provides a bridge between analytical result and actual visible damage.

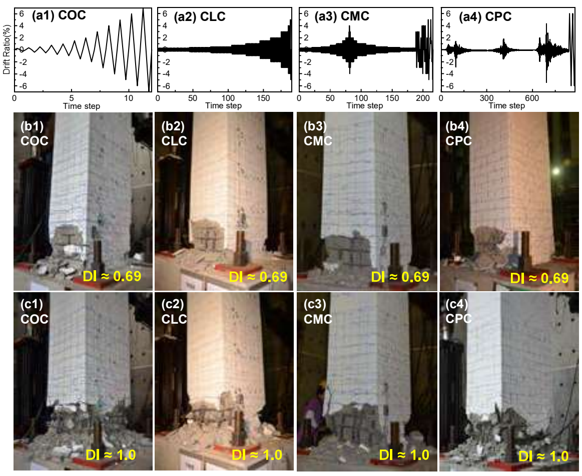

Fig. 1. correlation between damage index and actual damage condition: (a) various loading histories; (b) visual damage condition at DI≈ 0.69; (c) visual damage condition at DI≈ 1.0

Model Identification for RC Bridge Columns with Various Design Parameters

In order to consider the effects of design parameters of RC bridge columns on deteriorated hysteresis behaviors and thus on the computed capacity-based inelastic displacement spectra, model identifications from relevant experimental data are presented first in this section. The design parameters of RC bridge columns considered include the longitudinal and transverse reinforcement ratios, the aspect ratio, and the axial load ratio. Experimental data focusing on these effects are mainly obtained from the structural performance database of Pacific Earthquake Engineering Research Center (PEER 2003). For each of the column specimens, the model parameters capable of representing specific degradation characteristic were identified using the methodology proposed by Wang et al. (2017), allowing the effects of certain design parameter to be quantitatively evaluated.

Capacity-Based Inelastic Displacement Spectra

The proposed capacity-based inelastic displacement spectra are comprised of an inelastic displacement ratio spectrum and the corresponding damage index spectrum, forming a Dual spectrum to provide estimates not only for the displacement demand but also for the damage state of a system under earthquakes. This study focuses on the constant strength inelastic displacement ratio which is defined as

$$C_R = \frac{\Delta_{inelastic}}{\Delta_{elastic}} \tag{2}$$

where $\Delta_{inelastic}$ is the maximum inelastic displacement of a SDOF system with a 5% viscous damping ratio and a lateral yield strength F_y while $\Delta_{elastic}$ is the maximum elastic displacement of the corresponding elastic system having the same T_n and subjected to the same earthquake ground motion.

It should be mentioned that the subscript of C_R is intended to represent that the ratio is based on systems with a constant lateral strength. The lateral strength of the system is described by a relative strength ratio R (or strength reduction factor), which is defined as

$$R = \frac{mS_a}{F_y} \tag{3}$$

where m is the mass of the system, and S_a is the elastic spectral acceleration.

A total of 75 ground motion records including 30 far-field and 45 near-fault ground motions were selected from the ground motion database of Pacific Earthquake Engineering Research Center (PEER, 2013). The far-field records were further classified based on the site class. Two site classes, namely site classes C (denoted as FFC) and D (denoted as FFD) in accordance with the NEHRP classification (2004), were studied in this research. On the other hand, the near-fault records with the pulse-like characteristics were classified into three T_p ranges based on the magnitude of T_p. The three T_p ranges, denoted as NF1, NF2, and NF3, have period ranges of 0.5 s - 2.5 s (i.e., including 0.5 s but excluding 2.5 s), 2.5 s - 5.5 s, and 5,5 s - 10.5 s, respectively. The pulse period T_p of each near-fault record was extracted by Baker (2007) using wavelet analysis.

Mean C_R and the corresponding DI spectra for 30 far-field and 45 near-fault ground motions were computed by using 9 different hysteretic models (including one EPP model and 8 SHMs) to investigate the effects of ground excitation, column design parameter, and model type on the spectral ordinates. Among the 8 SHMs for various design parameters of columns, the M6 model is considered representative of commonly used design scenario of bridges in practice and is used to demonstrate the analyzed results.

Figure 2 shows the mean C_R and corresponding DI spectra for M6 model when subjected to near-fault ground motions with three pulse period T_p ranges. It can be observed that as the magnitude of T_p ranges increases from NF1 (T_p = 0.5 - 2.5 s) to NF2 (T_p = 2.5 - 5.5 s), the spectral ordinates of the C_R and DI spectra increase moderately in the whole spectral region. In contrast, the C_R and DI spectra do not show much difference between NF2 and NF3 (T_p = 5.5 - 10.5 s) when around T_n< 1.5 s, after which the spectral ordinates of NF3 tend to increase obviously whereas those of NF2 decrease with increasing T_n This reveals that the near-fault ground motions with T_p = 5.5 - 10.5 s would lead to increased seismic responses and damages in long period region. Moreover, for R = 5.0, nearly all of the practical design scenarios considered in this research could not survive NF3, while some of them (such as the M5, M6, M8 and M9 models) could not even survive when R = 4.0.

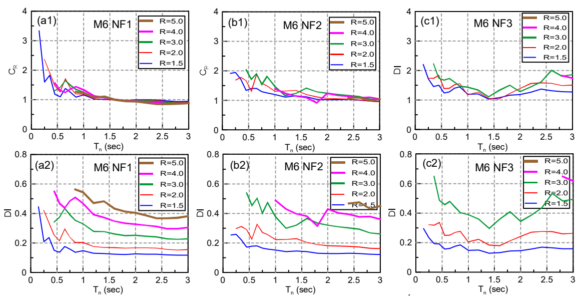

Fig. 2. Mean C_R and corresponding DI spectra for M6 (SHM) model under: (a) NF1; (b) NF2; (c) NF3

To demonstrate the near-fault effects, Figure 3 further compares C_R and DI differences between the far-field (FFC) and near-fault (NF3) ground motions for the M6 model. It can be evidently seen that the near-fault ground motions would give rise to significantly greater C_R and DI than far-field ground motions, and their differences increase with increasing R. As a result, more attention should be paid to designing and evaluating a bridge located near a causative fault (e.g., typically less than 20 km), even for long-period structures. Regarding the effects of column design parameters on the calculated C_R and DI spectra, it can be concluded that for far-field ground motions, C_R is approximately independent of column design parameters while DI correlates positively (i.e., DI increases with increasing amount of some design parameter) with longitudinal reinforcement and axial load ratios, but negatively (i.e., DI decreases with increasing amount of some design parameter) with transverse reinforcement and aspect ratios. For near-fault ground motions, C_R is approximately independent of column design parameters for NF1, while slightly affected by some of the column design parameters for NF2 and NF3. The C_R correlates positively with aspect ratios, positively with longitudinal reinforcement ratios when $R \leq 2.0$, and negatively with longitudinal reinforcement ratios when $R \geq 3.0$. On the other hand, the DI of near-fault ground motions with respect to the column design parameters follows similar trend to that of far-field ground motions.

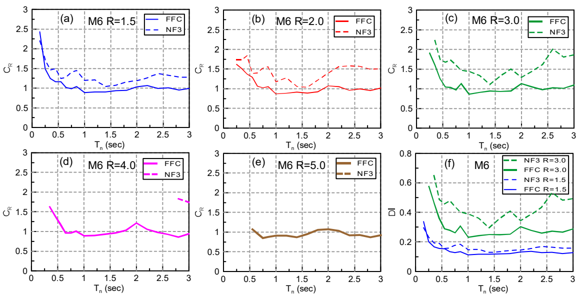

Fig. 3. Comparisons of C_R between far-field (FFC) and near-fault (NF3) ground motions for M6 model: (a) R=1.5; (b) R=2.0; (c) R=3.0; (d) R=4.0; (e) R=5.0; (f) comparison of DI

Proposed C_R and DI Formulae

Considering the C_R formula of FHWA (2006) can satisfactorily predict the calculated C_R spectrum for far-field ground motions recorded on site class C (FFC), the proposed C_R and DI formulae were constructed based on its functional form and were extended for the other cases. Figure 4 illustrates the proposed methodology used to determine the period limits in different design scenarios, where the period of vibrations corresponding to DI = 1.0 on the DI spectrum indicate the period limits that are applicable on the C_R spectrum. Also plotted in the figures are some of the calculated spectra for comparison. Notwithstanding this method would result in overestimation of DI in the vicinity of the period limit where there is only 20% probability of failure, it is thought to be expedient considering that approaching the period limit is normally prone to damage. By using nonlinear regression analysis of the calculated results, the proposed C_R and DI formulae for far-field and near-fault ground motions can be constructed. The detailed spectral formulae can be found in Wang et al. (2019).

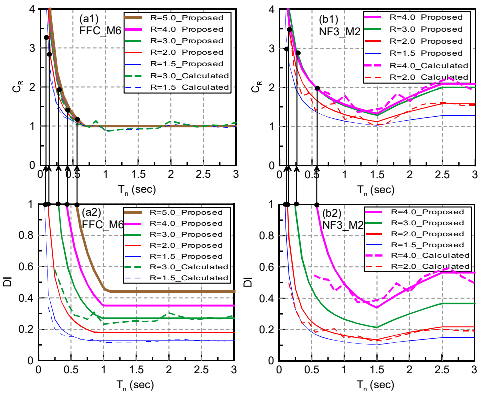

Fig. 4. Illustration of proposed C_R and DI spectra for: (a) far-field (FFC); (b) near-fault (NF3) ground motions

Conclusions

Capacity-based inelastic displacement spectra that comprise an inelastic displacement ratio (C_R) spectrum and the corresponding damage index (DI) spectrum are proposed in this study to aid seismic design and evaluation of reinforced concrete bridges. Comparisons of the C_R and DI spectra between FFC and NF3 show that the near-fault ground motions would give rise to significantly greater spectral ordinates than far-field ground motions, and their differences increase with increasing R. Therefore, more attention should be paid to designing and evaluating a bridge located near a causative fault, even for long-period structures.

References

Park YJ, Ang AHS. Mechanistic seismic damage model for reinforced concrete. Journal of Structural Engineering (ASCE) 1985; 111(4):722–739.

Ping-Hsiung Wang, Yu-Chen Ou, Kuo-Chun Chang (2017). A New Smooth Hysteretic Model for Ductile Flexural-dominated Reinforced Concrete Bridge Columns. Earthquake Engineering and Structural Dynamics, 46: 2237-2259.

Ping-Hsiung Wang, Kuo-Chun Chang, Yu-Chen Ou (2019). Capacity-Based Inelastic Displacement Spectra for Reinforced Concrete Bridge Columns. Earthquake Engineering and Structural Dynamics, 48(14): 1536-1555.

Piezoelectric Tuned Mass Damper Designed for Footbridges

Lap-Loi Chung[1] , Yan-Fu Teng[2], Yong-An Lai[3] , Wei-Ling Zhou[2]

鍾立來 [1]、鄧彥甫 [2]、賴勇安 [3]、周維苓 [2]

Abstract

Aesthetic appearance and a design that blends well with the environment are some important considerations when designing footbridges. Nowadays, footbridges are often designed to be lightweight long-span structures that lead to low vibrational frequency and low damping behavior. Pedestrian load is the main factor that causes footbridges to vibrate. The resonant phenomenon appears when the frequency of the structure falls in the region of the frequencies of the pedestrian load. Adding a tuned mass damper (TMD) on the structure is a common and effective way to reduce the vibration while maintaining the aesthetic appearance of the footbridge. Although a conventional TMD can effectively reduce the vibration, the vibrational energy is dissipated. With the aim to utilize the vibrational energy, we propose a new type of TMD, the piezoelectric tuned mass damper (Piezo-TMD), which converts the structural vibrational energy to electricity. In this article, we take as an example the Da-Yuan Bridge at Dharma Drum Institute of Liberal Arts located in New Taipei City and discuss the working of the Piezo-TMD.

Keywords: Footbridges; Piezoelectric tuned mass damper; Energy harvesting.

Human Walking Force and Comfort Classes

Human-induced vibration frequencies during a normal walk on a horizontal surface range between 1.6–2.4 Hz, as reported by Bachmann and Ammann (1987). Unfortunately, the vibration frequencies of footbridges often fall in this region, and the matching of the two frequencies causes resonance, which affects the serviceability of the footbridges. According to the comfort level (Fig. 1) that Service d'étude des transports, des routes et de leurs aménagement (Sétra)/ French Association Française de Génie Civil (AFGC) proposed, a vertical vibration acceleration larger than 2.5 m/s^2 is not acceptable.

To ensure user comfort and safety, applying a tuned mass damper (TMD) or stiffening the footbridges are two common methods to reduce the vibration acceleration. In this article, based on the comparison of the two methods, we consider the TMD, as it is more likely to maintain the footbridge's aesthetic design. A TMD consists of a mass, a spring, and a damping device. The mass and spring are specified such that the damper system frequency is tuned to the natural frequency of the structure. Therefore, the vibration of the structure will cause the TMD to vibrate. As the vibration energy is transformed to the TMD, the damping device dissipates the energy created by the motion of the mass, and the system can effectively reduce the vibration of the structure.

Defined comfort classes with limit acceleration ranges				
	Acceleration ranges (m/s^2)			
	0	0.5	1.0	2.5 (m/s^2)
Class 1	Max			
Class 2		Mean		
Class 3			Min	
Class 4				Unacceptable

Fig. 1. Comfort level of the footbridges (Sétra/AFGC).

Design of the Piezoelectric Tuned Mass Damper

In addition to effectively reducing the vibration of the footbridge, the energy harvesting will be discussed further. Instead of letting the vibration

[1] Professor, Department of Civil Engineering, NTU, Taipei, Taiwan
[2] Graduate student, Department of Civil Engineering, NTU, Taipei, Taiwan
[3] Professor, Department of Civil Engineering, NCU, Taoyuan, Taiwan

energy be dissipated directly by the damper, a new type of TMD, called the piezoelectric tuned mass damper (Piezo-TMD), which can convert part of the vibration energy to electricity, is proposed. The Piezo-TMD uses a piezoelectric material device in place of the damper in the conventional TMD (Fig. 2). The additional spring is equipped such that the mechanical frequencies of the Piezo-TMD can be tuned to the structure's natural frequency.

The design procedure for the Piezo-TMD is proposed, using some regression formula, as given below.

(1) Determine the parameters of the structure, including mass m_s, frequency ω_s, and damping ratio ζ_s.

(2) Decide the initial value of the parameters of the Piezo-TMD, including mass m_d, mass ratio R_m, stiffness of the single piezoelectric material k, parasitic capacitance C, and the piezoelectric coefficient Θ.

(3) Calculate the four non-dimensional parameters α, α_p, α_L, and α_R using the mass ratio R_m and the damping ratio ζ_s.

(4) Calculate the effective stiffness of the Piezo-TMD from the stiffness of the conventional TMD by Eq. (1).

$$\bar{k}_p = \alpha_p k_{d,conv} \tag{1}$$

(5) Initially assume the amount of piezoelectric material of a single layer, o =1, and calculate the number of layers n by Eq. (2). Verify the strain limitation after the time history analysis, and adjust o if needed.

$$n = \frac{oCk^2 + \Theta^2 ok}{\Theta^2 \bar{k}_p(\alpha+1)} \tag{2}$$

(6) Calculate the stiffness of the spring of the Piezo-TMD by Eq. (3).

$$k_d = \frac{o\bar{k}_p k}{ok - n\bar{k}_p} \tag{3}$$

(7) Calculate the remaining effective parameters of the Piezo-TMD by Eq. (4) and (5).

$$\bar{\Theta}_p = \sqrt{\bar{C}_p \bar{k}_p / \alpha} \tag{4}$$

$$\bar{C}_p = onC + \frac{n\Theta^2(ok - n\bar{k}_p)}{k^2} \tag{5}$$

(8) Calculate the inductance L and resistance R by t Eq. (6) and (7).

$$L = \alpha_L / \left(\bar{C}_p \omega_s^2\right) \tag{6}$$

$$R = \alpha_R / \left(\bar{C}_p \omega_s\right) \tag{7}$$

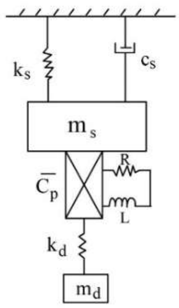

Fig. 2. The Piezo-TMD model.

Example Structure with the Piezo-TMD

As an example structure, we considered the Da-Yuan bridge at Dharma Drum Institute of Liberal Arts located in New Taipei City. Its total span is approximately 110.0 m and the width is 3.0 m. In the simulation, the Da-Yuan Bridge is simplified to be a single-degree-of-freedom (SDOF) structure. The first modal mass and frequency of the footbridge model are 21.35 ton and 2.32 Hz, respectively. The damping ratio is assumed to be 1.0% for small vibrations due to pedestrian loadings. The generated pedestrian loading is shown in Fig. 3. The pedestrian loading for the bridge is a periodic loading. According to many statistical data, the frequency of human walking could be defined as a Gaussian distribution with a mean value of 2.0 Hz and a standard deviation of 0.2 Hz. The phase lag between different passengers are assumed as a uniformly distributed random value between $-\pi$ and π. Considering the mode shape of the structure, the modal force for the SDOF simplified structure is generated.

The generated force is assigned to the SDOF simplified structure of the footbridge. Without control, the structure's maximum displacement and acceleration are 2.57 cm and 3.5747 m/s^2, respectively. The acceleration is not acceptable according to the comfort level presented in Fig. 1. The limit of acceleration is set to be the center value of the minimum comfort range, that is, 1.75 m/s^2, considering both safety and cost.

Following the aforementioned design procedure, the proof mass of the Piezo-TMD was selected as 266.875 kg, and the mass ratio is 0.0125. With the structure damping ratio and mass ratio, we can determine the four non-dimensional parameters by the design formula method. The amount of the layer of piezoelectric stacks selected (o = 1) is checked to verify the strain limitation after the time history analysis. The final number of layers selected is two. All the parameters are determined and listed in Table 1.

To evaluate the effectiveness of the Piezo-TMD, it is compared with the conventional optimal TMD. The time history of acceleration is shown in Fig. 4 and the frequency response of the structure acceleration is shown in Fig. 5. The conventional TMD and Piezo-TMD perform effectively and similarly at reducing the acceleration. In addition, the Piezo-TMD exhibits slightly better performance than the conventional optimal TMD in terms of the peak values of the frequency response. The time history analysis of the SDOF footbridge equipped with the Piezo-TMD shows that the structural displacement and acceleration are reduced to 1.69 cm and 1.57 m/s^2, respectively. An acceleration of 1.57 m/s^2 is less than the acceleration limit of 1.75 m/s^2.

The main difference of the performance between the conventional TMD and the Piezo-TMD is in the conversion of the vibration energy into electrical power. The input energy is calculated by integrating the product of force and structure with respect to time, while the energy harvested is calculated by integrating the product of the square of the electric current and the resistance with respect to time. The energy ratio of the Piezo-TMD, which is the harvested energy divided by the input energy, is 74.95% (Fig. 6). This high ratio shows that the Piezo-TMD converts the mechanical energy to electrical energy efficiently, while the structural damping dissipated 79.34% of the input energy.

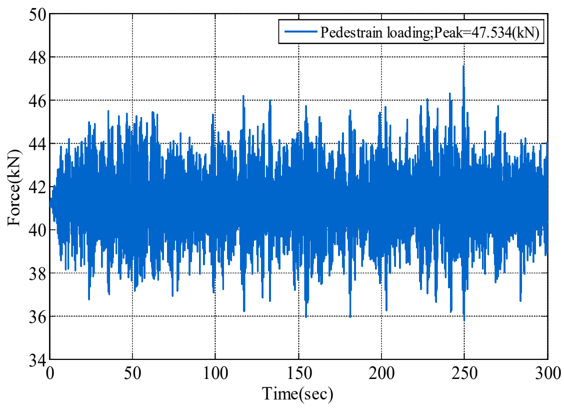

Fig. 3. Simulated pedestrian loading.

Table 1. Physical properties of the Piezo-TMD.

TMD, Structure Mass ratio R_m	0.0125
Mass of TMD m_d	0.0125
Number of stacks $o \times n$	2×127
Effective stiffness $\overline{k}_p$	5.5918×10^4 N/m
Parasitic capacitance $\overline{C}_p$	6.9718×10^{-4} F
Piezoelectric coefficient $\overline{\Theta}_p$	1.0290N/V
Spring stiffness k_d	5.9565×10^4 N/m
Resistance R	19.0473Ohm
Inductance L	6.4987H

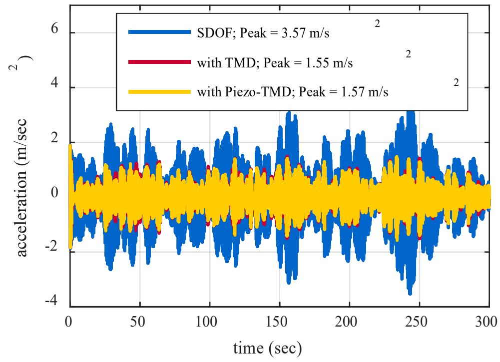

Fig. 4. Time history of the structure's acceleration.

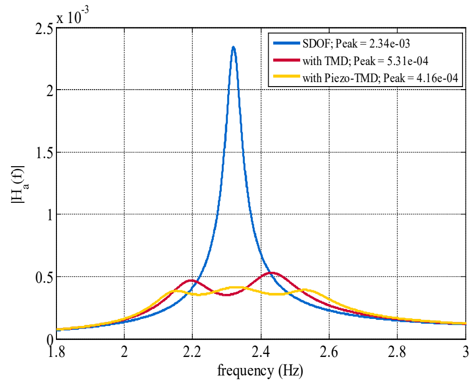

Fig. 5. Frequency response of the structure's acceleration.

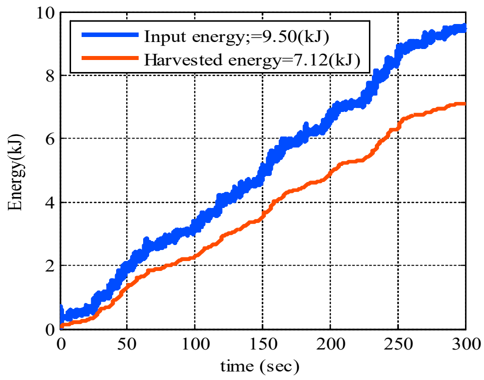

Fig. 6. Input and Harvested harvested energy of the Piezo-TMD.

Conclusions

This study introduced the common problem that the resonance of footbridges enlarges the vertical acceleration. Instead of utilizing the conventional TMD, a piezoelectric TMD (Piezo-TMD) was proposed for structural vibration reduction and energy harvesting. The design procedure offers engineers a more direct and simple method of construction and design of the Piezo-TMD. The performance of a footbridge equipped with the proposed Piezo-TMD subjected to a pedestrian loading was investigated. The results indicate that the Piezo-TMD performs similarly to the conventional TMD in reducing the structural vibration. In addition, the Piezo-TMD harvests the vibration energy with high efficiency, while a conventional TMD dissipates the energy. Proper utilization of the harvested energy is an interesting research topic as the issue of energy conservation is being gradually emphasized. We plan to test the theory by constructing a Piezo-TMD specimen and examining its application on more types of structures.

References

Bachmann H., Ammann W., “Vibrations in structures: induced by man and machines”, Structural Engineering Documents, Volume 3, International Association for Bridge and Structural Engineering, (1987).

Sétra/AFGC, “Footbridges – Assessment of vibrational behavior of footbridges under pedestrian loading”, Setra, (2006)

鍾立來、吳賴雲、賴勇安、連冠華、黃旭輝，「以結構位移均方最小化作調諧質塊阻尼器之最佳設計」，結構工程，第二十六卷，第四期，第 31-57 頁(2011)。

周維苓，「壓電調諧質量阻尼器之研究」，臺灣大學土木工程學系研究所學位論文(2018)

Shear Strength Tests on Slabs Applied to Seismic Retrofit of External RC Frames

Chun-Hung Chen[2], Xian-Feng Yeh[2], Tao Lai[2], Yu-Chih Lai[3], and Lap-Loi Chung[1]

陳俊鴻[2]、葉先峰[2]、賴濤[2]、賴昱志[3]、鍾立來[1]

Abstract

The retrofitting methods widely used in Taiwan are reinforced concrete (RC) jacketing, adding wing walls, and adding shear walls. However, if these retrofitting methods are applied to mid-to-high-rise buildings, this may cause opposition because the residents need to be resettled during the retrofitting process. Therefore, this research focuses on the application of external RC frames, a retrofitting method rarely used in Taiwan, in order to address the problems associated with conventional retrofitting methods.

In this method, the seismic force is transmitted through the slabs to the external RC frames. Therefore, the shear strength of the slabs is the key point of the research. According to shear strength tests conducted on slabs designed in this research, it is confirmed that, if the width-to-span ratio of the slabs is between 0.125 and 0.375, then the shear strength of the slabs is only related to the total span of the slabs and the failure mode is shear failure. Furthermore, it is confirmed that using the Concrete Structures Design Code (2017) of Taiwan for the design strength of slabs is conservative.

Keywords: mid-to-high-rise buildings; external reinforced-concrete frames; shear strength test of slabs.

Introduction

Taiwan is located at the junction of the Eurasian Plate and the Pacific Plate, so that earthquakes occur there frequently. There have been many devastating earthquakes there since records began, causing heavy losses of life and damage to property of residents. Reconstruction of half-collapsed and damaged, and suspected-to-be-damaged buildings after disasters, affects the normal function of the buildings, and the construction time and expenditure required may be difficult to estimate and afford. Therefore, old buildings with insufficient seismic resistance should be evaluated and retrofitted to improve their seismic performance without affecting their function.

This study focuses on a reinforcement method rarely used in Taiwan, that is, the addition of a reinforced concrete (RC) framework (Fig. 1). This method can mitigate the difficulties associated with common reinforcement methods such as RC jacketing and adding wing walls and shear walls. In order to improve the effectiveness of this reinforcement method, a shear wall is added to form an additional member of the RC frame, and the practical applications of the additional reinforcement motivated this research.

Lai (2016) presented a series of discussions on external RC frames and their application to public buildings. Lai designed a shear strength test to compare the relationship between the thickness and the shear strength of reinforcing specimen slabs. In addition, the research verified that using the Concrete Structures Design Code (2017) of Taiwan produces conservative designs for the strength of slabs. Several examples were used to confirm that reinforcement of the external RC frames can improve the seismic performance of the structures as well as their failure behavior.

However, in Lai's design, the experimental layout

[1] Professor, Department of Civil Engineering, NTU, Taipei, Taiwan
[2] Graduate student, Department of Civil Engineering, NTU, Taipei, Taiwan
[3] Researcher, National Center for Research on Earthquake Engineering

may require additional mounting for the specimens, and this may result in overestimates of the shear strength of specimens. There is some concern about the conclusion that using Lai's specification as the design strength for slabs is adequately conservative. Therefore, in this research, the experimental arrangement was improved in order to obtain results closer to the shear capacity of actual slabs. Tests were conducted to investigate whether the shear strength and failure condition of slabs with the same total span, but divided into one, two, and three segments, are similar. Finally, the results were compared with the design strength recommended by the Taiwanese design specifications.

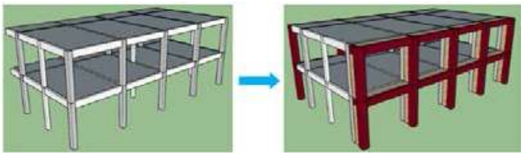

Fig. 1. The external RC frames.

Design of Specimens

This research aimed to investigate the behavior of slabs, which act as the coupling between the external RC frames and the existing structures. Thus, the result would depend on how well seismic forces can be transmitted from the existing structure to the external RC frames through the slabs. The added external RC frames may consist of multiple spans, resulting in the newly added slabs needing to be very long. This research therefore focused on the relationship between the length, the shear strength, and the failure conditions of the added slabs.

The bases of the specimens in this research were taken to represent the beams of the existing buildings. The dimensions of the bases were 800 cm long by 140 cm wide by 65 cm deep for each specimen, and the design compressive strength of concrete was 175 kgf/cm2. The main rebars were D25 steel bars, and the stirrups were D13 steel bars with a spacing of 20 cm; the design yield strength of the steel was 4200 kgf/cm2. In order to avoid sliding of the specimens during the reversing-side push tests, and the potential error and danger that might result, screws were applied to fasten the specimens.

The slabs of the specimens in this research were used to represent the force-transmitting members that connect the existing building and the reinforcing frame. All specimens had a width of 60 cm, thickness of 15 cm, and a total length (span) of 480 cm. The difference between the specimens was their length structure, as illustrated in Fig. 2. The first specimen (EFB-16) was a combination of three unit slabs each 160 cm long and separated by 1-cm-wide isolation gaps (filled with polystyrene foam). The second specimen (EFB-24) consisted of two unit slabs, each 240 cm long, with a 1-cm-wide isolation gap. The third specimen (EFB-48) was a single slab with a length of 480 cm. The main rebars were D10 steel bars and the stirrups were also D10 steel bars with a spacing of 20 cm.

The design compressive strength of the concrete constituting the slabs was 280 kgf/cm2, and the design yield strength of the steel was 2800 kgf/cm2. The main rebars of the slabs were connected to the bases as post-installed rebars. A D10 steel bar was used so that the design embedment depth of the post-installed rebars was 10 cm (in accordance with the convention in Taiwan, where embedment depth is 10 times the diameter of the steel bar). In addition, the concrete protective layers of the embedded parts of the post-installed rebars were removed in advance in order to ensure that the depth of the embedment was 10 cm from the core of the concrete.

The beams of the specimens in this research were considered to represent the beams of the external RC frames. The beams of the specimens were connected to the steel beams that applied force to the specimens-with screws, so that the lateral force applied by the actuator could be transmitted to the specimens through friction. The beams were each 50 cm wide by 50 cm deep by 570 cm long. Each specimen was constructed with sufficient flexural reinforcement (using D22 steel bar) and shear reinforcement (using D10 steel bar) to ensure that the beams would not be damaged during the reversing-side push test. Because the beams and slabs had to be cast at the same time, the design compressive strength of concrete for the beams was 280 kgf/cm2 and the design yield strength of the steel was 2800 kgf/cm2.

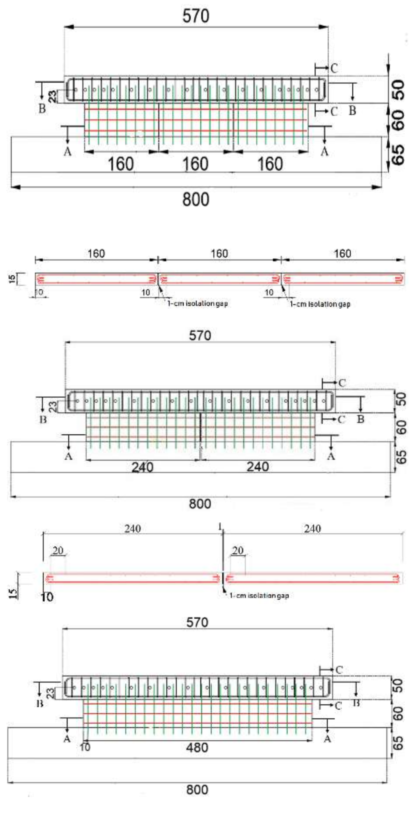

Fig. 2. The reinforcement of the specimens EFB-16 (top diagram), EFB-24 (middle), and EFB-48 (bottom).

Test Results and Discussion

The relationships between lateral force and corresponding displacement for specimens EFB-16, EFB-24, and EFB-48 are shown in Fig. 3. From the test results, the maximum lateral strength was 221.9 tf for specimen EFB-16, 222.2 tf for specimen EFB-24, and 236.3 tf for specimen EFB-48. The condition of the specimens after failure indicated that the initial crack development was a horizontal diaphragm failure mode. As the interlayer displacement angle gradually increased to approximately 1%, the failure condition changed to a shear friction failure mode. When the interlayer displacement angle increased to approximately 2%, the form of the crack in the slabs was completely controlled by the shear friction failure mode.

When cracks encountered the two isolation gaps in specimen EFB-16 and the isolation gap in specimen EFB-24, they stopped propagating, which indicated that the isolation gaps inhibit the development of cracks. However, due to a mistake during assembly, there were three initial horizontal cracks in specimen EFB-48 before the test (Fig. 4). The crack development in this specimen was initially in a horizontal diaphragm failure mode, but when the cracks encountered the initial horizontal cracks, they also stopped propagating.

Examination of specimens EFB-16 and EFB-24 at the end of the tests indicated that concrete peeling was concentrated on the left and middle sides of the slabs (Fig. 5). The reason for this was related to the direction in which the force was applied. When the specimens were first subjected to a positive force (directed to the right), the west sides of the slabs were in tension (see Fig. 5), which would cause a decrease of the equivalent area of the slabs and lead to the severe development of cracks. The situation was reversed later when they were subjected to a negative force (directed to the left), and this led to peeling off of the concrete in the left half of the specimens. The condition of specimen EFB-48 after the test (Fig. 5), showed that concrete spalling was concentrated around the initial horizontal cracks, indicating that the pre-existing cracks influenced crack development along the weak surfaces.

From the test results, it can be seen that, regardless of the presence of isolation gaps in the slabs, the shear strength and the failure conditions of slabs with the same total span are similar. From the fact that the test shear strengths of the three specimens were similar, despite having very different moments of inertia (*i.e.*, the spans of the component slabs were different) but the same shearing area (*i.e.*, the total span was the same), it could be inferred that the failure condition of the specimens was a shear friction failure mode.

According to Section 4.8.4 of the Concrete Structures Design Code (2017) in Taiwan, when the shear friction steel bars are perpendicular to the shear surface, the shear strength can be calculated from:

$$V_n = A_{vf} f_y \mu \leq \min(0.2 f_c' A_c, 56 A_c), \tag{1}$$

where A_{vf} (cm^2) is the cross-sectional area of the shear friction steel bar, f_y (kgf/cm^2) is the specified yielding strength of the steel, μ is the coefficient of friction, f_c' (kgf/cm^2) is the compressive strength of the concrete, and A_c (cm^2) is the area of the concrete section transmitting shear. An upper bound is placed on V_n to avoid overestimation of the shear strength using the shear friction method.

In addition, according to Section 15.9.7 of the design code an estimate for the shear strength of the horizontal diaphragm can be calculated from:

$$V_n = (0.53\sqrt{f_c'} + \rho_t f_y) A_{cv} \leq 2.12\sqrt{f_c'} A_{cv}, \tag{2}$$

where A_{cv} (cm^2) is the cross-sectional area of the horizontal diaphragm (which is the area of contact between the slab and the foundation), ρ_t is the horizontal reinforcement ratio (which is the ratio of the cross-sectional area of the reinforcement parallel to the force direction to that of the diaphragm perpendicular to the force direction). There is also an upper bound for V_n to avoid overestimation of the shear strength using the horizontal diaphragm method.

The design shear strengths of the three specimens, calculated using the above two methods, are compared with the experimental values in Table 1. The ratio of the test shear strength to the design strength calculated by Eq. (1) is 1.88–2.00. This formula underestimates the strength of the specimen, and it is too conservative. The ratio of the test shear strength to the design strength calculated by Eq. (2) is 1.15–1.20. The result is much closer to the measured strength of the specimens, although it is also conservative.

Table 1. Comparison of design shear strengths of the three specimens with experimental values.

Specimens	A (tf)	B (tf)	C (tf)	A/B	A/C
EFB-16	221.90	118.12	192.61	1.88	1.15
EFB-24	222.20	118.12	194.06	1.88	1.15
EFB-48	236.30	118.12	196.33	2.00	1.20

A: Maximum experimental shear strength
B: Shear strength calculated by shear friction design method (Eq. (1))
C: Shear strength calculated by horizontal diaphragm method (Eq. (2))

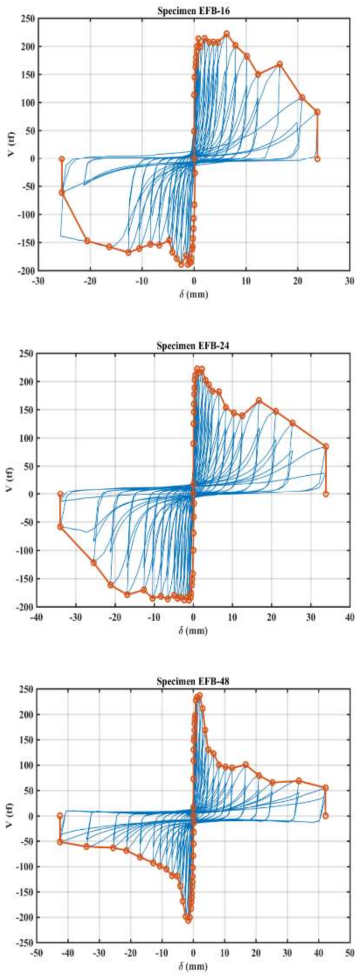

Fig. 3. The relationships between lateral force and corresponding displacement for specimens EFB-16, EFB-24, and EFB-48 (from top to bottom).

Fig. 4. Conditions of specimens EFB-16, EFB-24, and EFB-48 after the tests. (Left side is the west side.)

EFB-48

Conclusions

The three sets of experiments conducted in this research show that the ratio of the shear strength of specimen EFB-24 to that of specimen EFB-16 is 1.00, and that of specimen EFB-48 to specimen EFB-16 is 1.06. The test results show that the shear strength is similar when the width-to-span ratio of the slabs is between 0.125 and 0.375, and it is inferred that the failure condition of the slabs is controlled by the shear friction failure mode.

The test shear strength of the three specimens in this research is 1.88–2.00 times that calculated by the shear friction design method and 1.15-–1.20 times the shear strength calculated by the horizontal diaphragm method as recommended by the Concrete Structures Design Code (2017) of Taiwan. This means that both of the design shear strengths of the slabs calculated using the design code specifications are conservative. Therefore, engineers can safely use the smaller value obtained from the two methods as the design shear strength of the slabs for external RC frames.

References

Construction and Planning Agency, Ministry of the Interior, Taiwan, ROC (2017), “Concrete Structures Design Code”. Retrieved from https://goo.gl/iCbWCo

Lai, Y. C. (2016), “Experimental Study on Retrofit with External Reinforced Concrete Frames and Its Applications to Public Buildings”. Master’s thesis. Department of Civil Engineering, National Taiwan University, Taiwan, ROC.

Displacement Restraint Mechanism of Seismic Isolation Buildings

Yu-Jen Lai[1], Peng-Yu Lin[1], Cho-Yen Yang[2] and Lap-Loi Chung[3]

賴煜仁[1]、林芃妤[1]、楊卓諺[2]、鍾立來[3]

Abstract

In recent years, earthquakes have occurred more frequently around the world. On September 21, 1999, a 7.3 earthquake hit central Taiwan, which was called the Chi-Chi earthquake. Seismic codes were revised and became more restrictive in the aftermath of the disaster. However, many buildings in Taiwan that were built earlier are lacking seismic capacity and are not safe based on the revised Seismic Design Code. Therefore, building retrofits, such as seismic conventional retrofits and seismic isolation systems, are being implemented as measures to improve the safety of these old structures.

The effectiveness of the isolation system has been proven by many investigators; however, some other studies have also indicated that excessive displacement response due to near-fault ground motion may cause such a system with a long period to fail. Thus, a displacement restraint mechanism is suggested to be installed between the isolated structure and the retaining wall. It is clear from the simulation results that as the isolated structure strikes the displacement restraint system, the maximum absolute acceleration of the total system is increased due to the impact. Therefore, the displacement restraint system should be properly designed to maintain the design target. In addition, the corresponding displacement restraint system of different structures with different damping ratios and periods should be properly designed.

Keywords: building retrofit; seismic isolation system; displacement restraint mechanism

Introduction

For the displacement restraint system, k_1 is the stiffness and c_1 is the damping coefficient. D_m is the trigger distance, D_a is the allowable displacement, and D_u is the ultimate displacement, which cannot be surmounted by the structure's displacement response or the structure would collapse. m, k, and c are the linearized isolated structural mass, effective stiffness, and damping coefficient, respectively (Fig. 1). If the isolated structure's absolute value of the displacement response exceeds D_m, it will contact the displacement restraint system. The equation of motion is given by

$$m\ddot{x} + c\dot{x} + kx = f - m\ddot{x}_g \,, \tag{1}$$

where the control force f is defined as

$$f = \begin{cases} 0 & , |x| < D_m \\ -k_1 \left[x - D_m \operatorname{sgn}(x) \right] - c_1 \dot{x} & , |x| \geq D_m \end{cases} \,. \tag{2}$$

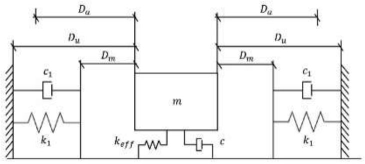

Fig. 1. Schematic diagram of the displacement restraint mechanism.

For the above equation of motion, the assumption is made that the displacement restraint mechanism would closely adjust to the structure as long as the structure's displacement exceeds D_m, which means that when the structure bounces back, the damping coefficient of the displacement restraint system is assumed not to slow down the system movement. The structure's responses including displacement, velocity, and acceleration are determined by dynamic analysis according to the equation of motion (Eq. 1).

[1] Master Student, National Taiwan University
[2] Research Fellow, National Center for Research on Earthquake Engineering
[3] Professor, National Taiwan University

Example Structure

The example structure is a two-story moment resisting frame (Fig. 2). It is 3 m in the *X*-direction (pushover direction), 5 m in the *Y*-direction, and the height of each story is 3.6 m. This example structure is situated in Ruisui Township, Hualien County, and thus the 5% design spectral acceleration parameter at short periods and a period of one second are $S_S^D = 0.8$ and $S_1^D = 0.45$ according to its Seismic Zone Category. The soil condition is classified as Type III (soft site) so that the short-period site coefficient is $F_a = 1.0$ and one-second site coefficient is $F_v = 1.5$. The distance from the site to the nearest fault is larger than 12 km so the near-fault adjustment factor for periods with constant acceleration N_A and the near-fault adjustment factor for periods with constant velocity N_V both equal one. Thus, the design spectral acceleration for the short-period structure S_{DS} is 0.8 (i.e., $S_{DS} = S_S^D \times N_A \times F_a$) and the spectral acceleration for the one-second-period structure S_{D1} is 0.675 (i.e., $S_{D1} = S_1^D \times N_V \times F_v$).

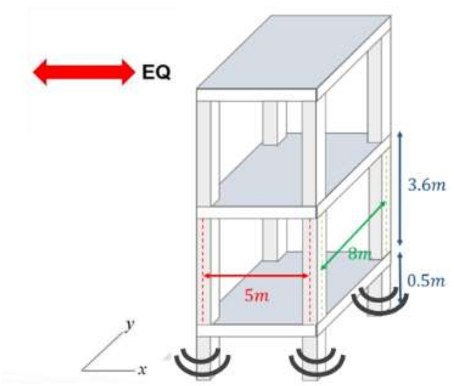

Fig. 2. Example structure with friction pendulum bearings (FPB).

The slab thickness of this structure is 15 cm, and the beam cross section is 24 cm × 60 cm in the width and depth, respectively. The column is 50 cm × 30 cm in the *X*- and *Y*-directions, respectively. From the size of the section, the total volume of the structure is obtained and its total weight W of 75.63 tf is also determined. The example structure is an emergency shelter, and thus the importance factor I is 1.5. The strength of the concrete f_c' is 190 kgf/cm^2 and the yielding strength of reinforcement f_y is 3200 kgf/cm^2. Based on the above information, the pushover analysis can be carried out.

Design of the Displacement Restraint Mechanism

The design procedure of the displacement restraint mechanism of a linear system is established and discussed in this section. Furthermore, an isolated structure with friction pendulum bearings (FPBs) (Fig. 2) is used as an example to demonstrate the design procedure.

Three important parameters of the displacement restraint system are the stiffness k_1, the damping coefficient c_1, and the trigger distance D_m (Fig. 1). The design goal is to appropriately design these values such that the displacement of an isolated structure can be reduced and the acceleration response will not exceed the structure's demand.

A displacement spectrum is established according to the time history of an earthquake. With the known value of the damping ratio and period of the isolated structure, the corresponding maximum displacement is obtained by the displacement spectrum. If the maximum displacement exceeds the ultimate displacement D_u, the displacement restraint system should be considered. The displacement and acceleration response of the structure should satisfy all design requirements after the displacement restraint system is installed.

The near-fault earthquake chosen for the design procedure is the Hualien Earthquake, which occurred on February 6, 2018. The time history of station HWA011 is chosen (Fig. 3), and its displacement and acceleration spectra are shown in Figs. 4 and 5, respectively. The design case is the example structure with FPBs, with a damping ratio and period of 18.67% and 3.373 s, respectively. Fig. 5 depicts the acceleration response of the structure compared with the design spectrum, and it is evident that the response considerably exceeds the demand. In addition, the maximum displacement response is 53.98 cm (Fig. 4). The maximum displacement (53.98 cm) exceeds the ultimate displacement (50 cm), so it is necessary to install the displacement restraint system, with the displacement expected to be reduced after installing the displacement restraint system. Nevertheless, the maximum acceleration response will increase due to the strike between the isolated structure and the restraint system. The acceleration cannot be too excessive or the striking force may exceed the structure's shear demand, causing the structure to fail. As a result, the parameters of the system have to be properly designed to reach the design target.

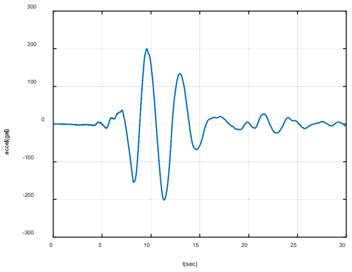

Fig. 3. HWA011 time history.

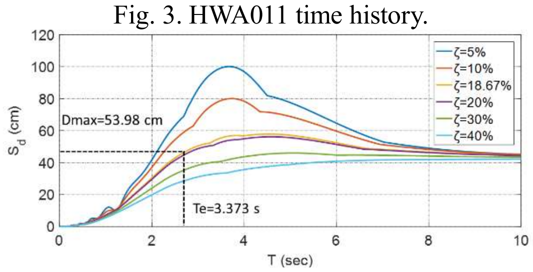

Fig. 4. Displacement spectrum of station HWA011 (NS) under the Hualien Earthquake.

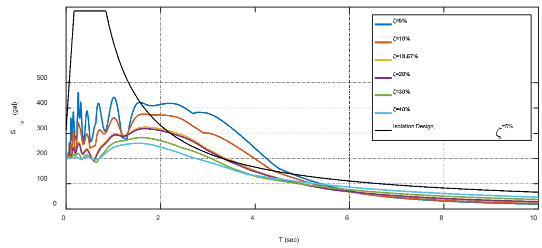

Fig. 5. Acceleration spectrum of station HWA011 (NS) under the Hualien Earthquake and the design spectrum.

For the example structure with FPBs, its maximum shear capacity V_{max} is 27.35 tf according to the seismic assessment. Therefore, the maximum acceleration should be less than the ultimate acceleration of 354.75 gal (i.e., V_{max}/W). Two design targets are determined by the above description. First, the displacement should be smaller than the ultimate displacement of 50 cm. Second, the acceleration should not exceed 350 gal (a more concise number than 354.75 gal). The design parameters are designed following these two design targets.

The first design parameter is α_1, which is k_1 divided by k. The second design parameter is α_2, which is c_1 divided by c. When the restraint system consists of a spring only, an α_1 of 3.3 is the best solution although it does not satisfy all design targets, and when α_1 is 10, the acceleration approaches 600 gal, which is three times the peak ground acceleration (200.1 gal) and is too large for the design. When the restraint system consists of a damper only, 0.95<α_2 <3.2, and when α_2 is 5, the acceleration approaches 450 gal, which is approximately 2.3 times the peak ground acceleration (200.1 gal), and is also too large for the design. Therefore, α_1 is chosen to be between 0 and 10, and α_2 is chosen to be between 0 and 5. The maximum displacement responses for different combinations of α_1 and α_2 in the above ranges are shown in Fig. 6, and the maximum acceleration response is plotted in Fig. 7. Next, these 3D figures are changed to 2D contour figures that contain *z* isolines, where *z* contains the height values on the *x*-*y* plane. The corresponding contour figure for Figs. 6 and 7 are depicted in Figs. 8 and 9. To present the available design range of α_1 and α_2, the maximum displacement response is divided by D_u, and the maximum acceleration response is divided by a_u. From this, the isolines of *z* equal to one can separate the contour figures into two ranges, with the colored range being the available design range. Fig. 10 shows the available range of displacement, and Fig. 11 shows the available range of acceleration. By overlaying Figs. 10 and 11, the intersection of the two figures is the final available range that satisfies the displacement and acceleration design targets. Consequently, the final result is shown in Fig. 12.

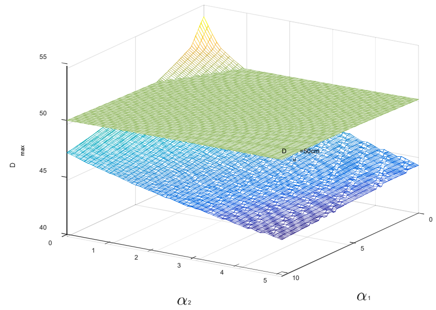

Fig. 6. Maximum displacement response of combined variance in α_1 and α_2.

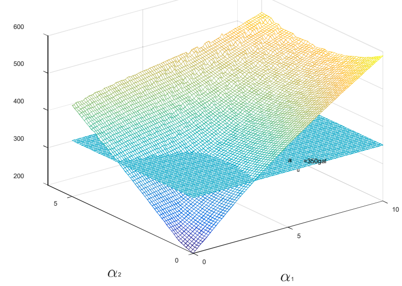

Fig. 7. Maximum acceleration response of combined α_1 and α_2 variance.

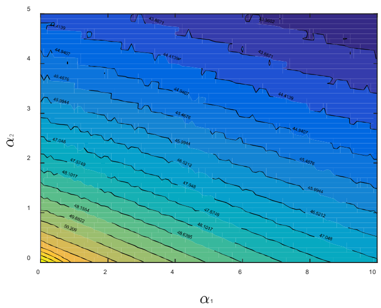

Fig. 8. Contour figure of the displacement response.

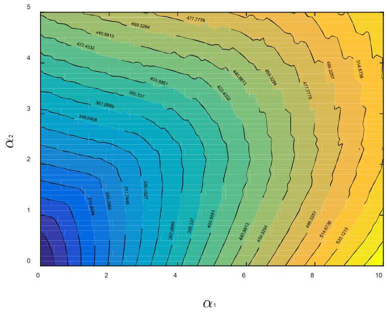

Fig. 9. Contour figure of the acceleration response.

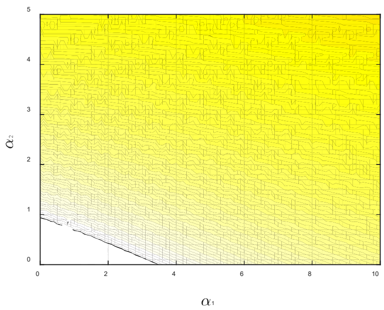

Fig. 10. Normalized contour of the displacement response.

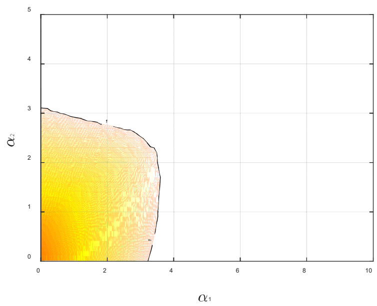

Fig. 11. Normalized contour of the acceleration response.

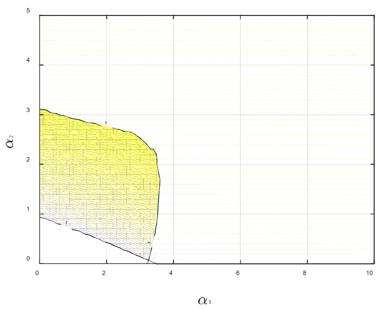

Fig. 12. Final design range of α_1 and α_2.

Conclusions

In the field of engineering, engineers can refer to the results of this study if an existing isolated structure needs to be made safer under unpredictable seismic loads. The simulation results show that the displacement restraint mechanism works well when its parameters are properly designed. In addition, casualties caused by near-fault earthquakes could be effectively averted through the displacement restraint mechanism. However, the displacement restraint mechanism is assumed to behave as a linear system. It will be more realistic and reasonable to design the displacement restraint mechanism as a nonlinear system, which could be further addressed in future research.

References

Hwang, J. S., Huang, Y. N., Hung, Y. H., and Huang, J.C.(2004), 'Applicability of Seismic Protective Systems to Structures with Vibration-Sensitive Equipment', *Journal of Structural Engineering*, **130**: 1676-1684

Chinese Institute of Civil and Hydraulic Engineering (2011), 'Application of concrete engineering design specifications (civil engineering 404-100) (Volume II)', *Taiwan, Technology book*.

Chung, L. L., Chen, C. H., Yang, Y. S. and Lai, Y. C. (2018), 'Structure Seismic Assessment: Real Earthquakes as Demand', *Engineers Times (submitting)*.

Ministry of Interior (2011), 'Seismic Design Code of Buildings', from https://goo.gl/h7dU6V.

Real-Time Hybrid Testing of Friction-Type Tuned Mass Damper System

S.Y. Chu[1]　C.J. Kang[2]　C.Y. Hsu[3]　S.W. Yeh[4]　L.Y. Lu[5]

朱世禹 1、康展榮 2、許敬昀 3、葉士瑋 4、盧煉元 5

Abstract

A friction-type tuned mass damper (FTMD) system is adopted in this study as the target for implementing the real-time hybrid testing technique. In the beginning, shaking table tests of the FTMD controlled by high/low friction setups are conducted. The vibration suppression of the main structure equipped with the FTMD subjected to earthquake loadings can be investigated and ensured. Then, the main structure is replaced by its numerical model and is embedded inside the real-time hybrid testing configuration. The total shear force (the equivalent inertial force) calculated from the measured acceleration is fed back into the simulation part to compute the absolute displacement command of the main structure. The shaking table is then adopted as the test bed of the real-time hybrid testing to behave like the main structure and to interact with the equipped FTMD system. The test results of both real-time hybrid tests and their corresponding shaking table tests illustrate similar control performance of the FTMD. Therefore, the real-time hybrid testing technique can be extended to friction-type control devices.

Keywords：Friction-Type Tuned Mass Damper, Shaking Table Test, Real-Time Hybrid Testing

Introduction

The Friction-Type Tuned Mass Damper (FTMD) is a nonlinear tuned mass damper (TMD) system. By applying static friction as the triggering mechanism the FTMD system stays inactive during small earthquakes and comes into operation during large earthquakes.

Traditionally, research on the control effect of the system under real earthquakes often requires full-scale shaking table testing (STT). However, full-scale STT often requires a lot of effort and resources, and down-scaled shaking table testing cannot fully demonstrate the true dynamic behavior during earthquakes. Therefore, Hakuno[1] had proposed the concept of hybrid testing, mainly using a numerical model to replace the main structure of the STT, and interacting with the true control device to obtain the real response of the structure.

The purpose of this study is to verify whether Real-Time Hybrid Testing (RTHT) can truly show the same control performance of the FTMD system on the main structure system as the STT. The main procedure of this study is as follows. Shaking table testing is done to verify whether the FTMD system can reduce the structural response. Then, different numerical models are embedded inside the Shaking table system to simulate the behavior of the main structure to interact with the FTMD through the RTHT configuration. Both results are compared to verify that the FTMD system can show the same control performance by RTHT as that of STT.

Theory

In this study, the rolling pendulum system (RPS) is used as the main structure. It is the part marked by the red dashed frame in Fig 1. It is mainly composed of rollers and curved slides, which provide the fundamental frequency and stiffness of the main structure. The passive

[1] Associate Professor, Dept. of Civil Engineering, National Kung University, Taiwan
[2] Ph.D. student, Dept. of Civil Engineering, National Kung University, Taiwan
[3] Engineer, Division of Structural Engineering, SINOTECH Engineering Consultants, Ltd., Taiwan
[4] Associate Technologist, National Center for Research on Earthquake Engineering
[5] Professor, Dept. of Civil Engineering, National Kung University, Taiwan

control device is an FTMD shown in the upper part of Fig. 1, which is a variation of the variable-friction mechanism invented by Lu[2]. It mainly consists of a sliding platform and a passive friction damper. The sliding platform mainly includes a linear slide rail, a linear slider, a tuned mass stage, and a restoring spring.

Fig. 2 is the mathematical model of the FTMD system installed on the RPS system. The equations of motion of the whole system can be derived as follows:

$$m_d(\ddot{x}_d(t)+\ddot{x}_g(t))+k_d(x_d(t)-x_s(t))+F_d(t)=0$$

$$\begin{aligned} &m_s(\ddot{x}_s(t)+\ddot{x}_g(t))+c_s\dot{x}_s(t)+k_s x_s(t) \\ &-k_d(x_d(t)-x_s(t))-F_d(t)=0 \end{aligned} \tag{1}$$

$F_d(t)$ denotes the total friction of the FTMD system. Eq. (1) can be converted to state-space and be discretized. The discrete-time state-space equation of the entire system can be obtained as follows:

$$\mathbf{z}(k+1)=\mathbf{A_d}\mathbf{z}(k)+\mathbf{B_d}F_d(k)+\mathbf{E_d}\ddot{x}_g(k) \tag{2}$$

$\tilde{F}_d(k)$ in Eq. (3) denotes viscous friction, and $\mathbf{D_{ds}}=[0,0,-1,1]$ is the velocity distribution matrix of the FTMD system and the main structure system. $\left|\tilde{F}_d(k)\right|<F_{d,\max}$ means that the FTMD system is stuck and $F_d(k)=\tilde{F}_d(k)$. $\left|\tilde{F}_d(k)\right|\geq F_{d,\max}$ implies that the FTMD system can start to slide and $F_d(k)=F_{d,\max}(k)$. This is given in Eq. (4).

$$\tilde{F}_d(k)=\mathbf{G}_w\mathbf{z}(k)+\mathbf{G}_x\ddot{x}_g(k)$$

$$\begin{aligned} &\mathbf{G}_w=-(\mathbf{D}_{ds}\cdot\mathbf{B_d})^{-1}(\mathbf{D_s}\cdot\mathbf{A_d}) \\ &\mathbf{G_x}=-(\mathbf{D}_{ds}\cdot\mathbf{B_d})^{-1}(\mathbf{D}_{ds}\cdot\mathbf{E_d}) \end{aligned} \tag{3}$$

$$F_d(k)=\min(\left|\tilde{F}_d(k)\right|,F_{d,\max}(k))sign(\tilde{F}_d(k)) \tag{4}$$

Substituting the calculated friction $F_d(k)$ into Eq. (2), the next-step response of the system can be calculated.

According to He[3], initial sliding friction of the tuned mass damper can be adjusted to control the response of the main structure. Therefore, this study discusses the control effectiveness of different control types (HF and LF) under different earthquakes. The purpose of the uncontrolled FTMD system is to fix the FTMD system to the main structure system so that the FTMD system does not generate a sliding control reaction. HF (high damping) control is to adjust the overall sliding friction of the FTMD system by using PFD preloaded bolts to make the system produce passive control force on the main structure. According to previous results, 40 N has the best control effect. LF (low damping) control is to loosen the preload bolts, so that the friction of the FTMD system is only due to the sliding rail.

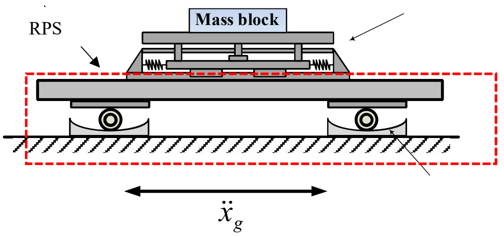

Fig. 1 Schematic drawing of the FTMD system

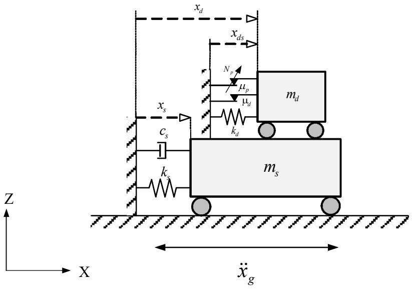

Fig. 2 Simplified mathematical model of the FTMD system

FTMD Shaking Table Testing

The specimen of the STT can be divided into two parts: the main structure and FTMD. The experimental configuration of the STT is shown in Fig. 3. The weight of the main structure is 946 kg. According to the optimization formula of the TMD system that Warburton[4] proposed, the best tuned mass of TMD can be calculated as 150 kg.

Before performing the FTMD shaking table testing, a system identification experiment is required. The purpose of this experiment is to identify the main parameters of the whole system. The parameters that should be identified are the equivalent stiffness, the roller-friction equivalent damping, the equivalent stiffness of FTMD, the equivalent coefficient of the slide friction of FTMD and the static friction of FTMD, respectively. The identification method is to apply a simple harmonic and measure the system response. The parameters of RPS are shown in Table 1 and the parameters of FTMD are shown in Table 2, respectively.

The objective of the STT is to investigate the control performance of different control types (HF or LF) under different earthquakes, which are White Noise, EL-Centro, KOBE, and Chi-Chi. Table 3 shows the peak values of the responses of the main system when the FTMD system is under different control types. Because the stroke of FTMD would exceed the threshold value when FTMD is under LF control and PGA is larger than 200 gal, the experiment of LF control is conducted only up to 150 gal.

From Table 3, it can be observed that the control performance of LF and HF of the FTMD system can significantly reduce the response of the main structure. In addition, the control effect of HF is better than that of LF during the larger PGA. If the same control performance can be achieved by the FTMD system in the RTHT configuration, it means that the RTHT can replace the STT and show the same behavior of the FTMD system.

Table 1 Main structure-identifying parameters

Mass m_s (kg)	946
Fundamental period T_s (sec)	1.96
Fundamental frequency ω_s (Hz)	0.51
Equivalent stiffness k_s (N/m)	9866.86
Roller-friction equivalent damping ζ_s (%)	2.48
Roller-friction coefficient μ_s	0.00153

Table 2 FTMD identifying parameters

Mass m_d (kg)	150.56
Fundamental period T_d (sec)	2.38
Fundamental frequency ω_d (Hz)	0.42
Equivalent stiffness k_d (N/m)	1027.49
Slide-friction equivalent coefficient μ_d	0.00262
Static friction (HF) $F_{d,\max}$ (N)	40.2
Static friction (LF) $F_{d,\max}$ (N)	3.87

Table 3 Root mean square of main structure system under each control of FTMD system

EQ_intensity	Uncontrol		HF		LF	
	$RMS(x_s)$ (cm)	$RMS(\ddot{x}_s^t)$ (gal)	$RMS(x_s)$ (cm)	$RMS(\ddot{x}_s^t)$ (gal)	$RMS(x_s)$ (cm)	$RMS(\ddot{x}_s^t)$ (gal)
WN_50	0.36	4.16	0.28	3.08	0.21	3.16
WN_150	1.54	15.53	1.48	15.00	0.92	11.65
WN_250	2.56	25.72	2.11	23.07	--	--
EL_50	0.26	2.87	0.33	3.66	0.17	2.46
EL_150	1.32	13.34	0.95	9.98	0.67	7.90
EL_250	2.16	22.15	1.37	15.23	--	--
KOBE_50	0.51	5.35	0.52	5.43	0.31	4.27
KOBE_150	2.16	21.84	1.16	12.51	1.35	18.37
TCU076_50	0.19	2.19	0.17	2.15	0.14	1.97
TCU076_150	1.13	11.40	0.89	9.15	1.02	13.35
TCU076_250	1.89	19.26	1.28	14.16	--	--

Fig. 3 Figure of shaking table testing of the main structure and FTMD system

FTMD Real-Time Hybrid Testing

The best method of real-time hybrid testing to fully mimic the complicated behavior of the STT is to replace the main structure by a numerical model, and send the resulting command of the response of the numerical model to the shaking table in real-time. The configuration of the proposed RTHT is shown in Fig. 4.

The mathematical model of the main structure of this RTHT is conducted by using the viscous damping model (VDM) and the Coulomb friction model (CFM), respectively. Their mathematical equations are shown in Eq. (5) and Eq. (6). $V_{ds}(t)$ denotes shear force of the FTMD. Which mathematical model can simulate the response closer to the STT will be discussed later.

$$m_s(\ddot{x}_s(t)+\ddot{x}_g(t))+c_s\dot{x}_s(t)+k_s x_s(t)=V_{ds}(t) \quad (5)$$

$$m_s(\ddot{x}_s(t)+\ddot{x}_g(t))+k_s x_s(t)+u_s(t)=V_{ds}(t) \quad (6)$$

As mentioned above, LF has better control performance under smaller PGA, and HF has better control effectiveness than LF under larger PGA. This study takes El Centro as an example to compare the hybrid-testing (HY) results of HY_VDM and HY_CFM with the STT under (100gal_LF) and (250gal_HF) situation. The results are shown in Fig. 5 and Fig. 6, respectively.

The CFM is suitable to simulate the response in the sticking state, and the VDM is suitable to simulate the response in free vibration. Therefore, as Fig. 5 shows, CFM is greater than VDM because the response of the main structure system is greatly affected by the friction between the roller and the sliding rail. Otherwise, Fig. 6 indicates that the response of the main structure system is affected less by the friction between the roller and the sliding rail, which makes the system response of the main structure simulated by the VDM better than the result of the CFM.

Because the RPS system and the FTMD system are both non-linear friction systems, the derivation process is too complicated to be simulated by a simple mathematical model. However, the response of the main structure predicted by the CFM in the RTHT is consistent with that simulated by VDM and STT results. It can be seen that the RTHT can simplify the verification of the experiment by choosing the appropriate numerical model.

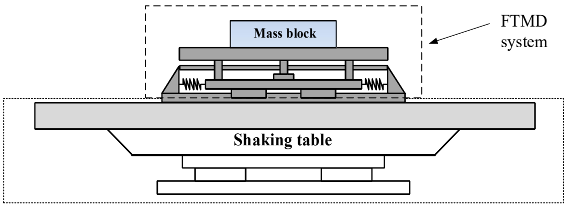

Fig. 4 Schematic drawing of the FTMD system of hybrid testing

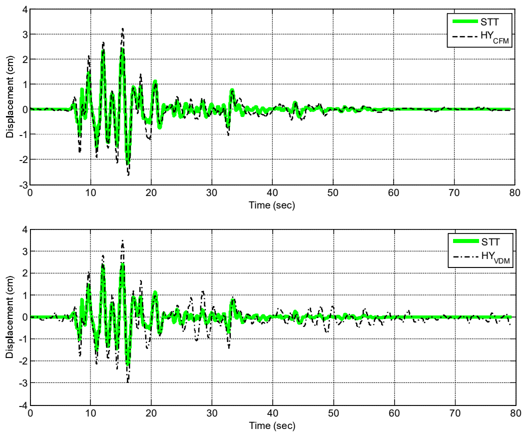

Fig. 5 Comparison of STT and HY (EL centro_100gal_LF)

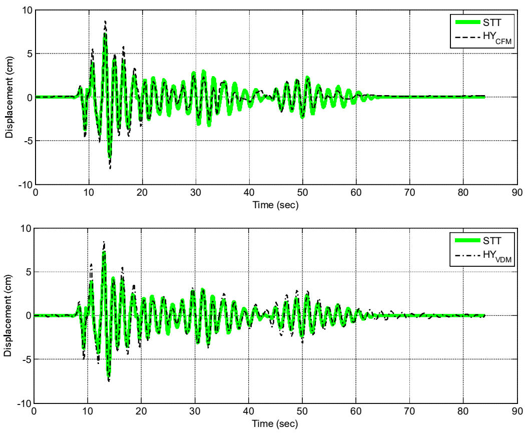

Fig. 6 Comparison of STT and HYT (EL centro_250gal_HF)

Conclusion and Comments

This study proposed a real-time hybrid testing configuration that can simplify or even replace the shaking table testing of the FTMD system. It first investigated the control effectiveness of the FTMD system on the main structure system by shaking table testing. The experimental results showed that FTMD can be effective in both HF and LF states. The responses of the main structure subjected to earthquake loadings were reduced, and the results of the STT were compared with that of the RTHT. It is found that the main structure can be replaced by either the VDM or the CFM, and the same behavior of the integrated FTMD system could be reproduced by the proposed RTHT configuration.

References

1. Hakuno, M., Shidawara, M. and Hara, T., “Dynamic destructive test of a cantileverbeam controlled by an analog-computer” Transactions Japan Society of Engineers, 1-9 (1969).
2. Lu, L.Y., Lin, P.Y., Lin, T.K., Yeh, S.W., Juang, S.Y., Ho, M.C.(2011), Research on the Application of Advanced Damping Elevated Floors to Equipment Seismic Prevention, 99th NSC project report, NSC 99-265-M-327-002.
3. He, Y.B.(2010), Shaking table test and vibration control analysis of semi-actively friction-typed tuned mass dampers, master's dissertation, National Cheng Kung University.
4. Warburton G.B., “Optimum Absorber Parameters for Various Combinations of Response and Excitation Parameters”, Earthquake Engineering and Structural Dynamics, Vol. 10, No. 3, pp.381-401, (1982).

Replacement Prioritization of Water Distribution Pipes of the Taipei Water Department

Chin-Hsun Yeh[1] and Gee-Yu Liu[1]

葉錦勳 [1]、劉季宇 [1]

Abstract

The water distribution pipelines of the Taipei Water Department are planned to be upgraded to NS pipes. This study collates and verifies the engineering borehole data in the Taipei Basin. The liquefaction susceptibility category map and the liquefaction potential map are updated according to the liquefaction critical acceleration of each site. To utilize the limited annual replacement budget, using the water supply district as a unit, three major indicators, namely seismic hazard potential, pipeline vulnerability, and replacement benefits, are taken into consideration in the prioritization scores for the replacement of existing water distribution pipelines. Three types of disaster scenarios, representing large near-field, moderate near-field, and large far-field earthquakes, are also selected to explore the rationality of the weight settings for seismic hazard potential and pipeline vulnerability.

Keywords: soil liquefaction potential, liquefaction critical acceleration, liquefaction susceptibility category, seismic disaster simulation

Introduction

Most of the water users of the Taipei Water Department (abbreviated as TpWD) are located in the Taipei Basin, which is a high liquefaction potential zone due to the flowing of the Xindianxi, Danshui, and Keelung rivers through the basin, as shown in Fig. 1. Furthermore, the area may suffer severe ground shaking due to the basin effect. The Sanchiao Fault, located on the northwest side of the Taipei Basin, has been determined as an active fault by the Central Geological Survey Bureau. To prevent disruption of the water supply system due to large earthquakes, the TpWD has adopted a dual trunk system to ensure that the main distribution system remains functional even after large-scale earthquakes. However, the damage of local distribution pipelines may still affect the time required for complete restoration. Therefore, it is necessary to replace old distribution pipelines with the more earthquake-resistant NS pipes.

The total length of distribution pipelines in the TpWD is 3,782 km. The operation scope in the TpWD is divided into 817 water supply districts (abbreviated as WSDs). As the number of water distribution pipes is large and widely distributed, it is expected that the total replacement time and cost may be extremely high. Hence, an optimal replacement prioritization scheme in units of WSDs is required.

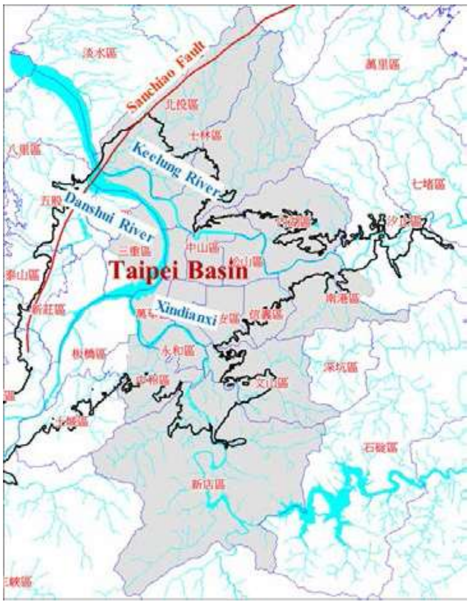

Fig. 1 Operation scope of the Taipei Water Department and its geographical environment.

There are three major tasks in the study. Task 1 is to update the liquefaction susceptibility category map and the liquefaction potential map in the Taipei Basin. Task 2 is to propose an optimal prioritization scheme in units of WSDs, considering seismic hazards, pipeline vulnerability, and replacement benefits. Task

[1] Researcher, Seismic Disaster Simulation Division, National Center for Research on Earthquake Engineering, NARL

3 is to conduct seismic disaster simulation by using Twater to explore the rationality of the weight setting used in the replacement prioritization score.

Update of Soil Liquefaction Potential Map

In recent years, both Taipei City and New Taipei City governments have undertaken projects to improve the accuracy of the soil liquefaction potential map in the Taipei Basin. Approximately 800 boreholes were newly drilled. These supplementary borehole data are highly reliable. In addition, thousands of existing borehole data that were contributed by other projects were also collected and reviewed to ensure data quality. Approximately 2,500 existing boreholes were screened and used in this study. The borehole density considered when selecting the supplementary borehole sites is at least 4 holes per square kilometer.

Considering the safety factor of each soil layer within 20 m below ground, the liquefaction potential index (P_L) proposed by Iwasaki (1982) has been widely used to estimate the occurrence probability and the severity of soil liquefaction. The traditional soil liquefaction potential map is defined as follows. Under the design earthquake, which is specified by the peak ground acceleration (PGA) and the control earthquake magnitude in seismic design codes, if $P_L \ge 15$, the site has "High" liquefaction potential; if $P_L \le 5$, the site has "Low" liquefaction potential. Otherwise, the site has "Moderate" liquefaction potential. One example is shown in Fig. 2.

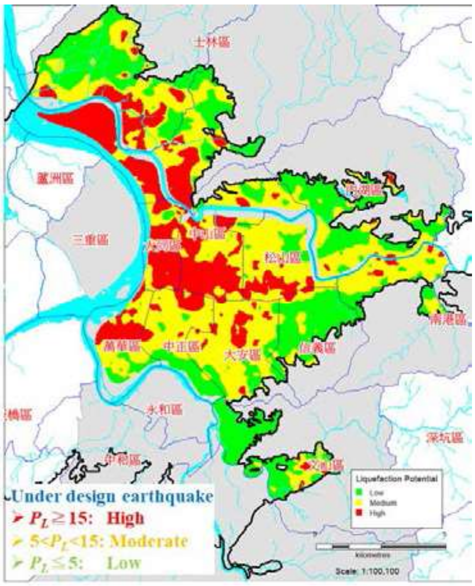

Fig. 2 Soil liquefaction potential map classified in terms of P_L.

Typically $P_L = 15$ is considered the threshold for likely soil liquefaction. Therefore, given a specific earthquake magnitude and groundwater depth, the PGA corresponding to $P_L = 15$ is termed the "liquefaction critical acceleration." Considering the seismicity in Taiwan, especially near the Taipei Basin, four combinations of earthquake magnitude and groundwater depth, denoted by C75, V75, V70, and V65, are selected as representative. The first character indicates the groundwater depth, which is either constant (1.5 m) or variable at each site; the remaining two digits indicate the earthquake magnitude (7.5, 7.0, and 6.5, respectively). The liquefaction critical accelerations corresponding to the four scenarios are denoted by a_{c75}, a_{v75}, a_{v70}, and a_{v65}. It is noted that a_{c75} has been used to classify the liquefaction susceptibility categories (Yeh et al, 2015), as shown in Fig. 3.

The weighted average, defined by

$$A_{lc} = 0.4 \cdot a_{v70} + 0.2 \cdot (a_{c75} + a_{v75} + a_{v65}), \tag{1}$$

may be used to quantify the level of liquefaction potential at each site. In other words, if $A_{lc} \le 0.25g$, this indicates that the site is likely to be liquefied under a small ground shaking intensity, and the liquefaction potential at the site is "Very High" or "High". If $0.25g < A_{lc} \le 0.35g$, the site will not be liquefied until the ground shaking intensity reaches 6, and the liquefaction potential at the site is "Moderate". All other alluvium regions may have "Low" or "Very Low" liquefaction potential depending on A_{lc}. The newly created liquefaction potential map using A_{lc} is shown in Fig. 4. It is obvious that the regions of high liquefaction potential in these two maps are similar. However, the newly created soil liquefaction potential map contains more information and may be divided into more meaningful levels.

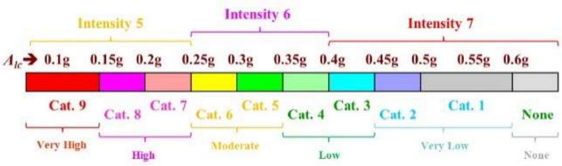

Fig. 3 Classification scheme of soil liquefaction susceptibility category and liquefaction potential.

Replacement Prioritization in Units of Water Supply District (WSD)

The proposed prioritization scheme considers three factors: seismic hazard potential, pipeline vulnerability, and replacement benefits. The seismic hazard potential score (H) is expressed as

$$H = 0.7 \cdot r_{crt-acc} + 0.3 \cdot r_{site-eff}, \tag{2}$$

where $r_{crt-acc}$ is the rank of liquefaction critical acceleration and $r_{site-eff}$ is the rank of the ground motion site effect. The score H has been normalized to 0–1.

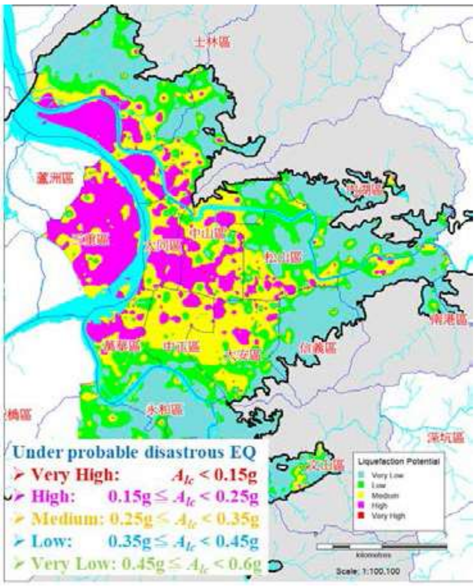

Fig. 4 Soil liquefaction potential maps classified by A_{lc}.

The pipeline vulnerability score (V) is defined by

$$V = 0.7\cdot(1-r_{seismic}) + 0.3\cdot(1-r_{repl})\ , \tag{3}$$

where $r_{seismic}$ is the length ratio of seismic pipelines, and r_{repl} is the length ratio of pipelines that have been replaced in the past ten years. Since $r_{seismic}$ and r_{repl} are between 0 to 1, the value of V is between 0 and 1.

The replacement benefit score (B) is defined by

$$B = \min(n_h,\ \ 10{,}000)/10{,}000\ , \tag{4}$$

where n_h is the number of households. It is noted that the value of B is also between 0 and 1.

While considering the seismic hazard potential and pipeline vulnerability, the aim is to reduce the total number of disasters, whereas while considering the replacement benefits, the aim is to maintain the number of households with water supply after strong earthquakes. Obviously, it is impossible to obtain the overall benefit and to consider all aspects solely by a single factor. Hence, the replacement prioritization score (R) is expressed as a weighted average of H, V, and B. Referring to the disaster simulation results, the weights of H and V can be set as equal. Hence, the replacement prioritization score (R) is defined as

$$R = 0.3\cdot H + 0.3\cdot V + 0.4\cdot B\ , \tag{5}$$

where H, V, and B are defined by Eq. (2), (3), and (4), respectively. This score is used as the basis for the optimal ranking of the individual WSD. The distribution map of different replacement priority ranks by WSD is shown in Fig. 5.

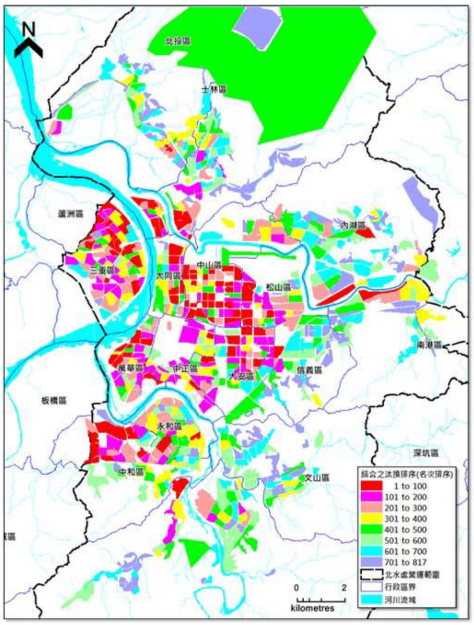

Fig. 5 Distribution of replacement priority rank per WSD.

Seismic Disaster Simulations

Three types of disaster scenarios representing large near-field, moderate near-field, and large far-field earthquakes were studied to explore the overall benefits of site-specific pipeline replacement by assigning different weights of H and V. The seismic source parameters are listed in Table 1.

Table 1 Seismic source parameters of the considered three scenarios.

Scenario Type	Fault Name	Magn. (M_L)	Depth (km)	Len. (km)
Large N-field	Sanchiao	6.9	8	56.0
Med. N-field	Sanchiao	6.2	10	12.4
Large F-field	Xincheng	7.3	10	29.0

Three weight assignments of H and V were studied: $0.7H+0.3V$, $0.5H+0.5V$, and $0.3H+0.7V$. For each weight assignment, the top 100 or 300 WSDs will be selected to replace the distribution pipelines by NS pipes. A portion of the simulation results of the six cases are shown in Table 2, 3, and 4, where S2 and S3 denote pipe sizes of 75–250 mm and 300–450 mm, respectively.

It is observed that the reduction ratio of pipeline damages is greater than the replacement ratio of pipeline lengths; thus, the proposed prioritization scheme is effective. Second, increasing the weight of the pipeline vulnerability score (V) is more effective for near-field earthquakes, while increasing the weight of the seismic hazard potential score (H) is more effective for far-field earthquakes. Furthermore, the disaster reduction ratio is not sensitive to the weight assignments of H and V . Therefore, it is recommended that both scores have the same weight.

Table 2 Results of the Sanchiao Fault earthquake with M_L 6.9 for replacing the top 100 WSDs.

Weight Setting	No. of Repairs		Repair Reduction Ratio	
	S2	S3	S2	S3
Original	1,865.5	124.4	-	-
0.7H+0.3V	1,637.6	109.3	12.2%	12.2%
0.5H+0.5V	1,634.0	109.2	12.4%	12.3%
0.3H+0.7V	1,629.1	108.6	12.7%	12.7%

Table 3 Results of the Sanchiao Fault earthquake with M_L 6.2 for replacing the top 100 WSDs.

Weight Setting	No. of Repairs		Repair Reduction Ratio	
	S2	S3	S2	S3
Original	669.1	40.7	-	-
0.7H+0.3V	567.4	33.7	15.2%	17.0%
0.5H+0.5V	567.2	33.8	15.2%	16.8%
0.3H+0.7V	565.9	33.7	15.4%	17.0%

Table 4 Results of the Xincheng Fault earthquake with M_L 7.3 for replacing the top 100 WSDs.

Weight Setting	No. of Repairs		Repair Reduction Ratio	
	S2	S3	S2	S3
Original	150.3	12.4	-	-
0.7H+0.3V	121.5	9.3	19.2%	24.7%
0.5H+0.5V	122.2	9.5	18.7%	23.2%
0.3H+0.7V	125.4	10.0	16.6%	19.5%

Supplementary notes are as follows:

1. Since the water distribution pipelines in the TpWD are very long and widely distributed, the total time and cost for replacement with NS pipes is extremely high. Therefore, it is necessary to carry out optimal ranking.
2. Under large far-field earthquakes, the ground shaking intensity is attenuated and the number of repairs in the water distribution pipelines is more or less smaller. However, under near-field earthquakes, either large or moderate in magnitude, the ground shaking intensity is generally large.
3. Taipei City has large chances of facing far-field earthquakes with smaller number of repairs and small chances of facing near-field earthquakes with a larger number of repairs.
4. Initial replacement of the water distribution pipeline is likely located in the high disaster potential area due to seismic hazards or pipeline vulnerability.
5. The division of water supply districts in the operation scope of the TpWD has not been completed. In addition, the importance of each WSD has not been taken into consideration. This requires further research in the future.

Concluding Remarks

Based on the grading of liquefaction critical acceleration at each site, the soil liquefaction potential map and the soil liquefaction susceptibility category map of the Taipei Basin were updated. Instead of using the liquefaction potential index, the liquefaction potential at each site may be classified by the liquefaction critical acceleration, which is divided into nine categories or five levels.

The proposed score used to prioritize the replacement sequence in the unit of the water supply district considers the seismic hazard potential, including soil liquefaction and ground-motion site effect, pipeline vulnerability, and replacement benefits.

Simulation tests of three types of disaster scenarios representing large near-field, moderate near-field, and large far-field earthquakes were conducted by using Twater. It was found that the disaster reduction rate is not sensitive to the weight combinations of seismic hazard and vulnerability. Therefore, the seismic hazard and vulnerability have the same weight for calculating the prioritization score.

References

Iwasaki, T., Arakawa, T., and Tokida, K., 1982, "Simplified Procedures for Assessing Soil Liquefaction During Earthquake", Proceedings of the Conference on Soil Dynamics & Earthquake Engineering, Volume II, pp. 925-939.

Yeh, C. H., G. Y. Liu and L. H. Huang 2015. "New Study on Soil Liquefaction Susceptibility Categories," 9th WRF/JWWA/CTWWA Water System Seismic Conference, Sendai, Japan.

Seismic Performance of RC Frames with BRBs connected to Corbels

An-Chien Wu [1], Keh-Chyuan Tsai [2]

吳安傑 [1]、蔡克銓 [2]

Abstract

This study investigated the performance of brace connections in new reinforced concrete (RC) frame buildings with buckling-restrained braces (BRB) arranged in a zigzag configuration. A 12-story buckling-restrained braced RC building following model building codes is proposed as a prototype. To verify the constructability and seismic performance of the proposed connection, the beam–column joint at the tenth floor was selected as a sub-assemblage specimen, designed, and fabricated. The full-scale sub-assemblage, including the BRB gusset bracket and a pair of RC corbels, in the proposed BRB RC frame structural system was tested using a cyclic loading procedure. The test results demonstrate that the proposed BRB-to-RC connection performs well without failure in the steel gusset bracket or the RC corbels. The design and construction of the sub-assemblage specimen shows the feasibility of the proposed system for practical applications.

Keywords: buckling-restrained brace, reinforced concrete structure, corbel, beam–column joint

Introduction

Buckling-restrained braces (BRB) are characterized by symmetric hysteresis behavior, high ductility, and a stable energy-dissipation capability [Wada and Nakashima 2004, Tsai *et al*. 2014], which has led to extensive research and applications in various structural systems. However, research and applications that adopt BRBs for reinforced concrete (RC) constructions appear to be rather limited and confined to the retrofitting of existing RC structures. Even though the performance of various BRB connections can be found in these reports, the details and construction procedures of the BRB end brackets and RC frames are still quite challenging. In addition, BRBs can develop significant axial forces, which may impose complicated and unfavorable loads on adjacent RC members. They may even significantly alter the expected force distribution of the adjoining members. Furthermore, the damage to adjacent RC members during earthquakes may gradually impair the expected BRB performance.

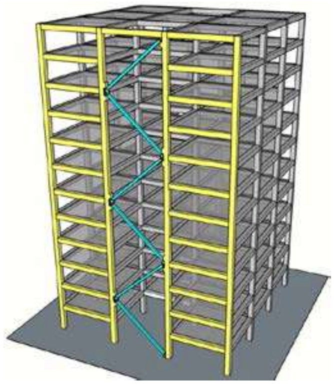

Fig 1. Structural perspective and BRB configuration.

To resolve some of the aforementioned unfavorable issues in the application of BRBs in new RC constructions, a novel bracing system [Qu *et al*. 2013, 2015] was adopted (Fig. 1). Details of the gusset-to-column connection and the construction procedures are modified in this study. During construction, the BRB gusset bracket is placed adjacent to the

[1] Associate Researcher, National Center for Research on Earthquake Engineering, acwu@ncree.narl.org.tw.
[2] Professor, Department of Civil Engineering, National Taiwan University, kctasi@ntu.edu.tw.

beam-to-column joint as part of the concrete formwork and connected to the beam's longitudinal reinforcements through couplers welded to the back of the gusset bracket. After the concrete hardens, the gusset bracket, the column, and the corbels are integrated together without gaps. This construction process is quite common in typical steel RC construction. A cyclic loading test was conducted on a beam-to-column joint sub-assemblage specimen selected from the tenth floor to verify the seismic performance of the proposed connection.

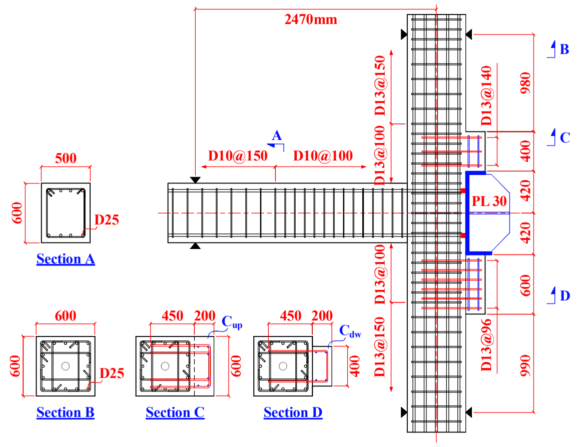

Fig 2. Dimensions and reinforcement layout of the test specimen.

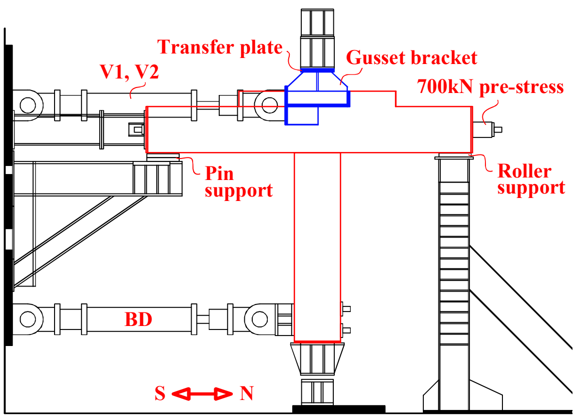

Fig 3. Experimental apparatus.

Test Program

The sub-assemblage specimen included a pair of RC corbels and a BRB gusset bracket, with a 2470-mm-span beam and a column extending 1800 mm high and 2010 mm high, respectively, above and below the joint. The reinforcement layout and detailed dimensions of the specimen are illustrated in Fig. 2. The beam cross section was 500×600 mm, reinforced with eight D25 longitudinal bars, while the column cross section was 600×600 mm, reinforced with sixteen D25 longitudinal bars. The column hoops and beam stirrups were D13 and D10 bars, respectively, spaced at 100 mm on the centers in the plastic hinge zones, which increased to 150 mm outside the plastic hinge zones.

In a traditional buckling-restrained braced frame, the BRB corner gusset is subjected to both brace forces and frame actions, which may lead to the premature failure of gusset connections and the impairment of the seismic performance of the system. In the proposed bracing system, there is no beam in the braced span. The gusset bracket connected with the two adjacent BRBs is attached to the side surface of the beam-to-column joint, thus preventing the frame action on the gusset. The gusset bracket is composed of a gusset plate joined to the BRBs and a U-shaped steel connected to the RC frame. This is designed as a force-controlled element so that it will remain essentially elastic when the BRBs reach their expected maximum capacities. A572 GR50 steel (nominal yield strength of 350 MPa) was adopted for the gusset bracket of the specimen. The gusset plate was detailed based on the BRB ends with the welded end-slot connection [Tsai *et al.* 2014].

The design limit states, including tensile yielding, compressive buckling, and block shear failure, were considered to resist the design force demands. Welding between the gusset plate and the U-shaped steel was designed to transfer the vertical resultant $V_{\max}$ from the two adjacent BRBs to the RC corbels and to transfer the horizontal resultant of $0.7T_{\max}$ to the longitudinal reinforcements of the braced RC beam. Instead of applying two physical BRB members, four electro-servo hydraulic actuators were used to simulate the horizontal and vertical resultants developed from the BRBs. Thus, to transfer the gusset's normal forces from a pair of actuators, a transfer plate was welded onto the free edge of the gusset and the U-shaped steel bracket assembly. The U-shaped steel end plate was also extended outward and properly stiffened, as shown in Fig. 3, to attach another pair of actuators for applying the corbel shear.

The RC corbels in the structural system were also considered as force-controlled elements, which are expected to resist the vertical shear demand of $V_{\max}$ coming from the gusset bracket. When the two adjacent BRBs reached their maximum capacities, $P_{T,\max}$ and $P_{C,\max}$, the calculated shear demands of the corbels above and below the specimen gusset bracket were 1729 and 1590 kN, respectively. In the proposed connection, however, the gusset bracket was connected to the beam's longitudinal reinforcements via the couplers. The beam longitudinal reinforcements can directly resist the horizontal tension from the BRBs, while indirectly providing vertical shear resistance. Thus, the shear demands on the pair of corbels are reduced.

To prevent an excessively conservative design result, the target shear capacities of the upper (C_{up})

and lower (C_{dw}) corbels were designed to be 60% and 70% of the above-mentioned shear demands, respectively. As shown in Fig. 2, the depths (H) of corbels C_{up} and C_{dw} were 400 and 600 mm, while their widths (B) were 600 and 400 mm, respectively. The lengths (L) of both corbels were 200 mm, and the length-to-depth ratios L/H were 0.5 and 0.33, respectively. Corbel C_{up} was reinforced by 140-mm-spaced D13 U-shaped double stirrups, while corbel C_{dw} was reinforced by 96-mm-spaced D13 U-shaped single stirrups. The corbel stirrups were embedded 450 mm deep into the column surface and secured by framing bars. The shear-resisting capacity V_u of the corbels was assessed by the modified strut-and-tie model [Qu *et al*. 2012]. As a result, the shear-resisting capacities of corbels C_{up} and C_{dw} were determined to be 1079 and 1097 kN. Alternatively, simple design provisions based on shear friction theory are provided in ACI 318-11 to evaluate the corbel shear resistance V_n. The shear resistance of corbels C_{up} and C_{dw} was 877 kN, which is more conservative than the resistances evaluated using the former method.

Test Results

During the loadings with a 0.5% drift ratio, the beam and column elements remained essentially elastic as expected and no evident cracking was observed on the sub-assemblage. The free-body diagram of the specimen is depicted in Fig. 4. The work point of the two BRBs was set at the column surface rather than the column centerline. Therefore, the vertical resultant V_{BRB} from the gusset bracket provided a moment demand of $V_{BRB}\times h/2$ on the column. Although the arm was short, significant forces in the BRBs were able to make the resultant moment contribution comparable to that of the eliminated beam. This moment demand on the column must be considered. The total column moment resistance $V_{c1}\times H_1+V_{c2}\times H_2$ in the sub-assemblage was obtained by combining the contribution of the beam moment $V_b\times L_b$ (L_b is measured from the cantilever load to the column centerline) and that of the BRBs $V_{BRB}\times h/2$. As shown in Fig. 5, the maximum moment contribution of the BRBs was approximately half that of the beam and approximately one-third of the total moment resistance of the specimen. When the frame roof drift was positive, the corresponding beam-end deformation of the specimen was negative, and the beam was compressed by the BRB horizontal resultant. Both the analytical and experimental results indicated that the beam moment resistance in compression was larger than that in tension. Specimen damage conditions (Fig. 6) at the end of the test revealed that concrete spalling occurred at the beam's fixed end, which is in compliance with the strong column–weak beam design principle. The flexural-shear cracks of the column appeared only within the range between the two corbels. Thus, it appears from the beam's P-M responses that the flexural behavior of the beam was not significantly influenced, despite its longitudinal reinforcements being connected to the gusset bracket.

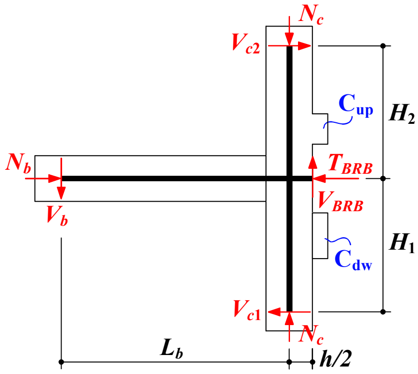

Fig 4. Free-body diagram of the sub-assemblage specimen.

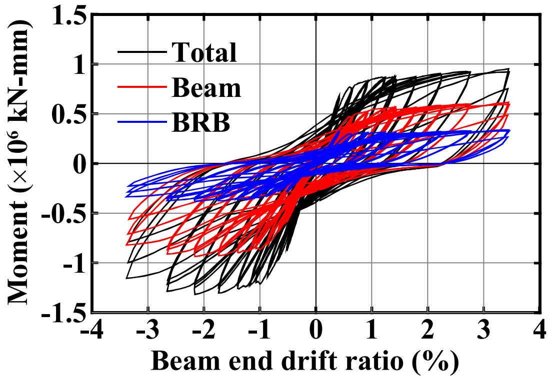

Fig 5. Bending moment components in the sub-assemblage specimen.

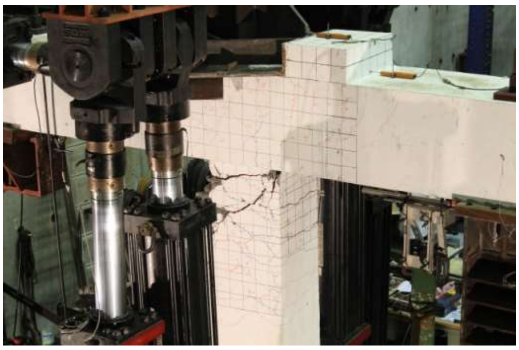

Fig 6. Damage condition of the test specimen at the end of testing.

The gusset bracket remained elastic and worked rather well throughout the entire test. The gusset bracket's force versus displacement relationships in the direction normal to the column surface are shown in Fig. 7. The maximum displacement measured was less than 0.5 mm, which was small enough to be neglected. When the gusset bracket was compressed, the measured small positive normal displacements, shown in Fig. 7, were most likely caused by the slip of the measurement gauges or the local elastic deformation of the gusset bracket. Cyclic upward pull tests on the gusset bracket were continued after the prescribed cyclic loading test on the sub-assemblage. At the end of test, the maximum tensile force sustained by the gusset bracket was approximately 1800 kN without any observed nonlinear behavior. The change in the corbel's shear force with deformation for C_{up} and C_{dw} are shown in Fig. 8. Throughout the tests, there was almost no cracking found on the two corbels and only slight crushing of the concrete was observed at the corbel edges due to bearing pressure from the gusset bracket. After the cyclic loading test, both corbels were monotonically pushed until the actuators reached their maximum capacities. No evident damage to the two corbels was observed prior to the end of testing. This could be attributed to the gusset bracket being cast with the column and corbels at the same time, resulting in no gaps or non-shrink grout between the steel bracket and concrete surface. The behavior of the corbels was not affected by the deformation and flexural-shear cracks in the column adjacent to the corbels and in the panel zone. The test results confirm that the two corbels can carry significantly more shear resistance than the expected design capacity. It appears that the beam longitudinal reinforcements anchored on the back of the gusset bracket provided a significant additional shear friction resistance.

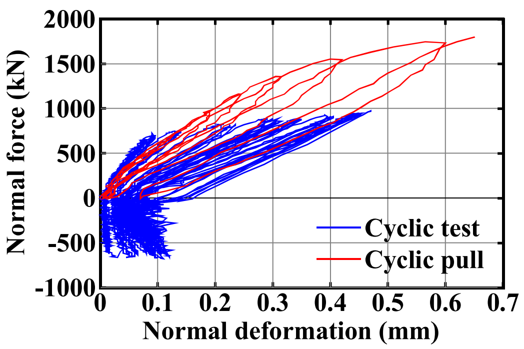

Fig 7. Normal force with displacement for the gusset bracket.

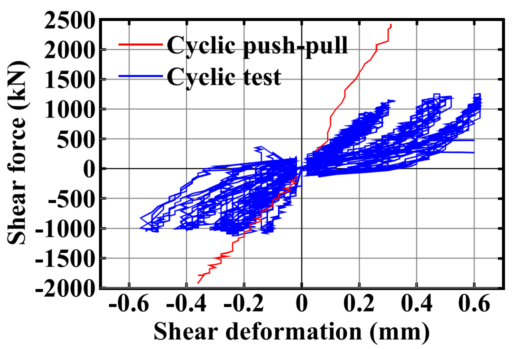

Fig 8. Shear force with deformation for the corbels.

Conclusions

This proof-of-concept test confirmed the feasibility of the proposed system for practical applications. The test results indicated that the beam moment resistances complied with the predicted yield surface. No evident damage to the two corbels was observed before the end of testing. This could be attributed to the gusset bracket being cast with the column and corbels at the same time, eliminating any gap or non-shrink grout between the steel bracket and concrete surface. The design shear capacity computed using American Concrete Institute (ACI) specifications for the proposed connection corbels was very conservative. It was confirmed that the beam's longitudinal reinforcements anchored on the gusset bracket could provide a significant additional shear friction resistance. The test results indicate that the proposed gusset anchor details can lead to a much stronger connection than those tested by others. However, RC corbels may fail in a very brittle manner under shear. It is recommended that the corbel shear resistance be at least computed from the modified strut-and-tie model to ensure an effective connection between the BRB and RC frame. Significant horizontal force demands could occur on the BRB connection at the top and bottom stories, or when two adjacent BRBs have notably different strengths. In addition, for BRBs connected to the top and bottom beams or columns that do not use corbels, the shear failure of the RC discontinuity regions due to the concentrated loads from the BRB must be prevented.

References

Wada A, Nakashima M, 2004. From infancy to maturity of buckling restrained braces research. The 13th World Conference on Earthquake Engineering, Vancouver, B.C., Canada.

Tsai KC, Wu AC, Wei CY, Lin PC, Chuang MC, Yu YJ, 2014. Welded end-slot connection and debonding layers for buckling-restrained braces. Earthquake Engineering and Structural Dynamics, 43(12), 1785-1807

Qu Z, Kishiki S, Sakata H, Wada A, Maida Y, 2013. Subassemblage cyclic loading test of RC frame with buckling restrained braces in zigzag configuration. Earthquake Engineering and Structural Dynamics, 42(7), 1087-1102.

Qu Z, Kishiki S, Maida Y, Sakata H, Wada A, 2015. Seismic responses of reinforced concrete frames with buckling restrained braces in zigzag configuration. Engineering Structures, 105, 12-21.

Qu Z, Maida Y, Kishiki S, Sakata H, 2012. Shear resistance of reinforced concrete corbels for shear keys. The 9th International Conference on Urban Earthquake Engineering and 4th Asia Conference on Earthquake Engineering, Tokyo, Japan.

Semi-active Control for Building Mass Damper Systems

Yu-Fang Liu1, Tzu-Kang Lin2, Kuo-Chun Chang3

Abstract

A concept for improving an optimum building mass damper (OBMD) system through a semi-active control method to enhance the efficiency of controlling structural responses is proposed. The proposed concept involves replacing the passive fluid viscous dampers used in an OBMD system with semi-active magnetorheological (MR) dampers, thereby transforming the system into a novel semi-active OBMD (SOBMD) system for better seismic performance. A numerical model based on the Bouc–Wen model was established to represent the behavior of MR dampers. An SOBMD system was then developed on the basis of the linear-quadratic regulator (LQR) method. The damping force in the SOBMD system can be manipulated according to the structural responses; therefore, the SOBMD system provides the possibility of improving displacement or acceleration responses compared with the original OBMD system. Both the numerical analysis and experimental verification demonstrated the superior seismic mitigation ability of the SOBMD system. In short, the benefits of both an active and passive control system are successfully combined in the proposed SOBMD system.

Keywords: semi-active control; MR damper; building mass damper

Introduction

Seismic isolation technologies and tuned mass dampers (TMDs) have been widely applied in controlling the dynamic responses of building structures in recent years. Based on the location of the isolation layer, seismic isolation can be divided into base isolation and mid-story isolation, and both can extend the vibration period of a building and reduce the seismic forces transmitted to the structure above the isolation layer to mitigate the damage to the structure. In comparison, the mid-story isolation provides better construction efficiency, space use, and easier maintenance, but it has more complex dynamic characteristics than the base isolation system [1-4]. Another system for vibration resistance involves using a TMD to reduce the vibrational energy of the main structure by resonating out of phase with the structural motion. The effectiveness of the TMDs in reducing the displacement and acceleration of structures has been proven by many studies [6,7]. The performance of a TMD highly corresponds to its mass ratio relative to the structure. Limited by the building space and economic efficiency, the mass ratio of most TMDs is lower than 10%, which is generally applied to reduce wind-induced vibration. Considering earthquake resistance, a TMD requires a relatively larger mass and displacement to effectively mitigate the associated seismic response, which is practically infeasible.

To overcome the limitations of traditional TMD systems, an optimum building mass damper (OBMD) design concept has been developed [5,8-9]. In the OBMD design, the advantages of the TMD and mid-story isolation system are expected to be combined to effectively control the dynamic response of both the superstructure and substructure. Considering the flexibility of the superstructure, a three-degree-of-freedom model derived from the conventional two-degree-of-freedom TMD design [10] is used to explore the optimum design parameters of an OBMD based on the dynamic response control concepts of TMD [5,8-9].

Although the OBMD system was proven to be able to enhance the seismic resistance of a mid-story isolated building [5], in some simulated earthquakes the controlling effectiveness of the building mass absorber was not sufficient to fully offset the enlarged displacement response at the substructure caused by the mid-story isolation system. To improve the imperfection of OBMD systems, a concept for enhancing the OBMD through a semi-active control method is proposed in this paper and will be further discussed in the following sections.

[1] Assistant Researcher, National Center for Research on Earthquake Engineering, Taipei, Taiwan, yfliu@ncree.narl.org.tw
[2] Professor, Dept. of Civil Engineering, National Chiao Tung University, Hsin-Chu, Taiwan, tklin@nctu.edu.tw
[3] Professor, Dept. of Civil Engineering, National Taiwan University, Taipei, Taiwan., ciekuo@ntu.edu.tw

Concept of the proposed system

An OBMD system combines the advantages of TMDs and a mid-story isolated design to control the seismic responses of both the substructure and superstructure of a building. In an OBMD system, the superstructure above the control layer serves as an absorber to overcome the problem of insufficient mass that is present in the traditional TMD design. The control layer comprising elastomeric bearings and additional dampers provides the necessary stiffness and damping for the entire system. A simplified structural model with three lumped masses assigned at the superstructure, the control layer, and the substructure is assumed to represent the dynamic characteristics of a building with an OBMD design, as shown in Figure 1 [5]. The minimum of the sum of the response in three degrees of freedom was set to be the objective function, which represents the optimum dynamic response control effectiveness of the superstructure, the control layer, and the substructure. Considering the appropriate mass ratio and damping ratio, the optimum parameters for such an OBMD system can be determined [5]. Although the control effectiveness of the OBMD design has been proven to be superior to that of a mid-story isolation system, the displacement amplification of the substructure has limited the performance of this design.

The proposed control concept involves replacing the fluid viscous dampers used in the OBMD system with MR dampers, thereby transforming the original passive OBMD system into the proposed SOBMD system. The variability of the semi-active control device is utilized to further reduce the dynamic response of the structure and enhance the control efficiency of the original OBMD system.

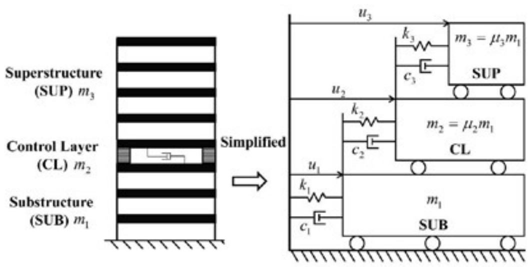

Fig. 1 Simplified three-lumped-mass structural model for an OBMD [5]

The Proposed SOBMD System

The passive fluid viscous dampers used in the OBMD system are replaced by semi-active MR dampers in the proposed SOBMD system to integrate the benefits of the active and passive control methods.

To obtain a damping force equal to the maximum force of the viscous dampers used in the OBMD system, six MR dampers, each with a maximum force of 2.2 kN, were adopted to ensure that the results can be compared with those from the OBMD system. The basic properties of the MR damper are presented in Table 1. The maximum stroke of the MR damper is 20 mm and the control voltage ranges between 0 and 0.8 V.

According to a study conducted in 1997 by Spencer et al. [11], the Bouc–Wen model is highly flexible for evaluating the hysteresis behavior of a nonlinear MR damper. Accordingly, the theoretical and experimental models of the MR damper are based on the Bouc–Wen model.

Table 1 - Specification of the MR damper

Specification	
Type	MR
Stroke	20 mm
Force Capacity	2.2 KN
Voltage	0-0.8 V

Experimental Verification of the SOBMD System

The reliability of the numerical model of the SOBMD was verified through a shaking table test conducted at the NCREE. Three control cases, namely the uncontrolled (UC), OBMD, and SOBMD systems, were analyzed and compared to examine the performance of the proposed SOBMD system. An eight-story steel structure was employed. The desired optimum damping of the OBMD system was provided by the fluid viscous dampers placed on the control layer, while the fluid viscous dampers were replaced by the MR dampers in the SOBMD system. The rubber bearings were placed on the control layer to provide the optimum stiffness for both the OBMD and SOBMD systems. Unlike the OBMD and SOBMD systems, the UC structure has no control layer. Each floor of the UC structure is a general floor without any diagonal braces, rubber bearings, or dampers.

Two earthquakes with different characteristics, namely the 1940 El Centro earthquake (representing a far-field earthquake) and the TCU072 earthquake (representing a near-fault earthquake), were used to examine the practical performance and reliability of the proposed system. Considering the limited stroke of the MR damper and the safety of the experimental process, the maximum strength of the El Centro earthquake was reduced to 60%, corresponding to a PGA of 210 gal, and that of the TCU072 earthquake was reduced to 40%, corresponding to a PGA of 190 gal. The dynamic responses and control performances of the three control cases were recorded and compared.

Based on the experimental results, the peak responses of the three control cases are compared in Figure 2 [13]. By observing the displacement time history, it was revealed that each displacement peak value was reduced by the SOBMD system compared with the OBMD system, and the improvement was obvious even for different earthquakes. Regarding the acceleration, the time history indicated that the peak values of the structural acceleration responses were effectively suppressed by the SOBMD system compared with the OBMD system. The experimental results showed that although the seismic response can be mitigated by the OBMD system, a higher level of control efficiency can be achieved by the proposed SOBMD system. The variable control characteristics of the SOBMD system can be utilized to overcome the displacement amplification problem of the substructure and optimize the structural response control more comprehensively [13].

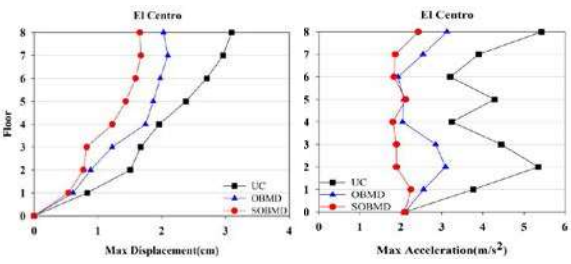

Fig. 2 Comparison of three cases (PGA: 210 gal) [13]

A comparison of the maximum story drift in the three control cases is shown in Figure 3 [13], indicating that the maximum story drift of the substructure is generally higher than that of the superstructure. In some earthquakes, the maximum story drift of the substructure in the OBMD system even surpassed that in the UC case. By contrast, the maximum story drift can be effectively reduced by the proposed SOBMD system. This advantage provides buildings employing the SOBMD system with superior comfort, cost efficiency, and usability. Comparisons of the experimental and numerical time histories are shown in Figure 4 [13], signifying that the trends in the numerical simulations are highly similar to those in practical experimentation, thereby verifying the reliability of the numerical simulations.

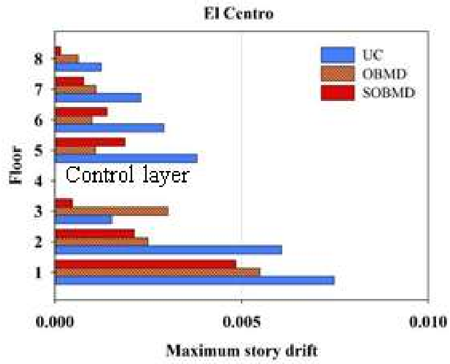

Figure 3. Comparison of the maximum story drift under El Centro (PGA: 210 gal) [13]

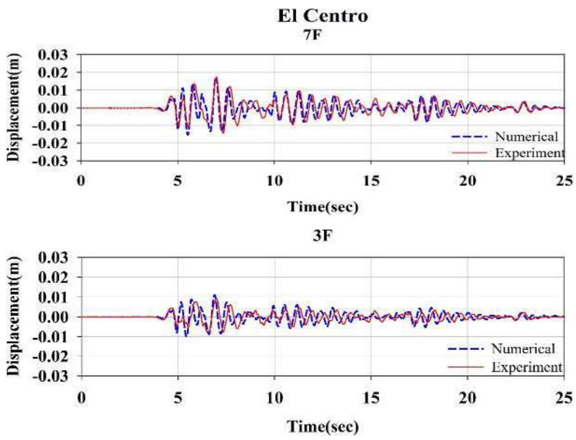

Figure 4. Displacement comparison of an SOBMD structure (PGA: 210 gal) [13]

Conclusions

In comparison with the OBMD system, the performance of our proposed system (the SOBMD system) was verified through a series of shaking table tests conducted at the NCREE. From the experimental verification results, the semi-active control system is superior to the passive control system. By combining the adjustable feature of the active control system and the reliable energy dissipation advantages of the passive control system, the semi-active control system successfully integrates the benefits of the active and passive control systems. With superior control effectiveness compared to the passive system and lower power consumption compared to the active control system, the semi-active control system provides an optimized solution for achieving a cost-effective structural design with satisfactory space efficiency and control performance.

References

[1] T. Koh and M. Kobayashi (2000): Vibratory characteristics and earthquake response of mid-story isolated buildings. Memoirs of the Institute of Sciences and Technology, Meiji University, vol. 39, no. 12, pp. 97–114.

[2] Wang, S. J., Chang, K. C., Hwang, J. S. and Lee, B. H (2010): Simplified analysis of mid-story seismically isolated buildings. Earthquake Engineering and Structural Dynamics, vol. 40, no. 2, pp. 119-133.

[3] Asher, JW, Young, RP and Ewing RD (2001): Seismic isolation of the Arrowhead Regional Medical Center. The structural design of tall buildings, vol. 10, pp. 321-334.

[4] T. Koh and M. Kobayashi (2004): Analytical study of modal coupling effect on mid-story isolation system by Eigen value analysis and random vibration analysis. Summaries of Technical Papers of Annual Meeting, Architectural Institute of Japan, B-2, Structures II, Structural Dynamics Nuclear Power Plants, pp. 333–334.

[5] Chang, K.C., Chuang, W.C., Wang, S.J. and Hwang, J.S (2015): From seismic isolation to building mass damper -an experimental and analytical study. Proc. of the Structural Engineering Frontier Conference, Yokohama, Japan.

[6] McNamara, R. J. (1997): Tuned mass dampers for buildings. Journal of the Structural Division, ASCE, vol. 103, pp. 1785-1798.

[7] Luft, R. W. (1979): Optimal tuned mass dampers for buildings. Journal of the Structural Division, ASCE, vol. 105, pp. 2766-2772.

[8] Wang, S.J., Lee, B.H., Chang, Y.W., Chang, K.C., Yu, C.H. and Hwang, J.S. (2017): Optimum Dynamic Characteristic Control Approach for Building Mass Damper Design. Proc. of the New Zealand Society for Earthquake Engineering Conference, Wellington, New Zealand.

[9] Wang, S.J., Lee, B.H., Chuang, W.C. and Chang, K.C. (2017): Optimum Dynamic Characteristic Control Approach for Building Mass Damper Design. Earthquake Engineering and Structural Dynamics, vol. 47, pp. 872-888.

[10] Tsai, H.C. and Lin, G.C. (1993): Optimum tuned-mass dampers for minimizing steady-state response of support-excited and damped systems. Earthquake Engineering and Structural Dynamics, vol. 23, pp. 957-973.

[11] Spencer B. F., Dyke S. J., Sain M. K. and Carlson J. D. (1997): Phenomenological model for magnetorheological dampers. Journal of Engineering Mechanics, vol. 123, no. 3, pp. 230-252.

[12] Lin, P. Y., Lin, T. K., and Hwang, J. S. (2013): A semi-active mass damping system for low-and mid-rise buildings. Earthquakes and Structures, vol. 4, no. 1.

[13] Liu, Y. F., Lin, T. K. and Chang, K. C. (2018): Analytical and Experimental Studies on Building Mass Damper System with Semi-active Control Device. Structural Control and Health Monitoring, vol. 25, no. 6.

Recent Variations of the Seismic and Geochemical Observations of the Tatun Volcano Group

Ya-chuan Lai[1], Hsiao-fen Lee[1], Li-Chin Chang[1], Chin-Hsing Liu[1] and Chia-Jui Teng[1]

賴雅娟[1]，李曉芬[1]，張麗琴[1]，劉進興[1]，鄧嘉睿[1]

Abstract

Among the volcanic activity in the northern Taiwan area, the geothermal and seismic activities of the Tatun Volcano Group (TVG) are still very strong. Recent studies over the past decade have suggested that the TVG can be considered as active volcanoes. The Taiwan Volcano Observatory at Tatun was established in 2011 to monitor volcanic activity and to evaluate the possibility of re-eruption in the TVG. Several different real-time observation systems including seismic observation, geochemical analyses, crustal deformation, and geothermal monitoring have been adopted for monitoring.

Recent geochemical observations show that a significant increase in the amount of helium (He) has been found from gas sampled from most of the fumaroles since early 2019. However, the helium isotopic ratio (3He/4He ratio) has not changed significantly. Meanwhile, the Stotal/HCl ratio of the gases indicates that there was a significant increase in the HCl concentration in all fumaroles from the end of 2018 to the first half of 2019. In addition, as compared with background data, the CO2/Stotal ratio of the gas composition suggests that the system has trended more towards hydrothermal activities. Several earthquakes with magnitude larger than M3.0 have recently occurred in the Tatun volcanic area. First, one sequence with two events occurred on January 28, 2019, accompanied by numerous aftershocks located in the Bayen area. Following the February 9 sequence, two earthquakes were detected in the Shilin area, south of Mt. Cising. An earthquake sequence occurred on August 6, also located at Mt. Cising, similar to the previous sequence. Combining the geochemical indicators and seismicity, we suggest that the activities of the TVG during late 2018 to 2019 are mainly caused by the disturbances of the hydrothermal system. The strong ground shaking of the two earthquakes that occurred in Bayen might have broken the stability of the hydrothermal system and opened a pathway to the surface. An increased amount of helium gas escaped from the smoother pathway, and thus an increasing amount of helium is detectable. In addition, the variation of HCl concentration is associated with the movement of fluid at great depths. At present, no obvious magmatic activity is suggested from the observations of the TVG; however, the volcano monitoring must be continued to forecast possible disasters caused by hydrothermal activities, such as phreatic eruptions.

Keywords: Tatun Volcano Group (TVG), volcano monitoring, seismic, geochemistry

Introduction

Hot springs and other geothermal activities of the Tatun Volcano Group (TVG) are still quite evident. The results of investigations over the prior decades, including seismicity, helium isotopes, volcanic gases, geothermal, and hot springs indicate that the volcanic activity may not have stopped. Moreover, such observations imply that a magma reservoir exists beneath the TVG (Lee et al., 2005; Lin et al., 2005a, 2005b; Song et al., 2000; Yang et al., 1999). The last eruption at the TVG was 5-6 thousand years ago as determined from ash dating (Belousov et al., 2010). It has been concluded that the TVG is an active volcano, using the definition that an active volcano is one that has erupted during the past 10,000 years. Furthermore, the magma reservoir at a depth of 20 km has been identified from S-wave shadows and P-wave delays in seismic observations (Lin, 2016).

The monitoring observations of the TVG in the past few years suggest that the magmatic system is

[1] National Center for Research on Earthquake Engineering

stable overall, and as such, no immediate eruption may be expected. However, the possibility of future re-eruption must still be considered. Given the substantial hydrothermal activities of the TVG, phreatic eruption may occur. Hence, detailed monitoring needs to be continued to detect significant volcanic activities. Recently, observations from geochemical and seismic monitoring have shown varying results, with a key observation being numerous earthquakes with magnitude greater than M3.0 occurred in the TVG, especially in 2019. Meanwhile, several important indicators from geochemical observations have also changed, indicating a slight change in activity in the Tatun volcanic area. This study focuses on the unusual phenomena of the TVG, as part of ongoing efforts to investigate and monitor possible hazards caused by hydrothermal activities.

Methods

Several different observation systems including seismic observations, geochemical analyses, crustal deformation, and geothermal monitoring were installed at the Taiwan Volcano Observatory at Tatun (TVO) for monitoring volcanic activity at the TVG. In the present study, the results of seismic observation and geochemical analyses are presented.

Since 2003, a dense seismic network was established for monitoring and investigating the seismicity of the TVG. Forty seismic broadband stations have been installed in the TVG, with the majority distributed southeast of the Shanjiao fault. With the network covering the area from Mt. Cising to Mt. Huangzui, where most of the microearthquakes have occurred, the spatial and temporal variations of seismicity of the TVG can be substantially detected. To understand the seismic characteristics of the TVG, the continuous waveform data was processed in detail, including microearthquake determination, spectrum analyses, etc. The location of seismic events is critical to clarify the activity of a volcano. Events are selected based on experience, and the P- and S-wave arrivals are carefully picked for the further locating the events.

The geochemical monitoring methods used by the observatory include direct sampling and continuous soil gas monitoring. The method used in the present study is direct sampling. Currently, more than ten fumaroles are active in the TVG. Six primary fumaroles were selected as regular sampling sites. The sampling frequency was once per month, and the gas compositions and helium isotopes were analyzed to monitor volcanic activity. The sampling locations are shown in Figure 1. Fumarolic gas was sampled using a Giggenbach bottle, which is commonly used by volcanologists. The volume of the Giggenbach bottle was approximately 170 mL, with 50 mL of alkali hydroxide solution kept in the bottle. The analysis covered H_2O, CO_2, H_2S, SO_2, HCl, CH_4, N_2, H_2, He, Ar, and CO. Iodine was adopted to obtain SO_2/H_2S ratios. Helium was collected and stored in vacuum glass bottles equipped with stopcocks at both ends. Helium isotopes were analyzed using a rare gas mass spectrometer (VG 5400) at the Department of Geosciences, National Taiwan University.

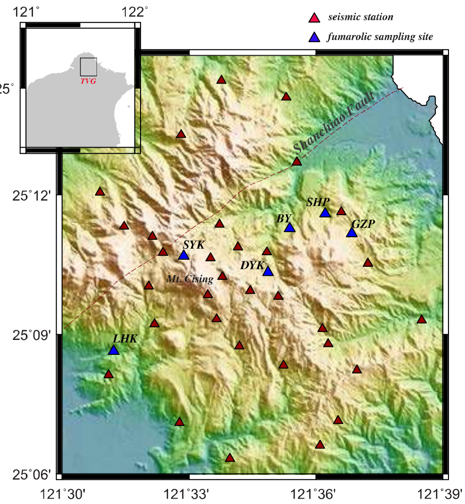

Fig. 1. Distribution map of seismic stations and fumarolic sampling sites.

Results and Discussion

1. Seismic event results

In the Tatun Volcano area, a total number of 3,657 microearthquakes were detected in 2019, which is much higher than the 2,327 detected in 2018. The seismicity has increased significantly, with approximately 300 earthquakes occurring per month on average, twice that of the background seismicity. In particular, several felt earthquake sequences occurred in the TVG recently, including earthquakes on January 28 in Bayen, on February 9 in the Shilin area, and on August 6 near Mt. Cising. All three sequences included several events with magnitudes greater than 3.0. Furthermore, there were twenty-nine earthquakes with magnitude larger than 2.5 detected in 2019. The three significant sequences that occurred in January, February, and August were all accompanied by a large number of aftershocks. Therefore, the number of earthquakes in these three months reached 827, 475, and 501, respectively.

Overall, the recent seismic activity of the Tatun volcano is mainly clustered in the Mt. Cising and Dayoukeng area, which is consistent with the background seismicity. However, the distribution of activity shows obvious spatial and temporal variations. In January, microearthquakes mainly occurred in the eastern part of the TVG, from Dayoukeng to the Bayen area. By contrast, from February to March, the distribution of microearthquakes moved westward, clustering at Mt. Cising. Then, the seismicity of the

TVG decreased until July, when the events near Mt. Cising were slight increased. Subsequently, the felt earthquake sequence occurred on August 6. Meanwhile, no large events occurred in the Dayoukeng and Bayen area, while the local seismicity continuously increased until October. It is worth noting that as the seismicity of Mt. Cising has recently risen, several earthquake swarms occurred in addition to the felt earthquake sequences.

On January 28, two earthquakes larger than magnitude 3.0 occurred in Bayen within two hours, accompanied by a large number of aftershocks. The significant number of aftershocks, 3-4 times the average of past sequences, indicates that a large amount of energy was released. Two months before this sequence, the geochemical observations also demonstrated anomalies, which may reflect the rising activity in the Bayan area.

The Shilin earthquake sequence on February 9 also included two felt earthquakes with magnitudes larger than 3.0. The epicenters of the main shock and aftershocks were located on the south part of Mt. Cising, a region where the most recent largest event, a ML 4.2 earthquake, occurred in 2014, yet where there is a low background seismicity of the TVG. The focal depth of this earthquake sequence is relatively deep, focused on 4-6 km. The source mechanism of the main shock was a non-double-coupled earthquake, similar to the result of the 2014 Shilin earthquake, and was related to the volcanic activity. However, as there is no essential anomaly synchronized with other observations, the possibility of large-scale magmatic activity has been excluded.

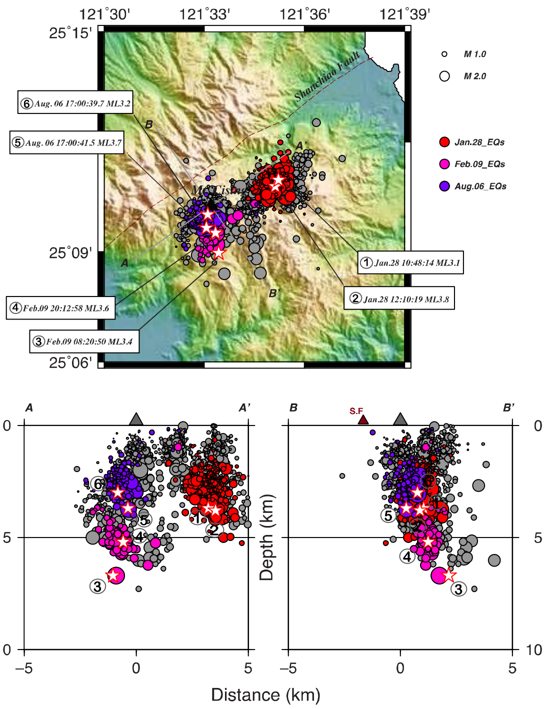

Fig 2. The distribution of the seismicity in 2019.

The distribution of the earthquake sequence on August 6, containing two earthquakes larger than 3.0, is similar to the background seismicity, with focal depths concentrated at 2-4 km. Although they were close to the epicenter distribution of the February 9 earthquake sequence, the sequences can be clearly distinguished (Fig 2).

2. Geochemical analysis results

The highest HCl concentration and $^3He/^4He$ ratio were detected in the Da-you-keng (DYK), which is the most active fumarole in the TVG area. This indicates a deep source of the gas composition in this area. Since August 2004, the HCl concentration and SO_2/H_2S ratio in the fumarolic gas samples has increased significantly. The HCl concentration and SO_2/H_2S ratio dropped after 2011 then increased slightly from the end of 2015 to 2016. However, the temperature of the fumarole has almost dropped to the boiling point since 2017. At the same time, the HCl concentration has dropped significantly. The volcanic activity in the DYK area seems to be more moderate from 2017 to 2018. Various indicators, except the SO_2/H_2S ratio, have decreased slightly from previous years and have been maintained at stable levels. However, there have been two sudden increases in the SO_2/H_2S ratio in 2019, in July and October, respectively. The SO_2/H_2S ratio is a key indicator of magmatic material. Although there is no fluctuation in other indicators, the source of the variations of the SO_2/H_2S ratio should be investigated.

The HCl concentration of gas samples from all fumaroles show an increasing trend since the end of 2018, especially after the January and February earthquakes at the beginning of 2019. The TVG area can be considered as more active than the previous two years based on the long-term trends of HCl. Combining all the geochemical indicators, the variations in the first half of 2019 were mainly caused by hydrothermal activities. However, it cannot be ruled out that the magmatic activities have also increased, especially in the second half of the year. In addition, the temperature of the Geng-zi-ping (GZP) geothermal area also changed significantly in 2019. The temperature of the fumarole changed by 10 ° C higher than in previous years, which is further evidence of the TVG becoming more active in 2019.

As shown in Figure 3 and 4, clear changes are evident in 2019. The triangle diagram of N_2-He-Ar clearly shows that the amount of helium from most fumaroles increased in 2019, especially in the BY geothermal area. However, the helium isotopic ratio ($^3He/^4He$ ratio) has not changed significantly. Therefore, the increase in helium may be caused by the pathway being smoother than usual, so more helium gas escapes. The helium isotopic ratio has not changed due to the same source. In addition, from the CO_2-HCl-S_{total} triangle diagram, there is an increase in HCl at all sampling sites, as well as an increase in hydrothermal activities. Overall, while the volcanic activities in 2017 and 2018 were dominated by hydrothermal activities, they were quieter than in previous years. In 2019, the TVG area has become more active. Although these activities are still dominated by hydrothermal activities, some magmatic events are observed in the second half of the year.

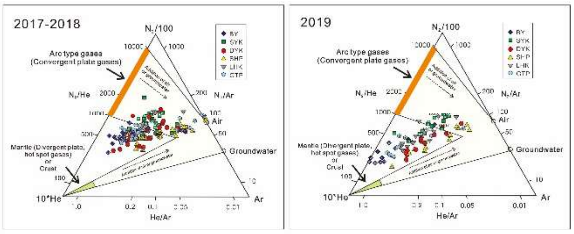

Fig. 3. The triangle diagram of N2-He-Ar.

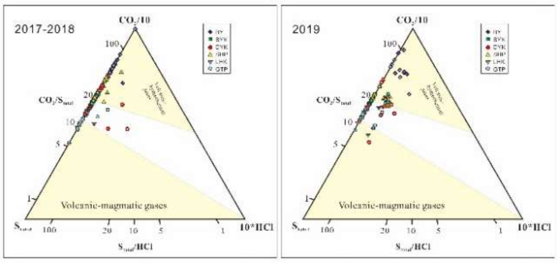

Fig. 4. The triangle diagram of CO_2-HCl-S_{total}.

Conclusions

Since early 2019, geochemical observations have shown that the amount of helium has clearly increased in most fumaroles, while the helium isotopic ratio ($^3He/^4He$ ratio) has not changed significantly. Almost simultaneously, from the end of 2018 to the first half of 2019, a significant increase in HCl concentration was detected in all fumaroles. Moreover, recent seismic observations illustrate the more active seismicity of the TVG, especially the several felt earthquakes with magnitudes larger than M3.0 that occurred in 2019.

Combining the significant variations of geochemical indicators and the unusually large earthquakes, the volcanic activity has gradually increased since the end of 2018. In the first half of the year, these activities were dominated by hydrothermal activities. The variations of geochemical observations are associated with the disturbance of the original system due to the felt earthquakes that occurred in January and February 2019. The pathway of gas became smother than usual, and thus the increase of helium and the change in the concentration of HCl concentration might due to the additional deep fluid migration. While there are a few signals of suspected magmatic events in the second half of the year, no substantial eruption will happen in the near future. At present, the volcano monitoring focuses on possible disasters caused by hydrothermal activities, such as phreatic eruptions.

References

1. Belousov, A., Belousova, M., Chen, C. H., Zellmer, G. F., 2010. Deposits, character and timing of recent eruptions and gravitational collapses in Tatun Volcanic Group, Northern Taiwan: Hazard-related issues. J. Volcanol. Geotherm. Res., 191, 205-221.
2. Lee, H.F., Yang, T.F., Lan, T.F., Song, S.R., Tsao, S., 2005. Fumarolic gas composition of the Tatun Volcano Group, northern Taiwan. Terr. Atmos. Oceanic Sci., 16, 843-864.
3. Lin, C.H., 2016. Evidence for a magma reservoir beneath the Taipei metropolis of Taiwan from both S-wave shadows and P-wave delay, Scientific Reports, Vol. 6, 39500.
4. Lin, C. H., Konstantinou, K. I., Pu, H. C., Hsu, C. C., Lin, Y. M., You, S. H., Huang, Y. P., 2005. Preliminary results from seismic monitoring at the Tatun volcanic area of northern Taiwan. Terr. Atmos. Ocean. Sci., 16, 563-577.
5. Lin, C. H., Konstantinou, K. I., Liang, W. T., Pu, H. C., Lin, Y. M., You, S. H., Huang, Y. P., 2005. Preliminary analysis of volcanoseismic signals recorded at the Tatun Volcano Group, northern Taiwan. Geophys. Res. Lett., 32, L10313, doi: 10.1029/2005GL022861.
6. Song, S.R., Yang, T.F., Yeh, Y.H., Tsao, S.J., Lo, H.J., 2000b. The Tatun volcano group is active or extinct? J. Geol. Soc. China, 43, 521–534.
7. Yang, T. F., Sano, Y., Song, S. R., 1999. 3He/4He ratios of fumaroles and bubbling gases of hot springs in Tatun Volcano Group, North Taiwan. Il Nuovo Cimento Soc. Ital. Fisica C, 22, 281-286.

Seismic Testing, Analysis, and Optimization of Low-Yielding-Strength Steel Panel Dampers in Moment-Resisting Frames

Ming-Chieh Chuang [1], Kung-Juin Wang[2], Keh-Chyuan Tsai[3], Ching-Yi Tsai[4], and You-Jin Zhon[5]

蔡克銓 [1]、鍾侑津 [2]、王孔君 [3]、莊明介 [4]、蔡青宜 [5]

Abstract

Steel panel dampers (SPD) are effective energy-absorbing devices that can be added in traditional moment-resisting frames (MRF) to enhance effectively the lateral stiffness, strength, and ductility capacities of MRFs. MRFs equipped with SPDs are referred to as SPD-MRFs in this study. An SPD is fabricated by joining three wide-flange sections together: the middle inelastic core (IC) and the top and bottom elastic joints (EJ). Under severe earthquakes, the IC dissipates energy through large shear deformation, while the EJs remain elastic. Stiffeners can be added on the IC to prevent premature buckling. This study developed an optimization design procedure that provides optimal designs of the SPDs and the associated boundary beams, such that the seismic-resistant requirements can be met with minimal steel usage. The efficacy of the proposed optimization procedure was investigated by considering six SPD-MRF models designed using three different design principles, with two different materials (LYP100 and SN400B) for the ICs. The products of the three design methods are referred to as: (1) the original design (OD), obtained using the traditional capacity design method; (2) the basic design (BD), obtained using the proposed optimization design procedure; and (3) the practical design (PD), obtained by enhancing the SPD and boundary beams' stiffness to be 1.5 times that of the BD for the three stories that have the largest inter-story drift ratio in its fundamental mode shape. Push-over analyses and nonlinear time-history analyses were performed on the six SPD-MRF models. The BDs were found to use 12% less steel than the ODs, while the BDs' initial stiffnesses were smaller than that of the ODs. Meanwhile, the PDs were found to use 6% less steel than the ODs, while their initial stiffnesses were approximately equal to that of the ODs. In addition, the total building drift of the PDs was found to be more evenly distributed across the six stories than in the corresponding ODs. The SPDs that used LYP100 and SN400B as the IC materials resist 40% and 37% of the story shear, respectively. To investigate experimentally the mechanical and seismic behaviors of the SPDs and the SPD-MRFs, cyclic and conventional hybrid tests were also performed on two full-size SPD specimens, which used LYP100 as the material for the ICs. An advanced online model updating technique was also utilized in the hybrid tests to improve significantly the associated numerical elements in the analyzed model. Nonlinear time-history analyses showed that under the maximum considered earthquake (MCE), the average demand of the IC shear strain was 4.13%, which is significantly lower than the capacities of the two specimens (9.8% and 14.4%, respectively). Experimental results also showed that the cumulative plastic deformation was larger than 1339, suggesting that the SPD-MRFs would survive at least four attacks of MCE-level earthquakes.

Keywords: Parameter identification, online model updating, hybrid simulation, optimization, steel panel damper.

[1] Professor, Department of Civil Engineering, National Taiwan University
[2] Graduate Student, Department of Civil Engineering, National Taiwan University
[3] Technologist, National Center for Research on Earthquake Engineering
[4] Associate Researcher, National Center for Research on Earthquake Engineering
[5] Postdoctoral Fellow, Department of Civil Engineering, National Taiwan University

Introduction

Steel panel dampers (SPD) are effective energy-absorbing devices that can be added to traditional moment-resisting frames (MRF), as shown in Fig. 1, to enhance effectively the lateral stiffness, strength, and ductility capacities of MRFs. In the present study, MRFs equipped with SPDs are referred to as SPD-MRFs. As illustrated in Fig. 2, an SPD is fabricated by joining three wide-flange sections together: the middle inelastic core (IC) and the top and bottom elastic joints (EJ). The flanges are identical and run continuously through the three segments, while the web of the IC is made of a thinner plate or weaker material such as LYP100. The idea is to allow the IC to develop significant inelastic shear deformation and thus dissipate earthquake-induced energy during severe earthquakes.

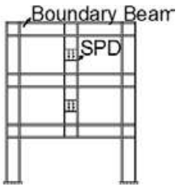

Fig. 1 SPD-MRF.

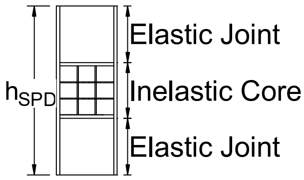

Fig. 2 SPD.

The present study improves an optimization design procedure originally proposed by Chang *et al.* [1]. To investigate the efficacy of the refined optimization design procedure, using a six-story SPD-MRF as the benchmark model [2], the seismic performances of different SPD-MRFs designed using different design methods are compared. In addition, the effects of using different materials for the ICs are also studied. An experimental investigation using a series of cyclic and hybrid tests was conducted at the National Center for Research on Earthquake Engineering (NCREE) laboratory to study the actual behaviors of SPDs and of the corresponding SPD-MRFs.

SPD Fundamentals

Inelastic core

The IC is the principle component that develops significant shear deformation and thereby dissipates input energy during seismic events. It can be considered as a "deformation control element" in seismic-resistant frames [3]. The shear strength of the SPD is determined by the IC's shear strength, which can be calculated by

$$V_y = A_{v,IC}\tau_y = d_{SPD}t_{w,IC}\tau_y \qquad (1)$$

where $A_{v,IC}$ is the IC web area, τ_y is the shear yield strength of the IC web, d_{SPD} is the depth of the SPD, and $t_{w,IC}$ is the thickness of the IC web.

Elastic joint

EJs are the segments that connect the IC to the upper and lower boundary beams. The lengths and sections of the top and bottom EJs can be equal. The EJs are designed to remain elastic even when the IC develops its maximum shear force, with both the material overstrength and strain hardening considered. EJs should be considered as "force control elements" as defined in seismic codes.

Stiffener

Stiffeners can be added to the SPDs to delay the premature buckling that might develop during severe earthquakes [1, 2, 4]. Horizontal end stiffeners are added to separate the IC and EJs. In addition, an SPD can have several buckling restraining stiffeners that run vertically or horizontally through the IC to restrain the IC's out-of-plane deformation. The efficacy of different added stiffening methods on SPDs was also studied using a numerical Abaqus simulation as well as experimental structural testing.

Optimization Designs of SPD-MRF

A previous optimization procedure [1] is refined in the present study to provide optimal designs for cruciform substructures composed of SPDs and boundary beams, as shown in Fig. 3. The substructure is taken out of the SPD-MRF by cutting the top and bottom SPDs and the boundary beam at the four inflection points. Given the strength demand of the SPD on a specific story and starting with an arbitrary initial design of the substructure, the optimization procedure iteratively finds the optimal sizes of the SPD and the boundary beam such that minimal steel is used while the seismic-resistant requirements are still satisfied. Once the optimal-design cruciform substructure is found, the optimization procedure can then be applied to find the optimal designs of cruciform substructures of adjacent stories.

The six-story SPD-MRF examined in this study is located on a hard site in Chiayi City, Taiwan. Its six-bay longitudinal frames are traditional MRFs, while SPDs are equipped in its transverse MRFs, as shown in Fig. 4. The efficacy of the optimization procedure was evaluated by comparing the stiffness and the steel usage of the products of three different design methods. The design that considers only the capacity design principle is referred to as the "original design" (OD) [2]. Using the OD as the initial design and applying the proposed optimization procedure, a "basic design" (BD) is then obtained. By increasing the stiffness by 1.5 times that of the BD for the three stories that have the maximum inter-story drift ratios in their fundamental mode shapes, a "practical design" (PD) is obtained. In addition, the effect of using low-yield-strength steel (LYP100) for the IC was also compared against using normal steel (SN400B). Pushover analyses and nonlinear time history analyses were performed on these SPD-MRF models.

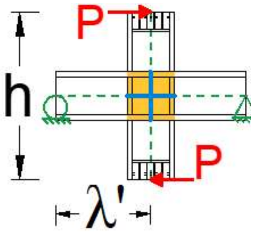

Fig. 3 The substructure to be optimally designed.

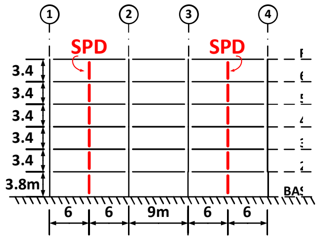

Fig. 4 The SPD-MRF plan view.

1st mode inter-story drift ratios

As shown in Fig. 5, modal analyses revealed that for both the OD and BD, the three stories that have the largest inter-story drift ratios are the second, third, and fourth floors. Therefore, by increasing the stiffness of these three stories by 1.5 times, the corresponding PD is obtained. The pushover analyses revealed that the PD had more evenly distributed inter-story drift ratios.

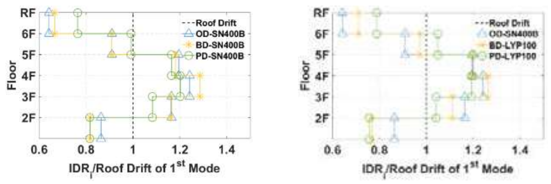

Fig. 5 The inter-story drift ratios in the first mode.

Periods, steel usage, and system overstrengths

Table 1 compares the periods, steel usage, and system overstrengths of the corresponding SPD-MRF models. BD uses 12% less steel than the OD, yet the period of BD is larger than that of the OD by more than 6.3%. The PD uses 6% less steel than the OD does. However, advantageously, the period of the PD is approximately the same as the period of the OD. System overstrength is the ratio of the actual base shear to the design base shear when the roof drift ratio is 2%. It can be seen that for all models the values range from 2.7 to 3, which is close to 3 as suggested in the seismic provisions [5].

Table 1 Periods, steel usage, and system overstrengths.

Model	Period (s)	Reduced steel (%)	System overstrength
OD-SN400B	1.26	---	2.86
BD-SN400B	1.36	12	2.72
BD-LYP100	1.34	12	2.71
PD-SN400B	1.25	6.3	3
PD-LYP100	1.26	10	2.86

Shear ratios

It was found that the average shear taken by the SPD with LYP100 IC is approximately 40% of the total shear. For SN400B, the ratio is approximately 37%. Advantageously, these numbers are close to the expected values for the OD.

Experimental Validation

Two specimens (4L0T and 5L0T) were tested at the NCREE lab. They have four and five longitudinal stiffeners, respectively, and zero transverse stiffeners. The IC material is LYP100. SN400B is used for all other parts in the SPD specimens. The two specimens differ only in the number of stiffeners. However, the total steel usage and hence the total stiffness for the stiffeners on the two specimens is equal. Cyclic tests and hybrid simulations were conducted. The purpose of these tests was to investigate: (1) the influence of the method of adding stiffeners onto the SPDs on the SPDs' shear deformation capacity, (2) the cumulative plastic shear deformation capacity, and (3) the seismic-resistant capacity of the SPDs with ICs made of the low-yield-strength steel LYP100.

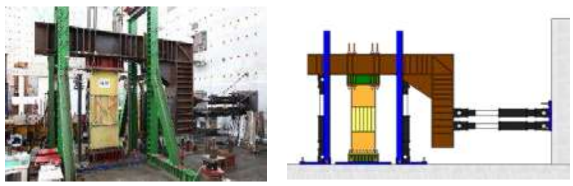

Fig. 6 The test configuration.

The capacities of the ICs' shear deformation for 4L0T and 5L0T are 9.8% and 14.4%, respectively. Meanwhile, the corresponding CPDs are 1339 and 2372, respectively. This suggests that the 5L0T's seismic-resistant capacity is higher than that of the 4L0T, and indicates that when using stiffeners to delay premature buckling, it is more effective to increase the number of the stiffeners instead of increasing the thickness of each stiffener. More details about the testing results of the hybrid simulation on 5L0T can be found in [8].

Nonlinear Response Time-History Analysis

Using 240 site records of ground excitations for Oakland, California [9], nonlinear response time-history analyses were performed to investigate the seismic-resistant behaviors and capacities of the SPD-MRFs. The 240 records include all three levels of ground motions: the maximum considered earthquake (MCE; 2475-year return period), the design-basis earthquake (DBE; 475-year return period), and the service-level earthquake (SLE; 72-year return period). The maximum time histories of the shear deformation responses under those 240 earthquake excitations of the

SPDs that use LYP100 as the IC material are shown in Fig. 7. The CPD demands for the ICs under the MCE are 298 and 322 for BD-LYP100 and PD-LYP100, respectively. By comparing with the CPD capacities (1339 and 2372 for the BD-LYP100 and PD-LYP100, respectively) obtained from experimental investigation, these results suggest that BDL-LYP100 and PD-LYP100 have sufficient capacity to survive respectively more than four and seven occurrences of the MCE. This clearly reveals that SPDs are excellent devices to be used in enhancing the seismic-resistance capacity of traditional MRFs.

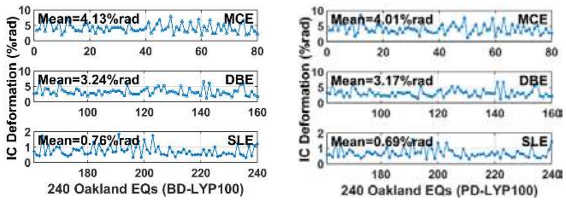

Fig. 7 The maximum IC shear deformation under the 240 ground excitations.

Conclusions

1. Starting from the OD, the proposed optimization design procedure can quickly and effectively provide a BD that uses the least amount of steel. The proposed optimization design procedure also supports providing a PD in which the stiffnesses of certain stories that have larger inter-story drift can be increased such that the total building drift can be more evenly distributed.
2. All the system overstrengths of the SPD-MRF models designed using the proposed design procedure are approximately 3, which is close to the requirement for MRFs in seismic-resistant building codes. In addition, the shear ratios of the BDs and PDs are found to be approximately the same as those of the ODs.
3. Both the capacities of the IC shear deformation and the CPD of 5L0T are larger than those of 4L0T are. This suggests that, when using stiffeners to delay premature IC buckling, increasing the number of stiffeners is more effective than increasing the stiffeners' thicknesses.
4. The test results showed that using 4L0T and 5L0T as the seismic-resistant devices allows the corresponding SPD-MRFs to survive respectively more than four and seven occurrence of MCE. This indicates that SPDs with ICs made of LYP100 material have excellent seismic-resistant capacity.

References

1. 張舉虹、蔡克銓，「含鋼板阻尼器構架最佳化設計研究」，結構工程，第 34 卷，第 1 期，第 27~56 頁，2019 年。
2. 許仲翔、李昭賢、金步遠、蔡克銓，「含鋼板阻尼器構架耐震設計與分析」，結構工程，第 32 卷，第 2 期，第 5~34 頁，2017 年。
3. ASCE 7-16 (2016) "Minimum Design Loads for Buildings and Other Structures" American Society of Civil Engineers.
4. Chen, Z., Ge, H., Usami, T. (2006) "Hysteretic Model of Stiffened Shear Panel Dampers." Journal of Structural Engineering, ASCE, 132, 478-483.
5. AISC 341-16 (2016). "Seismic Provisions for Structural Steel Buildings." American Institution of Steel Construction, Chicago.
6. 鍾侑津 (2019)「含低降伏鋼板阻尼器最佳化構架之耐震性能分析與試驗研究」，台大土木系結構組碩士論文。蔡克銓教授指導。
7. Wang K.J., Chuang M.C., Li C.H., Tsai K.C. (2019). "A Distributed Computing Platform for Conventional Hybrid Simulation," Proceedings of the COMPDYN 2019, Crete, Greece, Paper # 18910.
8. Chuang M.C., Hsieh S.H., Tsai K.C., Li C.H., Wang K.J., Wu A.C. (2018). "Parameter identification for on-line model updating in hybrid simulations using a gradient-based method," Earthquake Engineering and Structural Dynamics, 47(2): 269-293.
9. Baker, J. (2010). "PEER site-specific ground motions for Oakland: record selection notes."

Joint Modeling of the Receiver Function and Horizontal to Vertical Spectral Ratio for Shallow Shear Velocity Structures

Che-Min Lin[1], Chun-Hsiang Kuo[1], Jyun-Yan Huang[2] and Kuo-Liang Wen[3]

林哲民[1]、郭俊翔[1]、黃雋彥[2]、溫國樑[3]

Abstract

It has been proven, in our previous study, that receiver functions (RF) of strong-motion records are effective for estimating shallow subsurface structures, especially for bedrocks and basin structures. The shallow shear velocity profiles of over 700 strong-motion stations in Taiwan were estimated by modeling of receiver functions. The theoretical transfer functions of stations derived based on their velocity structures are calculated and compared with the average horizontal to vertical spectral ratio (HVSR) of historical records to evaluate the site amplification of the results. Most of the theoretical site amplifications agree well with the observed results. However, some stations show notable differences between the theoretical and observed amplification, indicating misestimates of the inverted velocity profiles from the receiver functions. Therefore, an approach is herein designed, termed the HVSREC method, to model the RF and HVSR jointly for estimating shallow velocity profiles beneath strong-motion stations, as RFs are primarily sensitive to velocity contrasts based on the time-domain converted phases, and HVSRs are also sensitive to velocity contrasts but based on the frequency domain site amplification. The joint modeling provides a reliable estimation of velocity structures that conform to the real site effects in the time and frequency domains. The velocity contrasts, generating the converted phases and controlling the site amplification, can be reconstructed in the estimated velocity structure. The differences between the results estimated from the RF, HVSR, and joint methods are also compared and discussed.

Keywords: shear velocity structure, joint modeling, receiver function, horizontal-to-vertical spectral ratio

Introduction

Taiwan is located at a complex convergent plate boundary with high seismicity. The high-speed geological activities, including rising, weathering, and erosion generate not only high mountains but also many broad and deep alluvium basins. Beneath a strong ground motion, the soft alluvium tends to amplify and extend the input seismic waves. The seismic site effect of a soft site may lead to an earthquake disaster. Therefore, when trying to predict or simulate strong ground motions, shallow underground structures present a significant challenge. However, the resolutions of most 3D tomography velocity models, including the body-wave and surface-wave method, at shallow depths are not sufficient to reproduce real site-effects. In our previous study, the shallow shear velocity profiles of over 700 strong motion stations (TSMIP) were estimated using the receiver function (RF) method and combined as a preliminary 3D model of Taiwan (Lin et al., 2018). The results agree well with the background geology. The major sedimentary basins can be identified by their low velocity. In addition, important site parameters such as engineering bedrock, Vs_{30}, and $Z_{1.0}$ were provided.

To confirm the shallow velocity structure from the RF method, the theoretical SH-wave transfer function (Haskell, 1960) of the estimated velocity profile was compared with the empirical transfer function, which is the average horizontal to vertical spectral ratio of historical seismograms. Most of the theoretical transfer functions correspond well with the

[1] Research Fellow, National Center for Research on Earthquake Engineering
[2] Assistant Researcher, National Center for Research on Earthquake Engineering
[3] Professor, Department of Earth Sciences, National Central University

empirical ones, meaning that the estimated shallow velocity structures of the stations can reproduce the observed real site characteristics.

However, it is clear that the theoretical transfer functions of the RF profiles estimated for some stations show apparent differences with the empirical results. The misestimating of velocity structures may result in inappropriate results when applied to ground motion predictions or earthquake simulations. Therefore, this study tries to develop a new method to better estimate the shallow shear velocity structure of the stations with improper prior results.

Joint Modeling Method for Shallow Shear Velocity Structures

The receiver function (RF) is a method to study shear velocity discontinuities using seismic waveforms. In this method, the radial component is divided by the vertical component in the frequency domain to eliminate the source and instrument effect to clarify the converted phase in the time domain. The generated converted phases can be simulated to provide information on underground structures. Therefore, the accuracy of the RF method is controlled by the waveform fitting in the time domain, and misestimating is possible as it ignores the site information of the frequency domain.

A simple method to solve the misestimating of the estimated velocity profile in the frequency domain is to combine the RF and HVSR method to do joint modeling, as there are some common points between them. They both only need the seismic data of a single station, and they are both based on the concept that the horizontal component divided by the vertical component in the frequency domain would eliminate source and path effects. Additionally, the joint modeling will provide a velocity profile that can regenerate the waveform in the time-domain and amplify it in the frequency-domain simultaneously. This would benefit future ground motion simulations.

Based on these concepts, this study develops a new method to simulate the RF waveform and HVSR simultaneously for joint modeling the shallow shear velocity structure. This new method was named the HVSREC method. Figure 1 illustrates the developed HVSREC joint modeling method. For a seismogram, the waveforms between P-wave and S-wave arrivals are captured to obtain the RF, which presents the converted phase from velocity contrasts beneath the target station. The waveforms after S-wave arrival are captured to calculate the HVSR from their three-component Fourier spectrum. Then, the average RF and HVSR are calculated from all of the historical seismic records of the target station, and they are simulated together by a forward modeling procedure to find a velocity profile.

In the forward modeling, a genetic algorithm (GA) is used to search for the Vs profile that best regenerates the observed RF and HVSR. The Green's function of the velocity profile is calculated based on the generalized R/T coefficient method (Kennett, 1983), where the fitness function of the RF is defined by the root-mean-square error between the observed RF and the synthetic Green's function. The Haskell-Thomson theoretical transfer function of SH-waves is used (Haskell, 1960) to simulate the observed HVSR in the joint modeling, and the fitness function of the HVSR was defined by the Pearson correlation coefficient and the difference of the pre-dominant frequency between the observed HVSR and the synthetic transfer function. The weights set are 60% and 40% for the fitness of the RF and HVSR, respectively, to obtain the combined fitness value of the GA joint modeling. The velocity model with the highest combined fitness value is the final result after over two million calculations of the forward modeling.

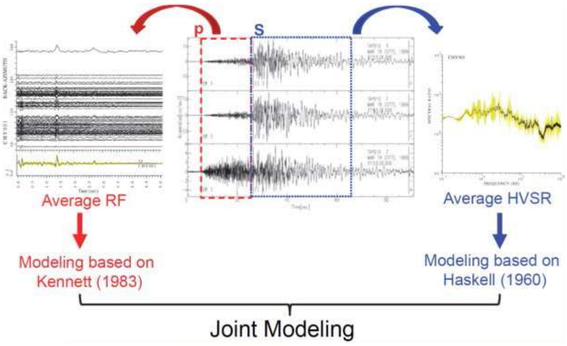

Fig. 1. Illustration of the HVSREC joint modeling method.

Strong-motion Stations Tests

Some TSMIP stations were selected to test the HVSREC joint modeling method to evaluate its feasibility and reliability. Figure 2 presents the results of the HVSREC method for station HWA004. The blue dashed line is the searching range of the velocity model. After the joint modeling, the bold black line is the final model. Its synthetic RF (black line at the upper-right corner of Fig. 2) shows good agreement with the observed data (red line at the upper-right corner of Fig. 2), especially for the waveform within the first one second. However, the later and smaller phases are not simulated by the synthetic RF very well. The synthetic HVSR (black line at the lower-right corner of Fig. 2) also mostly agrees with the observed data, except for an overestimation at the higher frequency band. The improvement of the HVSR simulation by using the joint modeling method is apparent and clear. Figure 3 shows the results of the HVSREC method for the other four stations. Overall, the linear variation and predominant frequencies of the HVSRs are all simulated well. The major and earlier phases of the RFs are also simulated well, while the later phases do not agree as well, similar to the result of station HWA004. The misestimate of the later phase of the RFs may result from the HVSRs being dominated by the upper and major underground structures with higher velocity contrasts. The joint method dilutes the influence of the deeper structure in the combined fitness.

Here, the RF modeling method, HVSR modeling method, and HVSREC joint modeling method are applied to four stations. Figure 4 compares the results, including the final velocity profiles, RFs, and HVSRs, from the three methods. While these three methods all generate similar shear velocity structures with some minor nonconformities, their corresponding RFs and HVSRs show relatively large differences in some cases. For station TTN035, the three estimated profiles all show a high-velocity bedrock near the ground surface. The three methods can obtain this kind of simple structure well. The synthetic RFs and HVSRs all fit the observations. In contrast, the results of the RF and HVSR methods show obvious differences for the other three stations. The synthetic HVSR of the model from the RF method does not agree with the observed HVSR, and the synthetic RF of the model from the HVSR method does not agree with the observed RF. In these cases, the HVSREC method is helpful for finding a compromising velocity model that shows a better agreement with the real site response both in the time and frequency domains by fitting the RF and HVSR simultaneously.

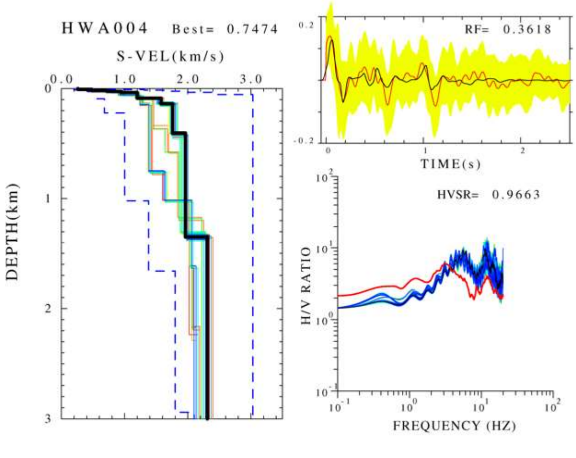

Fig. 2. Results of the HVSREC method for station HWA004.

Finally, the HVSREC joint modeling method was applied to the fifty TSMIP stations that showed discrepancies in the synthetic HVSR from the results of the RF modeling method (Lin et al., 2018). The differences of the RF fitness and HVSR fitness between the RF modeling method and the HVSREC joint modeling method are calculated and plotted in Figure 5. The RF fitness of the HVSREC method is mostly lower than the RF method, as the involvement of the HVSR would decrease the matching of the RF, as mentioned in the prior study. The decrease of the RF fitness is within 10 % for over half of the cases, and within 20 % for most cases, except one. However, the joint modeling method increases the HVSR fitness for at least 50 % of the cases as compared to the RF method. Over half of the cases even present a more than 100 % increase in the HVSR fitness. The improvement of the HVSR fitness is not only from the linear coefficient of the spectral ratio but also the predominant frequency. The results show that the use of only the RF method may lead to a misestimate as it would simulate the signal in detail and lose the other important information. The HVSREC joint modeling method may sacrifice a minor amount of RF fitness, yet has a much better agreement with the HVSR.

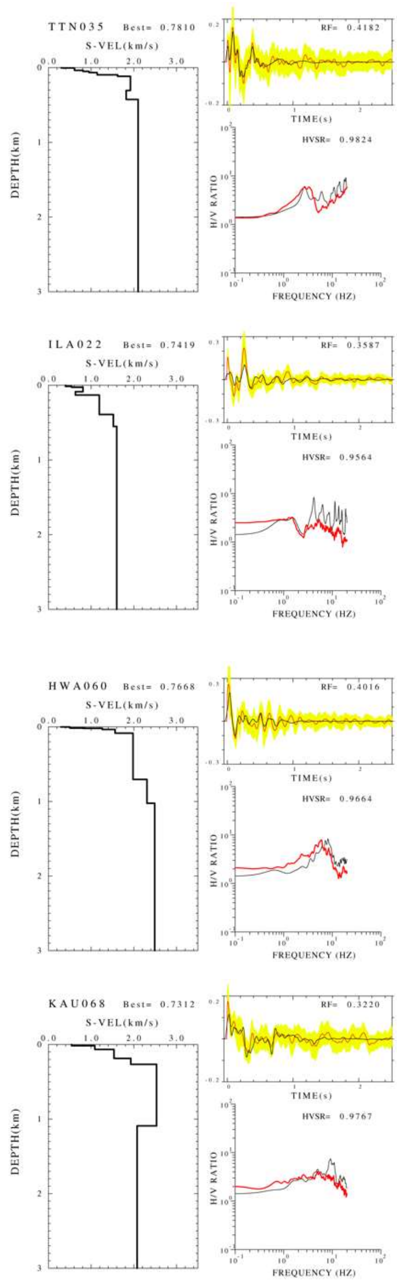

Fig. 3. Results of the HVSREC method for four stations.

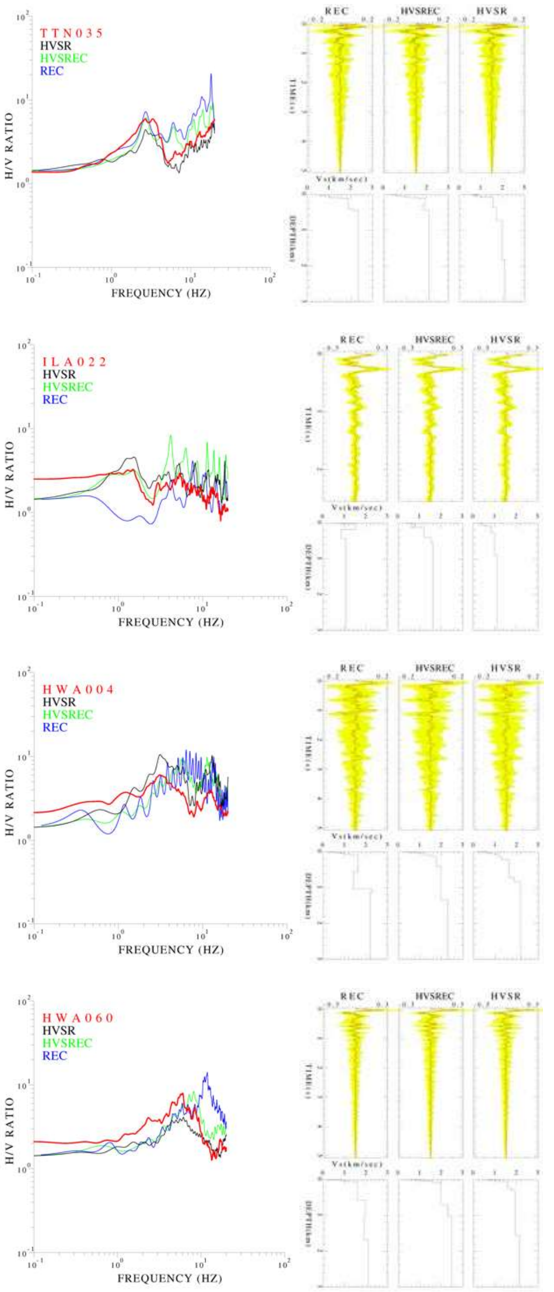

Fig. 4. Cross comparisons of results between the RF, HVSR, and HVSREC methods for four stations.

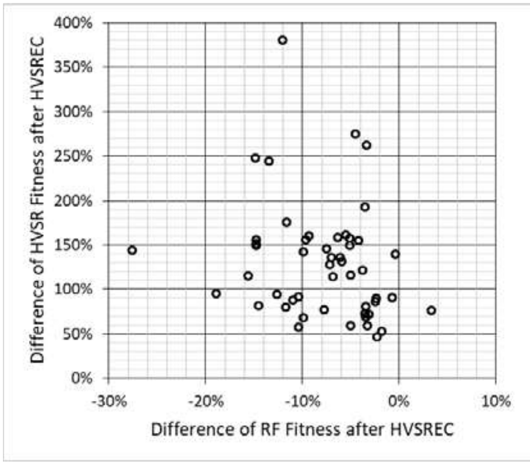

Fig. 5. Differences in RF and HVSR fitness of the HVSREC method as compared to the RF method.

Conclusions

The tests and comparisons presented herein prove that the proposed HVSREC joint modeling method for shallow shear velocity structures takes advantage of two kinds of site data, including the converted phased and arrival times of the receiver function from the velocity contrasts, and the site amplification and dominant frequency of the horizontal to vertical spectral ratio. The shallow velocity structures of the strong motion stations, estimated by the new method, could conform to the real site effect in the time-domain and frequency-domain simultaneously. The HVSREC method can be applied to the Taiwanese stations with questionable structures. The reliable results will contribute to the three-dimensional velocity model of Taiwan to reflect the observed characteristics of strong ground motion.

References

Haskell, N. A., (1960), “Crust reflection of plane SH-waves”, J. Geophys. Res., 65, pp. 4147-4150.

Kennett, B. L. N., (1983), “Seismic wave propagation in stratified media”, Cambridge University Press, 342pp.

Lin, C. M., Kuo, C. H., Huang, J. Y., Hsieh, H. H., Si, C. C., Wen, K. L., (2018), “Shallow Shear-wave Velocity Structures of TSMIP Stations in Taiwan”, NCREE-18-019, 141pp.

NARLabs

National Center for Research on Earthquake Engineering

No. 200, Sec. 3, Xinhai Rd., Taipei 106219, Taiwan(R.O.C.)

Tel: +886-2-6630-0888 Fax: +886-2-6630-0858

http://www.ncree.org.tw